University of Alberta

Ultrasonic Signal Processing for Non-Destructive Testing and Evaluation

by

Seied Mohammad Reza Hoseini

A thesis submitted to the Faculty of Graduate Studies and Research
in partial fulfillment of the requirements for the degree of

Doctor of Philosophy

Department of Mechanical Engineering

Spring 2013
Edmonton, Alberta

Abstract

In this thesis, ultrasonic B-scan signal processing is investigated. A B-scan displays a cross-sectional view of the test piece and defects within it. Compared to A-scan signals, B-scan images offer more reliable fault detection. Nonetheless, traditional ultrasonic signal processing methods are mostly based on A-scan signals and little research has been reported on ultrasonic B-scan signal processing. The aim of the current thesis is to investigate different aspects of ultrasonic B-scan signal processing including denoising, parameter estimation and fault identification.

The stationary wavelet transform (SWT) is used to denoise B-scan signals. SWT exhibits a good denoising performance. A thresholding scheme based on the amplitude of the analytic signal was reported to further improve the denoising performance of the stationary wavelet transform. In this work, the application of the analytic wavelet thresholding is extended to two dimensional signals for removing noise from B-scans. In addition, an extra step is proposed for removing noises caused by the waves reflected at the wedge-specimen interface.

The ultrasonic signal is further processed to extract fault related features. A model-based method is proposed for estimating parameters of ultrasonic echoes such as the time of arrival of echoes. Despite many advantages such as excellent estimation accuracy, the current model-based methods applied to ultrasonic signals suffer from a major disadvantage. These methods often involve solving an optimization problem with many parameters. Some researchers calculated the envelope of the ultrasonic

echo to reduce the number of parameters by removing phase and frequency from the parameter set. A quasi maximum likelihood estimator is proposed for estimating parameters of the echo envelope. Using experimental and simulated signals, it is shown that the proposed method improves the parameter estimation compared to the state of the art available in the literature.

Current crack sizing techniques often neglect the effect of the crack orientation when estimating the crack length. This introduces errors in estimating the length of inclined cracks. A modified relative arrival time technique is proposed for estimating the crack length and inclination angle using the relative time of arrival of the echo diffracted from the crack tip with respect to the echo reflected from the crack corner.

Acknowledgements

First and foremost, I offer my sincerest gratitude to my principal supervisor, Prof. Ming J. Zuo, for sharing his expertise and giving me guidance throughout my study and research. I would also like to thank him for the financial support during my PhD program. The good advice and support of my co-supervisor, Prof. Xiaodong Wang, has always been insightful and invaluable to me, for which I am extremely grateful.

In my daily work at Reliability Research Lab, I have been blessed with a friendly and cheerful group of fellow students, postdoctoral fellows and visiting scholars to only some of whom it is possible to give particular mention here. I would like to thank Ajit Sahoo for actively participating in conducting ultrasonic experiments and providing experimental data which I have used in this thesis, and Dr. Yonghong Zhang and Dr. Hanxin Chen for giving me insights into ultrasonic signal processing. Also, I would like to thank Tahmina Ferdousi Lipi and her husband Md. Noor-E-Alam, Ramin Moghaddass and Mayank Pandey for being great friends of mine.

During my PhD program, I had the chance to work on a project on condition monitoring of planetary gear sets. This project has greatly extended my knowledge in signal processing. Later, I have been benefited from it profoundly for my thesis. I would like to thank Prof. Zuo for giving me the opportunity to be involved in this project. During this project, I have also enjoyed and learned a lot from collaborating with my colleagues Dr. Yaguo Lei, Dr. Tejas Patel, Jian Qu, Mayank Pandey, and Zhiliang Liu.

I am truly grateful to Dr. Alireza Simchi for his valuable suggestions on statistical signal processing.

I cannot express my gratitude enough to my wife Fatemeh for her personal support and great patience at all times, and my dearest daughter for making even the toughest days brighter. My sincerest gratitudes and appreciation go to my parents for their faith and unequivocal support to me.

Contents

List of Tables

List of Figures

Acronyms

AIC	Akaikeps Information Criterion
CAIC	Consistent Akaikeps Information Criterion
CRB	Cramer-Rao Bound
DWT	Discrete Wavelet Transform
EDM	Electro-Discharge Machining
FEA	Finite Element Analysis
FEM	Finite Element Method
FIM	Fisher Information Matrix
FT	Fourier Transform
GEM	Gaussian Echo Model
GENVM	Gaussian Envelope Model
HF	High Frequency
HT	Hilbert Transform
LF	Low Frequency
LSE	Least Square Estimation
NDT	Non-destructive Testing
NDT&E	Non-destructive Testing and Evaluation
PDF	Probability Distribution Function

QL	Quasi Likelihood
QLL	Quasi Log-Likelihood
QML	Quasi Maximum Likelihood
QMLE	Quasi Maximum Likelihood Estimation
RATT	Relative Arrival Time Technique
SNR	Signal-to-Noise Ratio
SWT	Stationary Wavelet Transform
TOA	Time Of Arrival
TOF	Time Of Flight
TOFD	Time Of Flight Diffraction
UT	Ultrasonic Testing
WGN	White Gaussian Noise
WT	Wavelet Transform

List of Symbols

Symbol	Description
∇	Vector differential operator, $\nabla = \hat{x}\frac{\partial}{\partial x} + \hat{y}\frac{\partial}{\partial y} + \hat{z}\frac{\partial}{\partial z}$
α_t	Temporal bandwidth factor
α_x	Spatial bandwidth factor
δ	Crack length
ϵ	Error
γ	Crack angle
λ	Lame's first parameter
λ	Wavelength
μ	Lame's second parameter, see equation(2.1)
μ	Scale parameter of wavelet function, see equation(3.1)
ν	Poisson ratio
ω	Angular frequency
ϕ	Phase angle
Φ	Potential scalar
$\overrightarrow{\Psi}$	Potential vector
θ	Ultrasonic beam angle
$\boldsymbol{\theta}$	Parameter vector
ρ	Density
σ	Standard deviation, in particular, noise standard deviation
τ	Time of flight
τ	Translation parameter of wavelet function, see equation(3.1)
ζ	Signal-to-noise ratio defined as $\zeta = \frac{E_s}{\sigma^2}$
c_L	Longitudinal wave speed
c_s	Shear wave speed
$e(x,t)$	The envelope of a Gaussian echo signal
$\mathcal{E}$	Expectation operator
E	Modulus of elasticity

Symbol	Description
E_s	Signal energy
$\overrightarrow{f}$	Body force per unit volume
f_c	Transducer's center frequency
$f_{s,t}$	Temporal sampling frequency
$f_{s,x}$	Spatial sampling frequency
f_t	Temporal frequency
f_x	Spatial frequency
$g(x,t)$	Gaussian echo signal as a function of the time and the transducer position
$g_{\mu,\tau}(t)$	Wavelet function with a scale parameter, μ, and a translation parameter τ
h	Mesh size
H	Hilbert transform
$\mathcal{H}$	Gradient matrix
$\mathcal{I}(\boldsymbol{\theta})$	Fisher information matrix
$\hat{\mathbf{n}}$	Unit reference vector
$\hat{\mathbf{n}}_{\perp}$	Unit vector perpendicular to the reference vector
$L(\boldsymbol{\theta})$	Likelihood function
P_r	Amplitude of the reflected P-wave
P_t	Amplitude of the transmitted P-wave
$QL(\boldsymbol{\theta})$	Quasi likelihood function
R	Stress reflection coefficient
S	Shannon entropy
S_r	Amplitude of the reflected S-wave
S_t	Amplitude of the transmitted S-wave
t	Time
T	Stress transmission coefficient
$\overrightarrow{u}$	Displacement vector
x	Transducer position
Z	Acoustic impedance

Chapter 1

Introduction

Non-destructive testing and evaluation (NDT&E) has been extensively practiced for detection of defects in engineering structures. Among many different NDT methods available, the bulk of the market mainly uses five methods: ultrasonic testing (UT), eddy current, radiographic testing, dye penetrants and magnetic particles [2]. While each NDT method has particular capabilities suitable for special applications, UT has wide-ranging capabilities applicable to a variety of applications [3]. UT is widely used in aerospace, automotive, utility, and petrochemical industries [4]. In the 1990s, UT alone accounted for 28% of the NDT market, over twice its market share in the 1950s [4]. The UT market is still growing fast and a recent study reported a 37% market share for UT, surpassing the radiographic testing [5].

Eddy current testing uses electromagnetic induction for detecting faults on surface or near the surface of conductive materials [6]. The testing procedure is relatively simple and the cost is moderate [7]. It can be used for crack detection, material thickness measurement, coating thickness measurement and conductivity measurement [8]. There are several limitations, among them: it is only applicable to conductive materials, the surface of the material must be accessible to the probe, the rough finish of the material may cause bad readings, the depth of penetration into the material is limited, and flaws that lie parallel to the probe may be undetectable [8].

Radiographic testing employs x-ray to detect internal defects. Using this technique a wide range of materials with different shapes and sizes from a micro-miniature electronic part to a power plant structure can be inspected. The major disadvantage of this technique is the safety concerns due to the exposure to the radiation [6].

Dye penetrant inspection reveals flaws, such as surface cracks and pores, which are open to the surface, by bleed-out of a colored or fluorescent dye from the flaw. Before applying this method the surface has to be prepared and well cleaned of any

dirt, oil and grease [9].

Magnetic particle inspection uses magnetic field and small magnetic particles to detect surface and sub-surface defects such as crack, inclusion and porosity, in ferromagnetic materials [9]. This technique is fast and relatively easy to apply [8]. Yet, there are certain limitations for using this technique. It is only applicable to surface and subsurface defects in ferromagnetic materials and a thin layer of coating or paint can adversely affect sensitivity [6].

Ultrasonic testing uses high frequency elastic waves in the material to conduct examinations and make measurements [10]. Many factors contribute to the popularity of UT among the NDT practitioners. This includes its capability of detection of both surface flaws, e.g. cracks, and internal flaws, e.g. voids or inclusions of foreign material. It is also used to measure the wall thickness of tubes and pipes to assess the material loss due to corrosion or other causes [11]. It is applicable to a wide range of engineering materials, such as steel and concrete, and for considerable thickness of materials, for example greater than 300mm for steel. Furthermore, UT does not require implementing safety measures as needed for radiography. It can detect embedded flaws with a surface area of 1.3 mm^2 [12]. Its accuracy in sizing of crack-like flaws is unique and in many cases it is better than 1 mm [13–15].

Nonetheless, the suitable application of UT requires high expertise inspectors in order to interpret data and achieve reliable results [3, 15]. The use of advanced signal processing can assist inspectors in data analysis by removing the noise and generating a clearer signal, and by accurately estimating the parameters which are used for fault characterization.

Figure 1.1 shows the UT procedure which includes 1) data acquisition, 2) signal denoising, 3) parameter estimation, 4) fault identification and 5) decision making. In the first step, ultrasonic signal is collected using a proper test setup. The resulting ultrasonic signal is often noisy. Therefore, it is necessary to denoise this signal in order to be able to extract useful features from the signal. Based on the extracted features, faults in the material can be identified, i.e. they can be detected, located and sized. Finally, quality and maintenance decisions are made based on the number of faults and their severity.

The scope of this thesis includes the three middle steps; i.e. denoising, parameter estimation and fault identification. The first and the last steps are excluded from this thesis as they are less related to the ultrasonic signal processing. The first step is mainly concerned about the hardware technology, e.g. ultrasonic transducer [16–18], couplant [19], robots [20] used in ultrasonic testing. The decision making deal with

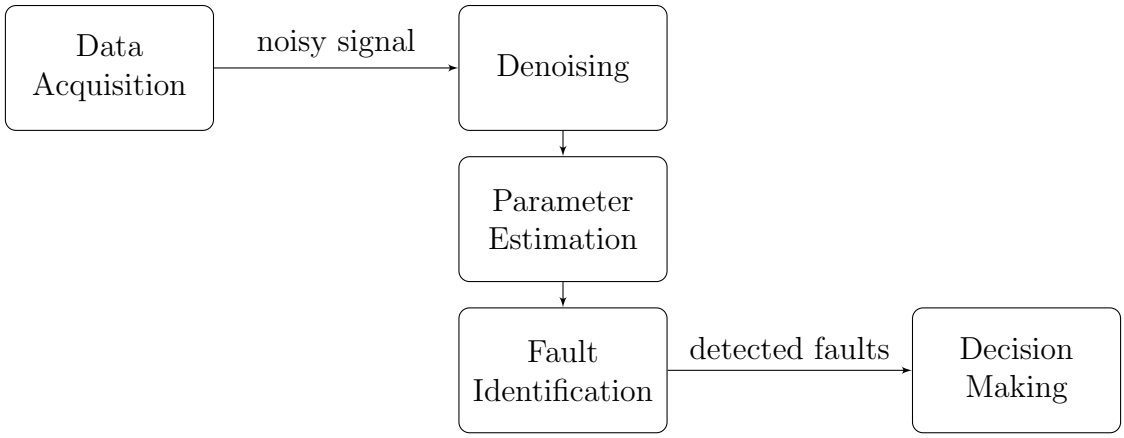

Figure 1.1: Ultrasonic Testing Procedure

topics such as reliability [21–26].

1.1 History of ultrasonic testing

The use of ultrasonics in NDT was originated in the early twentieth century. Sokolov (1929) at the V.I. Ulyanov (Lenin) Electrotechnical Institute conducted the first experiments using the quartz transducers to create ultrasonic vibrations in materials. He demonstrated a through-transmission technique for detecting flaws in metals [27]. Firestone (1940) in USA developed the pulse-echo ultrasonic flaw detector [28]. A few years later, Branson (1946) introduced the first portable thickness measuring instrument and in mid 1950's Erdman developed ultrasonic immersion B-scan and C-scan[1] instruments [27].

In the early 1970's, the advancement in hardware technology led to the ability to detect smaller flaws [8]. More parts were consequently being rejected even though the probability of failure did not change. This fact led to a change in the damage evaluation from a zero defect requirement to a test and evaluate strategy based on damage tolerance [29]. Therefore, only parts with cracks greater than the critical crack length, which was specified using fracture mechanics, were being rejected. Since then, the field of ultrasonic testing has grown at a remarkable rate as a result of rapid advancement in electronics and computer technology [28]. Now, it is used more frequently than radiography and is the most widely used NDT technique [28].

In Canada, UT was not a significant method until late 1960's [30]. Radiography and the surface methods such as magnetic particle and liquid penetrant testing

[1]Refer to Sec. 2.3 for the definition of B-scan and C-scan displays.

were the predominant methods used. This could be attributed largely to the lack of UT equipment and competent technicians. Then, in the period of 1965 to 1985 improvements in UT instrumentation and technician competence raised the level of industry confidence in UT in Canada to such a level that areas of inspection that were previously the sole domain of radiography are replaced by UT [30]. In 1990's the two largest pipeline operators in Canada, Trans Canada Corp. and Enbridge Inc., were developing plans to use ultrasonics as the primary NDT method instead of radiography for weld inspection. In 1993, Trans Canada Corp. became the first North American company to use ultrasonics as the primary nondestructive testing (NDT) method on a pipeline construction project [31].

1.2 Ultrasonic signal processing

As a consequence of the growing significance of ultrasonics, much research has been carried out on developing NDT techniques based on UT [32]. Nevertheless, the current practice of the ultrasonic testing is limited mainly due to the lack of adequate signal processing techniques to process and explain the detected signals [33]. Currently, there is also high demand for automatic ultrasonic signal processing techniques to not only remove the need for manual flaw detection and assessment, but also increase the accuracy, reliability and repeatability of the non-destructive evaluation [2, 34, 35].

Signal processing is a crucial aspect of any ultrasonic non-destructive testing. The objective of signal processing is to extract information from the collected signal to detect flaws in structures and to assess the severity of damage. Robustness to the high level of noise is indispensable for any signal-processing approaches in this field as high level of noise is expected in many UT applications such as pipeline inspection [36]. The surrounding environment, transducers, the data acquisition system are the main sources of the noise [37].

Once the signal has been denoised, proper parameter estimation methods can be used to extract interested features of the signal for detecting flaws and evaluating their severity. Therefore, the ultrasonic signal processing can be divided into two tasks [38]: a) Denoising and b) Parameter estimation for fault detection and evaluation.

Many signal processing techniques have been utilized in ultrasonics for signal denoising and feature extraction. This includes classical signal processing techniques such as signal averaging, matched filtering, frequency spectrum analysis [39], spectral correlation [40], neural nets, and autoregressive analysis [41] as well as emerging techniques such as wavelet transform (WT) and its variants such as stationary wavelet

transform and wavelet packet transform, and empirical mode decomposition. Some research has also been reported on the use of higher order statistics for ultrasonic signal processing [42–44].

Most of the above-mentioned methods are focused on A-scan signal processing. A B-scan image can provide more accurate fault detection and assessment by keeping the geometrical coherence of defects which leads to a better noise immunity [45]. It is, therefore, increasingly used in ultrasonic NDT&E. In this thesis, we investigate different aspects of ultrasonic B-scan signal processing including denoising, parameter estimation and fault identification.

1.2.1 Ultrasonic signal denoising

Donoho [46] pioneered a wavelet based noise removal scheme by applying soft and hard thresholding. This method and its variants are now widely used for denoising non-stationary signals which exhibit time-varying spectral characteristics [47]. Because of the non-stationary nature of ultrasonic signals, the use of wavelet transform for signal denoising and feature extraction of ultrasonic signals was extensively investigated.

Kreidl *et al.* [48] investigated the utilization of the wavelet thresholding for ultrasonic noise suppression. They compared different wavelet filters including the Daubechies, Symlet, Coiflet and Biorthogonal families as well as different methods for estimating the threshold value. Matz *et al.* [49] compared different wavelet functions and concluded that discrete Meyer filter outperforms others. Kananen *et al.* [50] found that the Daubechies-6 performs the best among Daubechies and Symlet families. Chen *et al.* [51] stated that the Morlet wavelet is the optimal choice for denoising ultrasonic signals. Then, they proposed an adaptive Morlet wavelet for ultrasonic signal denoising.

These methods were proposed for denoising A-scan signals. Although a two dimensional (2D) B-scan image can be denoised by removing noise from every single A-scan, the denoising performance can be improved if a 2D denoising method is used. Proper 2D denoising techniques should be developed to more effectively treat ultrasonic B-scans.

In Chapter 3, we propose a 2D method for denoising B-scan signals. The proposed method is based on the analytic wavelet thresholding technique [52] which has been adapted for 2D ultrasonic B-scan. The proposed method is shown to improve the denoising performance compared to standard wavelet thresholding.

1.2.2 Ultrasonic echo parameter estimation

The denoised ultrasonic signal can be used for fault detection and assessment. Existing ultrasonic techniques use time of flight (TOF), amplitude of the echo or spectral features of the received signal for crack sizing. TOF-based techniques such as time of flight diffraction [14] and relative arrival time technique [53, 54] are currently extensively used because of their reliability in crack sizing [55, 56].

The methods used for the TOF estimation are mostly based on the cross-correlation between the received signal and a reference signal. Cross-correlation methods are popular mainly because of their simplicity and the ability to detect flaws without any priori knowledge of the specimen under examination. However, a reference signal may not be available. Even if it is available, frequency dependent scattering and attenuation may distort the received echo by introducing a frequency downshift [57, 58]. In this case, the cross-correlation methods become ineffective especially when it comes to damage sizing.

Recently, Dimirli and Saniie [57] proposed a model-based method for TOF estimation. They assumed that the received signal is the result of superposition of a number of Gaussian echoes and estimated the parameters using maximum likelihood method. Satyanarayan *et al.* [35] performed parameter estimation with the aid of time domain finite difference model. Such methods not only overcome the above-mentioned disadvantages of cross correlation methods, they also provide more information about the defect which are represented by model parameters.

In Chapter 4, a model-based method similar to [57] is proposed, but the Quasi log-likelihood method is used to estimate the parameters of the envelope signal computed from the original ultrasonic signal. The proposed method is shown to provide a better estimation of the number of echoes and more consistent and accurate estimation of TOF.

In addition, we derive a theoretical expression showing the amount of improvement in the time of flight estimation accuracy achieved by using a B-scan signal. This theoretical expression also states minimum requirements for achieving a certain level of accuracy in parameter estimation. Subsequently, to estimate parameters of the ultrasonic echoes from the B-scan signal, we extend the proposed parameter estimation method to two dimensions.

1.2.3 Fault characterization using ultrasonic B-scan signals

After the TOF values are estimated, they are used for locating and sizing defects. When using crack sizing methods such as relative arrival time technique[1], it is assumed that the crack is normal to the surface. However, this assumption may not be true. To take into account the effect of crack orientation, in Chapter 5, we derive theoretical expressions relating the crack orientation and length with B-scan echo parameters. Using these expressions, equations are derived to calculate the crack length and orientation from a B-scan signal.

1.3 Objective and outline of the present work

As mentioned earlier, most of the existing ultrasonic signal processing methods are based on ultrasonic A-scan signals and little research has been conducted on the ultrasonic B-scan signal processing. The objective of the present work is to develop signal processing methods applied to ultrasonic B-scan signals. This includes the techniques used in denoising, parameter estimation and crack identification. To evaluate the performance of the proposed methods, we will use three kinds of ultrasonic signals:

- simulated signals generated from the mathematical model derived in Chapter 2
- simulated signals obtained from finite element analysis which is presented in Chapter 6
- experimental signals described in Chapter 7.

The remainder of this thesis is organized into the following chapters.

Chapter 2 presents a brief introduction to ultrasonic wave propagation in material, ultrasonic testing, and different test setups used in UT and crack sizing techniques. In addition, a mathematical model is proposed for ultrasonic pulse-echo B-scan signals. This model will be used for parameter estimation as well as generating simulated signals.

Chapter 3 presents our proposed denoising method based on analytic wavelet thresholding for ultrasonic B-Scan signal denoising. Simulated signlas and experimental signals, which are presented in Chapter 7, will be used to evaluated the performance of the proposed denoising method.

[1]Refer to Sec. 2.2.1 for the description of the relative arrival time technique.

Chapter 4 presents our proposed model-based methods for damage assessment. We employ quasi-maximum-likelihood method for estimating TOF for crack sizing. The performance of the proposed method is evaluated using simulated signals and the experimental signals presented in Chapter 7. This method is shown to improve the estimation results significantly.

Chapter 5 addresses the crack identification problem. In particular, we investigate the crack sizing problem for inclined cracks using B-scan images. Theoretical expressions are developed to calculate the length and the inclination angle of inclined cracks. Finite element simulation is used to support assumptions used in the theoretical derivation. To assess the accuracy of the derived expressions for the crack size and orientation, they are applied to finite element simulated signals presented in Chapter 6 and experimental signals presented in Chapter 7.

In Chapter 6, ultrasonic wave propagation in a specimen with a crack is modeled using finite element method. The FE simulated signals will be used in Chapter 5 for assessing the accuracy of the proposed crack sizing method. The advantage of using FE simulated signal over the experimental signal is that the FE simulated signal contains less noise. In addition, while the experimental signal only shows the response of the transducer, in the finite element model the wave propagation can be observed in the material. Therefore, the nature of different echoes, e.g. tip diffraction echo and corner reflection echo, can be determined with a greater certainty.

Chapter 7 describes the experimental setups used to collect ultrasonic signals. This includes the data collected under the pulse-echo and pitch-catch setups. These data are used to assess the performance of the methods proposed in Chapters 3-5 and to validate the finite element model in Chapter 6.

Finally, conclusions of this work are summarized in Chapter 8.

Chapter 2

Fundamentals of Ultrasonic Testing

This chapter presents a brief introduction to ultrasonic wave propagation and ultrasonic fault detection techniques. Covering all ultrasonic fault detection techniques is beyond the scope of this thesis, hence only those techniques which will be used later in this thesis are introduced. We will also review the existing mathematical models for the ultrasonic echo waveform and develop a model for ultrasonic echoes in two dimensions.

2.1 Ultrasonic wave propagation

The Navier equations describe the motion of an elastic isotropic solid [32],

$$(\lambda+\mu)\nabla\nabla\cdot\overrightarrow{u}+\mu\nabla^2\overrightarrow{u}+\overrightarrow{f}=\rho\frac{\partial^2\overrightarrow{u}}{\partial t^2} \tag{2.1}$$

where $\overrightarrow{u}$ is displacement vector, $\overrightarrow{f}$ body force per unit volume, ρ density, t time, and λ and μ Lame's first and second parameters, respectively. In addition, the ∇ operator is defined as $\nabla=\hat{x}\frac{\partial}{\partial x}+\hat{y}\frac{\partial}{\partial y}+\hat{z}\frac{\partial}{\partial z}$ in Cartesian coordinate system where $\hat{x},\hat{y}$ and $\hat{z}$ are unit vectors in their respective directions. When applied to a scalar field, the del operator denotes gradient, its dot product with a vector field denotes divergence, its cross product with a vector field is called curl, and ∇^2 denotes the Laplace operator defined as $\nabla^2=\frac{\partial^2}{\partial x^2}+\frac{\partial^2}{\partial y^2}+\frac{\partial^2}{\partial z^2}$.

In the absence of body forces, equation (2.1) simplifies to,

$$(\lambda+\mu)\nabla\nabla\cdot\overrightarrow{u}+\mu\nabla^2\overrightarrow{u}=\rho\frac{\partial^2\overrightarrow{u}}{\partial t^2}. \tag{2.2}$$

Using Helmholtz decomposition, the displacement vector can be expressed as the

gradient of a potential scalar, Φ, and the curl of a zero divergence potential vector, $\overrightarrow{\Psi}$ [32]:

$$\overrightarrow{u} = \nabla\Phi + \nabla \times \overrightarrow{\Psi},\ \nabla\cdot \overrightarrow{\Psi} = 0. \tag{2.3}$$

Substituting equation (2.3) into equation (2.2) and after some manipulation, we obtain the following set of equations,

$$\begin{cases} \nabla^2\Phi = \dfrac{\partial^2\Phi}{c_L^2\partial t^2} \\ \nabla^2\overrightarrow{\Psi} = \dfrac{\partial^2\overrightarrow{\Psi}}{c_S^2\partial t^2} \end{cases} \tag{2.4}$$

where

$$c_L = \sqrt{\frac{\lambda+2\mu}{\rho}} \text{ and } c_S = \sqrt{\frac{\mu}{\rho}} \tag{2.5}$$

are the longitudinal and transverse wave speeds, respectively. A longitudinal wave propagates in the same direction as the displacement of particles in the transmitting medium, while a transverse wave propagates in a direction perpendicular to the displacement of particles. If the rotational part, $\nabla \times \overrightarrow{\Psi}$ is zero; that is,

$$\overrightarrow{u} = \nabla\Phi, \tag{2.6}$$

equation (2.2) simplifies to,

$$\nabla^2\overrightarrow{u} = \frac{\partial^2\overrightarrow{u}}{c_L^2\partial t^2}. \tag{2.7}$$

The dilatational/longitudinal wave propagates with the velocity c_L. This wave is often denoted by P-wave (Primary wave or Pressure wave). Similarly, if the displacement has only rotational part, i.e. the irrotational part $\nabla\phi = 0$, then

$$\nabla^2\overrightarrow{u} = \frac{\partial^2\overrightarrow{u}}{c_S^2\partial t^2} \tag{2.8}$$

which shows a distortional/shear wave traveling with the velocity of c_S. This wave is often denoted by S-wave (Secondary wave or Shear wave).

2.1.1 Reflection, refraction and mode conversion

Ultrasonic testing involves the transmission of high frequency elastic waves into material. The transmitted ultrasonic waves may encounter and reflect from discontinuities such as cracks. The reflected waves carry critical information about the test piece

and the faults within. However, ultrasonic testing and evaluation requires understanding of the wave propagation process which includes reflection, refraction and mode conversion. In the following, these physical mechanisms are introduced.

Normal beam incidence

If a plane wave encounters an interface between two materials at normal angle (see Figure 2.1), it will be divided into two components: some energy is transmitted and some is reflected [32]. The relative acoustic impedance of the two materials determines the amount of energy which is transmitted and reflected. The acoustic impedance of a medium is defined as

$$Z = \rho c \tag{2.9}$$

in which c is the wave velocity, thus $c = c_L$ for a longitudinal wave and $c = c_S$ for a shear wave. Subsequently, the stress reflection coefficient, R, and the stress transmission coefficient, T, can be written as,

$$R = \left.\frac{\sigma_x^{(R)}}{\sigma_x^{(I)}}\right|_{interface} = \frac{Z_2 - Z_1}{Z_1 + Z_2} \tag{2.10}$$

and

$$T = \left.\frac{\sigma_x^{(T)}}{\sigma_x^{(I)}}\right|_{interface} = \frac{2Z_1}{Z_1 + Z_2} \tag{2.11}$$

in which σ_x is the normal stress in x direction along which the wave propagates, superscripts I, R, and T respectively denote the incident, reflected and transmitted waves, and Z_1 and Z_2 are the impedance of medium 1 and medium 2 as demonstrated in Figure 2.1. Note that we have $R + T = 1$. According to equations (2.10) and (2.11), for the special case that two media have the same impedance ($Z_1 = Z_2$), wave completely transmits into the second medium and no reflection occurs ($T = 1$ and $R = 0$). According to equation 2.10, the stress reflection coefficient can be positive or negative depending on Z_2 and Z_1 values. A negative R value infers shifting the reflection wave phase by π radians.

Oblique beam incidence

An ultrasonic wave encountering an interface at an inclined angle, refracts, reflects and undergoes mode conversion. Snell's law describes the relationship between the

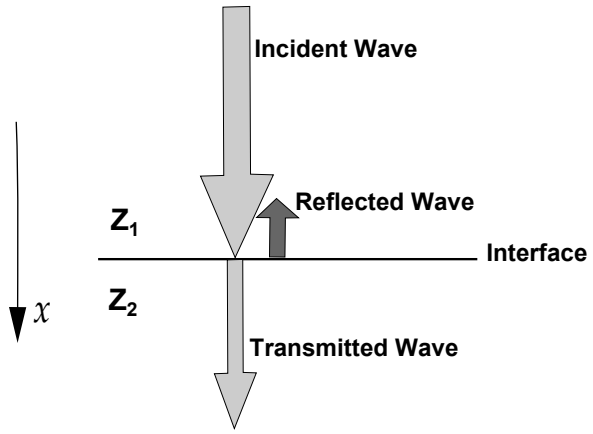

Figure 2.1: Normal incidence of an ultrasound wave on the interface of two media

angle of incidence and the angle of refraction:

$$\frac{sin(\theta_1)}{sin(\theta_2)} = \frac{c_1}{c_2} \tag{2.12}$$

in which θ_1 denotes the angle of incidence, θ_2 the angle of refraction, c_1 wave velocity in medium 1 and c_2 wave velocity in medium 2 as shown in Figure 2.2. The wave can be either longitudinal or transverse.

At a solid-solid interface, ultrasonic waves may undergo mode conversion; e.g. a longitudinal wave, depending on the angle of incidence, may convert to shear wave and/or surface wave. This complicates the formulation of wave propagation in the general case. In the following, we consider two cases which are of interest for NDT applications. In the first case, reflection and refraction at a solid-solid interface with smooth contact is presented. In the second case, the reflection at a stress free surface is presented.

Reflection and refraction at a solid-solid interface with smooth contact: Normal beam testing cannot often detect defects [8]. In this case, angle beam testing, which uses an incidence of other than 90°, is performed. An angle beam transducer used in NDT consists of a contact P-wave transducer and a wedge on which the transducer is placed, as shown in Figure 2.3. When couplant is applied between two solid media, the shear stress vanishes at the interface between the wedge and the test piece. In this case, the ratios between the stress amplitude of incident wave and the

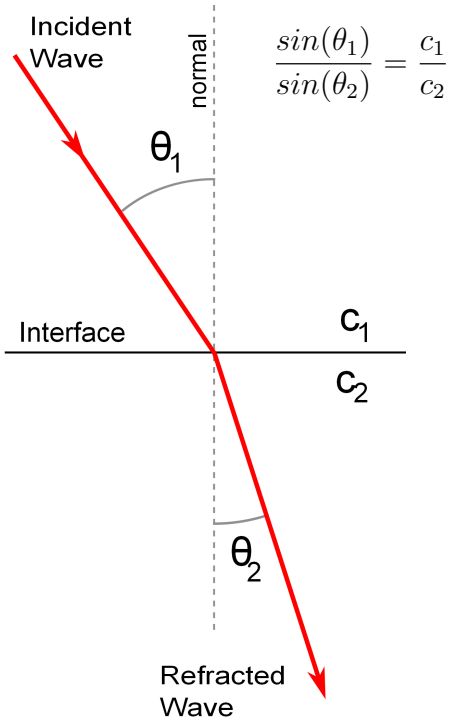

Figure 2.2: Snell's Law

stress amplitudes of reflected and transmitted waves are given by [59],

$$\begin{cases} \dfrac{P_t}{P_i} = \dfrac{\rho_2}{\rho_1}\dfrac{2cos(2\theta_{s1})cos(2\theta_{s2})}{\Delta} \\ \dfrac{P_r}{P_i} = \dfrac{\Delta_2 - \Delta_3}{\Delta} \\ \dfrac{S_t}{P_i} = \dfrac{\rho_2}{\rho_1}\dfrac{-2c_{s2}^2 sin(2\theta_{p2})cos(2\theta_{s1})}{c_{p2}^2\Delta} \\ \dfrac{S_r}{P_i} = \dfrac{-2c_{s1}^2 sin(2\theta_{p2})cos(2\theta_{s1})}{c_{p2}^2\Delta} \end{cases} \tag{2.13}$$

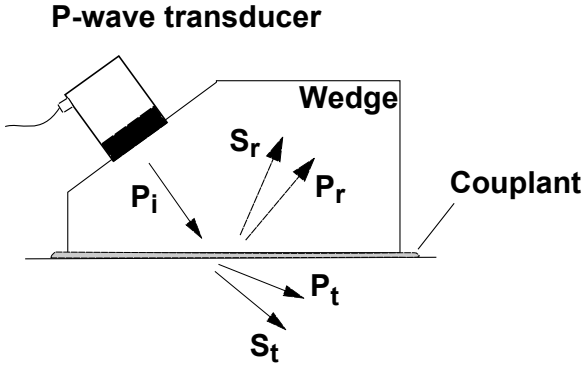

Figure 2.3: Ultrasonic angle beam testing

in which $\Delta = \Delta_1 + \Delta_2$ and

$$\begin{cases} \Delta_1 = \dfrac{c_{p1}cos\theta_{p2}}{c_{p2}cos\theta_{p1}}(cos^2(2\theta_{s1}) + \dfrac{c_{s1}^2 sin(2\theta_{s1})sin(2\theta_{p1})}{c_{p1}^2}) \\ \Delta_2 = \dfrac{\rho_2}{\rho_1}(cos^2(2\theta_{s2}) + \dfrac{c_{s2}^2 sin(2\theta_{s2})sin(2\theta_{p2})}{c_{p2}^2}) \\ \Delta_3 = \dfrac{c_{p1}cos\theta_{p2}}{c_{p2}cos\theta_{p1}}(cos^2(2\theta_{s1}) - \dfrac{c_{s1}^2 sin(2\theta_{s1})sin(2\theta_{p1})}{c_{p1}^2}) \end{cases} \tag{2.14}$$

P denotes the amplitude of P-wave, S the amplitude of S-wave, subscripts i, r, t, p, s, 1 and 2 denote incident, reflected, transmitted, P-wave, S-wave, medium 1 and medium 2, respectively. Figure 2.4 illustrates the notation too. Furthermore, the angles of incident, reflected and transmitted waves are given by generalized Snell's law as,

$$\frac{sin(\theta_{p1})}{c_{p1}} = \frac{sin(\theta_{s1})}{c_{s1}} = \frac{sin(\theta_{p2})}{c_{p2}} = \frac{sin(\theta_{s2})}{c_{s2}}. \tag{2.15}$$

Critical Angles: By increasing the angle of incidence, the angle of refracted wave increases. In particular case when $c_{p2} > c_{p1}$, for some specific value of θ_{p1}, the angle θ_{p2} becomes equal to 90°. At this angle, there would be no refracted longitudinal wave in the medium 2 and only the shear wave would propagate to the medium 2. This value of angle θ_{p1} is called first critical angle.

Generally, angles larger than the first critical angle are used for ultrasonic angle beam testing [60]. Beyond the first critical angle, the longitudinal wave totally reflects and only shear wave is transmitted into the specimen. This facilitates the interpretation of received echoes. We will use the angle-beam shear wave in our ex-

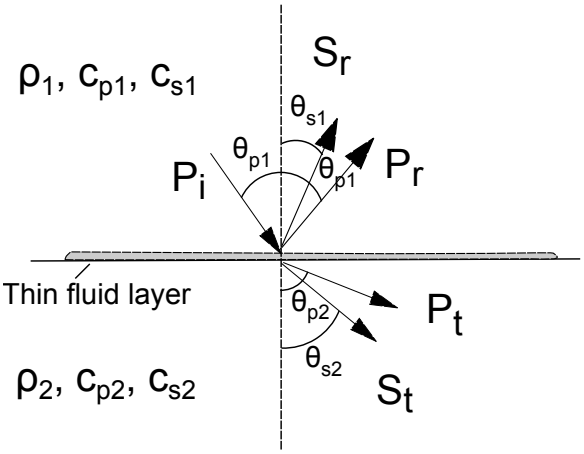

Figure 2.4: Incident, reflected and transmitted waves

perimental setup. Other types of ultrasonic wave are also used in ultrasonic testing and are introduced briefly in the following.

Just near and smaller than the first critical angle, creeping waves are produced. Creeping waves have the same properties as longitudinal waves. They are generated parallel to the scanning surface and travel near the surface. This enables the creeping waves to detect surface breaking defects without being affected by surface irregularities [60].

If $c_{s2} > c_{p1}$, there would be a second critical angle for which the refracted shear wave angle, θ_{s2} would be equal to 90°. At this point, no wave enters the second medium and shear wave appears as the surface wave propagating along the scanning surface. These surface waves, also called Rayleigh waves, can travel along flat and curved surfaces. Rayleigh waves are used in NDT for the detection of surface cracks and defects [60]. A major difference between Rayleigh wave and creeping wave is that the Rayleigh wave follows the surface contour while the creeping wave does not. This difference makes these two waves suited for different applications. For example, the creeping waves can be used for inspecting weld caps without flush grinding [60].

For the Lucite wedge and the steel specimen used in our experiments in Chapter 7, the first and the second critical angles are 26.5° and 56.5°, respectively. This range of incident longitudinal wave angle (26.5° − 56.5°) is the usable range in ultrasonic NDT. Figure 2.5 shows the ratio $\frac{S_t}{P_i}$ for different incident angles. As it can be seen, at an incident angle about 37° (equivalent to refracted shear wave of 45°), the amplitude of the shear wave transmitted into the test piece is close to maximum.

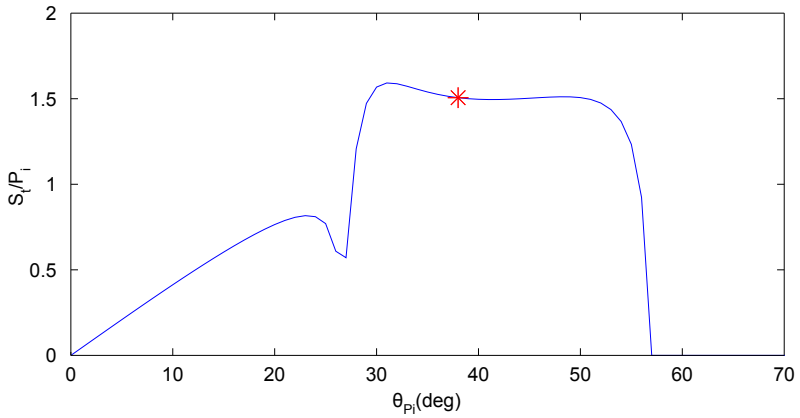

Figure 2.5: The stress transmission ratio for transmitted shear wave ($\frac{S_t}{P_i}$) for different angles of incidence

Reflection at a stress-free surface: In angle beam testing, ultrasonic waves may undergo different phenomena such as reflection, refraction, diffraction and attenuation. Reflection from a surface under stress-free condition frequently occurs in ultrasonic testing. For example, ultrasonic reflection from a crack surface can be modeled as reflection from a stress-free surface. As shown in Figure 2.6, for a stress-free surface there will be no transmitted wave and hence all energy will be reflected back. In this case the amplitude of reflected waves are [59],

$$\begin{cases} P_r = \dfrac{\Delta_1 - \Delta_2}{\Delta} P_i + \dfrac{2c_{p1}^2 sin(2\theta_{s1}) cos(2\theta_{s1})}{c_{s1}^2 \Delta} S_i \\ \\ S_r = \dfrac{-2sin(2\theta_{p1}) cos(2\theta_{s1})}{\Delta} P_i + \dfrac{\Delta_1 - \Delta_2}{\Delta} S_i \end{cases} \tag{2.16}$$

in which $\Delta = \Delta_1 + \Delta_2$ and

$$\begin{cases} \Delta_1 = sin(2\theta_{p1}) sin(2\theta_{s1}) \\ \\ \Delta_2 = (c_{p1}^2 / c_{s1}^2) cos^2(2\theta_{s1}) \end{cases} . \tag{2.17}$$

Based on equation (2.16), in general if a pure shear wave is incident on a stress-free surface, both longitudinal wave and shear waves are reflected from the surface. However, if the angle of incidence is either 0° or 45°, only the shear wave is reflected. In our experimental setup[1], we use a Lucite wedge which has a standard refracted

[1]Refer to Chapter 7 for details of experiments.

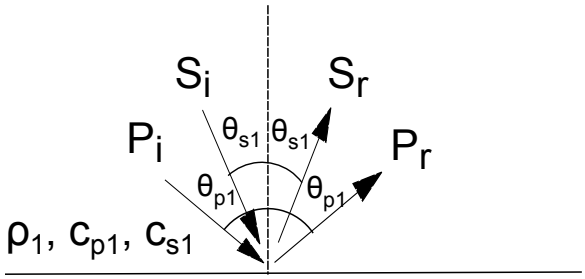

Figure 2.6: Incident and reflected waves at a stress-free surface

shear wave angle of 45° in steel. Therefore, when testing a steel block, if shear waves are incident on either the backwall or a crack normal to the surface, only shear waves are reflected.

2.2 Fault detection using ultrasonic testing

Whenever an elastic wave propagating in a medium hits an inhomogeneity or discontinuity, it reflects off it. Therefore elastic waves can be employed to detect such discontinuities. The smaller the wavelength, i.e. the higher the frequency, the smaller the discontinuity can be detected. Sound or elastic waves with the frequency above 20kHz are called ultrasound or ultrasonics (beyond the human hearing frequency range) [60]. Because of their short wavelength, ultrasonic waves are employed in NDT for detection of defects. In NDT applications, frequencies from 1 to 10 MHz are typically used, although lower or higher frequencies are sometimes required for specific applications [6].

Various types of instrumentations, test setups and couplings have been used. According to the method used to couple the test object and the transducer, there are two major test methods: contact and immersion methods. In the contact method, a thin layer of liquid transfers the ultrasonic energy to the test piece. In the immersion method, both the probe and the test piece are immersed in a fluid, e.g. water, through which the ultrasonic energy is transfered.

There are three general configurations used alone or in combination with each other to identify defects: through transmission, pulse echo and pitch catch. In the through transmission setup, an ultrasonic transmitter is used on one side of the test piece while a receiver is placed on the opposite side. Scanning of the material using this method will reveal the location of defects. This method requires the access to both sides of the material.

In this thesis, the other two methods are used, because in many applications,

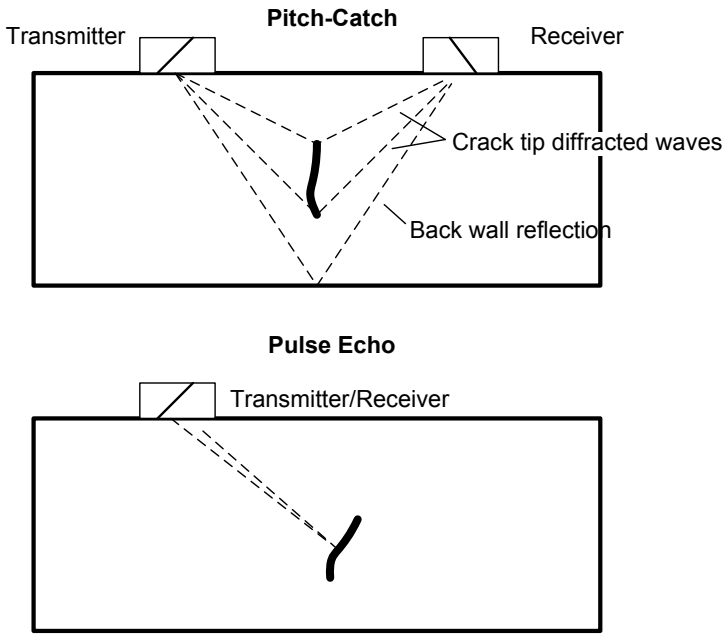

Figure 2.7: Transducer arrangements in the pitch-catch and pulse-echo setups

such as pipeline inspection, often only one side is accessible. In both pulse-echo and pitch-catch setups, a transducer emits ultrasonic pulses. These pulses travel through the object and respond to its geometry and mechanical properties. Ultrasonic signal is then either (a) transmitted to another transducer on the same side of the material, or reflected back to the original transducer (see Figure 2.7). Either way, the received signal is transformed back into an electrical signal. This observed signal provides a detailed account of the specimen under investigation. Using each of these methods, we can determine:

- the thickness of the specimen
- the presence of a flaw or defect and its size, shape and position

The so called pulse-echo reflection technique is used usually for ultrasonic flaw detection [10], whereas the pitch-catch setup is used to size the flaws, especially the crack-like flaws. Different methods were developed for locating and sizing defects. We explain in the following two popular methods used for crack size measurement: relative arrival time technique (RATT), which utilizes the pulse-echo arrangement, and time of flight diffraction (TOFD), which utilizes the pitch-catch arrangement. The other types of defects such as void and impurity are not studied in this thesis and need to be investigated in future studies.

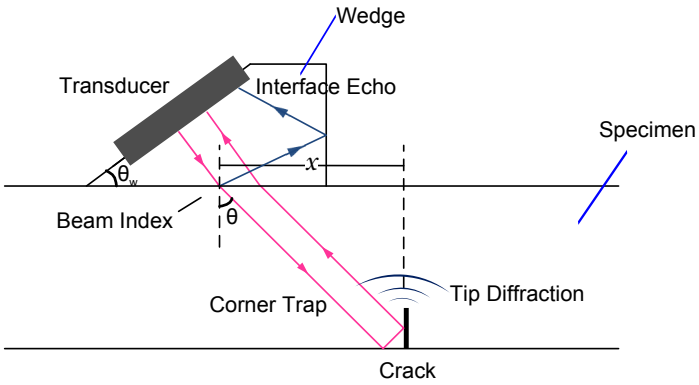

Figure 2.8: Ultrasound ray path in the wedge and the material

2.2.1 Relative arrival time technique

Figure 2.8 illustrates the schematic of the pulse-echo setup. As illustrated in Figure 2.8, the received signal consists of three echoes:

1. At the interface of the wedge and the specimen, a portion of the wave reflects back to the wedge due to the mismatch of the impedances. This echo is called the wedge echo or wedge noise [61].

2. The portion of the wave that is incident on the crack and is reflected back to the transducer is commonly referred to as the corner trap echo.

3. When the ultrasonic wave impinges on the crack tip, it backscatters in a circular form [61]. Some of these scattered waves make their way back to the transducer.

Relative arrival time technique (RATT) involves the measurement of echoes from the corner trap and the top tip diffraction [53, 54, 62]. As commonly assumed in deriving RATT, let us assume a crack normal to the specimen surface. Figure 2.9(a) illustrates the wedge/specimen interface. In this figure, ΔOAO' shows a wedge with an incidence angle of θ_w. To simplify the derivation of the RATT, we consider a hypothetical wedge which has the same physical property as the test object and has an angle θ equal to the refracted wave angle. By using Snell's law it can be shown that it takes an ultrasonic wave the same time to travel from point O to point A in the actual wedge as to travel from point O to point A' in the hypothetical wedge. From Snell's law we have $\frac{sin(\theta)}{sin(\theta_w)} = \frac{c_s}{c_w}$ and from the geometry we have $\frac{sin(\theta)}{sin(\theta_w)} = \frac{\overline{OA'}}{\overline{OA}}$, hence

$$\frac{\overline{OA'}}{c_s} = \frac{\overline{OA}}{c_w} = t_w/2 \tag{2.18}$$

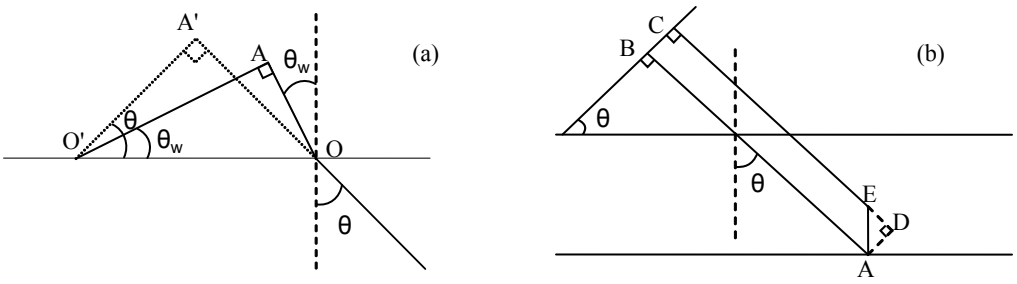

Figure 2.9: Derivation of the RATT, a) Wedge-specimen Interface b) Ultrasonic rays incident on the crack corner, BA, and crack tip, CE (points B and C are located on the hypothetical wedge)

where c_w, c_s and t_w are the wave speed in the wedge, the wave speed in the specimen and the wedge time delay, respectively. The wedge delay is defined as the time that the received ultrasonic wave has spent in the wedge. Clearly, by replacing the wedge with this hypothetical wedge there would be no refraction at the interface. Figure 2.9(b) illustrates the travelling paths of two ultrasonic rays incident on the crack corner and crack tip. Evidently, the difference between the travel distance of these two rays is equal to $\overline{ED}$ which is equal to crack length times $cos(\theta)$. The crack length, $\overline{EA}$, can then be related to the time of arrival of the corner trap echo, τ_{CT} and the time of arrival of tip diffraction echo, τ_{TD} as,

$$\text{crack length} = \frac{c_s(\tau_{CT} - \tau_{TD})}{2cos(\theta)}. \tag{2.19}$$

Therefore, when using the RATT, the first step is to determine whether an echo related to the crack is present in the received signal. Next, the time of arrival of corner trap echo and tip diffracted echo should be estimated. Finally, equation (2.19) is used to calculate the crack size using the estimated times of arrival of corner trap echo and tip diffracted echo.

2.2.2 Time of flight diffraction

The time of flight diffraction (TOFD) technique, which utilizes pitch-catch setup, was first developed in the late 1970s by Silk [63]. TOFD technique is increasingly used to find the crack location and size, based on the arrival time of the diffracted signals from the defective edges of the crack [14].

Let's consider a surface breaking crack which is located exactly at midway between two transducers as shown in Figure 2.10. In this case, the time of flight of ultrasonic

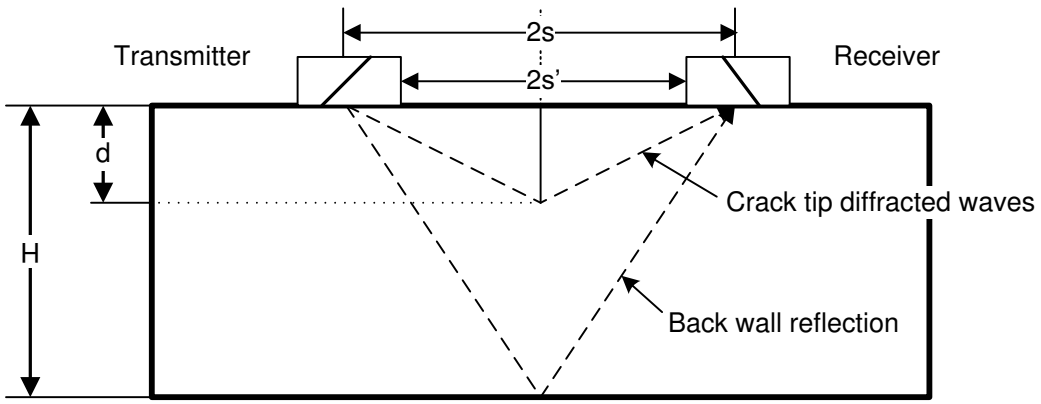

Figure 2.10: Schematic of the experimental setup

waves travelling from the transmitter to the receiver can be obtained as

$$t = \frac{2\sqrt{d^2 + s^2}}{c_s} \tag{2.20}$$

in which $2s$ denotes the distance between the beam index locations of the two transducers, and d denotes the length of the crack. The beam index is a location at the bottom of the wedge at which the center beam intersects the wedge bottom surface. The center beam path is often marked on the wedge so the distance between beam indexes can be easily measured. Rearranging equation (2.20) gives the crack length as,

$$d = 2\sqrt{(c_s t/2)^2 - s^2}. \tag{2.21}$$

Even if the transducers are not placed symmetrically around the crack, equation (2.20) is still applicable to most practical cases with an acceptable accuracy [51]. If we move both transducers by an equal small step ϵ along the specimen, i.e. the distances between the crack and the two transducers are $s - \epsilon$ and $s + \epsilon$, it can be shown the error in the estimated crack size is,

$$\Delta d = \frac{s^2 - d^2}{s^2 + d^2}(\frac{\epsilon^2}{2d}). \tag{2.22}$$

As it can be seen in equation (2.22), the error, Δd, is of the second order, hence the error would be negligible for small asymmetry.

If the crack is located inside the material, an echo will be diffracted from each of two edges. The same equation (equation (2.21)) can be used to estimate the length of each crack edge. Subsequently, the crack length can be calculated by subtracting

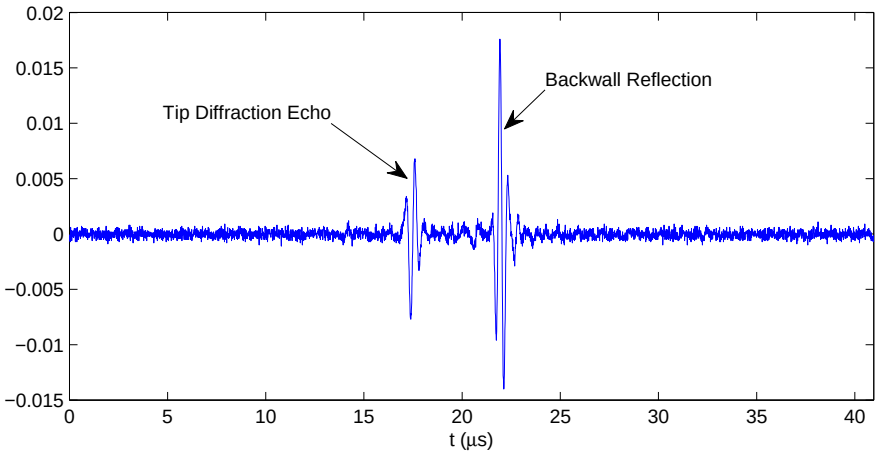

Figure 2.11: An example of an A-scan signal obtained using pitch-catch setup from a sample with a 12.5 mm crack

the length of two edges from each other.

2.3 Ultrasonic signal representation

There are several ways to display the ultrasonic signal. The most common displays are A-scan, B-scan and C-scan. Most of the commercial ultrasonic flaw detection equipment provides the A-scan display [6]. The A-scan displays the echo amplitude versus time so A-scan results in a one-dimensional signal. Knowing the speed of wave in the medium, the echo arrival time can be converted to the travel distance. The defect location can then be determined using the A-scan display.

An A-scan examines a specimen only at one point on its surface. By moving the transducer, a B-scan consisting of A-scans produced at multiple points along a line across the surface of test piece is produced. The B-scan display is used when the information on the cross section of defect is required. In a B-scan image, the distance between each consecutive two A-scans indicates the distance that the transducer moved between two adjacent A-scans [64]. Often, a position sensor is used to measure the position of transducer. An alternative way to produce a B-scan image is to use phased array transducers. A phased array transducer can produce a B-scan image without the need for moving the transducer. In this method, the B-scan is generated by proper timing of an array of transducers. An example of an A-scan signal and an example of a B-scan signal are depicted in Figure 2.11 and Figure 2.12, respectively.

In a C-scan presentation, an area of the specimen is scanned. The scanning is often accomplished using an automated positioning system which moves transducer

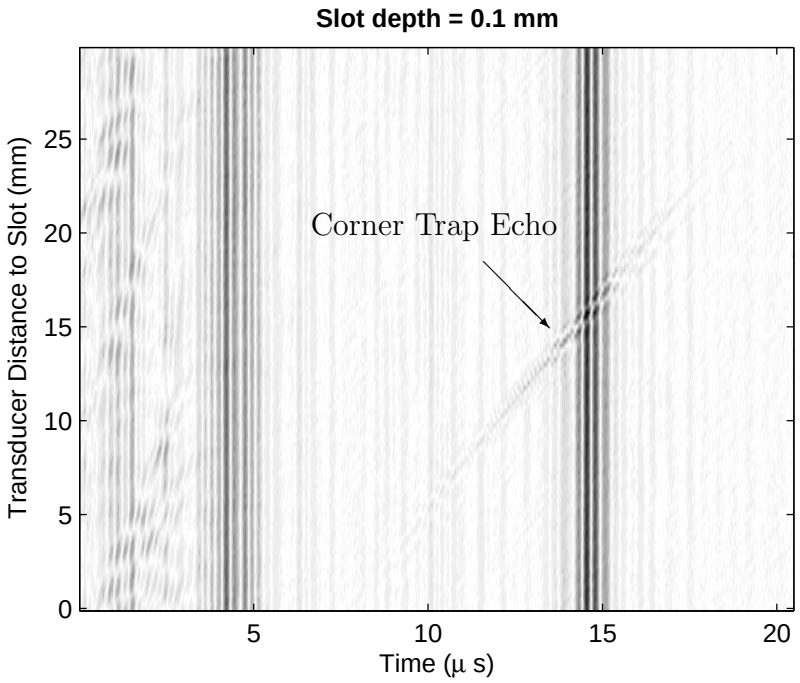

Figure 2.12: An example of a B-scan signal obtained using pulse-echo setup from a specimen with a slot length of 0.1 mm

by a specified step-size. Again, at each point an A-scan is produced. Each A-scan is then passed through a gate which can be placed either along a single time-line (corresponding to a single depth) to detect defects in the full volume of the component or at various depths within the thickness of the component to detect defects in a range of depths [65]. The peak amplitude of each A-scan within a gate is then recorded. Finally, the recorded peak values corresponding to A-scans collected at different points on the surface of the specimen are displayed as color or gray scale image. C-scan signals are not used in this thesis.

2.4 Mathematical models of the ultrasonic echo waveform

An A-scan signal may in general contain multiple echoes [57, 66–68]. Each echo can be modeled as,

$$g(t) = T(t-\tau)cos(2\pi f_c(t-\tau)+\phi) \tag{2.23}$$

in which $g(t)$ is the received echo waveform, T is the envelope of the echo, t is time, τ is time of arrival (also called time of flight), f_c is the transducer's center frequency,

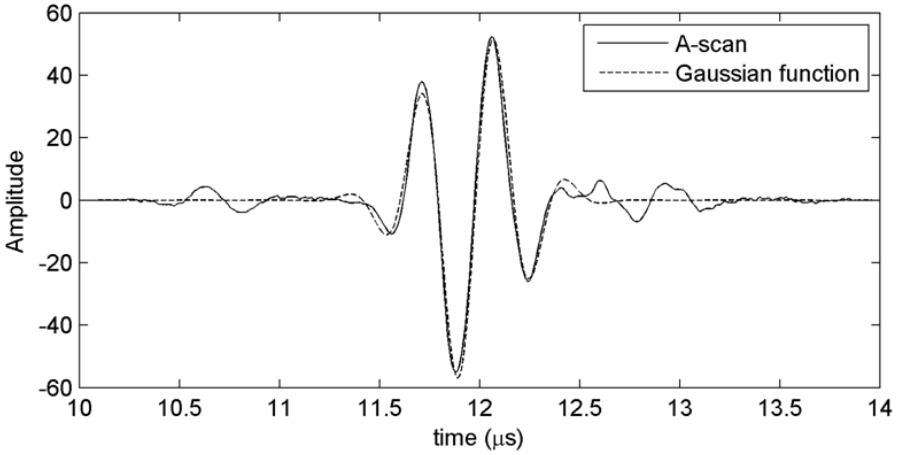

Figure 2.13: An ultrasonic A-scan signal to which a Gaussian echo model is fitted

and ϕ is phase. Gaussian echo is widely used to model the ultrasonic echo [57], in which T(t) is approximated by a Gaussian function so that

$$g(t) = \beta e^{-\alpha_t (t-\tau)^2} cos(2\pi f_c (t-\tau) + \phi) \tag{2.24}$$

in which β is amplitude and α_t is temporal bandwidth factor. Figure 2.13 shows an experimental ultrasonic signal to which a Gaussian echo model is fitted. As can be seen in Figure 2.13, Gaussian echo model gives a good approximation of the ultrasonic echo. In addition to the Gaussian echo model, there are other echo models proposed in the literature. Due to dispersion, echo envelope often rises sharply before the peak and slowly decays after [69]. Cavaccini *et al.* [70] simulated ultrasonic echo envelopes by adding two distorted Gaussian branches at left and right of the peak. Demirli and Saniie [69] proposed an envelope model composed of a linear combination of fixed-width and equally-spaced Gaussian functions. They also replaced the cosine term by a chirp signal to account for the fact that the wave group velocity depends on the frequency in dispersive media.

Modeling B-scans is more difficult as the echo is not only a function of time, but also a function of transducer position. In this case, the signal is two dimensional and can be written as,

$$g(x,t) = e(x,t) cos(2\pi f_c (t - \tau(x)) + \phi) \tag{2.25}$$

where e is the envelope and x is the transducer position. Compared to the A-scan model given by (2.23), in the B-scan model, the envelope, $e(x,t)$, and the time of arrival, $\tau(x)$, are functions of the transducer position. Assuming that all A-scan

echoes within a B-scan echo have similar waveforms except that each A-scan echo is time-shifted and amplitude scaled. The envelope, $e(x,t)$, can then be written as,

$$e(x,t) = X(x)T(t-\tau(x)) \tag{2.26}$$

where the amplitude of envelope, $e(x,t)$, at x is given by the function $X(x)$ and the envelope shape is determined by function $T(t)$ which is time shifted by $\tau(x)$. Substituting $e(x,t)$ from (2.26) into (2.25) gives,

$$g(x,t) = X(x)T(t-\tau(x))cos(2\pi f_c(t-\tau(x))+\phi). \tag{2.27}$$

As indicated in equation (2.27), both amplitude and time of flight are functions of x. In a pitch-catch arrangement, it is known that the time of flights of diffracted signals caused by a crack is represented in a B-scan image by parabolas [71, 72]. Maalmi *et al.* used Hough transform to detect these parabolas in the B-scan image [72]. In contrast to pitch-catch arrangement for which a mathematical model is available in the literature, B-scan signal in pulse-echo arrangement has not yet been properly modeled mathematically. Therefore, we devote the remainder of this section to modeling of the B-scan signal obtained from a pulse-echo arrangement. We will use this model in Chapter 4 in our model-based parameter estimation method.

Figure 2.14(a) illustrates the travel paths of two ultrasonic rays through the wedge and the specimen. We define the central ray as the one reflecting from the corner of the slot and it is represented by a solid line. Note that the central ray is *not* necessarily emitted/received from/by the center of the transducer. The other ray (we will call it the dashed ray) is represented by a dashed line. It can be shown that $\overline{BC}+\overline{CD}+\overline{DF} = (\overline{BC}+\overline{CH})+\overline{DF} = l_s$ and $\overline{AB}+\overline{GF} = l_w$, where l_s is the travel distance of the central ray in the specimen and l_w is its travel distance in the wedge. Thus, the total travel distance of a dashed ray is equal to the total travel distance of the central ray.

Figure 2.14(b) shows the travel paths of the central ray when the transducer is at two different positions. As it can be seen, travel paths of the central ray at these two positions are mostly coincident and the only difference is the distance between the two transducers. Therefore, the difference between the travel distances of the central ray at these two positions can be calculated as

$$\Delta l = 2\Delta x sin(\theta_w), \tag{2.28}$$

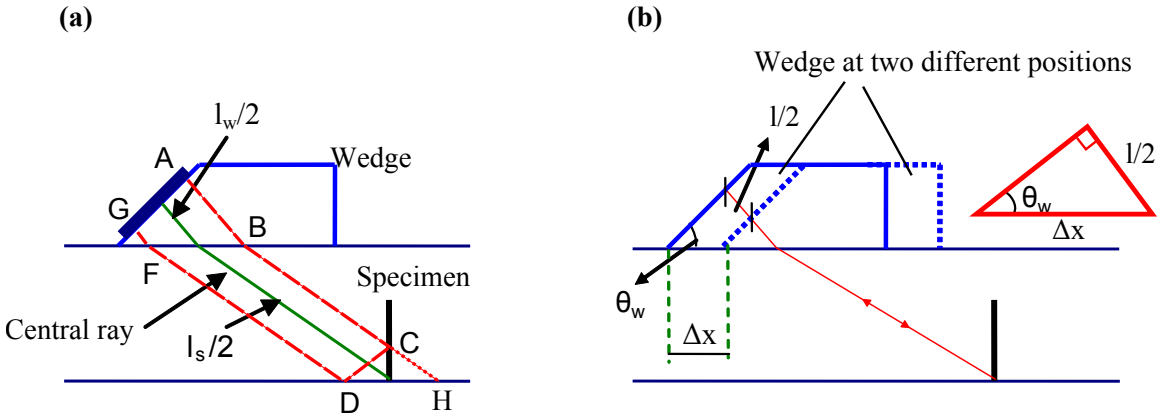

Figure 2.14: (a) Travel paths of two ultrasonic rays through the wedge and the specimen, (b) Travel paths of the central ray at two different transducer positions.

where x, l, and θ_w are respectively the horizontal distance from the transducer to the slot, the distance the wave travels to the slot and back to the transducer, and the angle of incidence at the wedge-specimen interface on the wedge side. Substituting $l = v_w\tau$ in equation (2.28) gives

$$\frac{\Delta\tau}{\Delta x} = \frac{2sin(\theta_w)}{c_w}, \tag{2.29}$$

in which τ and c_w are the time of arrival and wave velocity in the wedge, respectively. Alternatively from Snell's law, one may rewrite equation (2.29) as

$$\frac{\Delta\tau}{\Delta x} = \frac{2sin(\theta)}{c_s}, \tag{2.30}$$

where v_s is the wave velocity in the specimen and θ is the wave angle upon entering a specimen with a normal surface. As expected, the time of flight is a linear function of the distance between the transducer and the slot. All parameters in equation (2.30) are known before performing the test. For our experimental setup[1], the speed of the refracted shear wave in the specimen has been obtained using assisted calibration of Omniscan as 3229 m/s. Evaluating Equation (2.30) gives

$$\frac{\Delta\tau}{\Delta x} = \frac{2sin(\theta)}{c_s} = \frac{2sin(45)}{3.229} = 0.438\ \ \mu s/mm. \tag{2.31}$$

If the crack is not perpendicular to the surface, the ultrasonic rays will not stay

[1]Refer to Sec. 7.1 for details of this experiment.

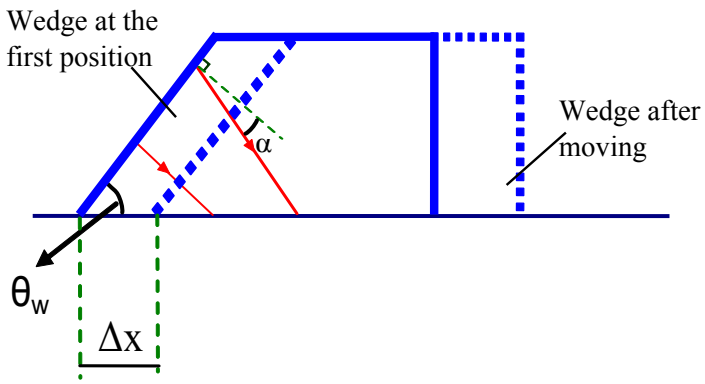

Figure 2.15: Travel paths of a ray at two different transducer positions

parallel to each other after reflecting from the crack surface. As a result, the reflected waves may arrive at the receiver at different angles. Therefore, the value of $\frac{\Delta\tau}{\Delta x}$ will be different from equation (2.31). Let us consider an ultrasonic ray that encounters the receiver at an angle α as shown in Figure 2.15. The difference between the travel distances of this ray at these two positions is equal to

$$\Delta l = \Delta x sin(\theta_w) + \Delta x sin(\theta_w)/cos(\alpha). \tag{2.32}$$

Hence,

$$\frac{\Delta\tau}{\Delta x} = \frac{sin(\theta)}{c_s}\left(1 + \frac{1}{cos(\alpha)}\right). \tag{2.33}$$

Because the longitudinal transducer responds only to normal component of the particle velocity [73], the response of the transducer to rays with large angle of incidence is weak. For small values of α, equation (2.33) can be approximated as,

$$\frac{\Delta\tau}{\Delta x} \approx \frac{sin(\theta)}{c_s}\left(2 + \alpha^2/2\right). \tag{2.34}$$

As can be seen in equation (2.33), the change in $\frac{\Delta\tau}{\Delta x}$ is proportional to α^2 for small α values. Therefore, it is expected that $\frac{\Delta\tau}{\Delta x}$ be slightly greater than the value given in equation (2.31), if the crack is not normal to the surface.

For an experimental B-scan image[1], we have calculated the time of flight values for corner trap echo and tip diffracted echo. The time of flight for each echo is calculated by finding the maxima of the signal envelope. The signal envelope, in turn,

[1]The B-scan image for this experimental data is shown in Figure 7.13.

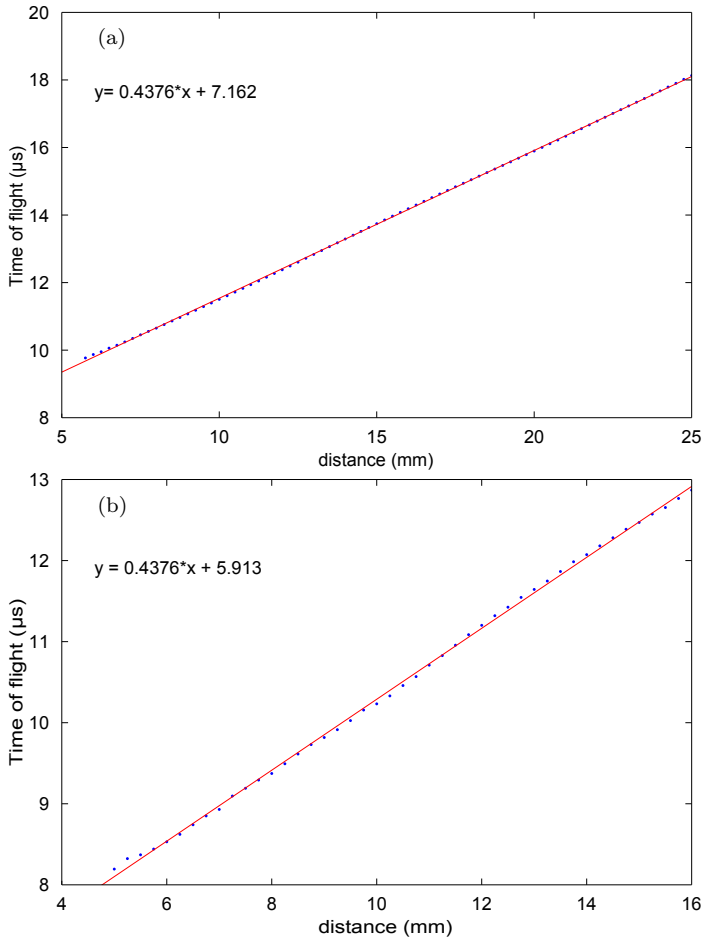

Figure 2.16: Time of flight of (a) the corner trap echo and (b) the tip diffracted echo, versus the transducer distance to crack

is calculated using the Hilbert transform. Figure 2.16 gives these calculated time of flight values at different transducer positions. From these experimental results, it can be observed that for both echoes the slope of the fitted line is in good agreement with the theoretical value given by equation (2.31); in both cases there is less than 0.5% deviation from theory.

The last parameter to determine is the amplitude, $X(x)$. When the transducer is far enough away from the crack, there would be no echoes received by the transducer. As the transducer gets closer to the crack the amplitude of the received signal gradually increases and reaches its maximum. We have performed curve fitting to an experimental dataset[1] and found that a reasonably accurate approximation to the amplitude of the ultrasonic echoes can be produced using Gaussian function, such

[1]This dataset is explained in Sec. 7.1.

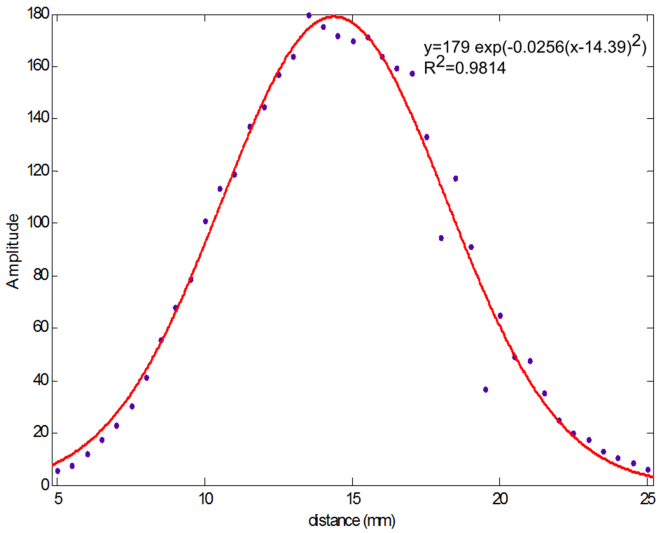

Figure 2.17: Amplitude of the corner trap echo

that

$$g(x,t) = \beta e^{-\alpha_x (x-x_0)^2} e^{-\alpha_t (t-\tau(x))^2} cos(2\pi f_c (t-\tau(x)) + \phi) \tag{2.35}$$

where α_x is spatial bandwidth factor and x_0 is the position where maximum amplitude occurs. For example, Figure 2.17 shows a Gaussian function fitted to the amplitude of a corner trap echo[1].

As will be discussed in Chapter 4, a model-based parameter estimation method can utilize the model developed in this section to accurately estimate the parameters of an ultrasonic B-scan echo. Comparing to conventional methods such as cross-correlation method, model-based methods allow a more accurate time-of-flight estimation.

2.5 Summary

In this chapter, the ultrasonic wave propagation, the ultrasonic non-destructive testing and the ultrasonic signal modeling have been introduced. The concepts introduced in this chapter will be used in later chapters frequently.

The study of the ultrasonic wave propagation helps us in the proper selection of parameters of the experimental setup[2]. It has been shown that in ultrasonic angle beam testing, if the angle of incidence is greater than the first critical angle, only the shear wave will transmit into the second media. This simplifies the signal processing which otherwise could be complex due to the presence of both longitudinal wave and

[1]The B-scan image for this experimental data is shown in Figure 7.13.
[2]Refer to Chapter 7 for details of experiments.

shear wave in the test piece. Furthermore, if a shear wave is incident on a stress-free surface at the angle of 45°, only shear wave will be reflected. Therefore, we have selected a wedge with standard refraction angle of 45° so that when the shear wave is incident on the backwall or a crack normal to the surface only shear wave will be reflected.

Two crack sizing methods have been introduced: time of flight diffraction and relative arrival time technique. The crack sizing accuracy for known cracks will be used as a performance index for denoising and parameter estimation methods proposed in this thesis.

In the literature, different mathematical models were reported for ultrasonic A-scans. Because, in this thesis, we seek signal processing of ultrasonic B-scans, a mathematical model has been developed for the ultrasonic B-scan signal. This model will be used for parameter estimation in Chapter 4. We will also use this model for the selection of the maximum scanning step size in the experimental work in Chapter 7.

Chapter 3

Denoising Ultrasonic Pulse-Echo B-scan Signals Using Two-Dimensional Analytic Wavelet Thresholding

When an ultrasonic angle-beam pulse-echo setup is used, two kinds of noise are present in the received signal: 1) random noise, and 2) wedge noise. In this chapter, we propose a method for removing both random noise and wedge noise using a two-dimensional stationary wavelet transform (2D SWT). To improve the performance of the 2D SWT, we employ analytic wavelet thresholding. In this method, the thresholding is performed based on the amplitude of the analytic signal (The amplitude of an analytic signal constructs the envelope of the corresponding signal.) of the stationary wavelet coefficients.

Currently, the formulation of analytic signals is mainly limited to 1D signals and no regular generalization of analytic signals to multi dimensions is available. We prove that under certain conditions, the envelope of the ultrasonic B-scan can be extracted exactly by introducing a reference vector. Such a reference vector defines the low frequency and high frequency components in the frequency domain. By utilizing this definition of the low frequency and high frequency components, we can get the 2D analytic signal.

The proposed denoising method is applied to simulated and experimental data to assess its performance. The results show that the proposed denoising method is able to reveal echoes reflected from a surface breaking crack as small as $0.1mm$. Major

contribution of this chapter has been published in [74, 75] [1].

3.1 Introduction

Raw ultrasonic signals typically contain high levels of noise. The presence of these noises and spurious signals diminish the probability of damage detection and increase the false alarm rate [76]. These noises are primarily caused either by electric sources, e.g. noises and spurious signals generated in amplifiers, or by acoustic sources, e.g. waves backscattered by structural inhomogeneities [77].

The ultrasonic denoising problem has been addressed by many researchers. However, most of the reported works deal with A-scan signals (for example see [76–85]). Recently, the use of B-scan images has become more common as a result of advances in signal processing and hardware technology. A B-scan image can provide more accurate fault detection and assessment by keeping the geometrical coherence of defects which leads to a better noise immunity [45]. A B-scan signal can be denoised by independently denoising each A-scan contained in the B-scan signal and then reconstructing the B-scan by combining denoised A-scans. But, the denoising performance might not be as satisfactory as a 2D denoising method which employs the signal dependency in both dimensions.

Little research has been reported on denoising B-scan signals. Most of the published works are on suppressing speckle noise from B-scan images (for example see [86–90]). Speckle noise is a random, deterministic, coherent interference in an ultrasound B-scan. Speckle noise occurs when many sub-resolution scatterers in the medium cause interference in the wave received from an object [87]. For instance, in NDT applications, grain boundaries in a medium such as cast stainless steel may cause speckle noise [91]. The use of ultrasonic non-destructive testing for such applications is limited [91]. In this thesis, we consider more typical applications of UT, such as structures made of mild steel, for which the grain boundaries are too small to reflect ultrasonic waves. Therefore, we do not investigate this type of noise.

The other types of noise which are present in the ultrasonic signal are: 1) background noise, and 2) non-coherent random noise. Non-coherent random noise does not correlate with the ultrasonic echoes. They are caused by different sources such as

[1] Versions of this chapter have been published in "M.R. Hoseini, M.J. Zuo, and X. Wang, Two dimensional analytic wavelet thresholding and its application to ultrasonic pulse-echo B-scan denoising, In Proceedings of CCECE. 2010, 1-5."; and "Mohammad R. Hoseini, Ming J. Zuo, Xiaodong Wang, Denoising ultrasonic pulse-echo signal using two-dimensional analytic wavelet thresholding, Measurement 45(3): 255-267, 2012."

electric sources and quantization errors. Removing this type of noise has been investigated in different fields including the ultrasonic testing. Yet again, the B-scan signal denoising has not been well studied. Cao et al. [92] proposed using Wiener filtering to denoise B-scan images. Wiener filtering requires some prior knowledge about the signal and noise. In addition, Wiener filter is not adaptive as it assumes the signal is stationary. Therefore, proper non-stationary methods need to be developed.

In ultrasonic contact testing, background noise is also present. It may be caused either by the interface between the wedge and the test piece in the pulse-echo setup or by the backwall in the pitch-catch setup. Wells *et al.* [93] removed background noise from B-scan by iteratively subtracting the average of A-scans from each A-scan. Although this method provides a simple way to remove background noise, it assumes that the background noise does not change as the transducer moves. Therefore, this method cannot compensate for the small changes in the amplitude and the time of arrival of background noise.

In this chapter, we propose a method based on the 2D wavelet transform to denoise ultrasonic pulse-echo B-scan images. The proposed method simultaneously takes into account both random noise and background noise. The remainder of this chapter is organized as follows. Section 3.2 briefly introduces the wavelet transform and investigates the analytical wavelet thresholding for a 2D signal. Section 3.3 explains the denoising method proposed. Section 3.4 presents a comparison between the proposed denoising method and two existing methods using simulated and experimental signals. Finally, conclusions are given in Section 3.5.

3.2 Wavelet denoising

The basic idea behind wavelet denoising is that most of the energy of a signal is concentrated in a few coefficients in the wavelet domain, whereas noise energy spread over a large number of coefficients. Therefore, insignificant coefficients are likely to contain mostly noise. In wavelet thresholding methods, a threshold is set and coefficients smaller than this threshold are discarded.

Like other transforms such as the Fourier transform, wavelet transform uses basis functions for signal transformation. The basis functions of the Fourier transform consist of sines and cosines which transform a signal from the time domain (or other domains such as spatial domain) to the frequency domain. But, wavelets, which are basis functions of the wavelet transform, transform a signal from time domain to time-frequency domain. This is achieved by replacing the Fourier basis by more

localized basis functions labeled by time and frequency (or scale) parameters [94]. Wavelets, $g_{\mu,\tau}(t)$, are generated by time scaling and translating of a prototype called mother wavelet as

$$g_{\mu,\tau}(t) = \frac{1}{\sqrt{\mu}} g\left(\frac{t-\tau}{\mu}\right) \qquad \mu, \tau \in R, \tag{3.1}$$

where $g(t)$, μ and τ denote the mother wavelet, the scale parameter and the time translation parameter, respectively. Then, the continuous wavelet transform, $W_f(\mu, \tau)$, of a signal $f(t)$ at the time parameter τ and the scale parameter μ is calculated as:

$$W_f(\tau, \mu) = \int_{-\infty}^{\infty} f(t) \bar{g}_{\tau,\mu}(t) dt, \tag{3.2}$$

where $\bar{g}$ is the complex conjugate of g.

Unlike the Fourier transform which uses fixed basis functions, i.e. sines and cosines, the wavelet transform offers flexibility in the choice of mother wavelets. There are different families of wavelets, e.g. Daubechies, symlet and coiflet families, that one can choose from. Generally, a properly selected wavelet matches well to the analyzed signal [95] and hence results in a sparse representation of the signal. In other words, the signal energy is concentrated in a few coefficients.

The continuous wavelet transform parameters (μ, τ) can be sampled to reduce the redundancy and to make the wavelet transform more practical in dealing with discrete signals [96]. This will lead to discrete wavelet transform (DWT). DWT is essentially a filter bank consisting of bandpass filters that effectively splits a signal into a number of subbands.

DWT can be performed using a simple and efficient algorithm called pyramidal algorithm [97]. As illustrated in Figure 3.1(a), the pyramidal algorithm decomposes a signal, $f_m[n]$, at level m (f_0 is the original signal to start with) by convolving it with a low-pass filter, h (scaling filter), to form an approximation signal, $f_{m+1}[n]$, at level $m+1$, and a high-pass filter, g (wavelet filter), to form a detail signal, $f'_{m+1}[n]$, at level $m+1$,

$$\begin{aligned} f_{m+1}[n] &= \sum_k h[2n-k] f_m[k] \\ f'_{m+1}[n] &= \sum_k g[2n-k] f_m[k] \end{aligned} \tag{3.3}$$

The resulting signals, $f_{m+1}[n]$ and $f'_{m+1}[n]$, are subsequently sampled at every other point in order to avoid redundancy. If needed, the approximation coefficient, $f_{m+1}[n]$,

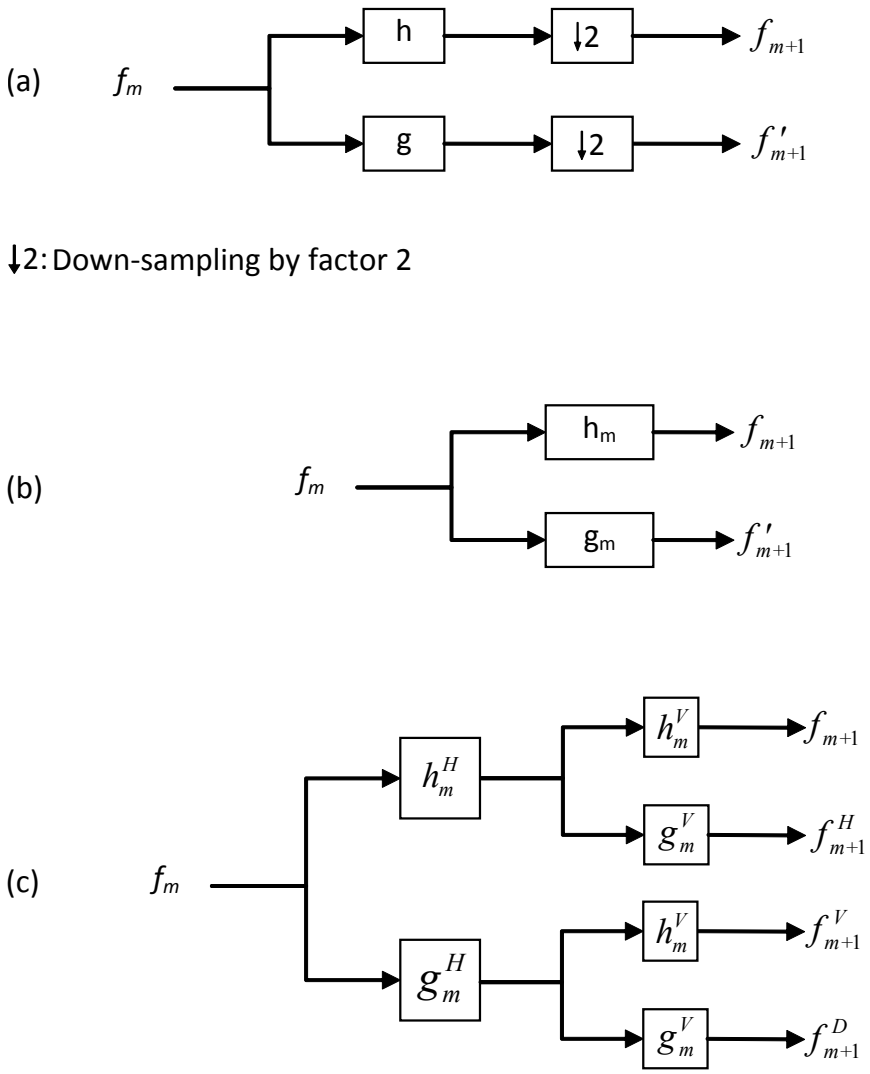

Figure 3.1: Decomposition of a signal, f_m, at level m into approximation and detail signals at level $m+1$, (a) wavelet decomposition, 1D signal, (b) SWT decomposition, 1D signal, (c) SWT decomposition, 2D signal.

is further decomposed to reach the desirable level of decomposition.

To illustrate how the discrete wavelet analysis is performed, we present an example in the following. Figure 3.2 shows examples of scaling filters and wavelet filters. These wavelet filters are from the Daubechies family denoted as 'dbN' where N is a positive integer. A Daubechies wavelet of order N has N vanishing moments. That is the scaling function can generate polynomials up to degree $N-1$. In other words, the wavelet coefficients are zero for polynomials of degree at most $N-1$. Another important property of Daubechies wavelets is their compact support, i.e. the function is non-zero only for a limited portion of its domain. A 'dbN' wavelet has a support size of $2N-1$. Wavelets with a shorter support length have the advantage of being

more localized in time.

Now, suppose we would like to analyze the signal shown in Figure 3.3 using one of the wavelet functions shown in Figure 3.2. As it can be seen in Figure 3.3, the signal is initially constant, then linear and eventually constant again. This suggests that 'db2' is the best wavelet among Daubechies family for analyzing this signal as it has two vanishing moments.

Figure 3.3 shows one level decomposition of the signal using 'db1'[1]-'db4'. As can be seen, all approximation and detail coefficients have half the length of the original signal (The length of coefficients is often a little different from exactly half the length of the original signal depending on how the signal boundaries are treated.). In general, the *approximation* coefficient is similar to the original signal except for some details which are captured by the *detail* coefficient. As mentioned earlier, we would like to achieve a transformation which results in a sparse representation of the signal, i.e. a signal representation that has fewer number of nonzero coefficients. Comparing the coefficients in Figure 3.3 shows that the 'db1' performs worst as the detail coefficients have many nonzero elements. The other filters are almost the same, 'db2' detail has 2 nonzero elements, 'db3' 4 nonzero elements and 'db4' 6 nonzero elements. Therefore as expected, the best representation of the signal is obtained by 'db2'.

For the above example, it is rather easy to determine which wavelet should be selected, however, in practice, signals are much more complex and are contaminated by noise. Therefore, selecting a proper wavelet can be challenging. A common selection criterion is the Shannon entropy.

Shannon entropy of a signal, s_i, $i = 1, 2, \ldots, n$ is defined as $S = -\sum_{i=1}^{n} p_i \log_e p_i$ where $p_i = s_i^2 / \sum_{i=1}^{n} s_i^2$. Shannon entropy, a measure of the randomness in a system, is an excellent indication of energy concentration [98]. The higher the energy concentration of a signal, the lower the Shannon entropy. Let us elaborate this concept by considering two extremes. Suppose all energy of the signal is captured by one coefficient (the highest possible energy concentration), i.e. all other coefficients are zero. In this case, $p_i = s_i^2 / \sum_{i=1}^{n} s_i^2 = 1$ and $S = 0$. This means that there is no randomness in this signal ($S = 0$). If s_i's are wavelet coefficients, it means that the signal is completely represented only by one coefficient (the best possible transformation). On the other extreme, if the signal energy is spread equally over all coefficients, i.e. $s_i = c$ and c is a constant, Shannon entropy takes its maximum $S = \log_e n$. Therefore to select the best wavelet basis, we need to minimize the Shannon entropy.

[1] 'db1' is also called Haar wavelet

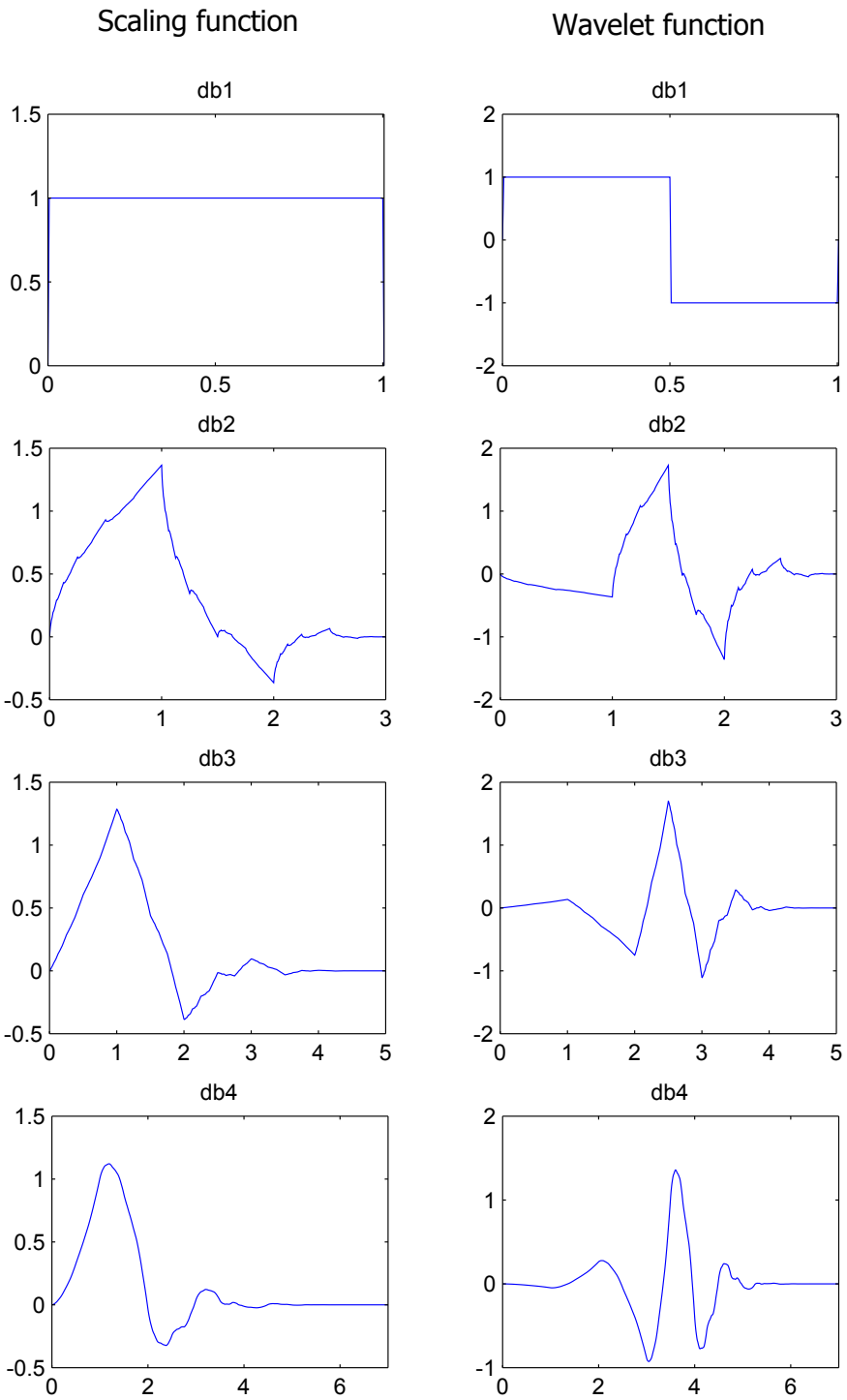

Figure 3.2: Scaling filters and wavelet filters of Daubechies wavelet family of order 1 to 4

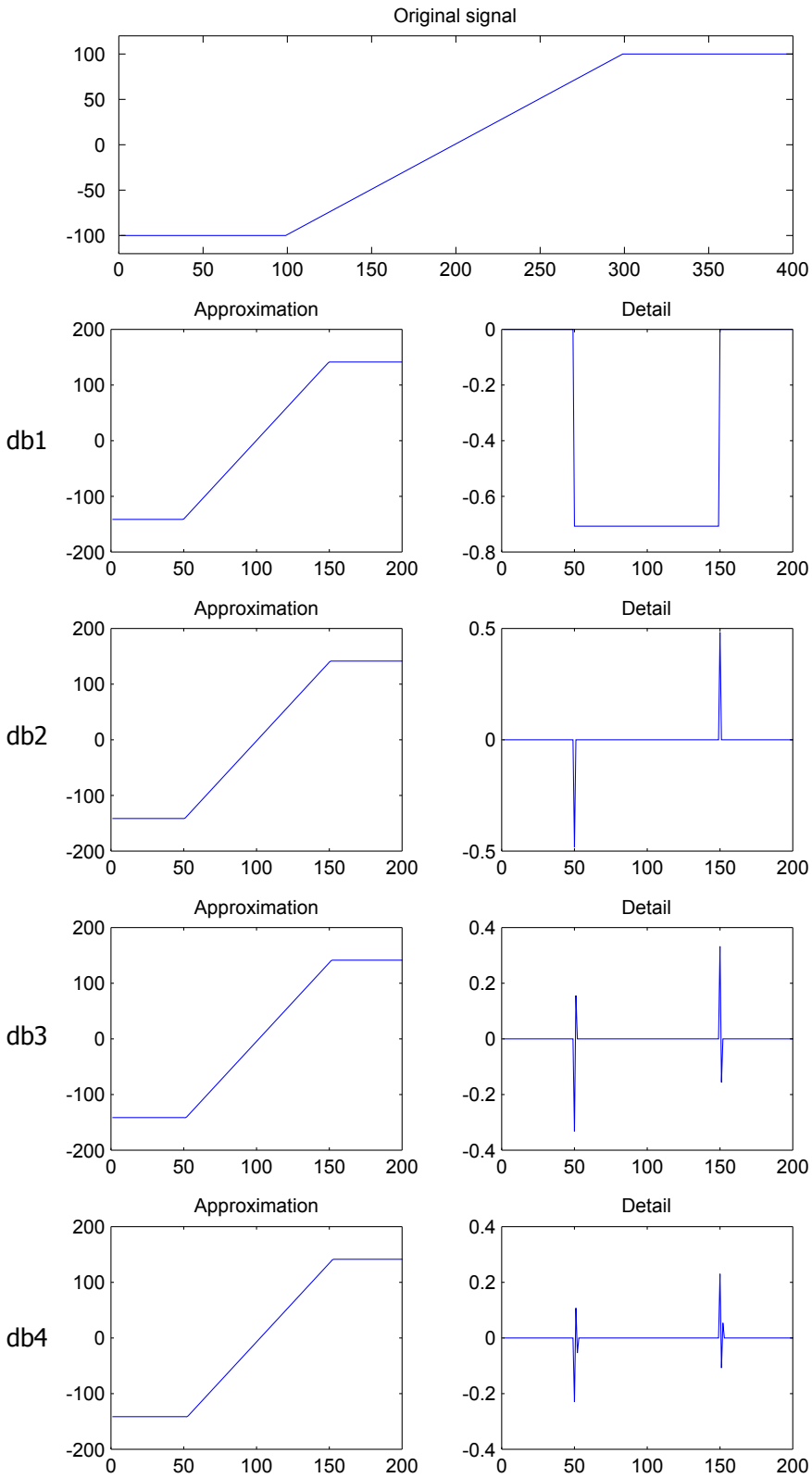

Figure 3.3: A sample signal decomposed by Daubechies wavelet filters of order 1 to 4 and the resulting wavelet coefficients

Although DWT is very efficient from the computational point of view, it is not translation invariant, i.e. translating the original signal may lead to different wavelet coefficients [99]. This degrades the quality of denoising [52]. To overcome this drawback, stationary wavelet transform (SWT) was proposed [100]. The only difference between SWT and DWT is that when calculating SWT the signal is not decimated, instead, at each level the filters are up-sampled, i.e.

$$\begin{aligned} f_{m+1}[n] &= \sum_k h_m[n-k] f_m[k] \\ f'_{m+1}[n] &= \sum_k g_m[n-k] f_m[k] \end{aligned} \tag{3.4}$$

in which the scaling filter is defined recursively as:

$$h_{m+1}[k] = h_m[k] \uparrow 2 = \begin{cases} h_m[k/2], & k \ even \\ 0, & k \ odd \end{cases} \tag{3.5}$$

where $h_0[k] = h[k]$ and $\uparrow 2$ denotes upsampling by a factor of 2. The wavelet filter, $g_m[k]$, can be defined similarly. Figures 3.1 (a) and (b) illustrate how DWT and SWT are performed, respectively.

The 2D wavelet transform can be formulated to be separable in the two dimensions so it can be computed by extending the 1D pyramidal algorithm transform. In other words, 1D wavelet decomposition is performed first in one direction, then in another direction. Thus, the 2D SWT of a 2D function, $f_m[n_1, n_2]$, is calculated as:

$$\begin{aligned} f_{m+1}[n] &= \sum_{k_1}\sum_{k_2} h_m^H[n_1-k_1] h_m^V[n_2-k_2] f_m[k_1,k_2] \\ f_{m+1}^H[n] &= \sum_{k_1}\sum_{k_2} h_m^H[n_1-k_1] g_m^V[n_2-k_2] f_m[k_1,k_2] \\ f_{m+1}^V[n] &= \sum_{k_1}\sum_{k_2} g_m^H[n_1-k_1] h_m^V[n_2-k_2] f_m[k_1,k_2] \\ f_{m+1}^D[n] &= \sum_{k_1}\sum_{k_2} g_m^H[n_1-k_1] g_m^V[n_2-k_2] f_m[k_1,k_2] \end{aligned} \tag{3.6}$$

where superscripts H, V, and D stand for horizontal, vertical, and diagonal coefficients, respectively. Figure 3.1 (c) illustrates how 2D SWT is performed using the pyramidal algorithm. As illustrated, a 2D signal is decomposed into an approximation signal and three detail signals. Because each detail signal is associated with the detail of the signal in one direction, they are called horizontal, vertical, and diagonal

Table 3.1: Frequency content of each wavelet coefficient

	Low Vertical Frequency	High Vertical Frequency
Low Horizontal Frequency	Approximation Coefficient	Horizontal Detail Coefficient
High Horizontal Frequency	Vertical Detail Coefficient	Diagonal Detail Coefficient

detail coefficients. Table 3.1 gives the frequency content of each wavelet coefficient. For example, the horizontal detail coefficient, which is passed through a scaling filter in horizontal direction and through a wavelet filter in vertical direction, contains the horizontal low frequency and vertical high frequency content of the signal.

3.2.1 Wavelet thresholding

Wavelet denoising is performed by transforming a signal to the wavelet domain, treating it in the wavelet domain and then transforming it back to the time/spatial domain. Wavelet thresholding, a widely used wavelet denoising method, is performed by estimating a threshold and removing noise according to a shrinkage rule. The shrinkage rule defines how the threshold is applied. There are two popular shrinkage rules:

- Hard thresholding sets any wavelet coefficient, f_i, less than or equal to the threshold to zero.
  if $f_i < thresh$
  $f_i \leftarrow 0$
  end

- Soft thresholding, in addition, subtracts threshold from any coefficient greater than the threshold.
  if $f_i < thresh$
  $f_i \leftarrow 0$
  else
  $f_i \leftarrow f_i - thresh$
  end

Wavelet thresholding combines simplicity and efficiency and exhibits certain asymptotic optimality properties [101]. It has become a standard technique used extensively for signal denoising. We have applied the wavelet thresholding algorithm in the following steps:

1. Perform the wavelet transform: In this work, we use the 2D SWT to decompose an ultrasonic B-scan image. SWT often produces a lower estimation risk than does DWT, thanks to its redundancy [102].

2. Estimate a threshold: There are many methods available for estimating the threshold. Coifman and Donoho [103] found that universal thresholding when used in conjunction with SWT produces a smaller number of noise spikes. The universal threshold for a signal contaminated by white Gaussian noise (WGN) is given by: $\sigma_n\sqrt{2\log n}$, where σ_n is the standard deviation of the noise and n is the number of coefficients. If σ_n is unknown, it can be estimated using the robust median absolute deviation of the finest scale,

$$\sigma_{MAD} = \frac{median(|f^D_{1,1}|, |f^D_{1,2}|, \ldots, |f^D_{1,n}|)}{0.6475} \tag{3.7}$$

   where $f^D_{1,i}$ is the i'th coefficient of the diagonal coefficient at the first level.

3. Apply a shrinkage rule to the wavelet coefficients: Coifman and Donoho [103] found that combining the hard shrinkage rule and SWT gave both good visual characteristics and good quantitative characteristics; hence, we have adopted the hard shrinkage rule throughout.

4. Perform the inverse transform of the wavelet coefficients.

Although SWT denoising often results in a high denoising performance, at least one of its aspects is unattractive; the thresholding of an SWT coefficient which is oscillatory about zero degrades the denoising efficiency. To overcome this problem, Olhede and Walden [52] proposed analytic wavelet thresholding. They applied wavelet thresholding to the amplitude (the envelope amplitude) of the signal rather than to its magnitude [1]. In other words, they suppressed the effect of the phase. In setting the threshold value, they proved that the amplitude of WGN asymptotically follows chi distribution and adapted the universal threshold value, $\sigma_n\sqrt{2\log(n\log n)}$, proposed by Sardy [104] for chi-distributed white noise.

The amplitude of a real-valued signal can be obtained by calculating its analytic signal. The analytic signal, $a(t)$, of a signal, $x(t)$, is a complex valued signal whose absolute is equal to the amplitude of the envelope of $x(t)$ and its argument is equal

[1]The terms amplitude and magnitude may be used interchangeably. The following example clarifies the difference between amplitude and magnitude, as used in this thesis. Let $s = A\cos(\omega t+\phi)$, then the magnitude of s is equal to its absolute value $|A\cos(\omega t+\phi)|$ and the amplitude is equal to A.

to the instantaneous phase of $x(t)$. In order to apply analytic thresholding to a 2D signal we need to calculate its analytic signal, but a regular generalization of the analytic signal is not available in multiple dimensions [105]. In the following section, we address this problem.

3.2.2 Analytic signal of two dimensional signals

The analytic signal plays an important role in signal processing because its magnitude and angular argument are frequently used to demodulate signals and define the instantaneous amplitude and phase of real-valued signals. This can be achieved using Hilbert transform under certain conditions stated in Bedrosian's theorem. According to Bedrosian's theorem, if the envelope and carrier are non-overlapping band-limited signals, the amplitude of the analytic signal is identical to the envelope [106]. The analytic signal, $a(t)$, arising from a 1D signal, $x(t)$, is defined as:

$$a(t) = x(t) + iH[x(t)] \tag{3.8}$$

where H denotes the Hilbert transform. For a signal, $x(t)$, the amplitude and the magnitude of the signal are defined as $|a(t)|$ and $|x(t)|$, respectively. Hilbert transform is an integral transform defined by:

$$H[x(t)] = \frac{1}{\pi} \int_{-\infty}^{\infty} \frac{x(\tau)}{t - \tau} d\tau \tag{3.9}$$

Analytic signals may be better understood in the frequency domain. If $X(\omega)$ is the Fourier transform of the real signal, $x(t)$, then

$$A(\omega) = (1 + \text{sign}(\omega))X(\omega) \tag{3.10}$$

where $A(\omega)$ is the Fourier transform of the analytic signal and the *sign* function is defined as:

$$\text{sign}(\omega) = \begin{cases} 1, \text{ if } \omega > 0 \\ 0, \text{ if } \omega = 0 \\ -1, \text{ if } \omega < 0 \end{cases} \tag{3.11}$$

In other words, the analytic signal is computed in the frequency domain by suppressing negative frequency components and doubling positive frequency components.

In order to generalize the concept of the analytic signal to multiple dimensions, the positive and negative frequencies in multiple dimensions need to be defined. A

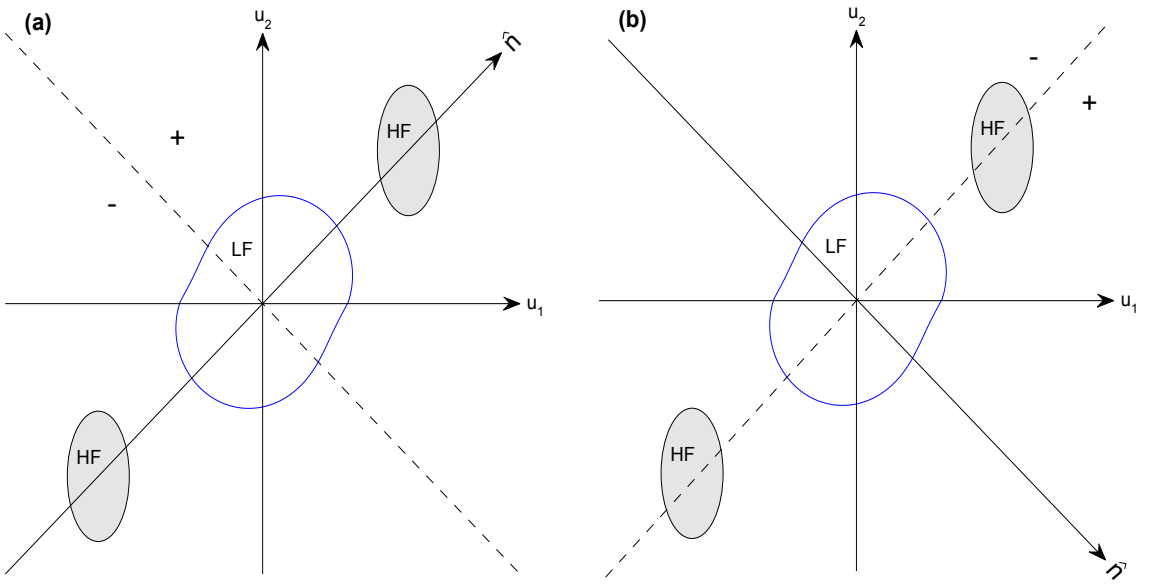

Figure 3.4: Illustration of high frequency (HF) carrier, low frequency (LF) envelope, reference vector and positive and negative frequency regions in two dimensions. (a) a properly selected reference vector, $\hat{\mathbf{n}}$, and (b) an improperly selected reference vector, $\hat{\mathbf{n}}$.

straightforward way to define positive and negative frequencies is to introduce a reference vector in the frequency domain. Introducing a reference vector, $\hat{\mathbf{n}}$, a frequency coordinate, $\mathbf{u}$, is labeled positive if $\mathbf{u}^T\hat{\mathbf{n}} > 0$ and negative if $\mathbf{u}^T\hat{\mathbf{n}} < 0$ [105]. Despite the argument put forward by Blow and Sommer [107] that this method is one-dimensional in nature, we will show that it is suited for our purpose.

The envelope of the signal is best recovered in the direction of the reference vector and worst recovered in the direction $\hat{\mathbf{n}}_\perp$ which is perpendicular to the reference vector [107]. However, there is no general rule for selecting the direction $\hat{\mathbf{n}}$. Figure 3.4 demonstrates a properly and an improperly selected reference vectors. For a properly selected reference vector, high frequency and low frequency components are projected to high frequency and low frequency regions of the reference vector, respectively. In addition, the projection of the high-frequency carrier on the reference vector does not overlap with the projection of the low-frequency envelope; hence, according to Bedrosian's theorem, the low frequency envelope can be extracted using the Hilbert transform (see Section 3.2.3 for the proof for 2D signals). In fact, the reference vector not only defines the negative and positive frequencies but also defines the concept of high frequency and low frequency in multiple dimensions. To determine the reference vector, it is often adequate to know roughly where the HF and LF components are located in the frequency plane.

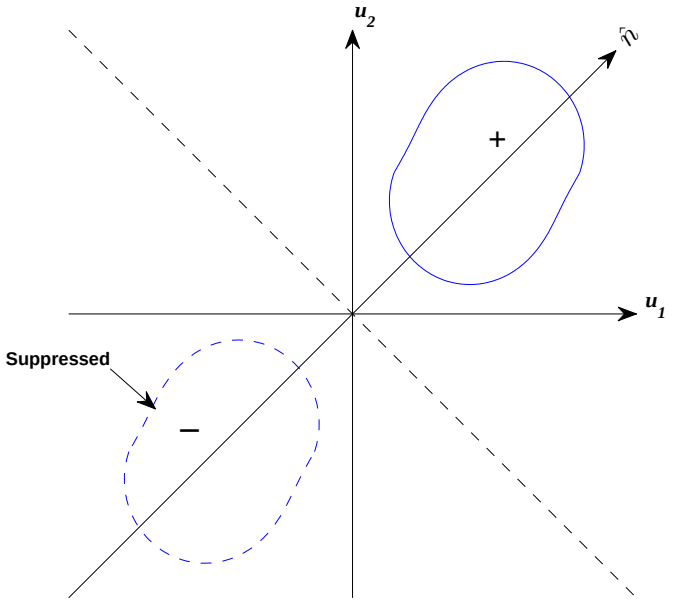

Figure 3.5: 2D frequency spectrum of the product of envelope and carrier.

Figure 3.5 depicts the 2D FT of the product of the envelope and carrier. As illustrated, selecting any reference vector among $\hat{\mathbf{n}}$, $\hat{\mathbf{u}}_1$ and $\hat{\mathbf{u}}_2$ and suppressing the negative frequency components defined by these reference vectors leads to the same result. If no prior knowledge about the HF and LF components is available, the reference vector can be chosen in the direction of the principal axis of the second moment of the area with minimum moment (compare Figures 3.4 (a) and (b)). Principal axes form a coordinate system in which the second moments of area assume their maximums and minimums.

Let's recall the 2D Gaussian echo model, equation (2.25),

$$g(x,t) = e(x,t)cos(2\pi f_c(t-\tau(x)) + \phi) \tag{3.12}$$

in which $\tau(x)$ is a linear function of x; that is $\tau(x) = ax + b$ where a and b are constants. Taking the Fourier transform of equation (3.12) gives,

$$\begin{aligned} G(f_x, f_t) = &\frac{1}{2}E(f_x + af_c, f_t - f_c)exp(i(\phi - 2\pi f_c b)) \\ &+\frac{1}{2}E(f_x - af_c, f_t + f_c)exp(-i(\phi - 2\pi f_c b)). \end{aligned} \tag{3.13}$$

According to equation (3.13), the envelope, $E(f_x, f_t)$, is shifted to carrier frequencies at $(af_c, -f_c)$ and $(-af_c, f_c)$. Therefore, equation (3.13) implies that the cosine term

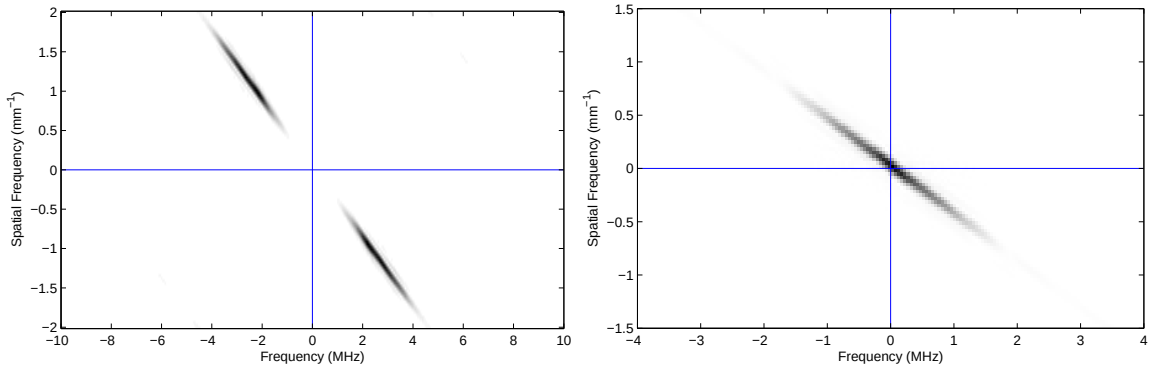

(a) (b)

Figure 3.6: a) 2D Fourier transform of a pulse-echo B-scan obtained from a specimen with a 3 mm crack after removing wedge noise, and b) its envelope spectrum.

in equation (3.12) shifts the envelope to the 2nd and 4th quadrants.

Figure 3.6(a) depicts the 2D FT of an experimental ultrasonic signal. It can be seen that the crack echoes in the frequency domain appear in the 2nd and 4th quadrants. It is easy, therefore, to introduce a reference vector in order to remove either the 2nd or the 4th quadrant and keep the other one. To calculate the envelope spectrum of this experimental signal, we have selected the y-axis as the reference vector. Figure 3.6(b) shows the envelope spectrum calculated by introducing y-axis as the reference vector.

3.2.3 Mathematical proof for recovering the envelope of a 2D signal

In the previous section, we have introduced a reference vector to recover the envelope of a 2D modulated signal. In this section, we prove that the envelope can be exactly recovered, if the reference vector is selected properly.

Theorem 1 *Let $f(x)$ and $g(x)$ be general complex functions of 2D real variable x. If*

(a) Fourier transform, $F(\mathbf{u})$, of $f(\mathbf{x})$ vanishes for $|u_1| > a$ and the Fourier transform, $G(\mathbf{u})$, of $g(\mathbf{x})$ vanishes for $|u_1| < a$, where a is an arbitrary positive constant,

or

(b) $f(\mathbf{x})$ and $g(\mathbf{x})$ are analytic signals with respect to a reference vector $\mathbf{u_1}$, i.e. both $F(\mathbf{u})$ and $G(\mathbf{u})$ vanish for $u_1 < 0$.

then the directional Hilbert transform (HT) of the product of $f(\mathbf{x})$ *and* $g(\mathbf{x})$ *is given by,*

$$H_1[f(\mathbf{x})g(\mathbf{x})] = f(\mathbf{x})H_1[g(\mathbf{x})] \tag{3.14}$$

in which the directional Hilbert transform of a function $f(\mathbf{x})$ *with respect to a reference vector* $\mathbf{u_1}$ *is defined as*

$$FT[H_1[f(\mathbf{x})]] = i \ sign(u_1)F(\mathbf{u}) \tag{3.15}$$

or

$$H_1[f(\mathbf{x})] = \frac{1}{(2\pi)^2}\int_U i \ sign(u_1)F(\mathbf{u})e^{i\mathbf{u}.\mathbf{x}}dU \tag{3.16}$$

in which FT denotes the Fourier transform, $dU = du_1du_2$*, and the integration is performed over the interval of* $(-\infty, \infty)$ *for two variables of* u_1 *and* u_2*.*

Proof The Fourier transform of the product of two functions is equal to the convolution of their Fourier transforms, thus

$$f(\mathbf{x})g(\mathbf{x}) = \frac{1}{(2\pi)^4}\int_V\int_U F(\mathbf{u})G(\mathbf{v})e^{i(\mathbf{u}+\mathbf{v}).\mathbf{x}}dUdV \tag{3.17}$$

Now from equations (3.15) and (3.17) we have

$$H_1[f(\mathbf{x})g(\mathbf{x})] = \frac{1}{(2\pi)^4}\int_V\int_U i \ \text{sign}(u_1+v_1)F(\mathbf{u})G(\mathbf{v})e^{i(\mathbf{u}+\mathbf{v}).\mathbf{x}}dUdV \tag{3.18}$$

But, either

(a) Functions f and g are band-limited signals, hence the product $F(\mathbf{u})G(\mathbf{v})$ is non-vanishing only when $|u_1| < a$ and $|v_1| > a$.

or

(b) Functions f and g are analytic, thus F(u)G(v) is non-vanishing only when $u_1 > 0$ and $v_1 > 0$.

In either case, for the non-vanishing region $\text{sign}(u_1 + v_1) = \text{sign}(v_1)$, hence equation (3.18) yields

$$H_1[f(\mathbf{x})g(\mathbf{x})] = \frac{1}{(2\pi)^4}\int_V\int_U i \ \text{sign}(v_1)F(\mathbf{u})G(\mathbf{v})e^{i(\mathbf{u}+\mathbf{v}).\mathbf{x}}dUdV \tag{3.19}$$

Integrating over U gives,

$$H_1[f(\mathbf{x})g(\mathbf{x})] = \frac{1}{(2\pi)^2} f(\mathbf{x}) \int_V i \ \mathrm{sign}(v_1) G(\mathbf{v}) e^{i\mathbf{v}.\mathbf{x}} dV \tag{3.20}$$

Finally from the definition of the directional HT, equation (3.20) becomes

$$H_1[f(\mathbf{x})g(\mathbf{x})] = f(\mathbf{x}) H_1[g(\mathbf{x})]. \tag{3.21}$$

Proof ends.

In this proof, for simplicity and without loss of generality we let the frequency axis, $\mathbf{u_1}$, be the reference vector. This theorem implies that the directional HT of the product of a low frequency envelope and a high frequency carrier is equal to the envelope multiplied by the directional HT of the carrier. Note that high frequency and low frequency are defined with respect to the reference vector. Likewise the analytic signal can be defined as amplitude of the analytic signal of this product; that is $A(\mathbf{u}) = (1+\mathrm{sign}(u_1))F(\mathbf{u})$ or $a(\mathbf{x}) = f(\mathbf{x}) - H_1[f(\mathbf{x})]$. Now, let $f(\mathbf{x}) = \mathrm{e}(\mathbf{x})\cos(\boldsymbol{\omega}.\mathbf{x})$ where $\mathrm{e}(\mathbf{x})$ is the low frequency envelope which takes only positive values. According to the above theorem, the directional HT and the analytical signal of $f(\mathbf{x})$ are:

$$H_1[f(\mathbf{x})] = H_1[\mathrm{e}(\mathbf{x})\cos(\boldsymbol{\omega}.\mathbf{x})] = \mathrm{e}(\mathbf{x}) H_1[\cos(\boldsymbol{\omega}.\mathbf{x})] = -\mathrm{e}(\mathbf{x})\sin(\boldsymbol{\omega}.\mathbf{x}) \tag{3.22}$$

$$a(\mathbf{x}) = \mathrm{e}(\mathbf{x})\cos(\boldsymbol{\omega}.\mathbf{x}) - i\mathrm{e}(\mathbf{x})\sin(\boldsymbol{\omega}.\mathbf{x}) = \mathrm{e}(\mathbf{x}) e^{i\boldsymbol{\omega}.\mathbf{x}} \tag{3.23}$$

Clearly, the amplitude of the analytic signal obtained from the directional HT is equal to the envelope signal.

The proposed denoising method for 2D signals uses a thresholding method based on the amplitude of the noisy signal. The amplitude is obtained by calculating the envelope of the signal. Calculation of the envelope of 2D signals are addressed in this section. The following section presents the proposed denoising method.

3.3 Proposed denoising method

This section presents the proposed denoising method. The proposed method removes background noise and random noise to enhance the B-scan image quality. In ultrasonic pulse-echo setup the background noise is caused by wave reflection at the wedge-specimen interface. In pitch-catch setup, the background noise is caused by the backwall echo. In either case, this background noise conveys no information on the

damage and corrupts the signal. In this study, we assume non-correlated random noise. Such noise may be generated by different sources, such as electrical interference and quantization.

The proposed method employs the 2D SWT because of its excellent denoising performance. To further improve the denoising performance, analytic thresholding is used. We also implement a step to remove the background noise. To illustrate, we apply the proposed method, step by step, to an experimental signal (shown in Figure 7.6).

Figure 3.7 illustrates the flowchart of the proposed denoising method. Firstly, the signal is decomposed using the 2D SWT. The horizontal wavelet filter is selected to best match the crack echo. Such a filter transforms signal energy to a few wavelet coefficients; in other words wavelet coefficients provide a sparse representation of the signal. The selection is made among three orthogonal wavelet families of Daubechies (dbN), symlet (symN), and coiflet (coifN), based on the Shannon entropy criterion [108].

As explained in Section 3.1, wavelet basis selection can be performed by minimizing the Shannon entropy. An A-scan signal is decomposed using dbN (N=1, 2, ..., 15), symN (N=1, 2, ..., 15), and coifN (N=1, 2, ..., 5) wavelets; this done, its entropy is calculated. Figure 3.8 depicts the entropy of wavelet coefficients for different wavelets. The minimum entropy belongs to *sym9* and the best level of decomposition for all wavelets is three.

We choose the Haar mother wavelet as the vertical filter. It is employed to separate wedge noise from the crack echo as much as possible. Haar wavelet has one vanishing moment. In other words, the approximation coefficient contains the locally constant portion of the signal, and the detail coefficients contain the varying portion. Because the wedge echo does not change when transducer is moved, it appears mainly in the approximation and/or vertical coefficients depending on its horizontal frequency; in contrast the time of flight of the crack echo changes as the transducer's position does, hence the crack echo appears in the horizontal and/or diagonal coefficients.

Figure 3.9 shows the SWT decomposition of the experimental signal. As illustrated, the approximation coefficient contains most of the energy; however, the crack echo is mainly captured by the horizontal detail. The image can be decomposed to higher levels to better separate the wedge and flaw signals, as well as to achieve better denoising. Using the fact that the crack echo and background noise are captured by different wavelet coefficients, Cygan *et al.* [45] extracted the crack echo from the original B-scan. Nonetheless, this separation is not perfect, in particular, the approx-

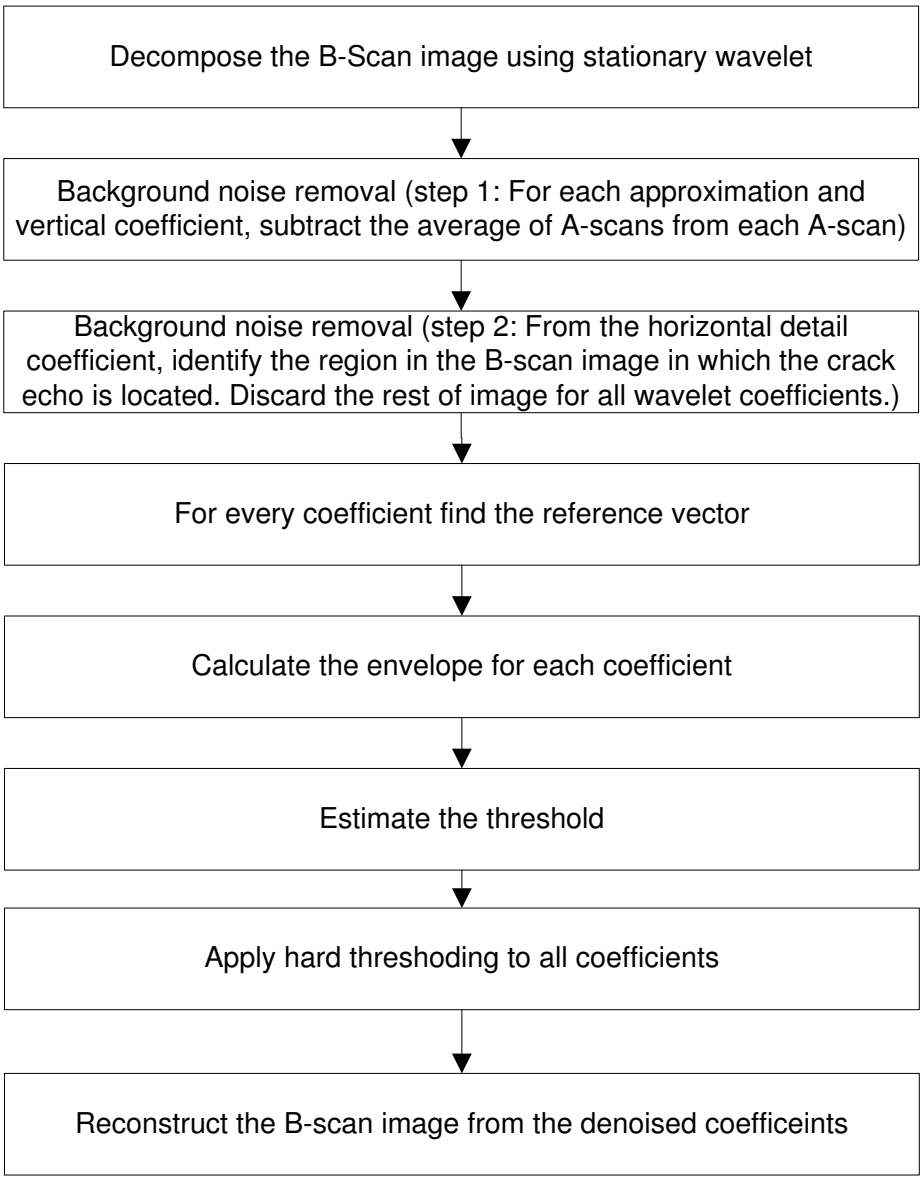

Figure 3.7: Flowchart of the proposed denoising method

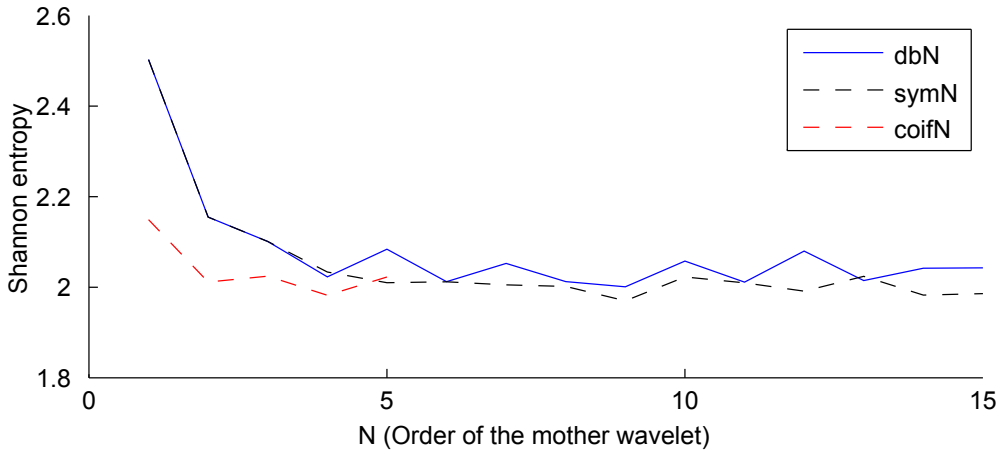

Figure 3.8: The Shannon entropy of wavelet coefficients of an A-scan signal for different mother wavelets

imation coefficient contains some of the flaw signal's energy as well. Therefore, some information will be lost if we discard this coefficient from our analysis. Moreover, the wavelet filter causes a delay which affects the size-estimation.

The next step is to remove the background noise caused by wedge-specimen interface. Mosey et al. [109] recommended calculating the mean of A-scans, iteratively subtracting the mean from all A-scans to remove the background of the B-scan image. Although this method is conceptually simple, it can't remove the wedge noise effectively when there are small variations in it or the signal-to-noise ratio (SNR) is low due to high level of random noise. Petcher and Dixon [110] proposed using the Hough transform to remove the surface waves from ultrasonic B-scans. Although this method improves the denoising, it cannot effectively compensate for local changes in the background noise. Recently, Cygan et al. [45] used wavelet transform to remove the wedge echo. They decomposed the B-scan image using wavelet transform, then suppressed the wavelet coefficients (which include wedge noise) and reconstructed the signal. Because wedge noise normally appears in the approximation and vertical detail coefficients, removing the approximation coefficient may cause major distortion in the reconstructed signal.

To overcome the shortcomings of the existing methods, we propose a two-step denoising scheme to remove the wedge echo. In the first step, the average value of all A-scans in the approximation/vertical is subtracted from each A-scan in the approximation/vertical coefficient. Figure 3.10 depicts the approximation coefficient after the first step background noise removal. It can be observed that the background noise has been significantly reduced; as a result the crack echo has emerged in the

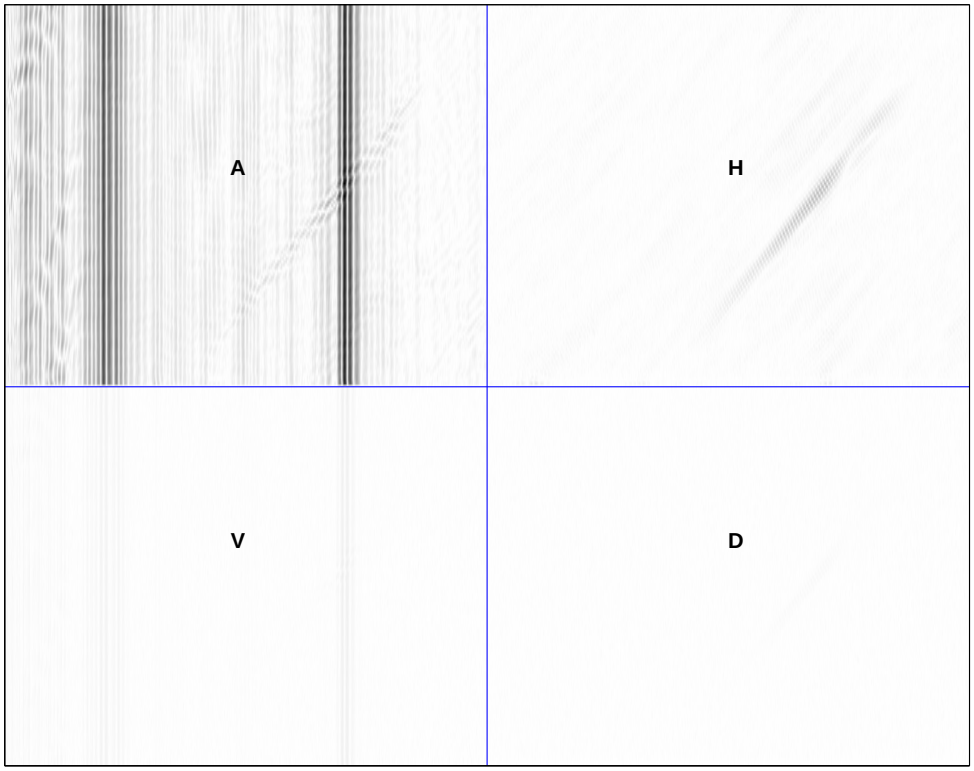

A: Approximation, H: Horizontal, V: Vertical, D: Diagonal.

For all wavelet coefficients:

x-axis: time ranging from 0 to 20.48 s

y-axis: transducer distance to the slot ranging from 0 to 30 mm

Figure 3.9: Stationary wavelet decomposition of signal shown in Figure 7.6

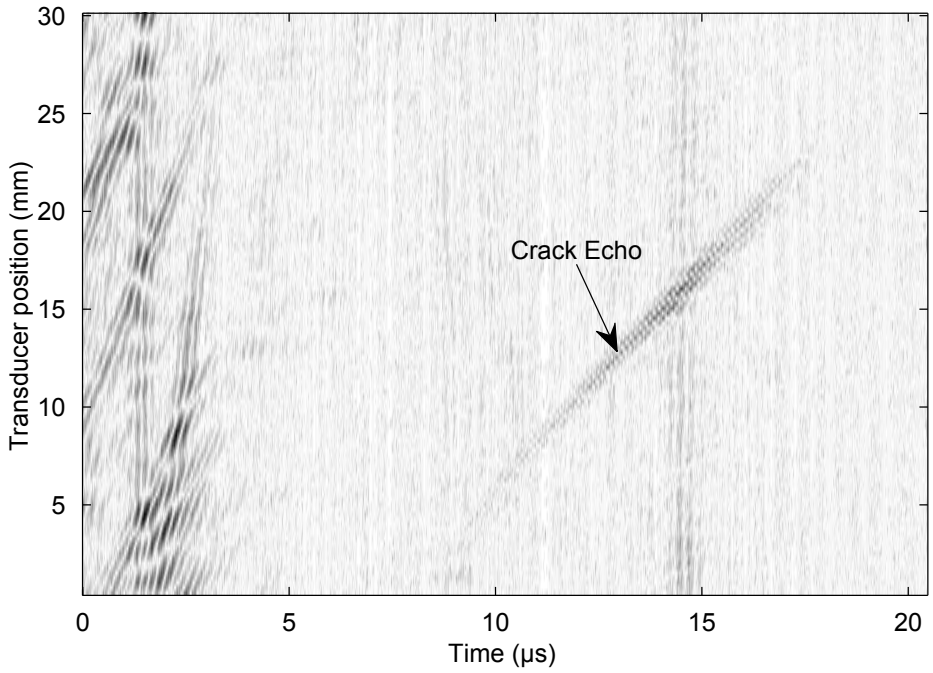

Figure 3.10: Approximation coefficient after the first step of background noise removal.

approximation coefficient while it was barely observable before removing background noise (Compare Figure 3.9 and Figure 3.10). Nonetheless, background noise is still present in this coefficient.

As can be seen in Figure 3.9, the horizontal detail coefficient mostly contains crack echo. Therefore, we can conclude that if the amplitude of the horizontal detail is smaller than noise level at a time and a position in the B-scan image, then the crack echo is not present at that point. Using this fact, we can further remove background noise as follows. If the amplitude of the horizontal detail is less than a threshold, then we set all other coefficients, i.e. approximation, vertical detail and diagonal detail, at the corresponding time and position to zero. The amplitude of the horizontal coefficient is calculated using the directional HT explained in Section 3.2.2.

To determine whether the horizontal detail amplitude is smaller than the noise level or not, we need to set a threshold value. In Section 3.2.1, we set a threshold for removing the random noise. The values in the signal which are smaller than this value are mostly noise, but not all. The threshold value for this step is set to $\alpha\sigma_n\sqrt{2\log(n\log n)}$, $0 < \alpha \leq 1$ which is a fraction of the threshold used for removing the random noise. By trial and error $\alpha = 0.75$ is selected. Selecting this value, effectively removes background noise while it hardly affects the crack echo. Figure 3.11 shows the approximation after the second step background noise removal. It can

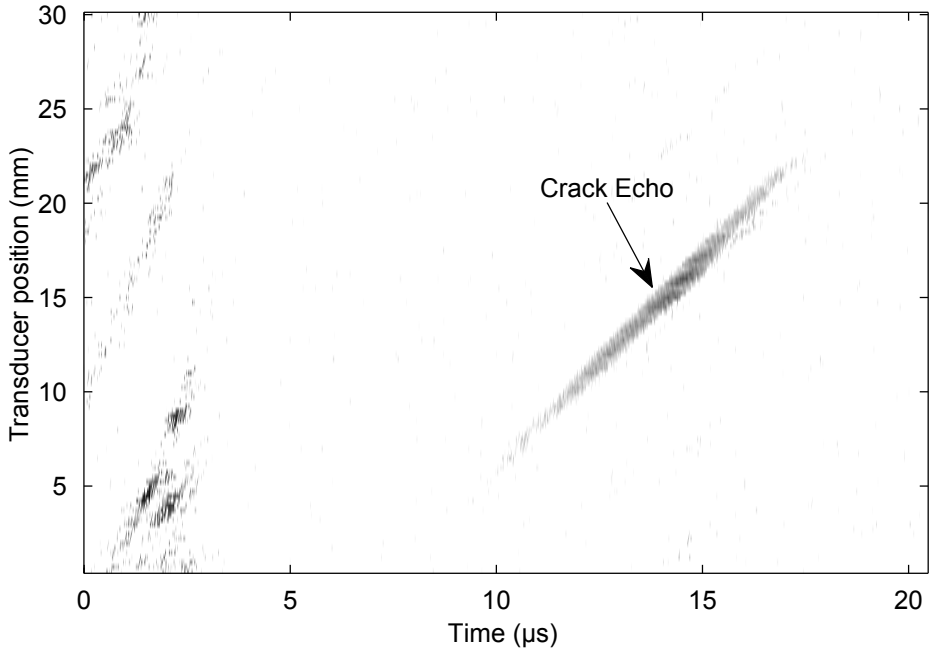

Figure 3.11: Approximation coefficient after the second step of background noise removal.

be observed that the background noise has been greatly reduced.

Finally, every coefficient is denoised and the B-scan image is reconstructed using the method explained in Section 3.2. The Sym9 and Haar mother wavelets are used as horizontal and vertical filters, respectively, for three-level SWT decomposition of the signal. Universal thresholding is used with a threshold value of $\sigma_n\sqrt{2\log(n\log n)}$. Then, the analytic signal of all coefficients (including the approximation) is calculated and they are hard thresholded.

Figure 3.12 shows the denoised coefficients. Compared to Figure 3.9, the reduction in wedge noise and random noise is evident. Finally, Figure 3.13 shows the denoised B-scan image. It can be observed that the noise has been greatly reduced. Yet, some artifacts can be observed in the left portion of Figure 3.13. We believe that these artifacts are caused by echoes reflected by irregularities near the surface. Since these echoes arrive earlier than any other echoes reflected by defects inside the material, they do not distort the echoes reflected by defects. To assess the performance of the proposed method quantitatively and compare it to other methods, in the following section, experimental signals as well as simulated B-scan signals with different levels of noise are denoised using the proposed method.

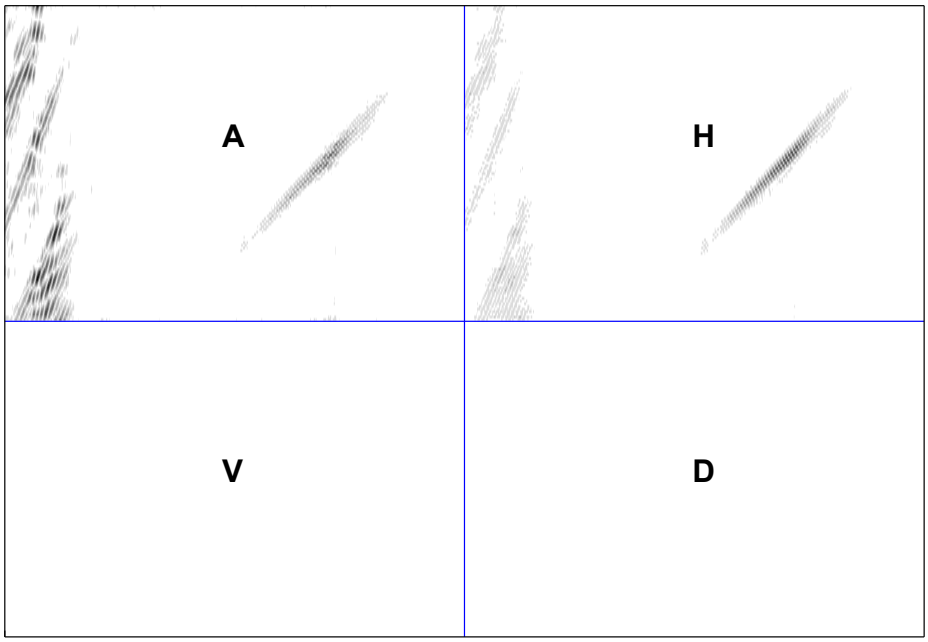

For all wavelet coefficients:

x-axis: time ranging from 0 to 20.48 s

y-axis: transducer distance to the slot ranging from 0 to 30 mm

Figure 3.12: Denoised stationary wavelet coefficients.

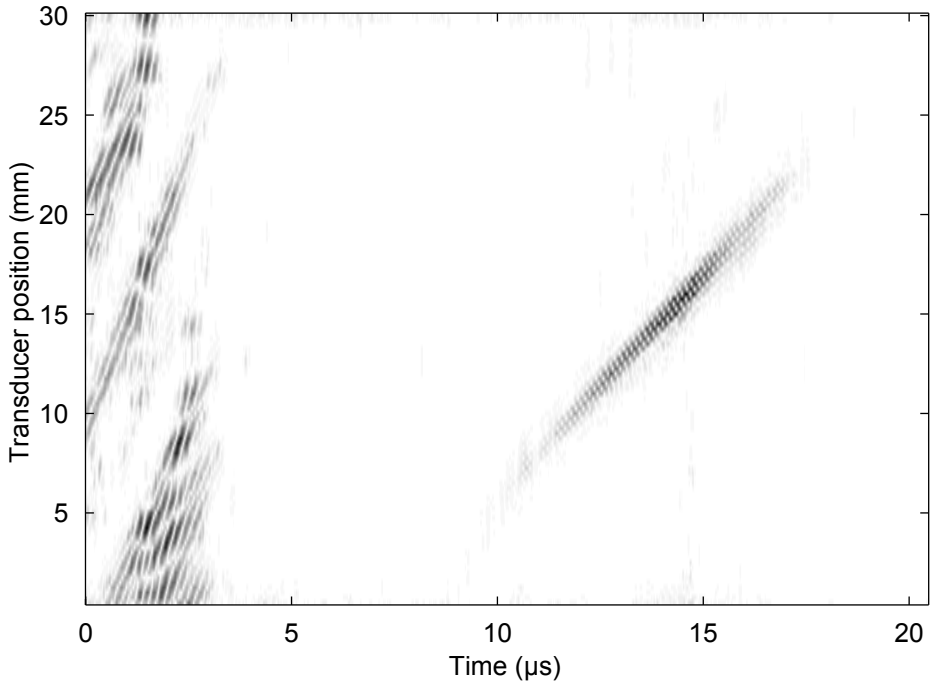

Figure 3.13: Denoised B-scan image

3.4 Evaluating the performance of the proposed method

In this section, we evaluate the performance of the proposed method using experimental and simulated signals.

3.4.1 Generating simulated B-scans

We set up a simulated B-scan as $b = c + w + r$, consisting of three terms: (1) c: crack echo (2) w: wedge noise (3) r: random noise. The parameters of each term are given as follows.

Crack echo

The crack echo is generated using the 2D ultrasonic model given by equation (2.35). The simulated signal is intended to be similar to the experimental signal, thus the parameters of equation (2.35) are estimated from the experimental signal. The parameters of function $X(x)$ in equation (2.35) are given in Figure 2.17. The time of arrival of the echo is given in Figure 2.16(a). The center frequency of the transducer is 2.25MHz. The parameters of function $T(t)$ is obtained by fitting a Gaussian signal to an envelope of an experimental A-scan and finally the amplitude is set to 1 for convenience. By substituting these parameters, equation (2.35) yields

$$\begin{aligned} &g(x,t) = e^{-0.0256(x-14.39)^2} e^{-5.67(t-\tau(x))^2} cos(4.5\pi(t-\tau(x)) + \phi) \\ &\text{where } \tau = 0.4376x + 7.162 \end{aligned} \tag{3.24}$$

Wedge echo

Similarly, the Gaussian echo model is used for generating wedge noise. The parameters of this Gaussian echo are obtained by curve fitting of an experimental signal. Unlike the crack echo, neither the amplitude nor the time of flight of the wedge echo changes with time. However, we allow small random changes in amplitude and time of flight to take into account variations in wedge echo caused by contact conditions which can be observed in the experimental data.

$$g(x,t) = \beta e^{-3.3(t-\tau)^2} cos(4.5\pi(t-\tau) + \phi) \tag{3.25}$$

where: $\beta = A_w(1+0.1rnd)$, $\tau = 14.4+0.02rnd$, rnd is a uniformly distributed random number between -1 and 1, and A_w is chosen with regard to required noise level.

Random noise

To incorporate the effect of random noise, a Gaussian distributed white noise with different powers is added to the signal.

3.4.2 Performance evaluation

Simulated signal

The signal-to-noise ratio (SNR) of the denoised B-scan image is calculated to indicate the performance of each method. SNR is defined as follows:

$$SNR = 10\log(\frac{P_{signal}}{P_{noise}}) \tag{3.26}$$

in which P is the power of a 2D signal defined as $P = \sum_i \sum_j x_{ij}^2$. Here, the signal is the crack echo and noise is the sum of random noise and background noise.

Figure 3.14 demonstrates the amount of improvement in SNR achieved by the proposed method compared to two other methods for different noise levels. In each plot the amplitude of wedge echo is fixed and the random noise level is varied. The range of random noise power added to the signal is the same for all plots. The amplitude of wedge echo, A_w, is set to 0.1, 0.2, 0.5, and 1 which are equivalent to signal-to-background noise ratio of 13.5 dB, 7.5 dB, -0.5 dB and -6.5 dB, respectively. Signal-to-background noise ratio is defined as $10\log(P_{signal}/P_{background\,noise})$. The two methods, which are compared with the proposed method, are 'swt' and 'dwt'. The first method, 'swt', is similar to the proposed method but its thresholding is based on the magnitude not the amplitude of the signal. The latter, 'dwt', is similar to 'swt' but it employs DWT instead of SWT. DWT and SWT are common denoising methods which are widely used as benchmark denoising methods. A step similar to the proposed method has been added to these two methods for removing the background noise.

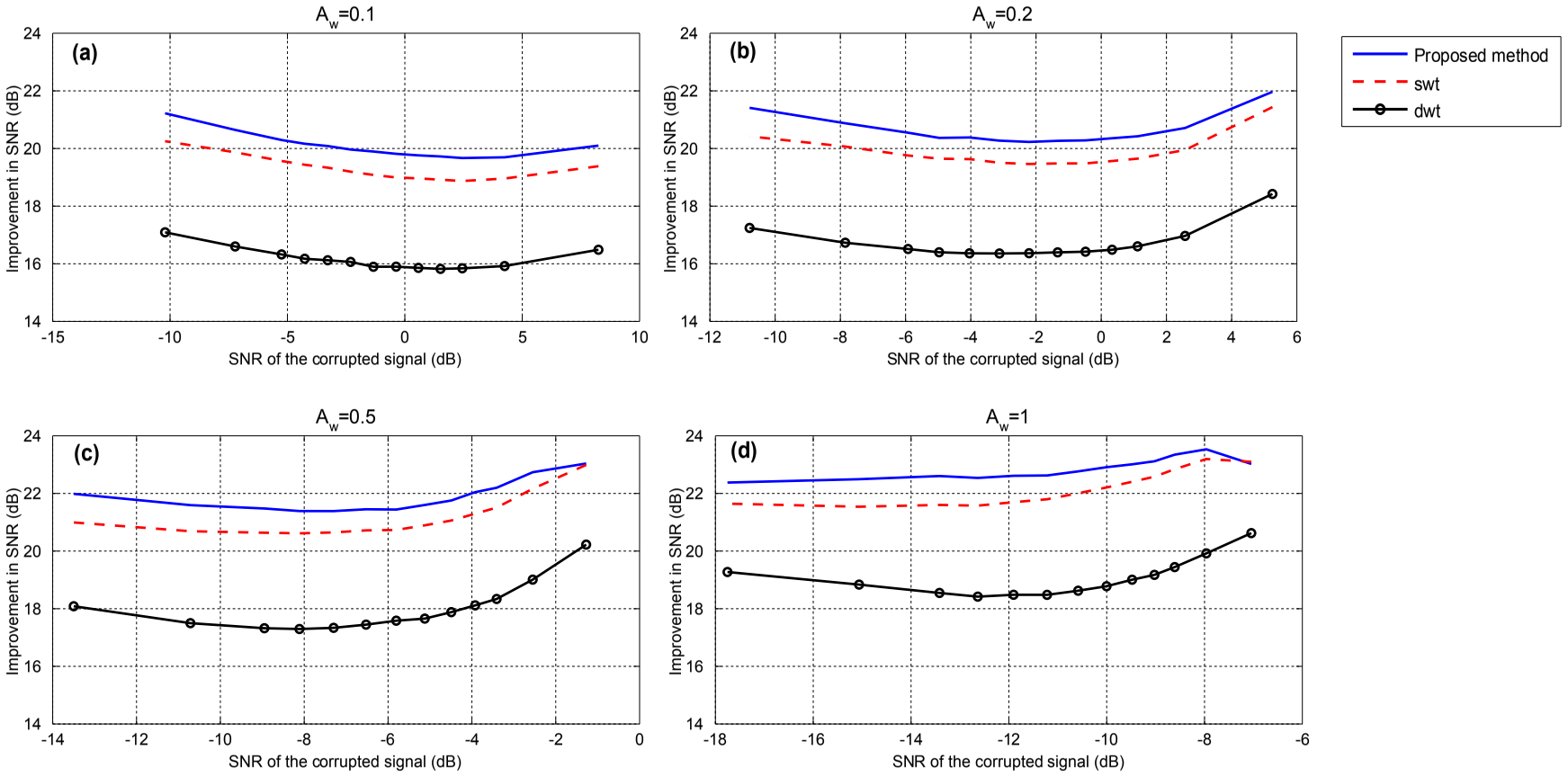

Figure 3.14: Improvement in SNR obtained by the proposed method, 'swt', and 'dwt'. (a) A_w=0.1, (b) A_w=0.2, (c) A_w=0.5, and (d) A_w=1.

It can be seen that the 'dwt' method always results in smaller improvement in SNR. This shows that using SWT instead of DWT can improve denoising. Comparing the proposed method and 'swt' shows that using analytic thresholding further improves denoising, especially when the random noise level is high. If the random noise level is low, both the 'swt' method and the proposed method provides almost identical performance. This is because the analytic thresholding, which is the the only difference between these methods, has not yet been applied. Therefore, if there is no random noise in the signal, the proposed method and 'swt' are exactly the same with regard to wedge noise removal.

Figure 3.15(a) shows a simulated B-scan image with an SNR of -18 dB and $A_w = 1$. Figures 3.15(b), (c), and (d) show the B-scan denoised by the proposed method, 'swt', and 'dwt', respectively. As can be observed, in all cases, wedge noise is perfectly removed and little random noise is left, but the proposed method retains the crack echo better than the two other methods do. This can be better seen by comparing A-scan signals as shown in Figure 3.16 in which the crack echo distortion is negligible when the proposed method is used.

Experimental signal

In order to evaluate the performance of the proposed method using experimental data, time of flight is estimated and compared with a theoretical value, for different slot lengths. The experimental setup is described in Section 7.1.3 for . The theoretical time of flight is $\tau = ax + b$ where a is given by equation (2.31), and constant b is calibrated using experimental data. From Figure 2.16(a), b's value is 7.162 μs.

Figure 3.17 shows the error for estimated time of arrival using experimental signals from specimens with different crack lengths. The error has been averaged over 3 trials of available data for each crack length. As can be seen in Figure 3.17, for cracks larger than 1mm all methods perform similarly because the SNR value is relatively high. For crack lengths smaller than 0.5mm, the time of arrival can be best estimated from images denoised by the proposed method. This can be attributed to better denoising performance of the proposed method.

3.5 Summary and conclusions

In this chapter, a method has been proposed for noise removal from ultrasonic pulse-echo B-scan images. The proposed method decomposes the B-scan image using 2D SWT and removes wedge noise present in the B-scan in two steps. In the first step, the

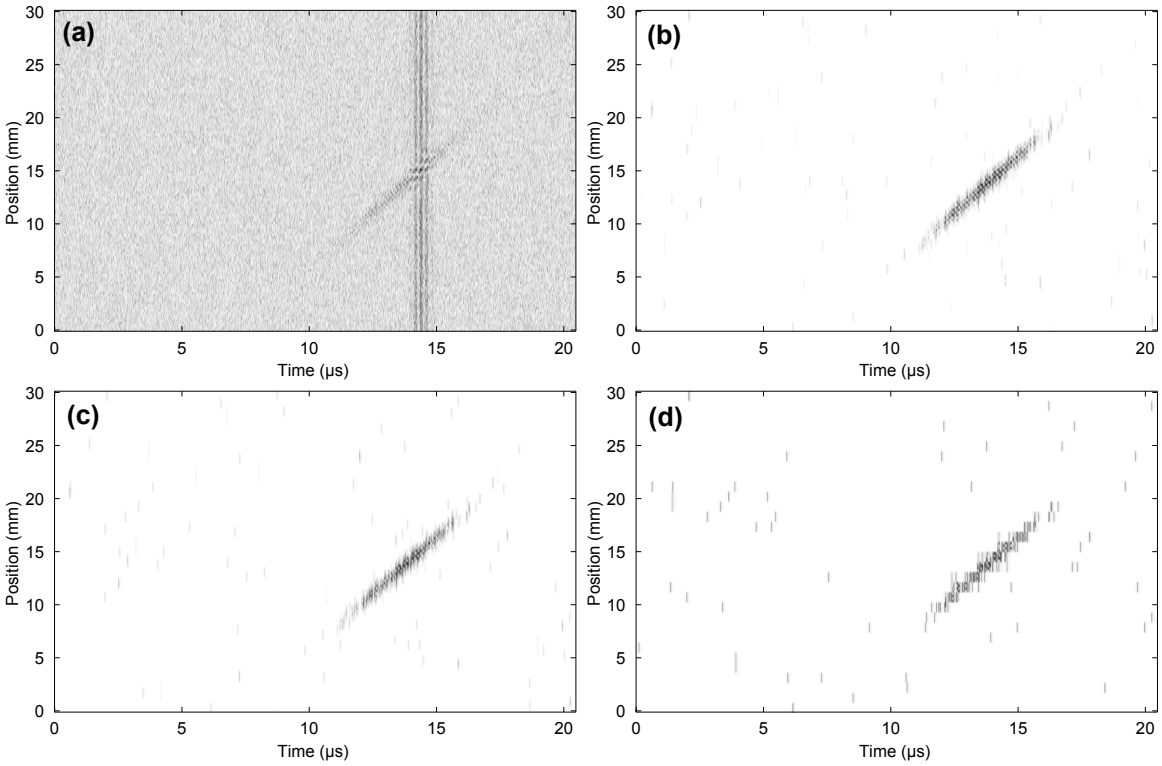

Figure 3.15: a) Simulated B-scan image with SNR of -18dB denoised by b) the proposed method, c) 'swt', and d) 'dwt'

average of all A-scans is subtracted from each A-scan in approximation and vertical detail coefficients. In the second step, the region that the crack echo is located in the B-scan image is identified by thresholding the horizontal detail coefficient. Next, the background noise has been removed by vanishing the rest of image. The only assumption on which our method of wedge noise removal is based is that changes in wedge noise are negligible as a transducer moves along a specimen. Thus, the proposed method can be applied without limitation to B-scan images unless conditions related to the transducer-specimen interface change dramatically causing large variations in ultrasonic reflection at the interface.

In removing random noise, we have used analytic wavelet thresholding. Generalizing the analytic signal concept to two dimensions has been studied in relation to ultrasonic B-scans. The performance of the proposed method has been evaluated by applying it to simulated and experimental signals; this has shown that analytic wavelet thresholding can enhance noise removal. It has also been observed that SWT performs better than discrete wavelet transform. Using the proposed method we have been able to detect echoes from a crack as small as 0.1 mm.

Once the raw ultrasonic signal is denoised, it is further processed for extracting

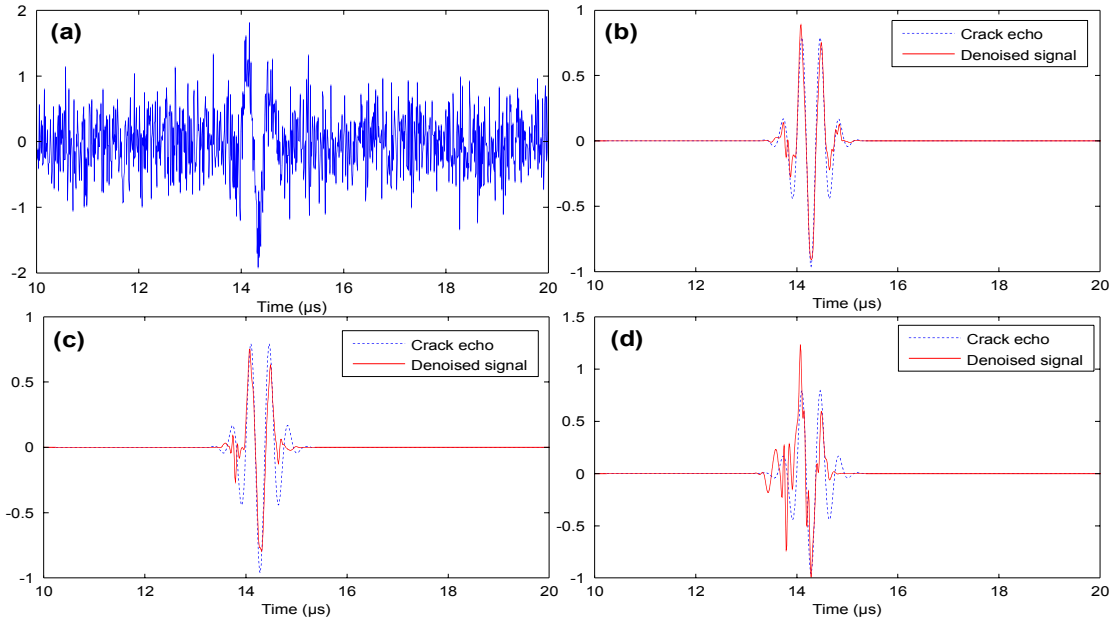

Figure 3.16: a) Simulated A-scan at $x = 15$ mm with SNR of -18dB denoised by b) the proposed method, c) 'swt', and d) 'dwt'

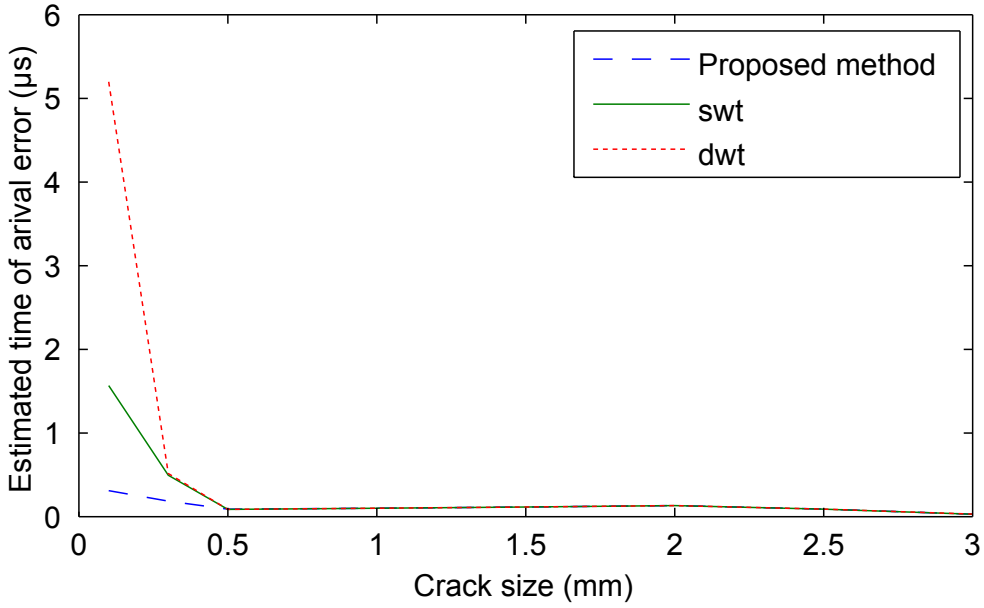

Figure 3.17: Errors of the estimated time of arrival using experimental signal denoised by proposed method, 'swt', and 'dwt'.

fault related features. Most importantly, proper criteria need to be developed for detecting echoes. In addition, features such as the time of flight of the detected echoes need to be estimated for sizing faults. In the following chapter, we propose a model-based technique to increase the probability of detection of ultrasonic echoes and to improve the accuracy of the time of flight estimation.

Chapter 4

Time of Flight Estimation Using Envelope and Quasi Maximum Likelihood Method

Time of flight (TOF) is widely used to detect, locate and size faults in ultrasonic non-destructive evaluation. Therefore, the estimation of TOF plays an important role in ultrasonic signal processing. The TOF estimation is carried out in different applications including non-destructive testing and evaluation [57, 111–113], medical imaging [114], and ultrasonic object detection [115]. In ultrasonic NDT&E, techniques based on TOF, such as time of flight diffraction [14] and relative arrival time technique [53, 54], are commonly used because they provide excellent probability of detection and accurate measurement of defects [55, 56, 115, 116]. The probability of detection depends upon whether or not the echoes associated with defects are detected. The accuracy of defect measurements is determined by the error in the TOF estimation.

The time-of-flight estimation is conventionally performed by gating and peak detection [117]. In this method a threshold is set for the echo signal and the TOF is estimated by locating the peaks greater than this threshold [118]. However, when the signal-to-noise ratio (SNR) is low, i.e. the noise level is close or higher than the signal amplitude, this criterion may not be effective. Other conventional methods such as overlap and phase slope methods suffer from the same problem [119]. While they can effectively estimate TOF for a clean and undistorted signal, they give poor TOF estimation when the signal is noisy or distorted [119].

The cross-correlation method can achieve a high signal-to-noise ratio (SNR) enhancement [120]. In fact, according to the maximum likelihood criterion, in the presence of white Gaussian noise (WGN), the cross-correlation estimator provides

the optimal solution if the signal is not distorted [121]. However, the frequency dependent scattering, dispersion and attenuation may distort the received signal [57,58], and the TOF estimates based on the cross-correlation may become significantly biased [121]. In addition, the cross-correlation method requires a reference signal which may not be available.

Model-based methods can overcome the shortcomings of the cross-correlation method. They do not need a reference signal. In addition, they can achieve high resolution TOF estimates, while the resolution of TOF estimates obtained by cross-correlation methods is limited by the sampling interval [57]. Nevertheless, these methods can run into difficulty as well. When there are multiple echoes in the signal, a large number of parameters need to be estimated by solving a non-linear optimization problem. In such cases, it is often desired to reduce the dimension of the problem through a transformation, while capturing the main features of the original signal [122, 123]. In general, one can expect more robust parameter estimation with reduced dimensions provided that the model is not misspecified [124].

By considering only the envelope of the ultrasonic signals, the number of parameters can be reduced [115, 121] and the probability of detection improves [125]. Lu *et al.* [115] used the least square method to estimate parameters of the denoised envelope of the ultrasonic signal. But it should be mentioned that the least square method is optimal only when the signal noise is WGN. The transformation applied for extracting the envelope from the original signal will change the existing noise to a non-WGN. Angrisani and Moriello [121] estimated the TOF by calculating the slope of the rising edge of the envelope. Clearly, this estimator does not utilize all information contained in the envelope.

We propose using quasi maximum likelihood (QML) method for estimating parameters of the envelope of ultrasonic echoes. The proposed estimator uses all data points in the signal for parameter estimation. In addition, instead of being limited to WGN, a more realistic probability distribution is used for the envelope. Furthermore, unlike the aforementioned works which only studied the TOF estimation using A-scan signals, we investigate the TOF estimation using B-scan signals.

Although significant research has been undertaken in recent decades to improve the TOF estimation, most of these works are based on A-scan signals and few have investigated the TOF estimation using B-scan images. Intuitively, by using a B-scan signal the TOF can be estimated more accurately because it contains more information than does an A-scan signal. To evaluate the improvement which can be achieved by using the B-scan, we derive the theoretical bounds on the variance of the

A-scan and B-scan TOF estimators.

The remainder of this chapter is organized as follows. Section 4.1 analytically evaluates the improvement in the accuracy of TOF estimation in terms of signal parameters when the B-scan is used. Section 4.2 formulates the quasi maximum likelihood estimation problem. Subsequently, in Section 4.3, the proposed method is applied to an A-scan signal. Section 4.4 presents the results of the TOF estimation using B-scan signals. Finally, Section 4.5 summarizes results and presents conclusions. Major contribution of this chapter has been published in [126] and a paper is in preparation [127] [1].

4.1 Theoretical lower bounds on the variances of A-scan and B-scan TOF estimators

The goal of this section is to compare the TOF estimation using A-scan and B-scan signals and to establish a theoretical relation between the accuracy of the TOF values estimated from A-scan and B-scan signals. This relation is obtained using the Cramer Rao bound (CRB). The CRB provides a lower bound on the variance of any unbiased estimator. An unbiased estimator has an expected value equal to the true parameter value. According to CRB, the variance of any unbiased estimator is at least as high as the inverse of the corresponding Fisher information matrix [128],

$$Var(\hat{\theta}_i) \geq [\mathcal{I}^{-1}(\boldsymbol{\theta})]_{ii} \tag{4.1}$$

where $\boldsymbol{\theta}$, $\hat{\theta}_i$ and $\mathcal{I}$ denote the parameter vector, the estimator of the i'th parameter and Fisher information matrix (FIM), respectively.

The Fisher information matrix describes the amount of information that data provide about unknown parameters. FIM is defined as the variance of the gradient of the log-likelihood function with respect to $\boldsymbol{\theta}$,

$$\mathcal{I}_{ij}(\boldsymbol{\theta}) = \mathcal{E}[(\frac{\partial}{\partial\theta_i}\log f(X;\boldsymbol{\theta}))(\frac{\partial}{\partial\theta_j}\log f(X;\boldsymbol{\theta}))] \tag{4.2}$$

where $\mathcal{E}$ denotes the expectation operator and $f(X;\theta)$ is the probability density

[1] Part of this chapter has been published in "Mohammad R. Hoseini, Xiaodong Wang, Ming J. Zuo, Estimating ultrasonic time of flight using envelope and quasi maximum likelihood method for damage detection and assessment, Measurement 45(8):2072-2080, 2012.". In addition, the following paper has been submitted: "Mohammad R. Hoseini, Xiaodong Wang, Ming J. Zuo, Using Ultrasonic Pulse-Echo B-scan Signals for Time of Flight Estimation, Submitted to Measurement."

function of the random variable X. If a signal, $s(t;\boldsymbol{\theta})$, is contaminated with white Gaussian noise (WGN), i.e. $x(t;\boldsymbol{\theta}) = s(t;\boldsymbol{\theta}) + w(t)$ where w is WGN and x, the noisy signal, is a realization of random variable X, then FIM can be simplified to [128]

$$\mathcal{I}_{ij}(\boldsymbol{\theta}) = \frac{1}{\sigma^2}\mathcal{H}^T\mathcal{H} \tag{4.3}$$

where σ^2 is the variance of noise and

$$\mathcal{H} = [\frac{\partial s(t;\boldsymbol{\theta})}{\partial \theta_i}] \tag{4.4}$$

is the gradient matrix of the signal $s(t;\boldsymbol{\theta})$ with respect to $\boldsymbol{\theta}$. In the following sections, we compare the lower bounds on the variance of the TOF values estimated from an A-scan and a B-scan.

4.1.1 Cramer-Rao bound on the TOF estimated from an A-scan

Let us recall the Gaussian echo model (GEM) for an A-scan given by equation (2.24). In discrete form, GEM can be represented by

$$\begin{aligned} s_n(\boldsymbol{\theta}) &= \beta e^{-\alpha_t(t_n-\tau)^2} cos(2\pi f_c(t_n-\tau)+\phi) \\ \boldsymbol{\theta} &= \begin{bmatrix} \tau & \phi & f_c & \alpha_t & \beta \end{bmatrix} \end{aligned} \tag{4.5}$$

where $t_n = nT, n = 1, 2, \ldots, N$ and T is the sampling interval. Demirli and Saniie [57] obtained FIM using equation (4.3) and then calculated the lower bounds for an ultrasonic A-scan as

$$\mathcal{I} = \zeta \begin{bmatrix} \gamma & -2\pi f_c & 0 & 0 & 0 \\ -2\pi f_c & 1 & 0 & 0 & 0 \\ 0 & 0 & \frac{\pi^2}{\alpha_t} & 0 & 0 \\ 0 & 0 & 0 & \frac{3}{16\alpha_t^2} & \frac{-1}{4\alpha_t\beta} \\ 0 & 0 & 0 & \frac{-1}{4\alpha_t\beta} & \frac{1}{\beta^2} \end{bmatrix} \tag{4.6}$$

$$\mathcal{I}^{-1} = \zeta^{-1} \begin{bmatrix} \frac{1}{\alpha_t} & \frac{2\pi f_c}{\alpha_t} & 0 & 0 & 0 \\ \frac{2\pi f_c}{\alpha_t} & \frac{\gamma}{\alpha_t} & 0 & 0 & 0 \\ 0 & 0 & \frac{\alpha_t}{\pi^2} & 0 & 0 \\ 0 & 0 & 0 & 8\alpha_t^2 & 2\alpha_t\beta \\ 0 & 0 & 0 & 2\alpha_t\beta & 1.5\beta^2 \end{bmatrix} \tag{4.7}$$

where $\gamma = \alpha_t + (2\pi f_c)^2$, $\zeta = \frac{E_s}{\sigma^2}$, $E_s = \sum_{n=1}^{N} s_n^2 = \frac{\beta^2}{2}\sqrt{\frac{\pi}{2\alpha_t}} f_{s,t}$ is the signal energy, and $f_{s,t}$ is the temporal sampling frequency.

4.1.2 Cramer-Rao bound on the TOF estimated from a B-scan

As mentioned in Section 2.4, the B-scan signal can be expressed as

$$\begin{aligned} s(x,t;\boldsymbol{\theta}) &= \beta(x) e^{-\alpha_t (t-\tau(x))^2} cos(2\pi f_c (t-\tau(x)) + \phi) \\ \tau &= ax + b. \end{aligned} \tag{4.8}$$

In Chapter 2, it is assumed that the amplitude, $\beta(x)$, can be modeled as a Gaussian function. However, in general, the function $\beta(x)$ may not be known. In this section, the lower bounds are derived for the case that the function $\beta(x)$ is not known. Then, we derive the lower bounds for the special case that $\beta(x)$ is a Gaussian function.

Unknown amplitude

If $\beta(x)$ is not known, the discrete B-scan signal can be expressed as

$$\begin{aligned} s_{mn}(\boldsymbol{\theta}) &= \beta_m e^{-\alpha_t (t-\tau_m)^2} cos(2\pi f_c (t_n - \tau_m) + \phi) \\ \tau_m &= a x_m + b \\ \boldsymbol{\theta} &= \begin{bmatrix} a & b & \phi & f_c & \alpha_t & \beta_1 & \beta_2 & \dots & \beta_M \end{bmatrix} \end{aligned} \tag{4.9}$$

where $x_m = m\Delta x, m = 1, 2, \dots, M$, Δx is the scanning step size and M is the number of A-scans in the B-scan image. As can be seen in equation (4.9), the parameter vector $\boldsymbol{\theta}$ has $5 + M$ variables. To simplify the analytical derivations, we define function $\bar{s}_{mn}$ as

$$\bar{s}_{mn}(\boldsymbol{\theta}) = \beta_m e^{-\alpha_t (t-\tau_m)^2} sin(2\pi f_c (t_n - \tau_m) + \phi). \tag{4.10}$$

Taking the partial derivatives of $s_{mn}(\boldsymbol{\theta})$ with respect to $\boldsymbol{\theta}$ gives,

$$\frac{\partial s_{mn}}{\partial a} = x_m(2\alpha_t(t_n - \tau_m)s_{mn} + 2\pi f_c \bar{s}_{mn}) \tag{4.11}$$

$$\frac{\partial s_{mn}}{\partial b} = 2\alpha_t(t_n - \tau_m)s_{mn} + 2\pi f_c \bar{s}_{mn} \tag{4.12}$$

$$\frac{\partial s_{mn}}{\partial \phi} = -\bar{s}_{mn} \tag{4.13}$$

$$\frac{\partial s_{mn}}{\partial f_c} = -2\pi(t_n - \tau_m)\bar{s}_{mn} \tag{4.14}$$

$$\frac{\partial s_{mn}}{\partial \alpha_t} = -(t_n - \tau_m)^2 s_{mn} \tag{4.15}$$

$$\frac{\partial s_{mn}}{\partial \beta_l} = \frac{s_{mn}}{\beta_l}\delta_{lm} \tag{4.16}$$

where δ_{lm} denotes Kronecker delta defined as

$$\delta_{lm} = \begin{cases} 0, & \text{if } l \neq m \\ 1, & \text{if } l = m \end{cases}. \tag{4.17}$$

The Fisher information is equal to

$$\mathcal{I}_{ij}(\boldsymbol{\theta}) = \frac{1}{\sigma^2}\mathcal{H}^T\mathcal{H} = \frac{1}{\sigma^2}\sum_{m=1}^{M}\sum_{n=1}^{N}\frac{\partial s_{mn}}{\partial \theta_i}\frac{\partial s_{mn}}{\partial \theta_j}. \tag{4.18}$$

Assuming that the sampling frequency is high enough, FIM given in equation (4.18) can be approximated by the following integral

$$\mathcal{I}_{ij}(\boldsymbol{\theta}) = \frac{f_{s,t}f_{s,x}}{\sigma^2}\int_{-\infty}^{\infty}\int_{-\infty}^{\infty}\frac{\partial s(x,t)}{\partial \theta_i}\frac{\partial s(x,t)}{\partial \theta_j}dxdt. \tag{4.19}$$

In the following, a few identities, which will be used in calculating the above integral, are given. From the Fourier transform table, we have

$$\frac{1}{\sqrt{2\pi}}\int_{-\infty}^{\infty} e^{-\alpha t^2} cos\omega t dt = \frac{1}{\sqrt{2\alpha}}e^{-\frac{\omega^2}{4\alpha}} \tag{4.20}$$

$$\frac{1}{\sqrt{2\pi}}\int_{-\infty}^{\infty} t^2 e^{-\alpha t^2} cos\omega t \; dt = \frac{e^{-\frac{\omega^2}{4\alpha}}}{(2\alpha)^{\frac{3}{2}}}\left(1 - \frac{\omega^2}{2\alpha}\right) \tag{4.21}$$

$$\frac{1}{\sqrt{2\pi}}\int_{-\infty}^{\infty} t^4 e^{-\alpha t^2} cos\omega t \; dt = \frac{e^{-\frac{\omega^2}{4\alpha}}}{(2\alpha)^{\frac{5}{2}}}\left(3 - \frac{3\omega^2}{\alpha} + \frac{\omega^4}{4\alpha^2}\right) \tag{4.22}$$

We also define $\zeta = E_s/\sigma^2$ where E_s is the signal energy, ζ is a parameter related to the signal-to-noise ratio: $SNR = 10\log(\frac{\zeta}{MN})$. The signal energy is equal to

$$\begin{aligned}
E_s &= \sum_m \sum_n s_{mn}^2 \\
&= \sum_m \sum_n \beta_m^2 \; e^{-2\alpha_t (t_n - \tau_m)^2} \cos^2\left(2\pi f_c \left(t_n - \tau_m\right) + \phi\right) \\
&= f_{s,t} f_{s,x} \int_{-\infty}^{\infty}\int_{-\infty}^{\infty} \beta^2(x) \; e^{-2\alpha_t (t - \tau(x))^2} \cos^2\left(2\pi f_c (t - \tau(x)) + \phi\right) dxdt \\
&= f_{s,t} f_{s,x} \int_{-\infty}^{\infty}\int_{-\infty}^{\infty} \beta^2(x) \; e^{-2\alpha_t (t - \tau(x))^2} \frac{1 + \cos\left(4\pi f_c (t - \tau(x)) + 2\phi\right)}{2} dxdt \\
&= \frac{1}{2}\sqrt{\frac{\pi}{2\alpha_t}}\left(1 + \cos(2\phi) e^{-\frac{(2\pi f_c)^2}{2\alpha_t}}\right) f_{s,t} f_{s,x} A^2
\end{aligned} \tag{4.23}$$

where $A^2 = \int_{-\infty}^{\infty} \beta^2(x) dx$. Ultrasonic transducers often act as passband filters [129]. Therefore, as mentioned in Section 2.4, the ultrasonic echo is often modeled as a low frequency envelope modulating a high frequency carrier. This bandpass condition requires that the radian center frequency be greater than the frequency bandwidth. For the bandpass condition[1] [57,115], i.e. $e^{-\frac{(2\pi f_c)^2}{2\alpha_t}} \ll 1$, equation (4.23) simplifies to

$$E_s = \frac{1}{2}\sqrt{\frac{\pi}{2\alpha_t}} f_{s,t} f_{s,x} A^2. \tag{4.24}$$

Each element of the Fisher information matrix can be calculated by taking the integral given in equation (4.18) using identities (4.20)-(4.22), such that

$$\begin{aligned}
\mathcal{I}_{11} &= \frac{1}{\sigma^2}\sum_m \sum_n \frac{\partial s_{mn}}{\partial a}\frac{\partial s_{mn}}{\partial a} \\
&= \frac{1}{\sigma^2}\sum_m \sum_n x_m^2 (2\alpha_t (t_n - \tau_m) s_{mn} + 2\pi f_c \bar{s}_{mn})^2 = (\alpha_t + (2\pi f_c)^2) C^2 \zeta
\end{aligned} \tag{4.25}$$

$$\begin{aligned}
\mathcal{I}_{12} &= \frac{1}{\sigma^2}\sum_m \sum_n \frac{\partial s_{mn}}{\partial a}\frac{\partial s_{mn}}{\partial b} \\
&= \frac{1}{\sigma^2}\sum_m \sum_n x_m (2\alpha_t (t_n - \tau_m) s_{mn} + 2\pi f_c \bar{s}_{mn})^2 = (\alpha_t + (2\pi f_c)^2) B \zeta
\end{aligned} \tag{4.26}$$

[1]This condition applies to our experimental data presented in Chapter 7. For these experimental signals: $e^{-\frac{(2\pi f_c)^2}{2\alpha_t}} \approx 0.002$.

$$\begin{aligned}\mathcal{I}_{13} &= \frac{1}{\sigma^2}\sum_m\sum_n \frac{\partial s_{mn}}{\partial a}\frac{\partial s_{mn}}{\partial \phi} \\ &= \frac{1}{\sigma^2}\sum_m\sum_n -\bar{s}_{mn}x_m(2\alpha_t(t_n-\tau_m)s_{mn}+2\pi f_c\bar{s}_{mn}) = -2\pi f_c B\zeta\end{aligned} \tag{4.27}$$

$$\begin{aligned}\mathcal{I}_{14} &= \frac{1}{\sigma^2}\sum_m\sum_n \frac{\partial s_{mn}}{\partial a}\frac{\partial s_{mn}}{\partial f_c} \\ &= \frac{1}{\sigma^2}\sum_m\sum_n -2\pi(t_n-\tau_m)\bar{s}_{mn}x_m(2\alpha_t(t_n-\tau_m)s_{mn}+2\pi f_c\bar{s}_{mn}) = 0\end{aligned} \tag{4.28}$$

$$\begin{aligned}\mathcal{I}_{15} &= \frac{1}{\sigma^2}\sum_m\sum_n \frac{\partial s_{mn}}{\partial a}\frac{\partial s_{mn}}{\partial \alpha_t} \\ &= \frac{1}{\sigma^2}\sum_m\sum_n -(t_n-\tau_m)^2 s_{mn}x_m(2\alpha_t(t_n-\tau_m)s_{mn}+2\pi f_c\bar{s}_{mn}) = 0\end{aligned} \tag{4.29}$$

$$\begin{aligned}\mathcal{I}_{1(5+m)} &= \frac{1}{\sigma^2}\sum_m\sum_n \frac{\partial s_{mn}}{\partial a}\frac{\partial s_{mn}}{\partial \beta_m} \\ &= \frac{1}{\sigma^2}\sum_m\sum_n \frac{s_{mn}}{\beta_m}x_m(2\alpha_t(t_n-\tau_m)s_{mn}+2\pi f_c\bar{s}_{mn}) = 0\end{aligned} \tag{4.30}$$

$$\begin{aligned}\mathcal{I}_{22} &= \frac{1}{\sigma^2}\sum_m\sum_n \frac{\partial s_{mn}}{\partial b}\frac{\partial s_{mn}}{\partial b} \\ &= \frac{1}{\sigma^2}\sum_m\sum_n (2\alpha_t(t_n-\tau_m)s_{mn}+2\pi f_c\bar{s}_{mn})^2 = (\alpha_t+(2\pi f_c)^2)\zeta\end{aligned} \tag{4.31}$$

$$\begin{aligned}\mathcal{I}_{23} &= \frac{1}{\sigma^2}\sum_m\sum_n \frac{\partial s_{mn}}{\partial b}\frac{\partial s_{mn}}{\partial \phi} \\ &= \frac{1}{\sigma^2}\sum_m\sum_n -\bar{s}_{mn}(2\alpha_t(t_n-\tau_m)s_{mn}+2\pi f_c\bar{s}_{mn}) = -2\pi f_c\zeta\end{aligned} \tag{4.32}$$

$$\begin{aligned}\mathcal{I}_{24} &= \frac{1}{\sigma^2}\sum_m\sum_n \frac{\partial s_{mn}}{\partial b}\frac{\partial s_{mn}}{\partial f_c} \\ &= \frac{1}{\sigma^2}\sum_m\sum_n -2\pi(t_n-\tau_m)\bar{s}_{mn}(2\alpha_t(t_n-\tau_m)s_{mn}+2\pi f_c\bar{s}_{mn}) = 0\end{aligned} \tag{4.33}$$

$$\begin{aligned}\mathcal{I}_{25} &= \frac{1}{\sigma^2}\sum_m\sum_n \frac{\partial s_{mn}}{\partial b}\frac{\partial s_{mn}}{\partial \alpha_t} \\ &= \frac{1}{\sigma^2}\sum_m\sum_n -(t_n-\tau_m)^2 s_{mn}(2\alpha_t(t_n-\tau_m)s_{mn}+2\pi f_c\bar{s}_{mn}) = 0\end{aligned} \tag{4.34}$$

$$\begin{aligned}\mathcal{I}_{2(5+m)} &= \frac{1}{\sigma^2}\sum_m\sum_n \frac{\partial s_{mn}}{\partial b}\frac{\partial s_{mn}}{\partial \beta_m} \\ &= \frac{1}{\sigma^2}\sum_m\sum_n \frac{s_{mn}}{\beta_m}(2\alpha_t(t_n-\tau_m)s_{mn}+2\pi f_c \bar{s}_{mn}) = 0\end{aligned} \tag{4.35}$$

$$\mathcal{I}_{33} = \frac{1}{\sigma^2}\sum_m\sum_n \frac{\partial s_{mn}}{\partial \phi}\frac{\partial s_{mn}}{\partial \phi} = \frac{1}{\sigma^2}\sum_m\sum_n \bar{s}_{mn}^2 = \zeta \tag{4.36}$$

$$\mathcal{I}_{34} = \frac{1}{\sigma^2}\sum_m\sum_n \frac{\partial s_{mn}}{\partial \phi}\frac{\partial s_{mn}}{\partial f_c} = \frac{1}{\sigma^2}\sum_m\sum_n 2\pi(t_n-\tau_m)\bar{s}_{mn}^2 = 0 \tag{4.37}$$

$$\mathcal{I}_{35} = \frac{1}{\sigma^2}\sum_m\sum_n \frac{\partial s_{mn}}{\partial \phi}\frac{\partial s_{mn}}{\partial \alpha_t} = \frac{1}{\sigma^2}\sum_m\sum_n (t_n-\tau_m)^2 s_{mn}\bar{s}_{mn} = 0 \tag{4.38}$$

$$\mathcal{I}_{3(5+m)} = \frac{1}{\sigma^2}\sum_l\sum_n \frac{\partial s_{ln}}{\partial \phi}\frac{\partial s_{ln}}{\partial \beta_m} = \frac{1}{\sigma^2}\sum_n \bar{s}_{mn}\frac{s_{mn}}{\beta_m} = 0 \tag{4.39}$$

$$\mathcal{I}_{44} = \frac{1}{\sigma^2}\sum_m\sum_n \frac{\partial s_{mn}}{\partial f_c}\frac{\partial s_{mn}}{\partial f_c} = \frac{1}{\sigma^2}\sum_m\sum_n 4\pi^2(t_n-\tau_m)^2\bar{s}_{mn}^2 = \frac{\pi^2}{\alpha_t}\zeta \tag{4.40}$$

$$\mathcal{I}_{45} = \frac{1}{\sigma^2}\sum_m\sum_n \frac{\partial s_{mn}}{\partial f_c}\frac{\partial s_{mn}}{\partial \alpha_t} = \frac{1}{\sigma^2}\sum_m\sum_n 2\pi(t_n-\tau_m)^3 s_{mn}\bar{s}_{mn} = 0 \tag{4.41}$$

$$\mathcal{I}_{4(5+m)} = \frac{1}{\sigma^2}\sum_l\sum_n \frac{\partial s_{ln}}{\partial f_c}\frac{\partial s_{ln}}{\partial \beta_m} = \frac{1}{\sigma^2}\sum_n -2\pi(t_n-\tau_m)\bar{s}_{mn}\frac{s_{mn}}{\beta_m} = 0 \tag{4.42}$$

$$\mathcal{I}_{55} = \frac{1}{\sigma^2}\sum_m\sum_n \frac{\partial s_{mn}}{\partial \alpha_t}\frac{\partial s_{mn}}{\partial \alpha_t} = \frac{1}{\sigma^2}\sum_m\sum_n (t_n-\tau_m)^4 s_{mn}^2 = \frac{3\zeta}{(4\alpha_t)^2} \tag{4.43}$$

$$\mathcal{I}_{5(5+m)} = \frac{1}{\sigma^2}\sum_l\sum_n \frac{\partial s_{ln}}{\partial \alpha_t}\frac{\partial s_{ln}}{\partial \beta_m} = \frac{1}{\sigma^2}\sum_n -(t_n-\tau_m)^2\frac{s_{mn}^2}{\beta_m} = \frac{-\beta_m\zeta}{4\alpha_t A^2 f_{s,x}} \tag{4.44}$$

$$\mathcal{I}_{(5+m)(5+m)} = \frac{1}{\sigma^2}\sum_l\sum_n \frac{\partial s_{ln}}{\partial \beta_m}\frac{\partial s_{ln}}{\partial \beta_m} = \frac{1}{\sigma^2}\sum_n \frac{s_{mn}^2}{\beta_m^2} = \frac{\zeta}{A^2 f_{s,x}} \tag{4.45}$$

where $B = \frac{1}{A^2}\int_{-\infty}^{\infty} x\beta^2(x)dx$ and $C^2 = \frac{1}{A^2}\int_{-\infty}^{\infty} x^2\beta^2(x)dx$.

Using all calculated elements, the Fisher information becomes

$$\mathcal{I} = \zeta\begin{bmatrix} \mathcal{I}_1 & 0 & 0 \\ 0 & \frac{\pi^2}{\alpha_t} & 0 \\ 0 & 0 & \mathcal{I}_2 \end{bmatrix} \tag{4.46}$$

where $\mathcal{I}_1$ and $\mathcal{I}_2$ are:

$$\mathcal{I}_1 = \begin{bmatrix} \gamma C^2 & \gamma B & -2\pi f_c B \\ \gamma B & \gamma & -2\pi f_c \\ -2\pi f_c B & -2\pi f_c & 1 \end{bmatrix}$$

$$\mathcal{I}_2 = \begin{bmatrix} \frac{3}{16\alpha_t^2} & \frac{-\beta_1}{4\alpha_t A^2 f_{s,x}} & \frac{-\beta_2}{4\alpha_t A^2 f_{s,x}} & \cdots & \frac{-\beta_M}{4\alpha_t A^2 f_{s,x}} \\ \frac{-\beta_1}{4\alpha_t A^2 f_{s,x}} & \frac{1}{A^2 f_{s,x}} & 0 & \cdots & 0 \\ \frac{-\beta_2}{4\alpha_t A^2 f_{s,x}} & 0 & \frac{1}{A^2 f_{s,x}} & \cdots & 0 \\ \vdots & \vdots & \vdots & \ddots & \vdots \\ \frac{-\beta_M}{4\alpha_t A^2 f_{s,x}} & 0 & 0 & \cdots & \frac{1}{A^2 f_{s,x}} \end{bmatrix}.$$

Taking the inverse of this matrix, we obtain

$$\mathcal{I}^{-1} = \zeta^{-1} \begin{bmatrix} \mathcal{I}_1^{-1} & 0 & 0 \\ 0 & \frac{\alpha_t}{\pi^2} & 0 \\ 0 & 0 & \mathcal{I}_2^{-1} \end{bmatrix} \tag{4.47}$$

where $\mathcal{I}_1^{-1}$ and $\mathcal{I}_2^{-1}$ are:

$$\mathcal{I}_1^{-1} = \begin{bmatrix} \frac{1}{\gamma(C^2-B^2)} & \frac{-B}{\gamma(C^2-B^2)} & 0 \\ \frac{-B}{\gamma(C^2-B^2)} & \frac{\gamma C^2 - (2\pi f_c)^2 B^2}{\alpha_t \gamma (C^2-B^2)} & \frac{2\pi f_c}{\alpha_t} \\ 0 & \frac{2\pi f_c}{\alpha_t} & \frac{\gamma}{\alpha_t} \end{bmatrix}$$

$$\mathcal{I}_2^{-1} = \begin{bmatrix} 8\alpha_t^2 & 2\alpha_t\beta_1 & 2\alpha_t\beta_2 & \cdots & 2\alpha_t\beta_M \\ 2\alpha_t\beta_1 & f_{s,x}A^2 + \frac{\beta_1^2}{2} & \frac{\beta_1\beta_2}{2} & \cdots & \frac{\beta_1\beta_M}{2} \\ 2\alpha_t\beta_2 & \frac{\beta_1\beta_2}{2} & f_{s,x}A^2 + \frac{\beta_2^2}{2} & \cdots & \frac{\beta_2\beta_M}{2} \\ \vdots & \vdots & \vdots & \ddots & \vdots \\ 2\alpha_t\beta_M & \frac{\beta_1\beta_M}{2} & \frac{\beta_2\beta_M}{2} & \cdots & f_{s,x}A^2 + \frac{\beta_M^2}{2} \end{bmatrix}.$$

The lower bounds on the variance of the TOF estimator is not explicitly expressed in equation 4.47, but $\tau = ax + b$ and the lower bounds on the variances of parameters a and b are expressed explicitly. For any dependent variable such as the TOF, the lower bounds can be obtained as

$$Var(\hat{\tau}) \geq \left[\frac{\partial \tau}{\partial \boldsymbol{\theta}}\right]^T \mathcal{I}^{-1} \left[\frac{\partial \tau}{\partial \boldsymbol{\theta}}\right]. \tag{4.48}$$

At position x_m, $\tau_m = ax_m + b$. Thus,

$$Var(\hat{\tau}_m) \geq \zeta^{-1} \left\{ \frac{(x_m - B)^2}{\gamma(C^2 - B^2)} + \frac{1}{\alpha_t} \right\} \tag{4.49}$$

Equation (4.49) gives the lower bound for any unknown function $\beta(x)$. To compare to the case that $\beta(x)$ is known to be Gaussian, we substitute B and C values for a Gaussian function in equation (4.49). By this substitution, equation (4.49) becomes

$$Var(\hat{\tau}_m) \geq \zeta^{-1} \left\{ \frac{4\alpha_x(x_m - x_0)^2}{\gamma} + \frac{1}{\alpha_t} \right\} \tag{4.50}$$

Gaussian amplitude

Let us assume that the amplitude can be modeled as a Gaussian function. Hence, the B-scan signal can be written as

$$\begin{aligned} s(x,t;\boldsymbol{\theta}) &= \beta e^{-\alpha_x(x-x_0)^2} e^{-\alpha_t(t-\tau(x))^2} cos(2\pi f_c(t-\tau(x)) + \phi) \\ \tau(x) &= ax + b \\ \boldsymbol{\theta} &= \begin{bmatrix} a & b & \phi & f_c & x_0 & \alpha_t & \alpha_x & \beta \end{bmatrix}. \end{aligned} \tag{4.51}$$

By discretizing, we obtain

$$\begin{aligned} s_{mn}(\boldsymbol{\theta}) &= \beta e^{-\alpha_x(x_m-x_0)^2} e^{-\alpha_t(t-\tau_m)^2} cos(2\pi f_c(t_n-\tau_m) + \phi) \\ \tau_m &= ax_m + b \\ \boldsymbol{\theta} &= \begin{bmatrix} a & b & \phi & f_c & x_0 & \alpha_t & \alpha_x & \beta \end{bmatrix}. \end{aligned} \tag{4.52}$$

Taking the partial derivatives of $s_{mn}(\boldsymbol{\theta})$ with respect to $\boldsymbol{\theta}$ gives,

$$\frac{\partial s_{mn}}{\partial a} = x_m(2\alpha_t(t_n - \tau_m)s_{mn} + 2\pi f_c \bar{s}_{mn}) \tag{4.53}$$

$$\frac{\partial s_{mn}}{\partial b} = 2\alpha_t(t_n - \tau_m)s_{mn} + 2\pi f_c \bar{s}_{mn} \tag{4.54}$$

$$\frac{\partial s_{mn}}{\partial \phi} = -\bar{s}_{mn} \tag{4.55}$$

$$\frac{\partial s_{mn}}{\partial f_c} = -2\pi(t_n - \tau_m)\bar{s}_{mn} \tag{4.56}$$

$$\frac{\partial s_{mn}}{\partial x_0} = 2\alpha_x(t_n - \tau_m)s_{mn} \tag{4.57}$$

$$\frac{\partial s_{mn}}{\partial \alpha_t} = -(t_n - \tau_m)^2 s_{mn} \tag{4.58}$$

$$\frac{\partial s_{mn}}{\partial \alpha_x} = -(x_m - x_0)^2 s_{mn} \tag{4.59}$$

$$\frac{\partial s_{mn}}{\partial \beta} = \frac{s_{mn}}{\beta} \tag{4.60}$$

By substituting these partial derivatives in equation (4.18), the Fisher information is obtained

$$\mathcal{I} = \zeta \begin{bmatrix} \mathcal{I}_1 & 0 & 0 & 0 \\ 0 & \frac{\pi^2}{\alpha_t} & 0 & 0 \\ 0 & 0 & \alpha_x & 0 \\ 0 & 0 & 0 & \mathcal{I}_2 \end{bmatrix} \tag{4.61}$$

where $\mathcal{I}_1$ and $\mathcal{I}_2$ are:

$$\mathcal{I}_1 = \begin{bmatrix} \gamma(\frac{1}{4\alpha_x} + x_0^2) & \gamma x_0 & -2\pi f_c x_0 \\ \gamma x_0 & \gamma & -2\pi f_c \\ -2\pi f_c x_0 & -2\pi f_c & 1 \end{bmatrix}$$

$$\mathcal{I}_2 = \begin{bmatrix} \frac{3}{16\alpha_x^2} & \frac{1}{16\alpha_x\alpha_t} & \frac{-1}{4\alpha_t\beta} \\ \frac{1}{16\alpha_x\alpha_t} & \frac{3}{16\alpha_t^2} & \frac{-1}{4\alpha_x\beta} \\ \frac{-1}{4\alpha_t\beta} & \frac{-1}{4\alpha_x\beta} & \frac{1}{\beta^2} \end{bmatrix}.$$

Taking the inverse of this matrix, we obtain

$$\mathcal{I}^{-1} = \zeta^{-1} \begin{bmatrix} \mathcal{I}_1^{-1} & 0 & 0 & 0 \\ 0 & \frac{\alpha_t}{\pi^2} & 0 & 0 \\ 0 & 0 & \frac{1}{\alpha_x} & 0 \\ 0 & 0 & 0 & \mathcal{I}_2^{-1} \end{bmatrix} \tag{4.62}$$

where $\mathcal{I}_1^{-1}$ and $\mathcal{I}_2^{-1}$ are:

$$\mathcal{I}_1^{-1} = \begin{bmatrix} \frac{4\alpha_x}{\gamma} & \frac{-4\alpha_x x_0}{\gamma} & 0 \\ \frac{-4\alpha_x x_0}{\gamma} & \frac{1}{\alpha_t} + \frac{4\alpha_x x_0^2}{\gamma} & \frac{2\pi f_c}{\alpha_t} \\ 0 & \frac{2\pi f_c}{\alpha_t} & \frac{\gamma}{\alpha_t} \end{bmatrix}$$

$$\mathcal{I}_2^{-1} = \begin{bmatrix} 8\alpha_t^2 & 0 & 2\alpha_t\beta \\ 0 & 8\alpha_x^2 & 2\alpha_x\beta \\ 2\alpha_t\beta & 2\alpha_x\beta & 2\beta^2 \end{bmatrix}.$$

Finally, the CRB on the TOF estimator is equal to

$$Var(\hat{\tau}_m) \geq \zeta^{-1} \left\{ \frac{4\alpha_x (x_m - x_0)^2}{\gamma} + \frac{1}{\alpha_t} \right\}. \tag{4.63}$$

It can be seen that equation (4.63) is identical to equation (4.50). Therefore, it can be concluded that knowing that $\beta(x)$ is a Gaussian function does not improve the Cramer Rao bound on TOF. Nonetheless, the computational cost of the model with unknown $\beta(x)$ is much higher than the model with Gaussian $\beta(x)$. Therefore, to overcome this computational burden, we assume the Gaussian function for parameter estimation in Section 4.4.

4.1.3 Comparison

As calculated in Section 4.1.1, for an A-scan recorded at position x_m, the CRB on the TOF estimator is equal to $\text{CRB}_{\text{A-scan}} = \zeta_m^{-1} \frac{1}{\alpha_t}$. As shown in Section 4.1.2, for a B-scan signal, the CRB on the TOF estimator has been obtained to be $\text{CRB}_{\text{B-scan}} = \zeta^{-1} \left\{ \frac{4\alpha_x (x_m - x_0)^2}{\gamma} + \frac{1}{\alpha_t} \right\}$. Hence,

$$\begin{aligned} \frac{\text{CRB}_{\text{B-scan}}}{\text{CRB}_{\text{A-scan}}} &= \frac{\zeta_m}{\zeta} \left\{ \frac{4\alpha_x \alpha_t (x_m - x_0)^2}{\gamma} + 1 \right\} \\ &= \frac{E_{s_m}}{E_s} \left\{ \frac{4\alpha_x \alpha_t (x_m - x_0)^2}{\gamma} + 1 \right\} \\ &= \frac{e^{-\alpha_x (x_m - x_0)^2}}{f_{s,x} \sqrt{\frac{\pi}{2\alpha_x}}} \left\{ \frac{4\alpha_x \alpha_t (x_m - x_0)^2}{\gamma} + 1 \right\} \\ &\leq \frac{1}{f_{s,x}} \sqrt{\frac{2\alpha_x}{\pi}} \end{aligned} \tag{4.64}$$

Therefore, if a B-scan signal is used for estimating TOF instead of an A-scan signal, the CRB improves at least by a factor of $\frac{1}{f_{s,x}} \sqrt{\frac{2\alpha_x}{\pi}}$ (This is equal to the reciprocal of the ratio of the energy of the B-scan signal to the energy of the A-scan signal whose energy is maximum among all A-scans within the B-scan; i.e. the A-scan which is recorded at $x_m = x_0$.). For example, for the experimental data presented in Section 7.1, the B-scan CRB for TOF is at least 25 times smaller than the A-scan CRB. Therefore, much more accurate estimation can be obtained by using B-scan signals.

4.2 Estimating parameters of the echo envelope

Let us consider a single-echo ultrasonic signal corrupted by WGN,

$$x_i(\boldsymbol{\theta}) = s_i(\boldsymbol{\theta}) + w_i \tag{4.65}$$

where w_i is WGN, x_i is the noisy signal and s_i is either an ultrasonic A-scan signal given by equation (4.5) or an ultrasonic B-scan signal given by equation (4.52). The envelope of this signal can be written as,

$$a_i(\boldsymbol{\theta}) = \lambda_i(\boldsymbol{\theta}) + v_i \tag{4.66}$$

in which v_i is noise, a_i is the envelope of x_i, and λ_i is the envelope of s_i. Since the phase information is lost when extracting the envelope, equation (4.66) has two parameters, i.e. center frequency and phase, fewer than equation (4.65). Hence, we have achieved dimension reduction. In addition to reduced dimension, the Gaussian envelope model (GENVM) is a more general model than the GEM, because GENVM can be used for any signal with Gaussian envelope. For example, when the dispersion effect is significant the GEM may not be effective [69]. In this case, models such as Gaussian chirplet echo model can be used [111]. Since the Gaussian chirplet model has Gaussian envelope, the GENVM will be sufficient to model the dispersed signal.

It is worth noting that by estimating the parameters of GENVM, both TOF and amplitude which are used for crack sizing are obtained. But in the following discussion, the focus will be on the accuracy of the estimated TOF values because of its key role in ultrasonic non-destructive testing.

Nevertheless, there is a major difficulty in parameter estimation from the envelope signal. Unlike w_i, v_i is neither white nor Gaussian distributed. In fact, the joint probability distribution of v_i is not known in general. Therefore, traditional estimation methods such as maximum likelihood estimation (MLE) cannot be used when applying to GENVM. We will use the quasi maximum likelihood estimation (QMLE) to estimate unknown parameters of a_i. Unlike maximum likelihood method, QMLE does not need the exact distribution function for parameter estimation. This method uses a function related to the log-likelihood for parameter estimation. In the following section, we formulate the QMLE for estimating parameters from the envelope of the signal.

4.2.1 Quasi maximum likelihood estimation

Maximum likelihood estimation is a standard approach used in estimation and inference in statistics. However, its application is limited to the cases where the joint probability distribution function is well defined. Quasi maximum likelihood method can, however, draw statistical inference and estimate parameters for cases that the exact joint probability distribution is not available [130]. This method estimates parameters of a statistical model by maximizing the quasi likelihood (QL) function, which is often a simplified form of the actual likelihood function. As long as this quasi likelihood function is not overly simplified, the quasi maximum likelihood estimator remains consistent [131].

A common assumption used in forming the quasi likelihood function is to treat certain data as being independent, even though they are dependent. This then enables us to substitute conditional probabilities by marginal probabilities [131]. Fortunately, the marginal probability distribution of a_i is known to be Rician distribution,

$$f(a_i) = \frac{a_i}{\sigma^2} e^{-\frac{a_i^2+\lambda_i^2(\boldsymbol{\theta})}{2\sigma^2}} I_0\left(\frac{\lambda_i(\boldsymbol{\theta})a_i}{\sigma^2}\right) \tag{4.67}$$

where $I_v(\bullet)$ is the modified Bessel function of the first kind of order v. Now, the QL function can be formed by multiplying the marginal distributions given in Equation (4.67),

$$QL\left(\boldsymbol{\theta}, \sigma^2\right) = \frac{1}{\sigma^{2N}} e^{-\sum_{i=1}^{N} \frac{a_i^2+\lambda_i^2}{2\sigma^2}} \prod_{i=1}^{N} a_i I_0\left(\frac{\lambda_i a_i}{\sigma^2}\right) \tag{4.68}$$

It is common to work with logarithm of the likelihood/quasi-likelihood function, because it is often more convenient to take derivatives from the quasi log-likelihood (QLL) function. Taking the logarithm of Equation (4.68) apart from a constant yields,

$$QLL\left(\boldsymbol{\theta}, \sigma^2\right) = \sum_{i=1}^{N} \ln a_i - N \ln \sigma^2 - \sum_{i=1}^{N} \frac{a_i^2 + \lambda_i^2}{2\sigma^2} + \sum_{i=1}^{N} \ln I_0\left(\frac{\lambda_i a_i}{\sigma^2}\right) \tag{4.69}$$

The estimated values of parameter vector $\boldsymbol{\theta}$ can be determined by maximizing the QLL function. By taking partial derivatives of equation (4.69) with respect to variables $\boldsymbol{\theta}$ and σ^2 and setting them equal to zero, the following set of equations are

obtained

$$\begin{cases} -\sum_{i=1}^{N} \lambda_i \frac{\partial \lambda_i}{\partial \theta_j} + \sum_{i=1}^{N} a_i \frac{\partial \lambda_i}{\partial \theta_j} g\left(\frac{\lambda_i a_i}{\sigma^2}\right) = 0 \\ -N\sigma^2 + \frac{1}{2}\sum_{i=1}^{N}(a_i^2 + \lambda_i^2) - \sum_{i=1}^{N} \lambda_i a_i g\left(\frac{\lambda_i a_i}{\sigma^2}\right) = 0 \end{cases} \tag{4.70}$$

where $g(x) = \frac{I_0'(x)}{I_0(x)} = \frac{I_1(x)}{I_0(x)}$. The remaining issue is to replace λ_i with A-scan and B-scan signals and solve the resulting equations.

4.3 A-scan signal parameter estimation

In general, the reflected signal may contain multiple echoes and the number of echoes is often unknown. Therefore, in addition to parameters of the echo, the number of echoes need to be estimated. To simplify the analysis, we first assume a single echo problem. Then, a multiple echo problem with an unknown number of echoes is solved.

4.3.1 Estimating parameters of a single echo

In this section, we derive equations for estimating parameters of a single echo signal from its envelope. By substituting the Gaussian envelope, $\lambda_i = \beta e^{-\alpha_t (t_i - \tau)^2}$, in equation (4.70) and after some simplifications, the following set of equations are obtained

$$\begin{cases} \sum_{i=1}^{N} l_i = 0 \\ \sum_{i=1}^{N} t_i l_i = 0 \\ \sum_{i=1}^{N} t_i^2 l_i = 0 \end{cases} \tag{4.71}$$

where $l_i = -\lambda_i^2 + a_i \lambda_i g\left(\frac{\lambda_i a_i}{\sigma^2}\right)$ and $\sigma^2 = \frac{1}{2N}\sum_{i=1}^{N}(a_i^2 - \lambda_i^2)$. To solve this system of non-linear equations for the parameter vector $\boldsymbol{\theta}$, an iterative method based on trust-region dogleg method is employed [132]. The reason for selecting this method is that the trust-region techniques improve the robustness even when the initial guess is far from the solution. In addition, these techniques can handle the case when the Jacobian matrix is singular, while Newton's method may get into difficulties [133].

The performance of the proposed method, which estimates parameters of the envelope signal using QMLE, is compared with two other methods. A model-based method and a cross-correlation method are selected for the comparison because of their robustness to noise. In the first method, the least square estimation (LSE)

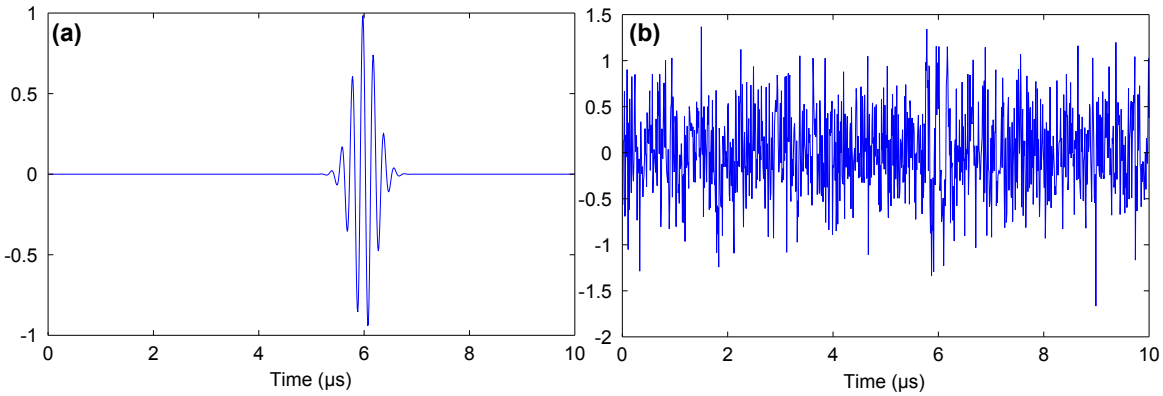

Figure 4.1: A simulated signal single-echo with (a) no noise (b) an SNR of -10dB

is used to estimate parameters of the original signal. In the second method, first the cross-correlation signal is calculated. Then, the envelope of this cross-correlation signal is calculated and its peak location is taken as TOF.

The cross-correlation method requires a reference signal. Reference signals are often obtained from a calibration or reference specimen. Therefore, they have generally a waveform similar to ultrasonic signals collected from the test specimen. We generate a reference signal following the Gaussian echo model as

$$r_i = e^{-8(t_i-6)^2} \cos\left(8\pi\left(t_i-6\right)\right),\ \ i = 1,\ 2,\ ...,\ 1000 \tag{4.72}$$

To compare the performance of these methods, they are applied to a simulated single-echo signal which is generated as follows,

$$x_i = e^{-10(t_i-6)^2} \cos\left(10\pi\left(t_i-6\right)+\pi/4\right) + w_i,\ \ i = 1,\ 2,\ ...,\ 1000 \tag{4.73}$$

The shape distortion is introduced in this simulated signal by altering the center frequency and the bandwidth factor. The relative change in these two parameters is selected to be close to that of the experimental signal presented in Section 7.2. Both reference and simulated signals are sampled at a sampling frequency of 100MHz. Figure 4.1 depicts the signal generated from equation (4.73).

Initial guess values for QMLE and LSE methods are generated based on the properties of the Gaussian echo signal such as its bandwidth as follows. First, the envelope, a_i, is smoothed using a moving average filter to avoid selecting spontaneous spikes caused by noise as the maximum points. This smoothed signal is denoted by a_i'. The initial guess values for amplitude and TOF are selected to be $\beta_0 = max(a_i')$ and $\tau_0 = \arg\max(a_i')$. The initial value for α_t is calculated as $\alpha_{t_0} = \frac{4\ln 2}{FWHM}$, where FWHM

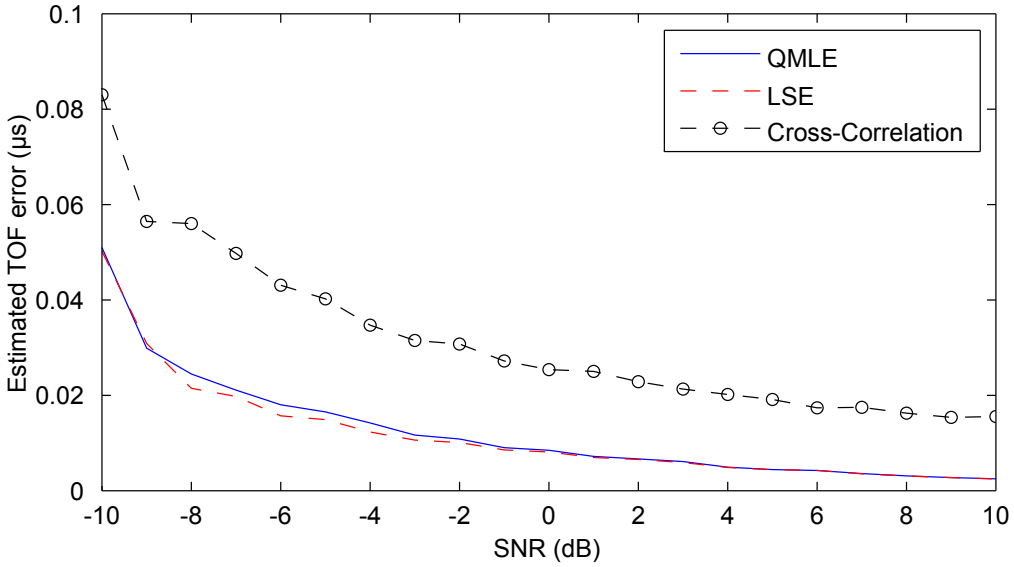

Figure 4.2: TOF estimation error for a simulated single-echo signal

denotes the full width at half maximum [134]. LSE method requires two more initial values for the frequency and the phase. The initial value for frequency is obtained by counting zero-crossings and the initial value for phase is obtained by letting the maximum point phase equal to $\pi/2$.

In the calculation of the TOF for QMLE method, the dogleg method starts from the generated initial guess values and finds the solution of equation (4.71). It stops whenever the error is smaller than some predefined value. Similarly, for LSE method, the dogleg method is used to find the solution of the non-linear least square problem. Finally, for 'cross-correlation', the TOF is computed by simply locating the peak of the envelope of the cross-correlation [135].

Monte Carlo simulation is used to evaluate the parameter estimation accuracy and reliability of each method. Signals with different noise levels ranging from -10dB to 10dB are generated. At each signal-to-noise ratio, 500 trials of the signal are generated and the echo parameters are estimated using QMLE and LSE methods.

Figure 4.2 compares the absolute error of TOF estimates averaged over 500 trials. Clearly, the cross-correlation method results in larger errors for all SNR values. The errors from QMLE and LSE methods are very close. Therefore, for the single echo case, the proposed method achieves the same accuracy as the LSE method does. This shows that estimating TOF from the envelope of a Gaussian echo can be as accurate as estimating TOF from the original signal. This indicates that no information on TOF has been lost when calculating the envelope.

4.3.2 Multiple echo problem

Let us consider a signal composed of J Gaussian echoes, i.e. $s_i = \sum_{j=1}^{J} s_{ij}$. Unlike the single-echo case, the instantaneous amplitude of a multi-echo signal depends on the phase parameter. Since the envelope does not preserve phase information, the instantaneous amplitude has to be estimated. The instantaneous amplitude is estimated by the average amplitude given by $\lambda_i = (\sum_{j=1}^{J} \lambda_{ij}^2)^{1/2}$ where $\lambda_{ij} = \beta_j e^{-\alpha_{t_j}(t_i-\tau_j)^2}$ [136]. Substituting λ_i into equation (4.70) gives,

$$\begin{cases} \sum_{i=1}^{N} l_{ij} = 0 \\ \sum_{i=1}^{N} t_i l_{ij} = 0 \\ \sum_{i=1}^{N} t_i^2 l_{ij} = 0 \end{cases} \tag{4.74}$$

where $l_{ij} = -\lambda_{ij}^2 + a_i \frac{\lambda_{ij}^2}{\lambda_i} g\left(\frac{\lambda_i a_i}{\sigma^2}\right)$ and $\sigma^2 = \frac{1}{2N} \sum_{i=1}^{N} (a_i^2 - \lambda_i^2)$.

An important parameter in the current process is the model order which is equal to the number of echoes times the number of parameters of each echo. Akaike's information criterion (AIC) [137] is widely used in the context of model order selection. AIC is a penalized log-likelihood criterion which is defined by

$$\mathrm{AIC} = -2 \ln L(\hat{\boldsymbol{\theta}}) + 2p \tag{4.75}$$

in which $L(\hat{\boldsymbol{\theta}})$ is the likelihood function for the estimated parameters $\hat{\boldsymbol{\theta}}$, and p is the model order. In the special case of WGN for which MLE simplifies to LSE, AIC accordingly simplifies to [138]

$$\mathrm{AIC} = -2 \ln \frac{RSS}{N} + 2p \tag{4.76}$$

where RSS stands for the residual sum of squares. Although a complicated model is penalized by the $2p$ term, in general AIC tends to select complicated models when N is large [139]; i.e. it overfits the signal. The consistent AIC (CAIC) proposed by Bozdogan [140] satisfies the consistency in common cases as the sample size becomes large. CAIC is defined by:

$$\mathrm{CAIC} = -2 \ln L(\hat{\boldsymbol{\theta}}) + p(\ln N + 1). \tag{4.77}$$

For the special case of WGN, CAIC simplifies to,

$$\text{CAIC} = -2\ln\frac{RSS}{N} + p(\ln N + 1) \tag{4.78}$$

In order to select the model order for LSE method, we will use equation (4.78). The proposed method uses the envelope for which the log-likelihood function is not available. Therefore, CAIC cannot be calculated for the proposed method. Because QLL function approximates log-likelihood function, likewise CAIC can be approximated by substituting QLL in the place of log-likelihood function in equation (4.77). Hence the CAIC for the proposed method can be approximated as

$$\text{CAIC} = -2QLL + p(\ln N + 1) \tag{4.79}$$

To find the number of echoes, we first set $J = 0$, estimate the parameters, and evaluate CAIC. Next, we add one echo at a time until the CAIC reaches the minimum and starts increasing. The number of echoes corresponding to the minimum CAIC will be selected. The solution of each step is used as the initial guess for the next step. For the newly added echo, the initial guess is calculated similar to the single echo case, but the signal is replaced by the residual, which is the difference between the estimated signal and the observed signal.

The performance of the proposed method is compared with those of LSE and cross-correlation methods. For the LSE method an algorithm similar to that of the proposed method is used. The initial values for the two extra parameters, i.e. frequency and phase, are determined in a similar way to the single echo case, except that the original signal is replaced by the residual signal when calculating the initial values for the parameters of the new echo.

The reference signal for the cross-correlation method is given by equation (4.72). In NDT applications, often the TOF of echoes is found from the peak of the signal envelope to account for the signal phase [141]. Therefore, after calculating the cross-correlation, its envelope is recovered using the Hilbert transform. Number of echoes is estimated by setting a threshold and counting the number of peaks in the cross-correlation envelope which are greater than the threshold. The choice of the threshold value inevitably involves a trade-off between false alarms and missed defects [142]. The threshold value is determined adaptively based on the noise level to achieve a false alarm probability of 10%. Finally, the peak location gives the TOF value.

For performance comparison, a simulated signal consisting of two echoes is gener-

Table 4.1: The results of a Monte Carlo simulation with 500 trials for estimating the number of echoes of a signal with 2 echoes corrupted by different levels of noise.

		Actual number of echoes=2					
		Estimated number of echoes					
	SNR (dB)	0	1	2	3	4	5
Cross-correlation	-10	3.2%	91.6%	5.2%	0.0%	0.0%	0.0%
	-5	0.0%	95.0%	4.4%	0.6%	0.0%	0.0%
	0	0.0%	87.2%	12.6%	0.2%	0.0%	0.0%
	5	0.0%	48.2%	49.8%	2.0%	0.0%	0.0%
	10	0.0%	0.2%	91.0%	8.6%	0.2%	0.0%
LSE	-10	58.8%	41.2%	0.0%	0.0%	0.0%	0.0%
	-5	5.2%	61.2%	33.4%	0.2%	0.0%	0.0%
	0	0.6%	14.2%	76.0%	8.6%	0.6%	0.0%
	5	0.0%	0.8%	88.6%	7.8%	2.2%	0.6%
	10	0.0%	0.0%	99.8%	0.0%	0.2%	0.0%
QMLE	-10	11.2%	79.0%	9.6%	0.2%	0.0%	0.0%
	-5	0.0%	3.8%	94.6%	1.4%	0.2%	0.0%
	0	0.0%	0.0%	97.6%	2.4%	0.0%	0.0%
	5	0.0%	0.0%	98.0%	2.0%	0.0%	0.0%
	10	0.0%	0.0%	99.6%	0.4%	0.0%	0.0%

ated as,

$$\begin{aligned} x_i &= 0.6e^{-10(t_i-5)^2}\cos\left(12\pi\left(t_i-5\right)+\pi/4\right) \\ &+e^{-10(t_i-6)^2}\cos\left(10\pi\left(t_i-6\right)+\pi/2\right)+w_i, \quad i=1,\,2,...,\,1000 \end{aligned} \tag{4.80}$$

Table 4.1 presents the percentage of trials with the estimated echo numbers from different methods. These values are obtained using a Monte Carlo simulation with 500 trials. Monte Carlo simulation has been conducted for different SNR values for each method. According to Table 4.1, the proposed method is more likely to result in the correct number of echoes, while the LSE and cross-correlation methods are more likely to either underfit or overfit the model. For example, at SNR of 0 dB, the chance of selecting the true value 2 as the number of echoes for QMLE, LSE and cross-correlation is 97.6%, 76% and 12.6%, respectively. With the decrease of the SNR value, the advantage of the proposed method over the other two methods becomes more obvious.

The simulated signal in equation (4.80) contains two echoes with TOFs of $5\mu s$ and $6\mu s$. Figure 4.3 compares the error of the estimated TOFs for the first echo and the second echo at different SNR values. Because the estimated number of echoes can be smaller or greater than two, we have calculated the error only using the trials

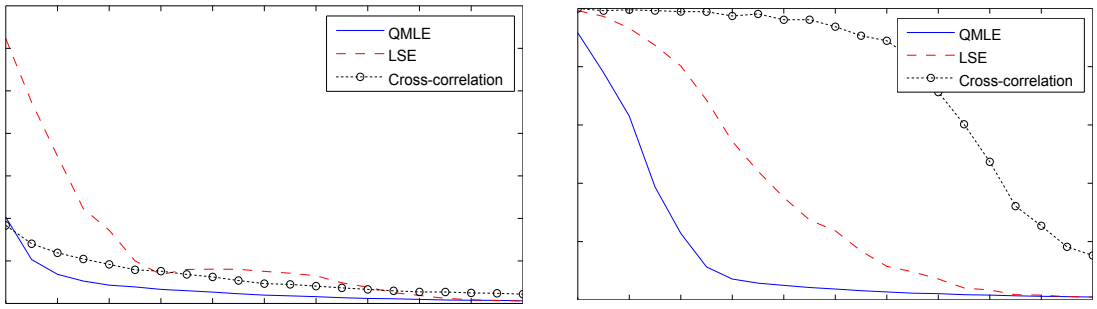

Figure 4.3: TOF estimation error for a simulated 2-echo signal, (a) first echo, and (b) second echo

that these echoes are detected. Whether an echo is detected or not is decided by comparing the estimated TOF with the exact TOF given by equation (4.80). If the estimation error is within a specified range, the echo is said to be detected. On this range, the echo has a sizable amplitude. If the estimated TOF is outside this range, the model is fitted to noise and not to the echo. Therefore, in this case, it is said that the echo is not detected. The maximum acceptable error is considered to be 0.5 s. This value corresponds to approximately 10 dB reduction in the amplitude from the peak. The maximum error, i.e. 0.5 s, has been considered for all cases that the echo is not detected. The estimation error is then averaged over all trials. Based on Figure 4.3, it is clear that the proposed method outperforms LSE method when applied to the simulated signals. In next section, the performance of these methods are compared using experimental signals.

4.3.3 Experimental results

The main concern in NDT applications is to detect defects and then to assess the severity of defects. In this section, we compare the performance of the proposed method with LSE and cross-correlation methods using the following two measures: (1) probability of detection of a crack, and (2) the error of the estimated TOF. We define the probability of detection as the fraction of trials that the error of TOF is smaller than $0.5\mu s$. The error of TOF estimator indicates the reliability of TOF estimation and henceforth the accuracy of the crack size estimation. We have calculated the error only for cases that the crack tip is detected as defined for calculating the probability of detection.

The experimental setup is described in Section 7.2. Table 4.2 presents the estimated TOF values of tip diffraction echo. For the wedge distance of 10 mm, the

Table 4.2: TOF of tip diffraction echo estimated using cross-correlation, LSE and QMLE methods for signals collected at different wedge distances

		Wedge distance (mm)					
		0	2	4	6	8	10
	Theoretical TOF (μs)	17.03	17.48	17.94	18.42	18.91	19.80
Cross-correlation	Estimated TOF (μs)	17.43	17.52	18.16	18.55	19.15	19.52
	Error (μs)	-0.30	-0.04	-0.22	-0.13	-0.24	0.28
	Relative Error (%)	1.76	0.23	1.23	0.70	1.27	1.41
LSE	Estimated TOF (μs)	16.92	17.47	17.98	18.46	18.67	0.00
	Error (μs)	0.11	0.01	-0.04	-0.04	0.24	0.00
	Relative Error (%)	0.65	0.06	0.22	0.22	1.27	0.00
QMLE	Estimated TOF (μs)	17.12	17.46	17.94	18.40	18.88	19.90
	Error (μs)	-0.09	0.02	0.00	0.02	0.03	-0.10
	Relative Error (%)	0.53	0.11	0.00	0.11	0.16	0.51

LSE method has not detected the tip diffraction echo, while the cross-correlation and QMLE methods have detected the tip diffraction echo in all cases. In order to calculate the estimation error, the estimated TOF values are compared to the theoretical values given by equation (2.20). The average estimation errors for cross-correlation, LSE and QMLE methods are 0.20 s, 0.09 s and 0.04 s, respectively. Although the proposed method again outperforms the other two methods, the difference between them is relatively small because of the high SNR.

The experimental signals are collected under lab conditions hence they contain low level of noise. In order to simulate the noise that is usually present in field measurements, we have added different levels of white Gaussian noise to the signal collected at the wedge distance of 2 mm. The SNR is calculated assuming that the original signal contains no noise.

Figure 4.4 depicts the probability of detection for all three methods. Clearly, the proposed method results in a higher probability of detection, especially for lower SNR values. Figure 4.5 is generated in the same way as Figure 4.3. As seen, the proposed method results in smaller TOF estimation error than the other two methods. This is in agreement with simulated results.

4.3.4 Discussion

It has been shown that the QMLE improves the accuracy of TOF estimation by estimating the parameters of the envelope of the echo. It should be noted that this method can be used with cross-correlation to further improve the TOF estimation. In

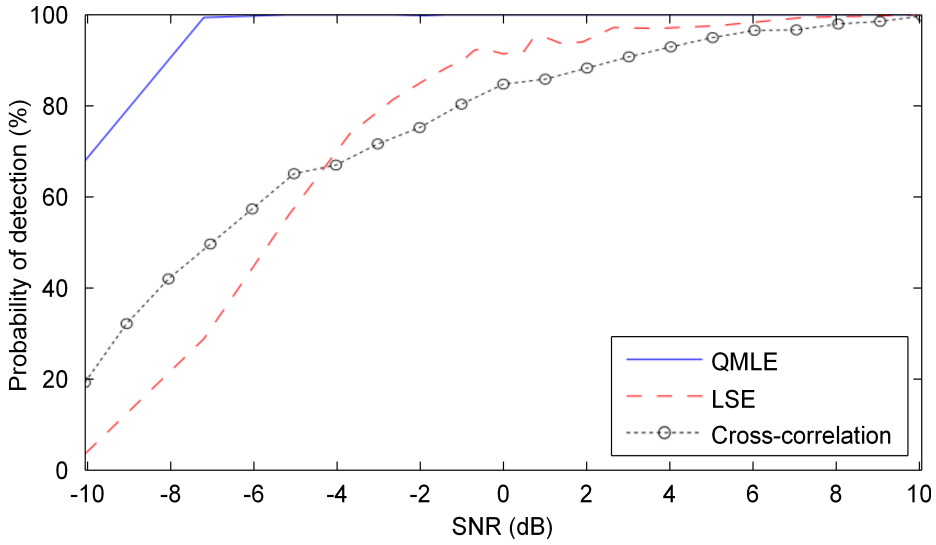

Figure 4.4: Probability of detection at different SNR values obtained using QMLE, LSE and cross-correlation methods

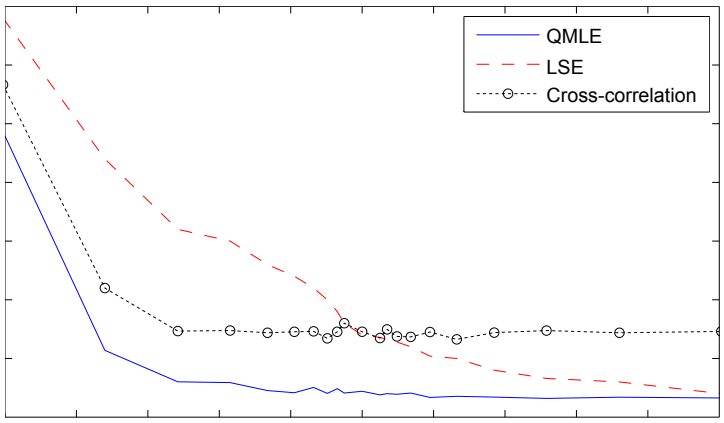

Figure 4.5: TOF estimation error for an experimental A-scan signal with added noise

particular, if both the received signal and reference signal can be estimated by GEM and the distortion of the received signal is negligible, it can be shown that the cross-correlated signal can be modeled by GEM as well. Therefore, in this case, the same equations given in this chapter for estimating parameters of the envelope of the echo can be used to estimate parameters of the envelope of the cross-correlated signal. In the following, we prove that the cross-correlation of two GEM with negligible distortion; i.e. with the same bandwidth factor and center frequency, is a Gaussian echo.

Let's assume a Gaussian echo signal,

$$s(t) = \beta e^{-\alpha_t (t-\tau)^2 + j(2\pi f_c (t-\tau) + \phi_1)}. \tag{4.81}$$

To simplify the proof, complex notation is used in equation (4.81). With no loss of generality, we assume the reference signal as

$$r(t) = e^{-\alpha_t t^2 + j(2\pi f_c t + \phi_2)}. \tag{4.82}$$

The cross-correlation of these two signals is given by

$$\begin{aligned}
(s \star r)(t) &= \int_{-\infty}^{\infty} s^*(u) r(u+t) du \\
&= \int_{-\infty}^{\infty} A e^{-\alpha_t (u-\tau)^2 - j(2\pi f_c (u-\tau) + \phi_1)} e^{-\alpha (u+t)^2 + j(2\pi f_c (u+t) + \phi_2)} du \\
&= \beta e^{j(2\pi f_c (t-\tau) + \phi_2 - \phi_1)} \int_{-\infty}^{\infty} e^{-\alpha_t (2u^2 - 2u(t+\tau) + t^2 + \tau^2)} du \\
&= \beta e^{-\frac{\alpha_t}{2}(t-\tau)^2 + j(2\pi f_c (t-\tau) + \phi_2 - \phi_1)} \int_{-\infty}^{\infty} e^{-2\alpha_t (u - \frac{t+\tau}{2})^2} du \\
&= \beta e^{-\frac{\alpha_t}{2}(t-\tau)^2 + j(2\pi f_c (t-\tau) + \phi_2 - \phi_1)} \int_{-\infty}^{\infty} e^{-2\alpha_t u^2} du \\
&= \beta \sqrt{\frac{\pi}{2\alpha_t}} e^{-\frac{\alpha_t}{2}(t-\tau)^2 + j(2\pi f_c (t-\tau) + \phi_2 - \phi_1)}
\end{aligned} \tag{4.83}$$

where $\star$ denotes the cross-correlation operator and superscript * denotes complex conjugate. According to equation (4.83), the cross-correlated signal is also a Gaussian echo signal. Furthermore, based on equation (4.7), the ratio of the CRBs of TOF for the original signal and the cross-correlated signal can be written as

$$\frac{CRB_{\text{Cross-correlated}}}{CRB_{\text{Original signal}}} = \frac{2\sqrt{2}\alpha_t}{\pi f_{s,t}^2} \frac{\sigma'^2}{\sigma^2} \tag{4.84}$$

where σ'^2 is the variance of noise in the cross-correlation signal. This ratio is often a small number because the variance of noise is often reduced considerably when the signal is cross-correlated, and $\frac{2\sqrt{2}\alpha_t}{\pi f_{s,t}^2}$ is a small number[1]. Therefore, estimating parameters from the cross-correlation signal can significantly decrease the estimation error. Nevertheless, such an improvement can be achieved only when the received echoes is negligibly distorted.

The goal of this chapter is to develop an effective model-based method for estimating the parameters of B-scan echoes. In this section, we have applied the proposed method to a simpler case, i.e. A-scan echoes. The proposed method has performed well when applied to simulated and experimental signals. In the following section, we investigate the parameter estimation of B-scan echoes.

4.4 B-scan signal parameter estimation

In this section, we derive equations for estimating parameters of a single echo B-scan signal from its envelope. Similar to an A-scan signal, we first consider a single echo signal, then a multi-echo signal. As observed for the A-scan signal, QMLE and LSE methods perform better than the cross-correlation method. Therefore, in this section, we only compare the performance of QMLE and LSE method. Similar to the A-scan signal parameter estimation, the single echo problem and the multiple echo problem are investigated.

4.4.1 Single echo

By substituting the two dimensional Gaussian envelope, $\lambda_{ij} = \beta e^{-\alpha_t(t_i-\tau_j)^2-\alpha_x(x_j-x_0)^2}$, in equation (4.70) and after some simplification, the following set of equations can be

[1]The transducer, we have used in our experiments in Chapter 7 has a frequency bandwidth of 1.5 MHz which is equivalent to $\alpha_t = 16(MHz)^2$. The minimum sampling frequency, we have used, was 50 Mhz. This gives $\frac{2\sqrt{2}\alpha_t}{\pi f_{s,t}^2} = 0.006 \ll 1$.

obtained

$$\begin{cases} \sum_{j=1}^{M} L_j = 0 \\ \sum_{j=1}^{M} x_j L_j = 0 \\ \sum_{j=1}^{M} x_j^2 L_j = 0 \\ \sum_{i=1}^{N}\sum_{j=1}^{M} t_i^2 l_{ij} = 0 \\ \sum_{i=1}^{N}\sum_{j=1}^{M} \tau_j t_i l_{ij} = 0 \\ \sum_{i=1}^{N}\sum_{j=1}^{M} x_j \tau_j t_i l_{ij} = 0 \end{cases} \tag{4.85}$$

where $L_j = \sum_{i=1}^{N} l_{ij}$, $l_{ij} = -\lambda_{ij}^2 + a_{ij}\lambda_{ij} g\left(\frac{\lambda_{ij} a_{ij}}{\sigma^2}\right)$ and $\sigma^2 = \frac{1}{2MN}\sum_{i=1}^{N}\sum_{j=1}^{M}\left(a_{ij}^2 - \lambda_{ij}^2\right)$.

For comparing the performance of LSE and QMLE methods, a simulated B-scan signal is generated according to equation (3.24). For parameters in common with A-scan signal, i.e. β, α_t, f_c and ϕ, firstly the A-scan which has the maximum amplitude among all A-scans within the B-scan signal is selected. These initial values are then calculated the same way as we have performed for the A-scan signal in Section 4.3. The A-scan with maximum amplitude is selected because it has supposedly the highest SNR. Other initial values are determined as follows. The initial guess for x_0 is determined by the location of the peak, a is given by theory, $b = \tau_0 - a x_0$ where (τ_0, x_0) is the location of the peak, and $\alpha_x = 4\ln 2/FWHM - a^2\alpha_t$ in which FWHM is the full width at half maximum at time $t = \tau_0$.

Parameters of this single echo signal is estimated by solving equation (4.85). The simulated signals are generated with SNRs of -10 dB to 10 dB. Figure 4.6 shows an example of a simulated signal with SNR of -10 dB and signals reconstructed with parameters estimated using QMLE and LSE methods. The TOF error is evaluated at $x = x_0$. Figure 4.7 depicts the TOF error averaged over 100 trials for each SNR. As shown in this figure, both methods perform similarly for SNRs greater than -2 dB, but the QMLE method clearly performs better than LSE method for SNRs smaller than -2 dB.

4.4.2 Multiple echo signal

Let's consider a signal composed of K Gaussian echoes, i.e. $s_{ij} = \sum_{k=1}^{K} s_{ijk}$. Similar to the A-scan signal, the instantaneous amplitude of the B-scan signal is estimated by the

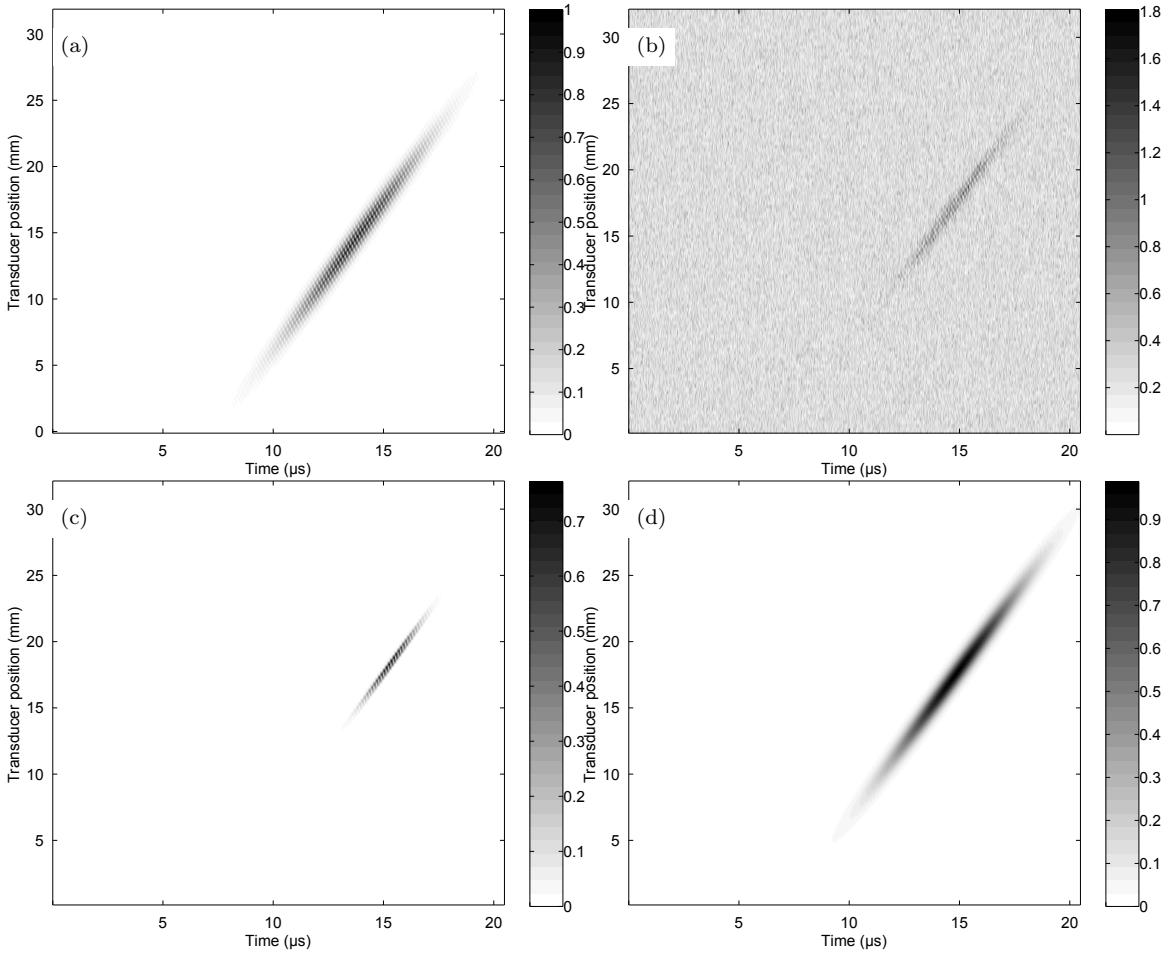

Figure 4.6: An example of a simulated B-scan signal (a) with no noise, (b) with an SNR of -10 dB, (c) signal reconstructed with parameters estimated using LSE method, and (d) the envelope of the signal reconstructed with parameters estimated using QMLE method.

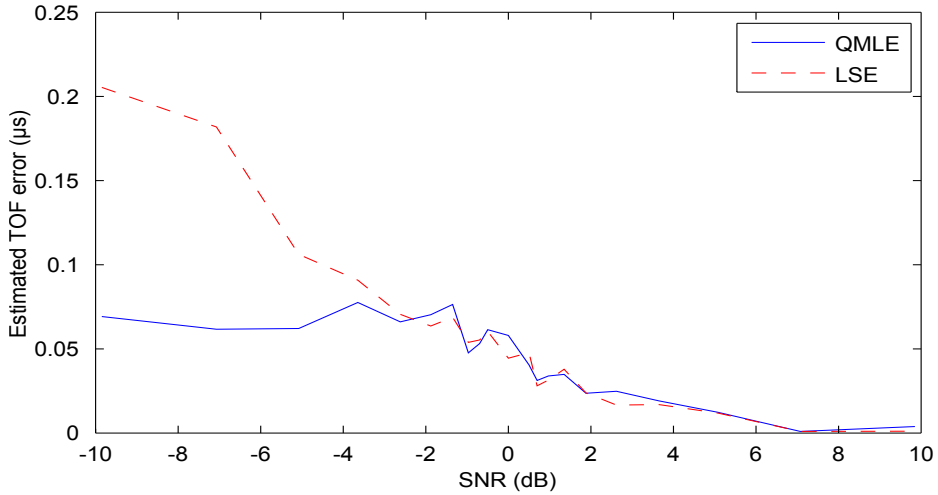

Figure 4.7: TOF estimation error for a simulated single-echo B-scan signal

average amplitude given by $\lambda_i = (\sum_{k=1}^{K} \lambda_{ijk}^2)^{1/2}$ where $\lambda_{ijk} = \beta_k e^{-\alpha_{t_k}(t_i-\tau_{jk})^2-\alpha_{x_k}(x_j-x_{0_k})^2}$. Substituting λ_{ijk} into equation (4.70) gives,

$$\begin{cases} \sum_{j=1}^{M} L_{jk} = 0 \\ \sum_{j=1}^{M} x_j L_{jk} = 0 \\ \sum_{j=1}^{M} x_j^2 L_{jk} = 0 \\ \sum_{i=1}^{N}\sum_{j=1}^{M} t_i^2 l_{ijk} = 0 \\ \sum_{i=1}^{N}\sum_{j=1}^{M} \tau_{jk} t_i l_{ijk} = 0 \\ \sum_{i=1}^{N}\sum_{j=1}^{M} x_j \tau_{jk} t_i l_{ijk} = 0 \end{cases} \tag{4.86}$$

where $L_{jk} = \sum_{i=1}^{N} l_{ijk}$, $l_{ijk} = -\lambda_{ijk}^2 + a_{ij}\frac{\lambda_{ijk}^2}{\lambda_{ij}} g\left(\frac{\lambda_{ij}a_{ij}}{\sigma^2}\right)$ and $\sigma^2 = \frac{1}{2MN}\sum_{i=1}^{N}\sum_{j=1}^{M}\left(a_{ij}^2 - \lambda_{ij}^2\right)$.

A two-echo B-scan signal has been generated as follows

$$\begin{aligned} g(x,t) = {} & e^{-0.0256(x-17.5)^2} e^{-5.67(t-\tau_1(x))^2} cos(4.5\pi(t-\tau_1(x)) + \pi/4) \\ & + 0.3e^{-0.032(x-12.5)^2} e^{-4(t-\tau_2(x))^2} cos(4.5\pi(t-\tau_2(x)) + \pi/2) \end{aligned} \tag{4.87}$$

where $\tau_1 = 0.4376x + 7.162, \tau_2 = 0.4376x + 5.913$.

In equation (4.87) one echo has an amplitude 3.3 times greater than the other. A practical example, for such a signal is a pulse-echo B-scan signal containing a corner reflection echo and a tip diffraction echo. Often the amplitude of corner reflection echo is much greater than that of tip diffraction echo. If the corner reflection is detected, then the crack is detected as well. If the tip diffraction echo is also detected, the crack size can be estimated using the time of flights of corner trap echo, τ_{CT}, and tip diffraction echo, τ_{TD}. According to equation (2.19), the error of the estimated crack size is proportional to the error of $\tau_{CT} - \tau_{TD}$.

The simulated signals are generated with SNRs of -10 dB to 10 dB. Figure 4.8 shows an example of a simulated signal with SNR of -10 dB and signals reconstructed with parameters estimated using QMLE and LSE methods. The performance of these two methods are compared using two criteria. First the probability of detection is compared. That is the probability that at least one of the echoes is detected. Another criterion is whether the size of crack can be estimated and, if it can, what would be the error. To size the crack, both corner trap and tip diffraction echoes should be

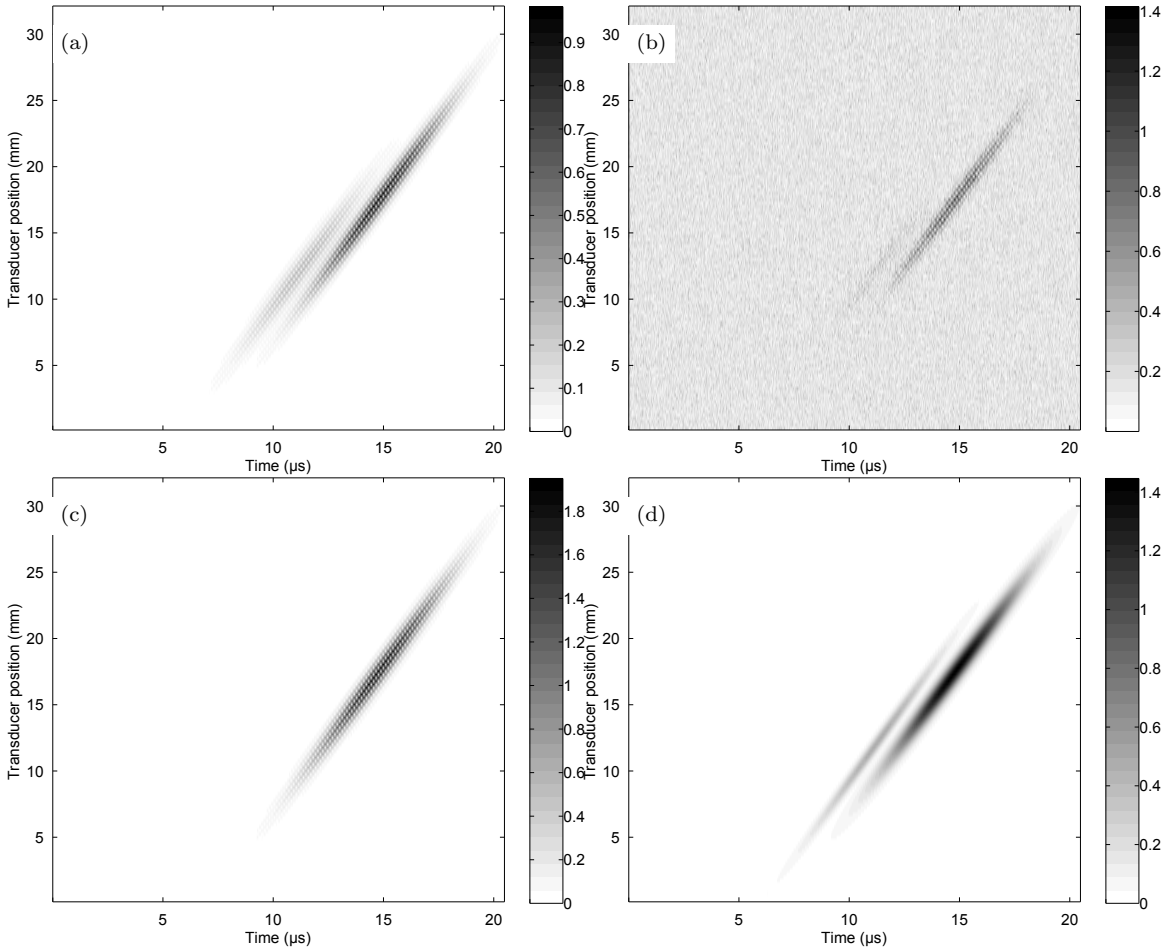

Figure 4.8: An example of a simulated B-scan signal containing 2 echoes (a) with no noise, (b) with an SNR of -10 dB, (c) signal reconstructed with parameters estimated using LSE method, and (d) the envelope of the signal reconstructed with parameters estimated using QMLE method.

detected. The error is estimated by calculating the error of $\tau_{CT} - \tau_{TD}$.

Table 4.3 presents the probability of detection and the probability that the crack size can be estimated. According to this table, the probability of detection for both methods is about 100%. This shows that both methods are likely to detect the corner reflection. However, the probability that the crack size can be estimated is higher for QMLE method at lower SNRs and is about 100% at higher SNRs for both methods. Figure 4.9 shows the error of $\tau_{CT} - \tau_{TD}$. As shown, at SNRs higher than 0 dB the LSE method performs slightly better, while the QMLE improves the crack size estimation accuracy greatly in lower SNRs. To further compare the performance of these methods, in the next section, they are applied to experimental B-scan signals.

Table 4.3: The probability of detection (POD) and the probability of sizing (POS) obtained using a Monte Carlo simulation with 50 trials for QMLE and LSE methods

		QMLE		LSE	
		POD	POS	POD	POS
SNR (dB)	-10	94%	56%	94%	24%
	-5	100%	74%	100%	62%
	0	100%	100%	100%	90%
	5	100%	100%	100%	100%
	10	100%	100%	100%	100%

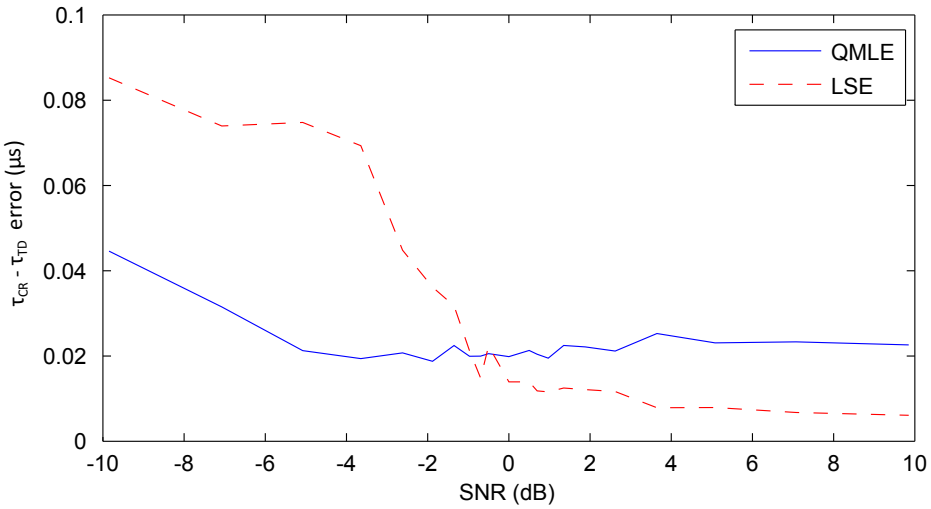

Figure 4.9: Relative TOF estimation error for an experimental B-scan signal

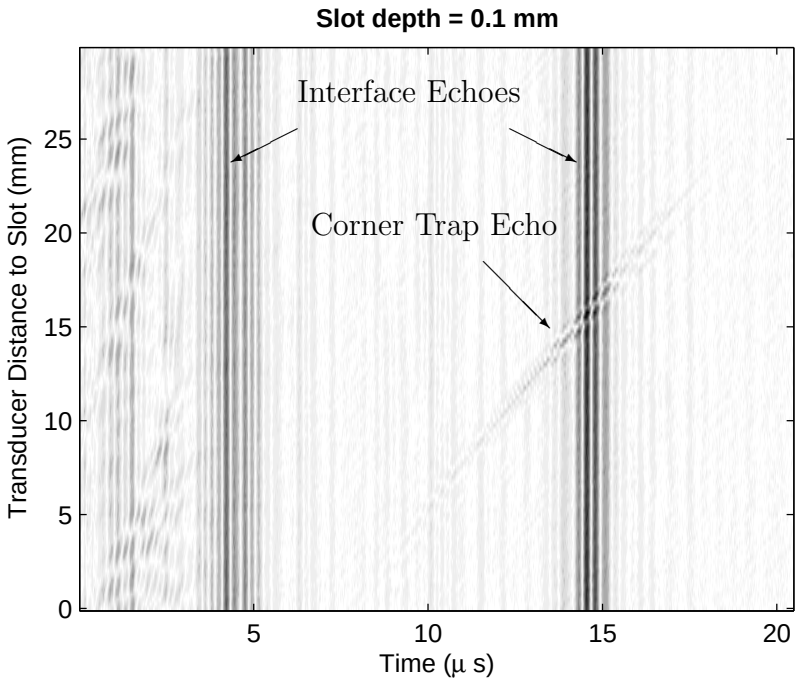

Figure 4.10: B-scan image of a specimen with 0.1 mm slot

4.4.3 Experimental signal

The proposed method has been applied to the experimental B-scans described in Section 7.1.3. Figure 4.10 depicts a B-scan image of a specimen with 0.1 mm slot. In this B-scan image, even the corner trap echo is barely observed due to interface echoes and random noise. However, using the method proposed for removing noise from the B-scan signals in Chapter 3, we can effectively remove both the interface echoes and random noise. For example, as shown in Figure 4.11, the corner trap echo can be easily observed after denoising.

After denoising the B-scan signals, the proposed parameter estimation method is applied to these signals for estimating the TOF. The slot is detected, if any of echoes is detected in the received signal. As indicated in Table 4.4 both LSE and QMLE could detect slots in all specimens. Table 4.4 also presents the error of the slot length estimation for both methods. According to this table, neither of LSE and QMLE methods could detect the tip diffraction echo for the specimen with 0.1mm slot and hence the slot length cannot be estimated for this case. However, the QMLE method is able to estimate the size of the specimen with 0.3mm, while the LSE method is not. For larger slots, both methods are able to size the slot and their estimation errors are close to each other.

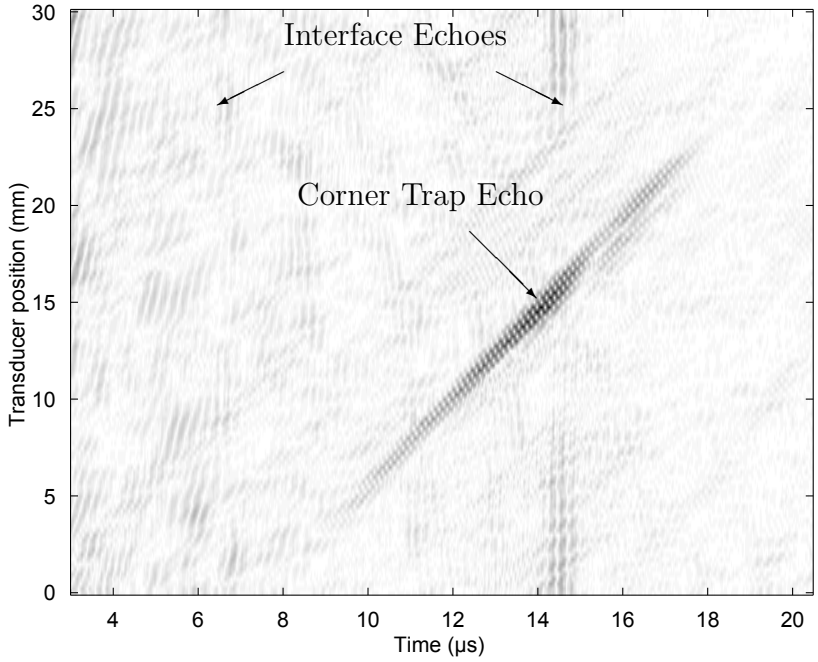

Figure 4.11: Denoised B-scan image of a specimen with 0.1 mm slot

Table 4.4: The error in estimation of the length of slots ($\delta_{est} - \delta_{act}$) for experimental signals

		QMLE		LSE	
		Detected?	$\delta_{est} - \delta_{act}$ (mm)	Detected?	$\delta_{est} - \delta_{act}$ (mm)
Slot Length (mm)	0.1	Yes	N/A	Yes	N/A
	0.3	Yes	0.43	Yes	N/A
	0.5	Yes	0.08	Yes	0.70
	1	Yes	0.58	Yes	-0.71
	1.5	Yes	-0.70	Yes	-0.54
	2	Yes	0.24	Yes	0.15
	2.5	Yes	0.11	Yes	0.15
	3	Yes	-0.11	Yes	-0.08

4.5 Summary and conclusions

In this chapter, a novel model-based method for TOF estimation is proposed. It has been shown that model-based methods have clear advantages over conventional cross-correlation methods in estimating parameters of ultrasonic echoes. However, when there are multiple echoes in the received signal a high-dimensional nonlinear optimization problem needs to be solved. This optimum solution can be difficult to achieve. To reduce the number of parameters of the model and to achieve a more robust estimation, the envelope of the signal is extracted. Envelope of an ultrasonic echo preserves the main features of the ultrasonic echo, i.e. TOF and amplitude, which are commonly used for damage assessment in the ultrasonic non-destructive evaluation. Subsequently, the parameters of the envelope of the echo are estimated using the quasi maximum likelihood method. It has been shown this proposed method improves the parameter estimation accuracy, especially at lower SNR values.

Analytically, it has been proved that using a B-scan image instead of an A-scan signal can significantly improve the accuracy of the TOF estimation. The proposed method is then applied to a set of experimental B-scan signals. Through this analysis, it has been shown that the proposed model based parameter estimation method combined with the denoising method proposed in Chapter 3 is able to detect cracks as small as 0.1 mm and size cracks as small as 0.3 mm.

Estimated TOF values are used to size and locate faults such as cracks. The existing crack sizing techniques, such as relative arrival time technique, assume that cracks are normal to the test piece surface. This assumption reduces the crack sizing accuracy. In the following chapter, a modified relative arrival time technique is proposed for estimating the length of inclined cracks.

Chapter 5

Modified Relative Arrival Time Technique for Estimating Crack Size and Orientation

In Chapters 3 and 4, we have investigated denoising and parameter estimation of B-scan signals. The next step is to identify the faults based on the estimated parameters. A critical parameter of a crack to be determined is its size. If the crack size is known, it is possible to estimate the remaining life and reliability of a part using fracture mechanics [14].

Current crack sizing techniques, such as relative arrival time technique (RATT) which has been used in Chapter 4, do not take into account the effect of crack orientation [143]. These techniques often assume that the crack is normal to the surface of the test piece. Clearly, this assumption introduces errors in estimating the length of inclined cracks. Ciorau [144] investigated the inherent error in using RATT for sizing inclined cracks by evaluating the crack sizing error for different crack orientations. However, they did not provide a method to account for this error.

Recently, Satyanarayan *et al.* [53] simulated the ultrasonic phased-array B-scan image for different crack orientations and observed that the change in crack orientation changed the position of tip diffraction echo with respect to corner reflection echo. However, they did not evaluate how to determine whether a change is caused by the crack orientation or the change in crack size. They did not estimate the crack orientation in this work.

Klima *et al.* [145] studied the relation between the crack orientation and the amplitude of the echo. They used this relation to explain why the echoes received from the surface cracks which are at different angles with respect to the transducer

have different amplitudes. However, they did not use these results to estimate the crack length. Moreover, the amplitude of the echo can be influenced by other factors such as surface roughness of the specimen [14, 146]. Thus, it does not provide a reliable crack size estimation.

In this chapter, we propose a modified relative arrival time technique for estimating the length of inclined cracks from a pulse echo B-scan image. In addition, the proposed modified RATT provides an estimate of the inclination angle of the crack. A paper is in preparation from the contents of this chapter [147] [1].

5.1 Modified relative arrival time technique

The relationship between the crack angle, the angle of incidence and the parameters of the corner trap echo and the tip diffraction echo can be established theoretically using ray tracing method for special cases under some assumptions. In the ray tracing method [148–150], ultrasonic waves are modeled as rays, each of which propagates independent of other rays. These rays may reflect, refract, diffract, attenuate, and undergo mode conversion as discussed in Section 2.1.1. The ray tracing method was successfully used for simulating ultrasonic fields [150]. The same concept has been used in crack sizing techniques such as TOFD and RATT. Similarly, we derive an equation for estimating the crack size and angle for special cases using the ray tracing method. Then, we use the derived equations for the crack depth and angle for other crack angles to assess its applicability in more general cases.

Assume an unfocused transducer which generates an axisymmetric ultrasonic beam profile with a maximum at the center of the beam. The axisymmetric assumption holds because of the symmetric shape of ultrasonic transducers. The intensity of ultrasonic beams decreases abruptly with distance from its central axis [151], and hence the maximum wave intensity is assumed to occur at the center of the beam.

Figure 5.1 depicts the schematic of a specimen with a crack with an angle of γ to which an ultrasonic angle beam with an incident angle of θ is emitted. The crack is assumed to be normal to the x-z plane and our objective is to the determine the crack orientation in the x-z plane. It should be noted that the present work is different from the work in Ref. [152] which determined the crack orientation in the x-y plane using horizontally polarized shear waves.

[1] The following paper is in preparation from the contents of this chapter: "Mohammad R. Hoseini, Xiaodong Wang, Ming J. Zuo, Modified Relative Arrival Time Technique for Sizing Inclined Cracks, In preparation."

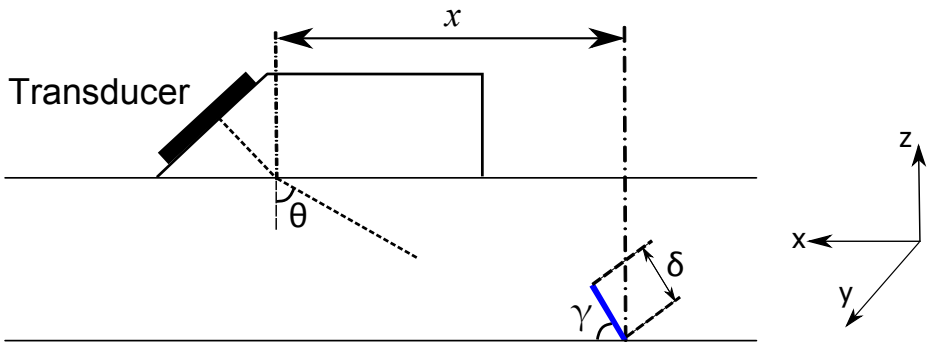

Figure 5.1: Schematic of a specimen with a crack with an angle of γ

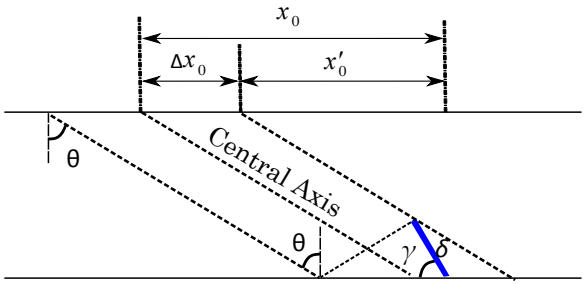

Figure 5.2: The ultrasonic beam reflected by the crack

When the ultrasonic wave is incident on the crack, a portion is reflected, which forms the corner echo, and a portion is diffracted from the crack tip, which forms the tip diffracted echo. Figure 5.2 shows the ultrasonic beam which is reflected by the crack. This beam is confined by the following two rays: the ray which is incident on the crack tip, and the ray which is reflected from the backwall and its reflection is incident on the crack tip. In general, only part of this beam is received by the transducer. However, for three special cases: $\gamma = \theta$, $\gamma = \pi/2$ and $\gamma = \pi - \theta$, it can be easily shown geometrically that this beam is completely received by the transducer (For $\gamma = \theta$ and $\gamma = \pi - \theta$, the beam is reflected exactly on the same path back toward the transducer. For $\gamma = \pi/2$, every pair of rays located evenly about the ray incident on the corner, travel the same path, but in opposite directions.).

As assumed, if the central axis is at the middle of this beam, the energy received by the transducer will be maximum. Maximum amplitude of the tip diffraction echo occurs when the beam center encounters the crack tip [27]. If the maximum amplitude of the corner trap occurs at x_0 and the maximum amplitude of tip diffracted echo occurs at x_0', we define $\Delta x_0 = x_0 - x_0'$. From Figure 5.2, the relation between Δx_0 and parameters θ, γ and δ can be obtained as,

$$\Delta x_0 = \delta \sin\gamma \tan\theta. \tag{5.1}$$

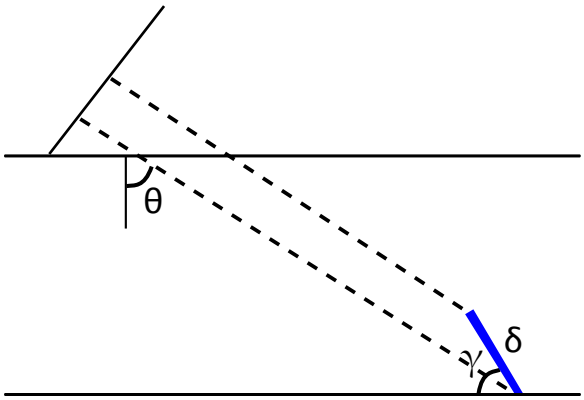

Figure 5.3: Relative arrival time technique for inclined cracks

The relative arrival time technique (RATT) utilizes the difference between the TOF of corner trap echo, τ, and tip diffraction echo, τ', to estimate the crack length. Deriving a general theoretical formula for $\Delta\tau = \tau - \tau'$ is difficult, hence we attempt to approximate $\Delta\tau$. Assume that the rays reflected from the crack, in average, travel the same distance as the ray incident exactly on the corner of the crack. It can be shown that this assumption holds if $\gamma = \theta$, $\gamma = \pi/2$ or $\gamma = \pi - \theta$, because all rays travel the same distance in these special cases (For example, see Section 2.4 for proof when $\gamma = \pi/2$). From Figure 5.3, we have,

$$\Delta\tau = \frac{2\delta}{c_s}\sin(\gamma + \theta). \tag{5.2}$$

Conventional RATT uses equation (5.2) for crack sizing assuming that $\gamma = \pi/2$. This assumption causes an error equal to

$$\epsilon = \frac{c_s \Delta\tau}{2}\left(\frac{1}{cos(\theta)} - \frac{1}{\sin(\gamma + \theta)}\right). \tag{5.3}$$

Figure 5.4 shows the relative error in sizing inclined cracks using the conventional RATT. As it can be seen, the RATT overestimates the crack size for $\gamma \leq \pi/2$ and underestimates the crack size for $\gamma \geq \pi/2$. This observation is in agreement with findings of [144].

From a B-scan signal, $\Delta\tau$ and Δx_0 can be estimated. Subsequently, unknown parameters δ and γ can be obtained by simultaneously solving equations (5.1) and (5.2). In a B-scan image, Δx_0 is determined by finding the positions of the peak of the tip echo and the peak of the corner echo. $\Delta\tau$ is calculated by selecting an A-scan within the B-scan signal and then calculating the difference between the times of

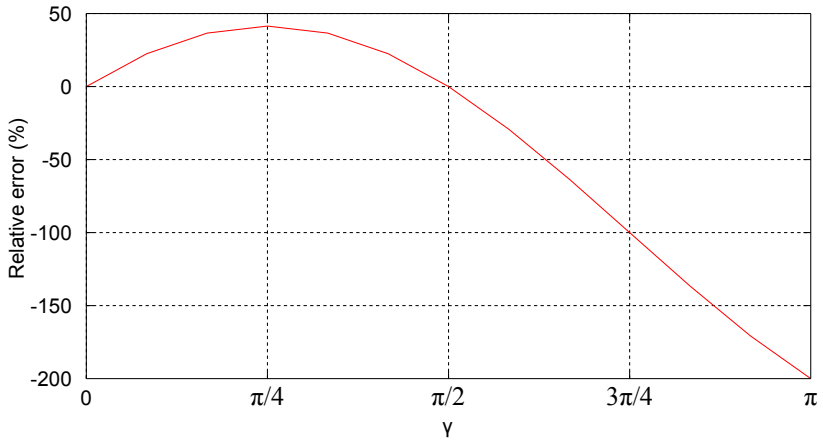

Figure 5.4: Relative error in sizing inclined cracks using the conventional RATT for $\theta = \pi/4$.

arrival of the tip echo and the corner echo. Clearly, the value of $\Delta\tau$, and hence γ and δ, depends on the selected A-scan signal.

According to equation (4.63), the error in evaluating the TOF is minimum at the position that the amplitude of the corresponding echo is maximum. Therefore, the expected error in sizing cracks is minimum, if τ is evaluated at x_0 and τ' is evaluated at x_0'. Let τ_0 be the TOF of the corner echo at x_0 and τ_0' be the TOF of the tip echo at x_0'. In Section 2.4, it has been shown that the TOF is a linear function of the transducer position. Therefore, τ_0 and τ_0' can be written as $\tau_0 = ax_0 + b$ and $\tau_0' = a'x_0' + b'$, respectively. According to equation (2.34), $a' \approx a \approx \dfrac{\Delta\tau}{\Delta x} \approx \dfrac{2\sin(\theta)}{c_s}$. Hence,

$$\Delta\tau_0 = \tau_0 - \tau_0' = a\Delta x_0 + b - b'. \tag{5.4}$$

But $b - b' = (ax + b) - (ax + b') = \tau - \tau' = \Delta\tau$. Substituting $\Delta\tau$ from equation (5.2) and Δx_0 from equation (5.1) into equation (5.4) gives

$$\Delta\tau_0 = \frac{2\delta}{c_s}\left(\sin\theta\cos\gamma + \frac{\sin\gamma}{\cos\theta}\right). \tag{5.5}$$

By solving equations (5.1) and (5.5) for γ and δ, we obtain

$$\begin{aligned} \gamma &= \cot^{-1}\left(\frac{c_s\Delta\tau_0}{2\Delta x_0\cos\theta} - \frac{2}{\sin 2\theta}\right) \\ \delta &= \frac{\Delta x_0}{\sin\gamma\tan\theta}. \end{aligned} \tag{5.6}$$

Figure 5.5 shows the relative position of the corner trap echo and the tip diffraction

echo for different crack orientations when $\theta = \pi/4$. The following observations can be made form Figure 5.5:

1. The change in the position of the tip diffraction echo is relatively small for $\gamma \leq 90^\circ$ (This can also be observed from equation (5.2). According to this equation, the maximum change in TOF occurs at 135°.).

2. It is always true that $x_0' < x_0$. This property can be used to identify the tip diffraction echo when there are multiple echoes in the B-scan.

3. For $\gamma \leq 180 - \theta$, the tip diffraction echo arrives earlier than the corner trap echo. For $\gamma \geq 180 - \theta$, the tip diffraction echo arrives later than the corner trap echo.

To ensure that the ray tracing assumptions used for deriving modified RATT do not significantly deviate from the physics of the wave propagation, a finite element simulation is conducted. The details of the finite element model and simulation parameters are provided in Chapter 6.

Figure 5.6 shows the displacement contours at different times for $\gamma = 60^\circ$. To obtain a sharp contrast image, only the specimen is displayed. From Figure 5.6, the formation of the reflected wave and the circular diffracted wave can be clearly observed. However, for $\gamma = 135^\circ$ shown in Figure 5.7, only one echo is observed. This phenomenon can be explained using Figure 5.3. For $\gamma = 135^\circ$ and $\theta = 45^\circ$, the incident wave arrives at the tip of the crack and the corner of the crack at the same time. Therefore, at $\gamma = 135^\circ$, the tip diffracted echo is merged into the corner reflected echo. As a result, the tip diffracted echo can be hardly distinguished from the corner reflection echo in the B-scan image. Figure 6.47 shows the B-scan signal from a specimen with a 135° crack. In Figure 6.47, as expected, only one echo can be observed. Therefore, the application of the modified RATT for sizing a crack with an inclination angle close to $\gamma = 180 - \theta$, e.g. $\gamma = 135^\circ$ for the incident angle of $\theta = 45^\circ$, is not practical.

We have compared the TOA of the corner reflection and the tip diffraction waves approximated from the displacement contours with the TOA of the waves observed in the simulated B-scans to ensure that each pulse in the B-scan is correctly associated with the corresponding wave type as assumed in the theoretical derivation of the modified RATT formula. The comparison shows the ray tracing assumptions are in good agreement with physics of the wave propagation as modeled using the finite element method.

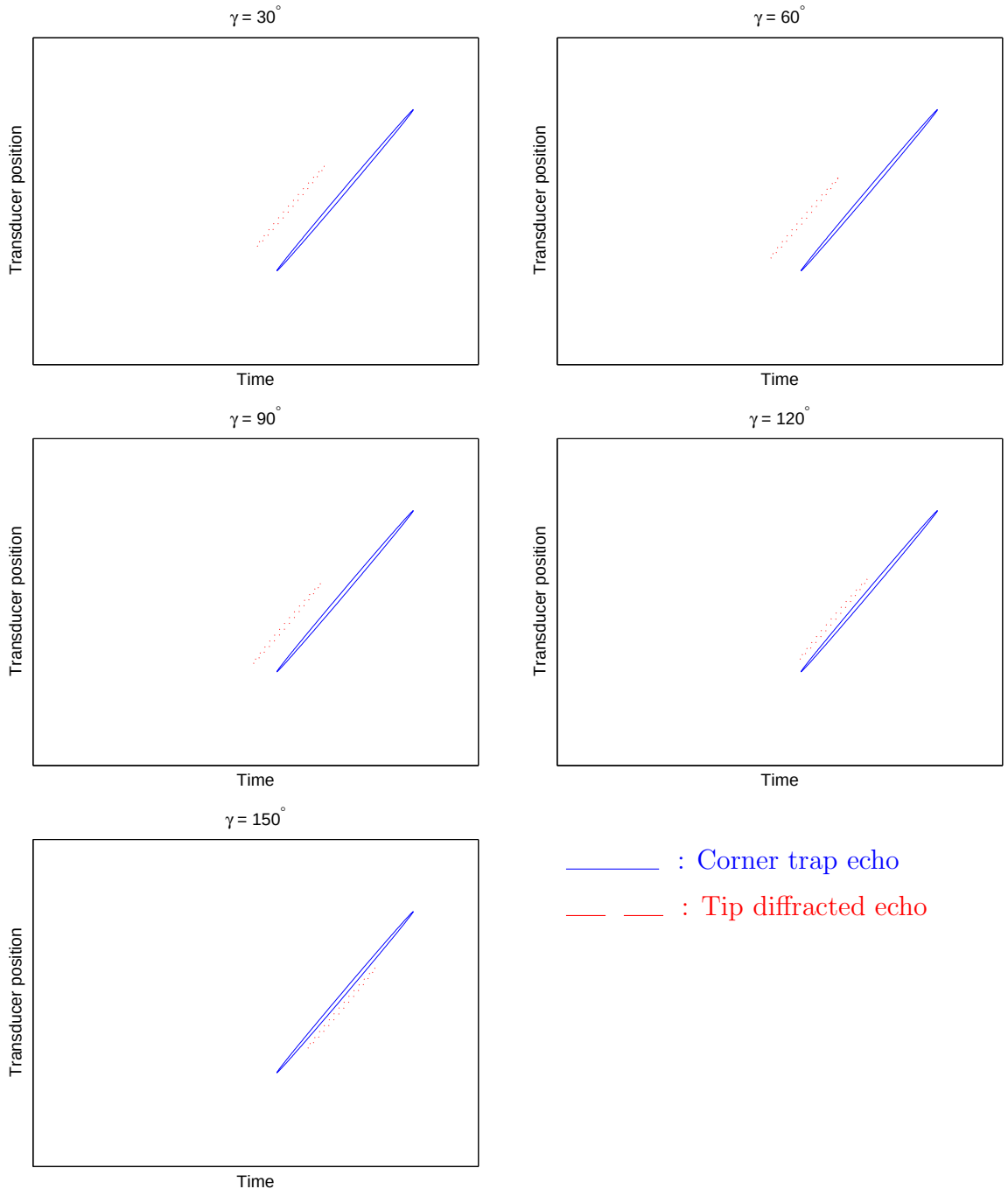

Figure 5.5: The schematic position of the corner trap echo and tip diffraction echo in the B-scan image for different crack orientations.

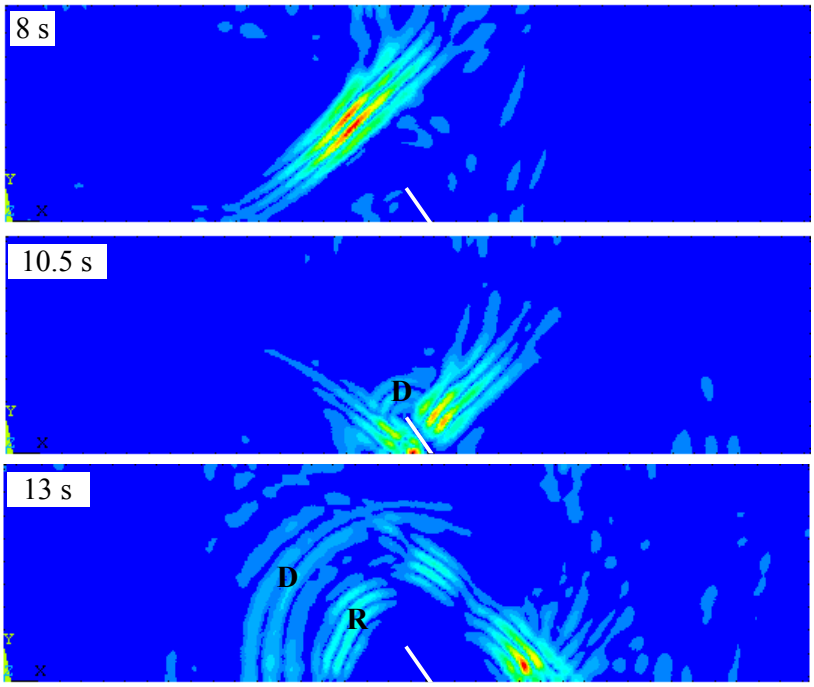

Figure 5.6: Wave propagation in the specimen with a 60° crack at different time instances, R: Reflection corner echo, D: Diffracted tip echo

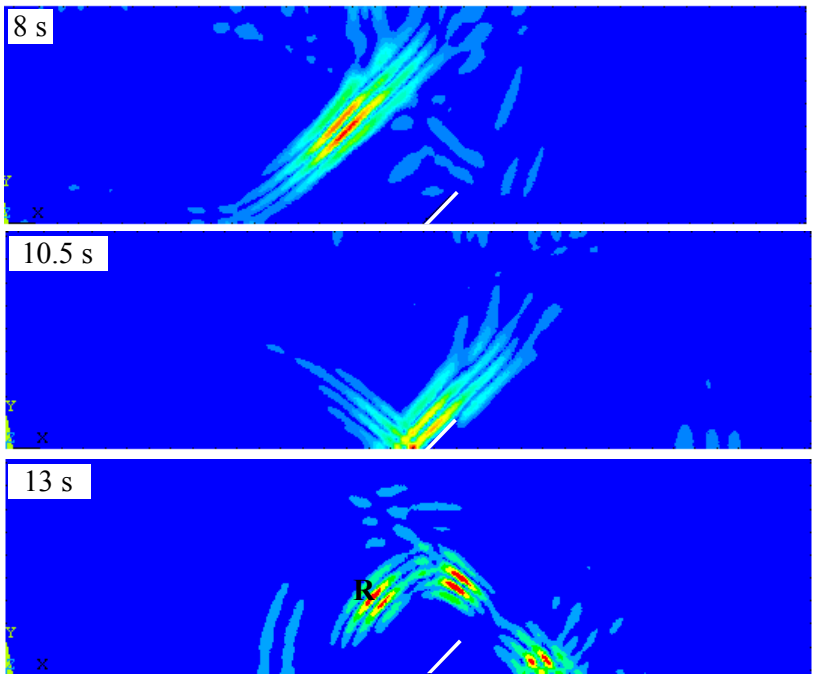

Figure 5.7: Wave propagation in the specimen with a 135° crack at different time instances, R: Reflection corner echo, D: Diffracted tip echo

In the following sections, we use equation (5.6) to estimate the crack orientation and its length for finite element (FE) simulated B-scans and experimental B-scans. The FE B-scans essentially contain less noise and no uncertainty associated with human error. Therefore, we can validate the equations derived in this section. Then, we estimate the crack length and orientation for experimental data to assess the applicability of equation (5.6) to real experimental data.

5.2 Analyzing FE simulated B-scans

The FE simulated B-scans, of which the details are presented in Chapter 6, are used to assess the accuracy of the method proposed to estimate the crack orientation and estimate the crack length for inclined cracks. The B-scans are first denoised using the 2D analytic wavelet thresholding method proposed in Chapter 3. The echo parameters including the TOF and the peak location are then estimated using the method proposed in Chapter 4. The echo with maximum amplitude is considered to be the corner trap echo and the other echo is considered to be the tip diffraction echo. If the estimated number of echoes is greater than two, the closest echo to the corner trap echo satisfying the condition $x_0' < x_0$ is chosen to be tip diffraction echo.

Figures 5.8 and 5.9 show the estimated crack angle and length for different given crack angles, respectively. Table 5.1 presents the corresponding estimation results. For cracks with 120° and 135° orientations, only the corner trap has been detected. Thus the crack angle and the crack length are not estimated for these two angles. This is expected because at these angles, the TOAs of the corner trap echo and the tip diffracted echo are very close and hence these echoes overlap. Thus, it is likely that the echo with smaller amplitude, i.e. the tip diffraction echo, is not detected.

For cracks with 45°, 90° and 135° orientations, the exact ray tracing solution is available. Therefore, it is expected that the error be smaller for these crack angles provided that both echoes are detected. This is in agreement with the results obtained for FE B-scans. As can be seen from Figures 5.8 and 5.9, the maximum error in estimating the crack orientation belongs to 15° crack and the maximum error in sizing belongs to 165° crack. This is expected because these angles are farthest crack angles among the simulated crack angles from the exact ray tracing solutions. Furthermore, they are obtained by extrapolating the equations for exact solutions.

In general, we have observed a good agreement between theory and the results obtained using the FE simulated B-scans. In the following section, we apply the modified RATT to experimental B-scans.

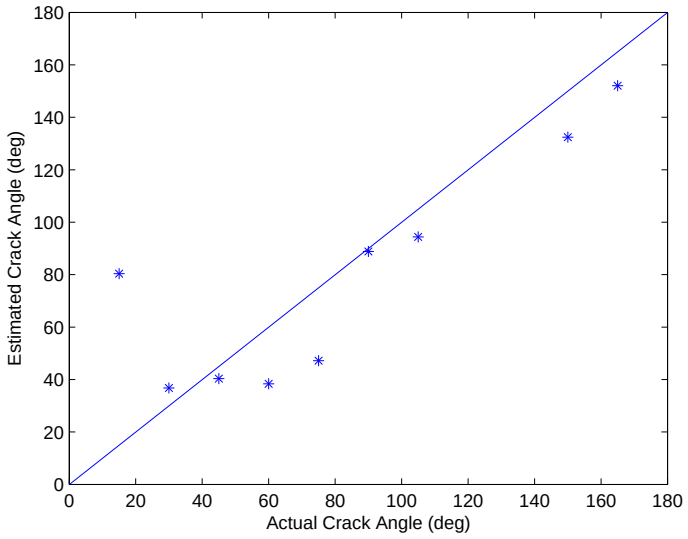

Figure 5.8: Estimated crack angle versus actual crack angle

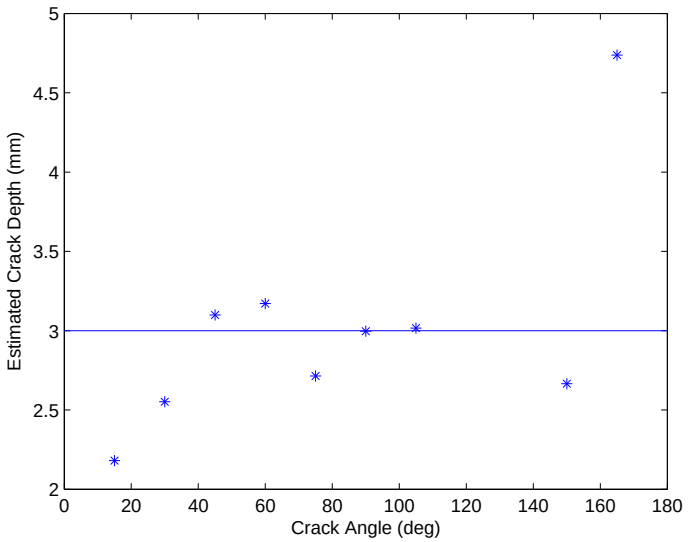

Figure 5.9: Estimated crack length for different crack angles, actual crack length = 3mm

Table 5.1: Estimated crack lengths, δ, and estimated crack angles, γ, for different crack angles; actual crack length = 3mm

		γ (deg)	Relative Error	δ (mm)	Relative Error
Crack Angle (deg)	15	80	436%	2.18	-27%
	30	37	23%	2.55	-15%
	45	40	-10%	3.10	3%
	60	38	-36%	3.17	6%
	75	47	-37%	2.71	-10%
	90	89	-1%	3.00	0%
	105	94	-10%	3.02	0%
	120	N/A	N/A	N/A	N/A
	135	N/A	N/A	N/A	N/A
	150	132	-12%	2.67	-11%
	165	152	-8%	4.74	58%

5.3 Experimental signal parameter estimation

In this section, the experimental B-scans recorded from samples with different crack orientations (Data presented in Section 7.1.4) are analyzed. The experimental signals are processed similar to FE signals in the previous section.

Figures 5.10 and 5.11 show the estimated crack angle and length for different crack angles, respectively. Table 5.2 presents the estimation results. In general, the estimation results are similar to the FE case. For the experimental data, the tip diffraction echo for 120° crack is detected, while it could not be detected for FE simulated signals. This can be attributed to the longer pulse-width of the FE signals which is caused by the numerical damping as discussed in Chapter 6. The shorter pulse width of the experimental signal makes it easier to distinguish between corner trap and tip diffracted echoes. We can also observe that:

- In general, the crack angle error is greater for $\gamma < \pi/2$.
- In general, the crack length error is greater for $\gamma > \pi/2$.

These observations can be attributed to the fact that the relative position of the tip diffraction echo to the corner reflected echo is less sensitive to the crack angle for $\gamma < \pi/2$.

Table 5.3 presents crack sizing results using the conventional RATT. To obtain the relative times of arrival, the TOF is evaluated at $x = x_0$ where x_0 is the position at which the amplitude of the corner trap echo is maximum. For $\gamma = 150°$, the corner echo arrives earlier than the tip echo; therefore, as can be seen in Table 5.3,

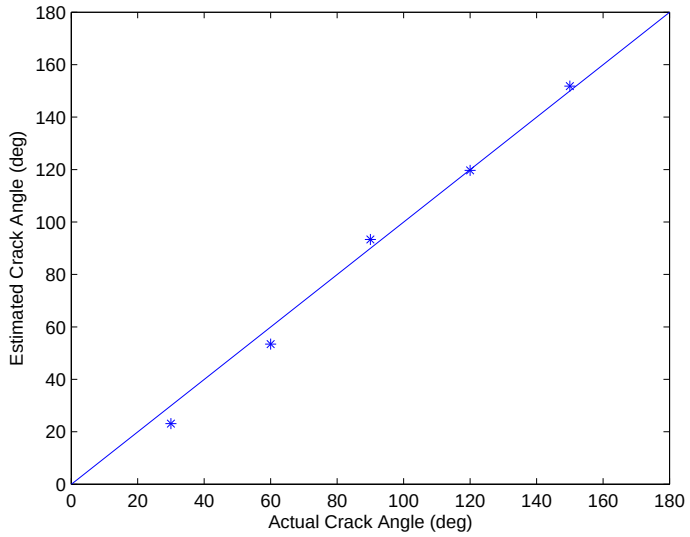

Figure 5.10: Estimated crack angle versus actual crack angle

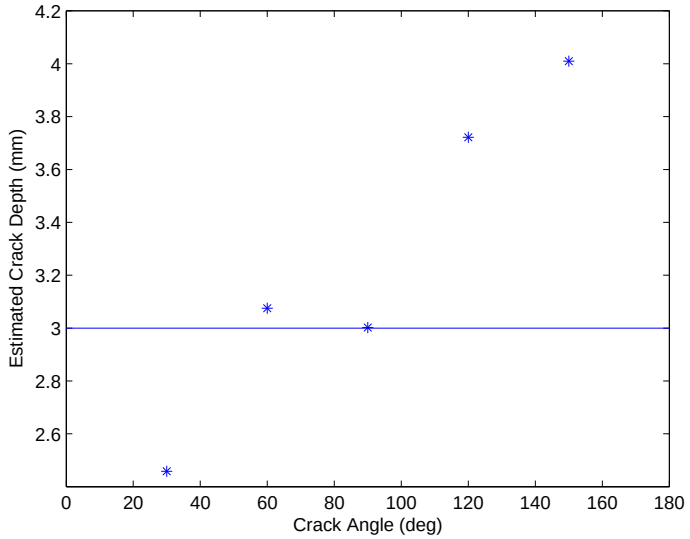

Figure 5.11: Estimated crack length for different crack angles, actual crack length = 3mm

Table 5.2: Estimated crack lengths, δ, and estimated crack angles, γ, for different crack angles; actual crack length = 3mm

		γ (deg)	Relative Error	δ (mm)	Relative Error
Crack Angle (deg)	30	23	-23%	2.46	-18%
	60	53	-11%	3.07	2%
	90	93	4%	3.00	0%
	120	119	0%	3.72	24%
	150	152	1%	4.01	34%

Table 5.3: Crack lengths, δ, estimated using the conventional RATT; actual crack length = 3mm

		δ (mm)	Relative Error
Crack Angle (deg)	30	3.16	5%
	60	4.20	40%
	90	2.70	-10%
	120	1.49	-50%
	150	-1.80	-160%

the conventional RATT formula results in a negative value for the crack length. For other crack angles, in general, the conventional RATT results in much greater error.

5.4 Summary and conclusions

In conventional relative arrival time technique, it is assumed that cracks are perpendicular to the specimen's surface. This assumption causes errors in crack sizing. In this chapter, a modified relative arrival time technique is proposed for estimating the size and orientation of inclined cracks. The proposed technique utilizes ultrasonic B-scan signals for estimating crack size and orientation. The modified RATT is obtained by deriving a relation between the crack length and orientation, and the parameters of the corner echo and the tip echo.

The proposed technique is applied to FE simulated B-scans and experimental B-scans. Comparing the results obtained using the modified RATT and the conventional RATT shows that the modified RATT results in smaller errors. Based on estimation results obtained for both experimental and FE simulated signals, we have observed that

- generally, the error is smaller for cases that the exact theoretical solution for the crack length and orientation is available; i.e. $\gamma = \theta$, $\gamma = \pi/2$ and $\gamma = \pi - \theta$,
- the estimation error for crack angle is greater when $\gamma < \pi/2$,
- the estimation error for crack length is greater when $\gamma > \pi/2$.

These observations are in agreement with the theoretical predictions obtained using ray tracing method. Therefore, in summary, we can conclude that the modified RATT can overcome the shortcomings of the conventional RATT in dealing with inclined cracks.

Chapter 6

Finite Element Simulation of the Ultrasonic Wave Propagation

Numerical analysis provides insights into the ultrasonic wave propagation and its interaction with the medium. In addition, through this numerical analysis, simulated signals can be generated when the experimental data either is not available or is available only for a limited number of cases.

The ultrasonic wave propagation can be modeled using numerical methods including finite element, finite difference, finite volume, boundary element, pseudo-spectral and mesh-less methods [153]. Among these methods finite element and finite difference are the most commonly used methods.

The finite difference has the advantage of simple implementation, however it requires rectangular grid. Finite element method (FEM) uses unstructured meshes which can accurately model complex geometries and nonlinearities [154].

In this chapter, the ultrasonic angle beam testing is simulated using finite element method, using Ansys, to generate simulated ultrasonic signals. Finite element method allows us to properly model a crack by using a finer mesh close to the crack and a coarser mesh everywhere else. In addition, the geometry of the specimen and wedge can be easily meshed using FEM.

To successfully perform finite element analysis (FEA), some parameters need to be determined prior to the analysis, most importantly mesh size and time-step. In this chapter, the proper values of these parameters are first investigated. Next, the FE model is validated by comparing the FE simulated signals to existing experimental data. Finally, simulation is conducted to generate typical ultrasonic signals.

The simulated ultrasonic signals have been used in Chapter 5 for evaluating the performance of the proposed method for estimating crack depth and orientation. In

addition, in Chapter 5, we have used the ray tracing method to derive the modified relative arrival time technique. However, the ray tracing method involves a major simplifying assumption; it assumes that the ultrasonic waves travel on the straight lines. We have used the finite element analysis to simulate the wave propagation inside the material. From the simulation, the propagation of the tip diffraction echo and the corner reflection echo has been examined and compared to the ray tracing. Note that the experimental signals presented in Chapter 7 do not provide show how the ultrasonic waves propagated as they are only measured at the transducer. By contrast, the wave propagation inside the material can be clearly observed by displaying the stress contours or other physical quantities at any time step.

6.1 Parameter selection of the finite element model

Among different parameters used in a finite element analysis, the most critical ones are the time-step and mesh size which are important for achieving the required accuracy and numerical stability. The selection of these parameters, in turn, depends upon the FE solver. Implicit and explicit solvers have been used by other researchers to solve FE problems [155]. In explicit methods, the system state at a later time, $X(t + \Delta t)$, is given explicitly by the system state at the current time, $X(t)$; that is,

$$X(t + \Delta t) = F(X(t)) \tag{6.1}$$

In contrast to explicit methods, in implicit methods, there is an implicit relation between the state of the system at a later time and the state of the system at the current time; that is,

$$G(X(t), X(t + \Delta t)) = 0 \tag{6.2}$$

Clearly, explicit methods significantly reduce the computational demand for calculating the system state for each iteration. Because of this computational efficiency, the explicit methods are often used for solving problems involving high frequency dynamic phenomena, such as impact and wave propagation problems [156]. Nevertheless, explicit methods may become unstable if the time step is not selected small enough. For linear problems, the critical time step, called Courant number, is given by,

$$\Delta t = \frac{T_n}{\pi} \tag{6.3}$$

where Δt and T_n denote the time step and the smallest period for a given FE dis-

cretization, respectively. The critical time step can be estimated based on the size of the smallest element in the FE mesh and the wave speed in the material as [157],

$$\Delta t = \frac{h}{c_L} \tag{6.4}$$

where h and c_L denote the element size and the longitudinal wave speed, respectively.

Our objective is to simulate ultrasonic wave propagation in a specimen with a surface crack to generate simulated B-scan images of the specimen. In order to model the crack properly, a very fine mesh is required near the crack tip [158]. Therefore, according to equation (6.4), a very small time step should be used. On the other hand, the highest accuracy of explicit solvers is achieved by integrating with a time step equal to the critical time step and the accuracy is less when a smaller time step is employed [157]. Therefore, a uniform mesh is the optimal mesh for the explicit FEM [159]. This means either a uniform fine mesh should be used for the whole model or the accuracy will be reduced due to use of non-uniform mesh.

We employ the Newmark method which is a commonly used implicit method in structural dynamics. In contrast to explicit methods, implicit methods can be formulated to be unconditionally stable at the expense of longer computation time [155]. Yet, the time step and mesh size should be selected such that the applied loads and the physics of the problem are represented properly. In the following, we investigate the selection of the time step and mesh size by studying one dimensional ultrasonic wave propagation.

In this section, pulse-echo ultrasonic wave propagation is modeled in one dimension to investigate the proper selection of time step and mesh size. A steel block is modeled with the length of $L = 20mm$ and width of $W = 2mm$ as depicted in Figure 6.1. The mechanical properties of steel used in this model are: modulus of elasticity, $E = 200GPa$, density, $\rho = 7850kg/m^3$ and Poisson's ratio, $\nu = 0.3$. Given these mechanical properties, the longitudinal wave speed in this medium can be calculated as,

$$c_L = \sqrt{\frac{E(1-\nu)}{\rho(1+\nu)(1-2\nu)}} = 5.856\, mm/\mu s \tag{6.5}$$

Symmetric boundary condition is applied on two opposite sides along the length of rectangle. The right side is fixed as illustrated in Figure 6.1. On the left side, the transducer is located. Exciting the transducer generates ultrasonic waves inside the specimen. Ultrasonic waves travel along the length of the specimen, are reflected back from the right edge of the specimen, and are received by the transducer.

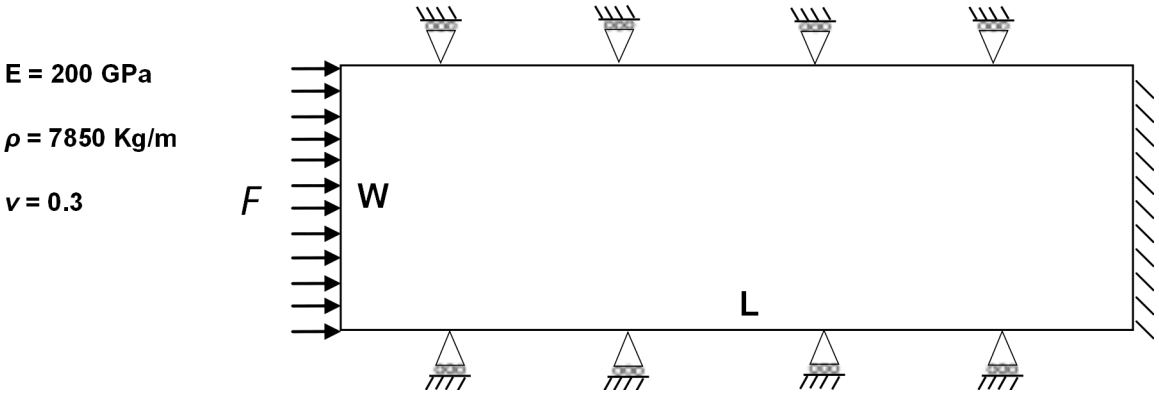

Figure 6.1: One-dimensional model geometry

A 5 MHz 3-cycle Hanning function is used as the excitation force. Figures 6.2 and 6.3 show the excitation which is applied as pressure on the left side of the specimen in the time domain and frequency domain, respectively. In general an N-cycle Hanning window can be expressed as

$$x = (1 - cos\frac{2\pi n}{L_H - 1})cos\frac{2\pi N n}{L_H - 1}, \quad n = 0, 1, \ldots, L_H - 1 \tag{6.6}$$

where L_H is the length of the N-cycle Hanning function which can be calculated as,

$$L_H = \frac{2\pi f_s N}{f} \tag{6.7}$$

where f_s is the sampling frequency and f is the center frequency of the excitation force. The value of f_s is selected to be the reciprocal of the FE solver time step.

We will use the normal acceleration at the transducer surface as the transducer output signal. The actual output of the transducer could be calculated using the voltage-to-surface acceleration impulse response of the transducer [160]. However, to simplify the FE model, the piezoelectric transducer is not included in the FE model.

The FE model is built and analyzed in Ansys®. The 2-D *Plane182* element type is used in the analysis. Plane182 is defined by four nodes; each having two degrees of freedom: translations in the nodal x and y directions (Figure 6.4) [161]. The element may be used as a plane element (plane stress, plane strain and generalized plane strain) or as an axisymmetric element [161]. The plane strain option is used for this analysis.

Although a higher order element, such as *Plane183* with a quadratic displacement, is more favorable for structural stress problems because of the continuity of the stress and strain fields [162], based on our simulation results in this section, Plane183

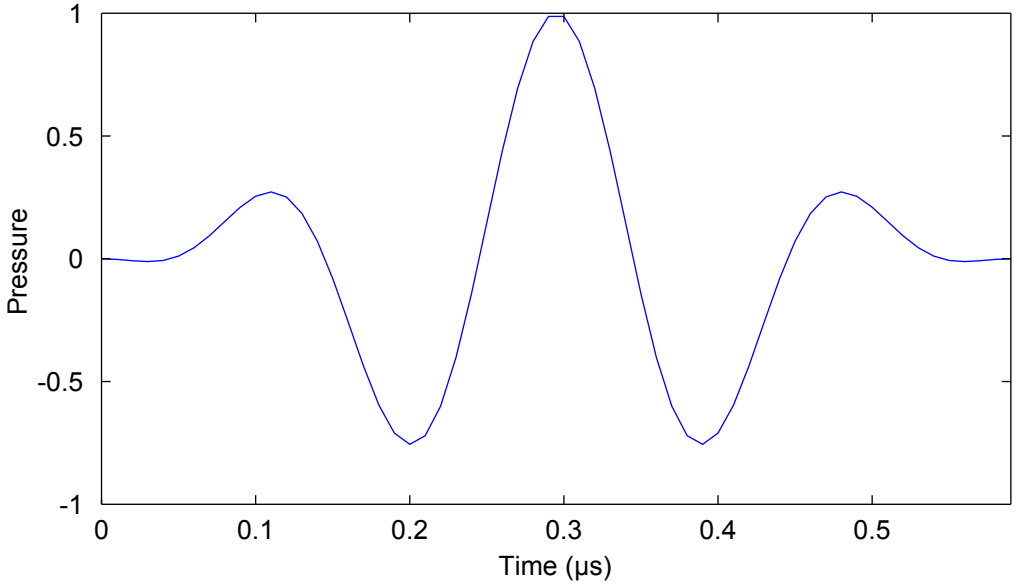

Figure 6.2: A 5 MHz 3-cycle Hanning function

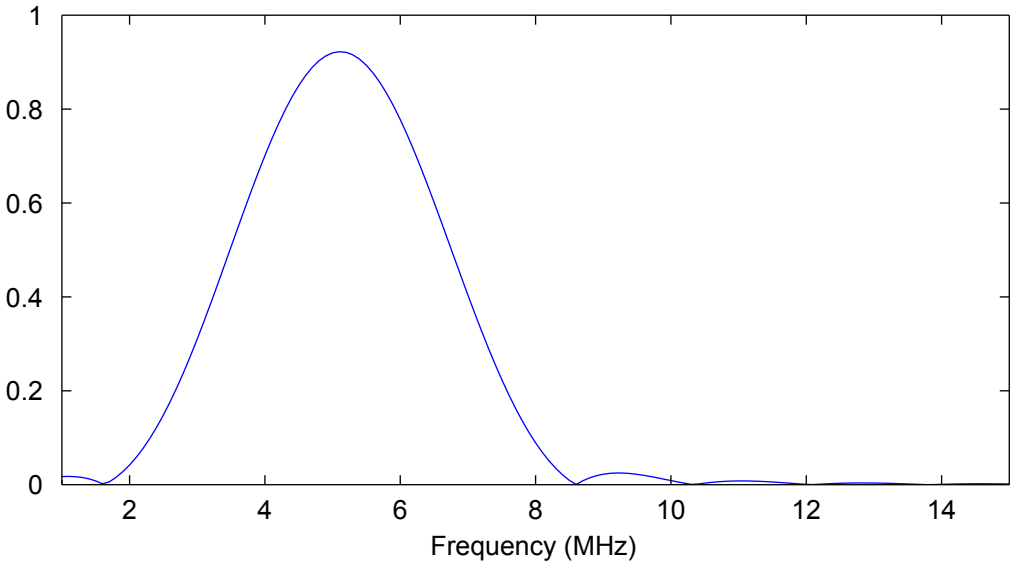

Figure 6.3: The frequency spectrum of a 5 MHz 3-cycle Hanning function

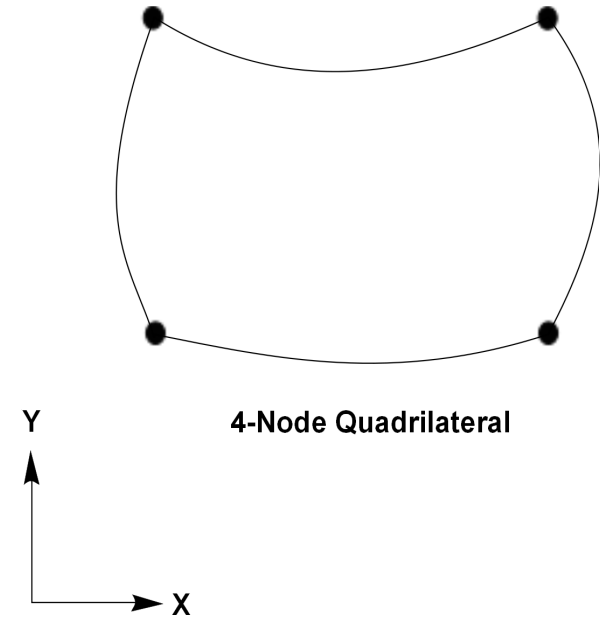

Figure 6.4: Plane182 geometry

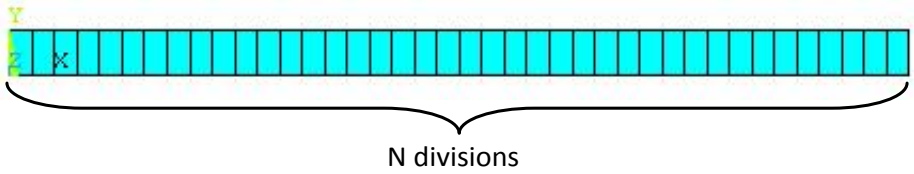

Figure 6.5: Meshed model

element offers no advantage over Plane182 when dealing with wave propagation problems which involve large gradients, while it significantly increases the problem size. Figure 6.5 depicts the meshing. As can be seen in Figure 6.5 the length of specimen has been divided into N elements. Therefore, each element length will be L/N.

As shown in Figure 6.3, most of the energy of excitation force (99.9% of the energy) is contained within the range $5 \pm 3MHz$. Therefore, the maximum frequency of interest is selected to be $f_{max} = 8MHz$. Correspondingly, the minimum wavelength to be considered is $\lambda_{min} = c/f_{max} = 0.73mm$. For the Newmark method, it is suggested to use time step size and element size as $\Delta t = 1/(20f_{max})$ and $\Delta x = \lambda_{min}/20$, respectively [163].

The Newmark method with parameter $\gamma = 0.01$ is used. The parameter γ ensures stability by damping out the high frequency oscillations, when no structural damping is applied [161]. Nevertheless, this numerical damping may cause a frequency downshift and loss of accuracy [164, 165]. Through trial and error, $\gamma = 0.01$ has been selected.

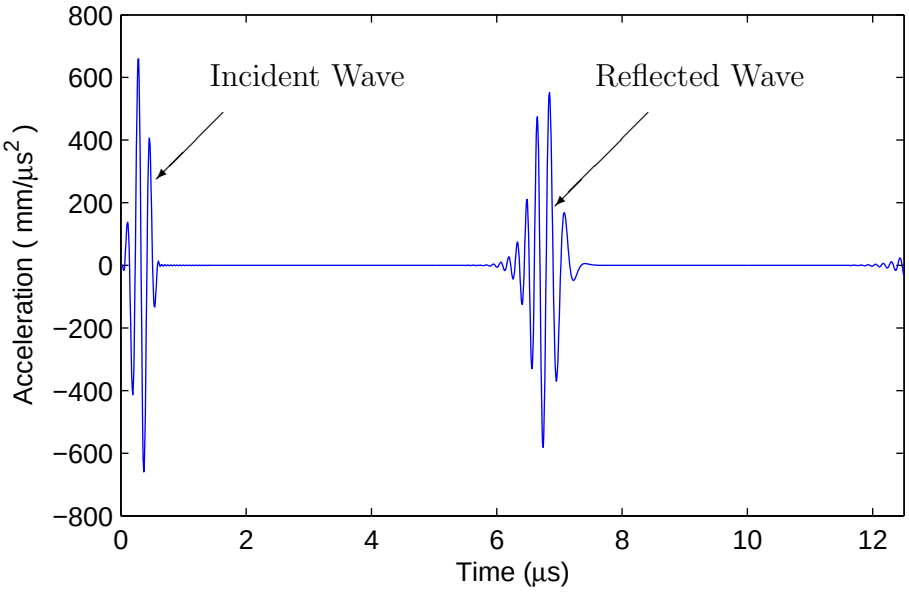

Figure 6.6: Transducer response for $r_t = 15$ and $r_x = 5$

In the following, we first compare different time steps and element sizes. Then, we compare two element types: Plane182 and Plane183.

6.1.1 Effect of the time step and element size

The FE simulation has been conducted for different time steps and element sizes. We express the two parameters, time step and element size, in terms of the following non-dimensional ratios: $r_t = 1/(f_{max}\Delta t)$ and $r_x = \lambda_{min}/\Delta x$, respectively.

Figures 6.6 shows the transducer response for $r_t = 15$ and $r_x = 5$. Two pulses are observed: the first pulse corresponds to the emitted wave and the second one corresponds to the echo. In the time domain, a noticeable difference between the incident wave and the reflected wave is their pulsewidths. Comparing the full width at half maximum (FWHM)[1] of the echo and the emitted signal shows that the FWHM of the echo is 48.6% greater than that of the emitted signal. Another difference is the reduction of the amplitude of the reflected wave. This reduction occurs mainly due to damping which dissipates the signal energy and the numerical diffusion [166] which spreads out the signal energy in time and space.

Figure 6.7 shows the frequency spectrum of the received echo. The frequency spectrum of the echo is calculated by taking the Fourier transform of the received signal from $2.5\mu s$ to $10\mu s$. Therefore, only the echo signal is included in the frequency

[1]FWHM is the distance between points on a curve at which the function reaches half its maximum value [134]. This measure is commonly used to express the width of a bump on a curve

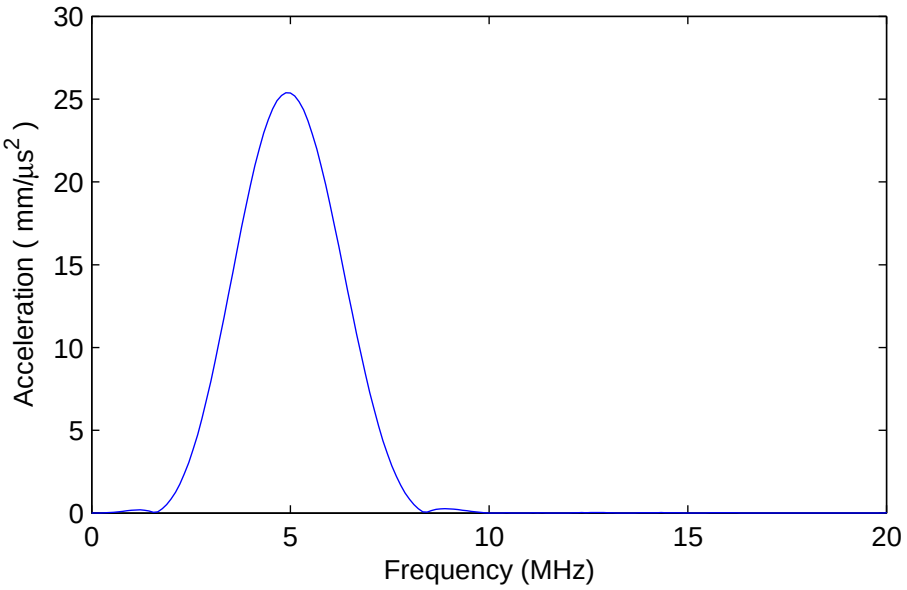

Figure 6.7: Frequency spectrum of the echo signal for $r_t = 15$ and $r_x = 5$

spectrum and the excitation is excluded. As can be seen in Figure 6.7, the frequency spectrum of the echo signal is similar to that of the excitation force shown in Figure 6.3. Figure 6.8 shows the excitation and response spectra, each normalized by its peak for comparison. As shown in Figure 6.8, the excitation force spectrum and the echo spectrum are almost identical. In order to quantitatively evaluate the difference between the two spectra, we define the difference, $d\{\mathbf{a}, \mathbf{b}\}$, between two spectra, $\mathbf{a}$ and $\mathbf{b}$, as

$$d\{\mathbf{a}, \mathbf{b}\} = \frac{|\mathbf{a} - \mathbf{b}|^2}{|\mathbf{a}||\mathbf{b}|}. \tag{6.8}$$

Using equation (6.8), the difference between the normalized spectra of the excitation force and the echo is calculated to be 0.6%.

By comparing the spectra of the transducer response and the excitation force, it can be observed that the amplitude of higher frequency components of the received signal is slightly smaller than that of the excitation force. This has resulted in a slight shift in the center frequency of the echo from $5MHz$ to $4.9MHz$.

Frequency downshift is caused by the numerical damping which has been added for the solution stability. This becomes more evident as γ increases. For example, Figure 6.9 shows the spectrum of the transducer response and the spectrum of the excitation force when γ parameter of the Newmark method has been increased to 0.05. Clearly, the frequency downshift has increased from the case that γ was set to 0.01 shown in Figure 6.8. By increasing γ from 0.01 to 0.05, the center frequency has

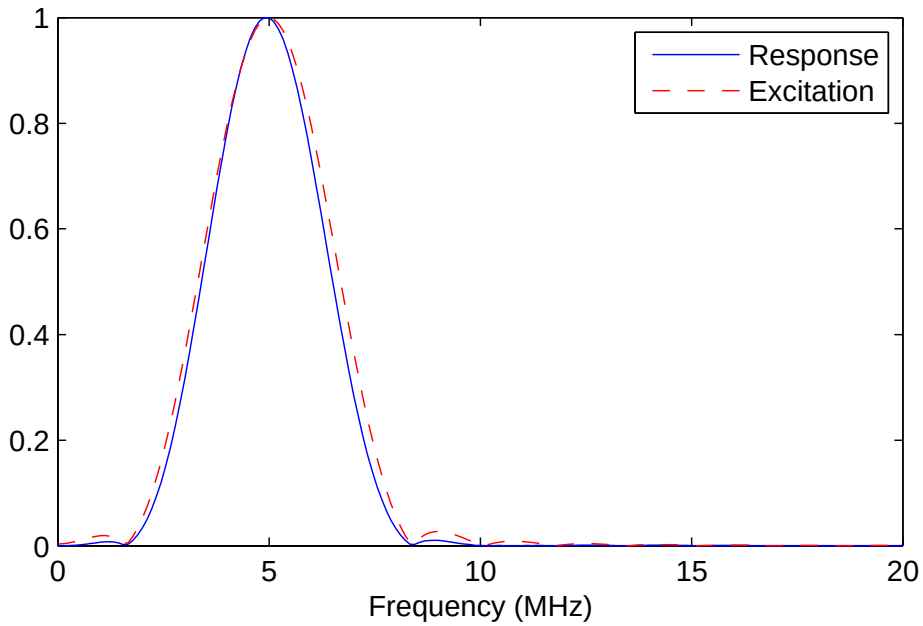

Figure 6.8: Comparison of the excitation force spectrum and the echo signal spectrum for $r_t = 15$ and $r_x = 5$ with normalized y-axis

decreased from 4.9 MHz to 4.3 MHz.

Figures 6.10 and 6.11 show the received signal for $r_t = 10$ and $r_x = 5$ in the time domain and the frequency domain, respectively. Figure 6.12 shows the normalized spectra of the excitation and the response for the same settings. The results are generally similar to the case that $r_t = 15$. Yet, some differences can be observed. The echo amplitude has slightly decreased by reducing r_t. The difference between the spectra of emitted signal and the echo has increased to 1.3%. In addition, the center frequency of the echo has decreased to $4.8MHz$. These results show that there is no major distortion in the received signal due to selection of a large time step or element size for $r_t = 10$ and $r_x = 5$.

These changes become more evident by further decreasing of r_t to 5 as shown in Figures 6.13 to 6.15. As depicted in Figure 6.13, clearly the amplitude of the echo has decreased. The difference between two spectra increased to 9% and the center frequency decreased to $4.4MHz$. Moreover, it is observed in Figure 6.13 that a large time step has caused the so-called numerical dispersion. The numerical dispersion causes a frequency dependent alteration in the wave speed [167, 168]. As a result, as can be seen in Figure 6.13, lower frequency waves arrive first and then higher frequency waves arrive.

The effect of numerical dispersion can be more clearly observed from the time-

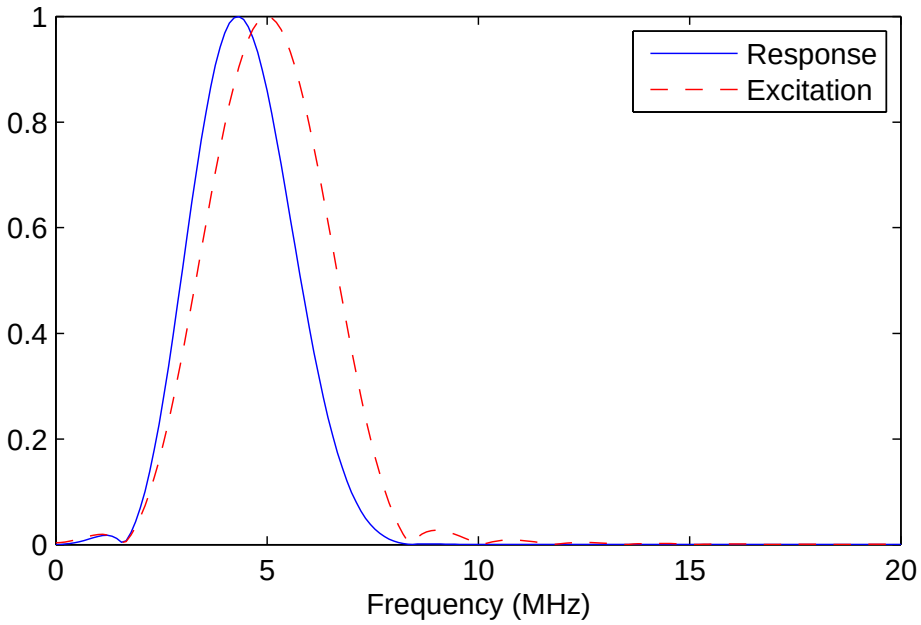

Figure 6.9: Comparison of the excitation force spectrum and the echo signal spectrum for $r_t = 15$, $r_x = 5$ and $\gamma = 0.05$ with normalized y-axis

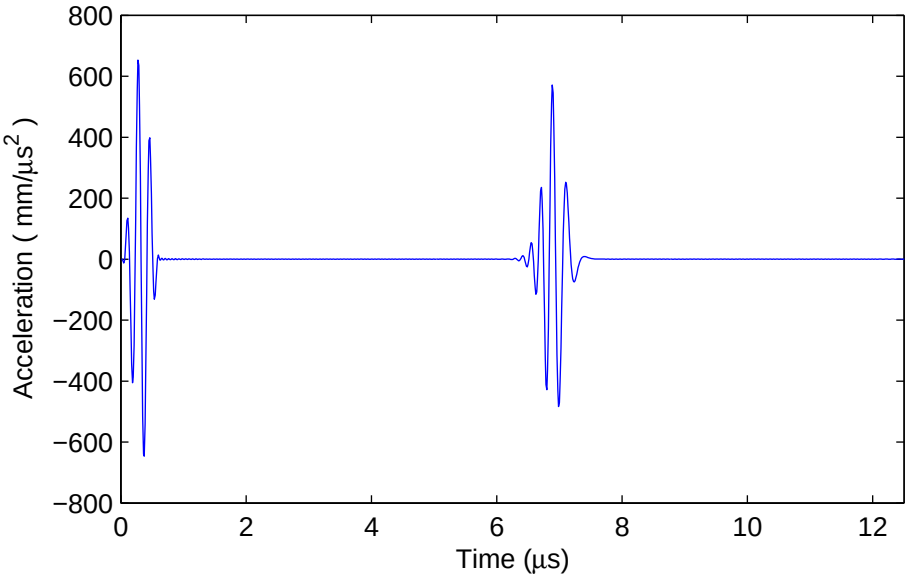

Figure 6.10: Transducer response for $r_t = 10$ and $r_x = 5$

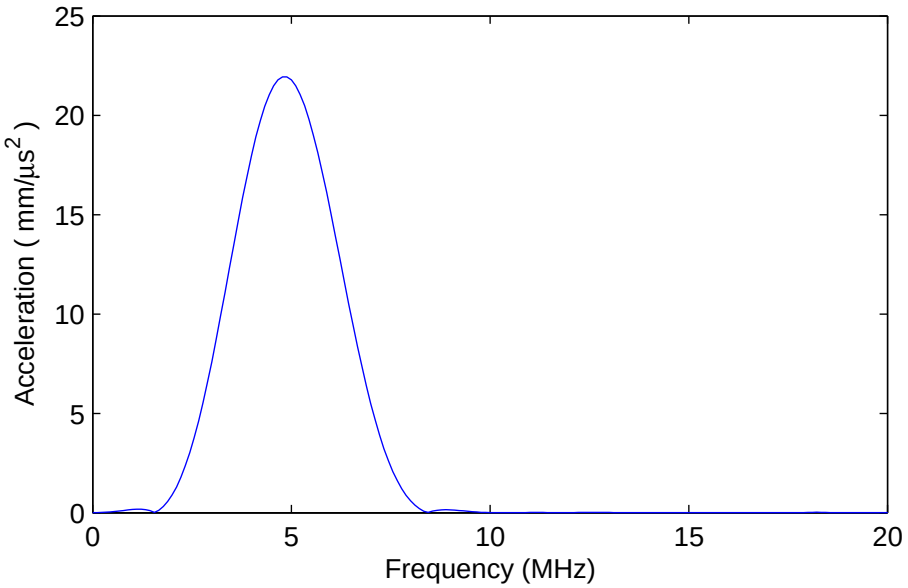

Figure 6.11: Transducer response spectrum for $r_t = 10$ and $r_x = 5$

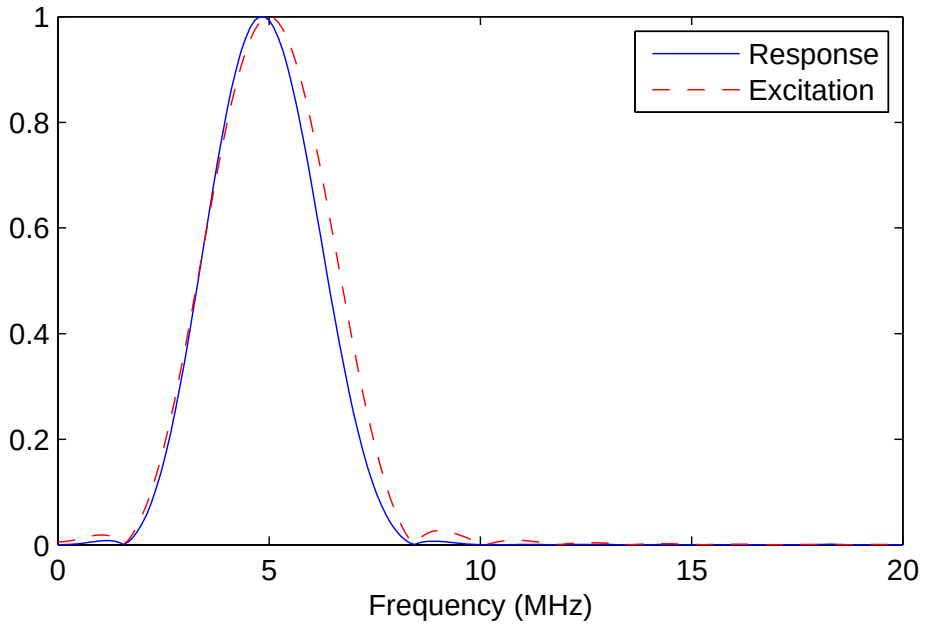

Figure 6.12: Comparison of the excitation force spectrum and the echo signal spectrum for $r_t = 10$ and $r_x = 5$ with normalized y-axis

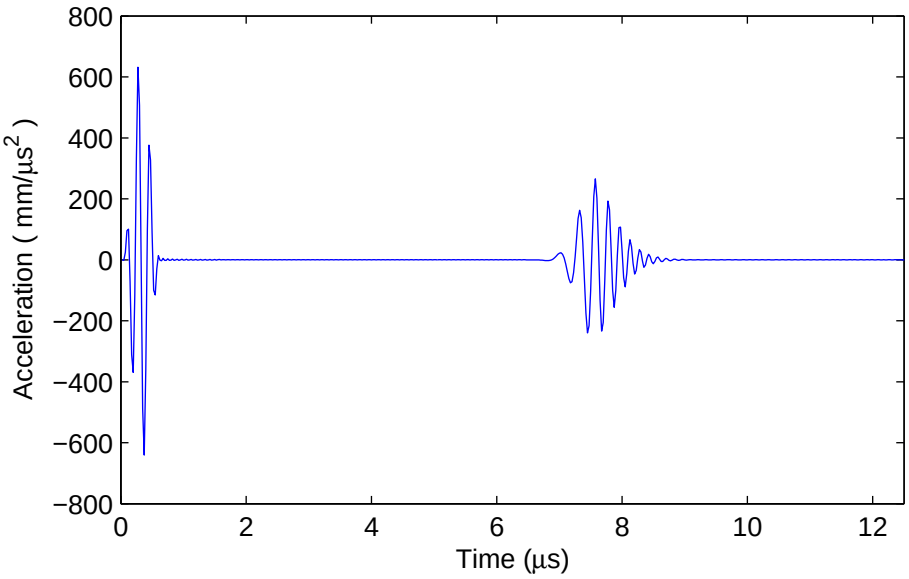

Figure 6.13: Transducer response for $r_t = 5$ and $r_x = 5$

frequency representation (TFR) of the received signal. Figures 6.16 and 6.17 show the short-time Fourier transforms of the received signals for $r_t = 15$ and $r_x = 5$, and $r_t = 5$ and $r_x = 5$, respectively. The x-axis represents time, the y-axis indicates frequency and the amplitude is plotted in gray scale. It can be seen for $r_t = 15$ the TFR of the echo is almost identical to the TFR of the emitted signal, except that it is time-shifted, while for $r_t = 5$ the numerical dispersion is obviously present, i.e. as time passes the frequency of the echo signal increases.

Figures 6.18 and 6.19 show the transducer response for $r_t = 15$ and $r_x = 3$ in the time domain and the frequency domain, respectively. It is clear the response has been distorted. This difference can be obviously seen in Figure 6.20 by comparing the frequency spectra of the emitted and received signals. As can be seen more peaks appear in the received signal due to selection of large element size.

Based on the results of the FE simulation for the one dimensional wave propagation, we set the following criteria for our FE analysis:

$$r_t \geq 10, \quad r_x \geq 5 \tag{6.9}$$

As seen, these values are minimum requirements for which the distortion in the response waveform is negligible.

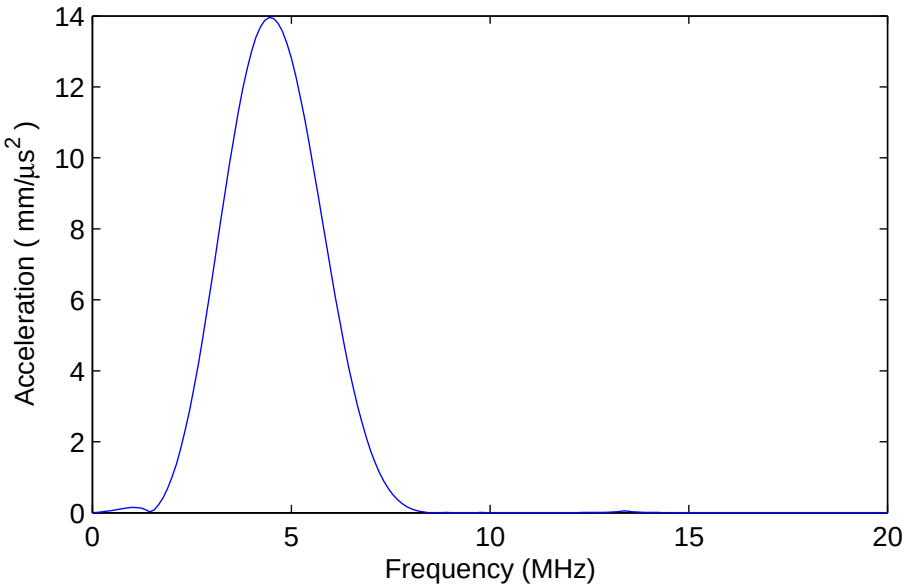

Figure 6.14: Transducer response spectrum for $r_t = 5$ and $r_x = 5$

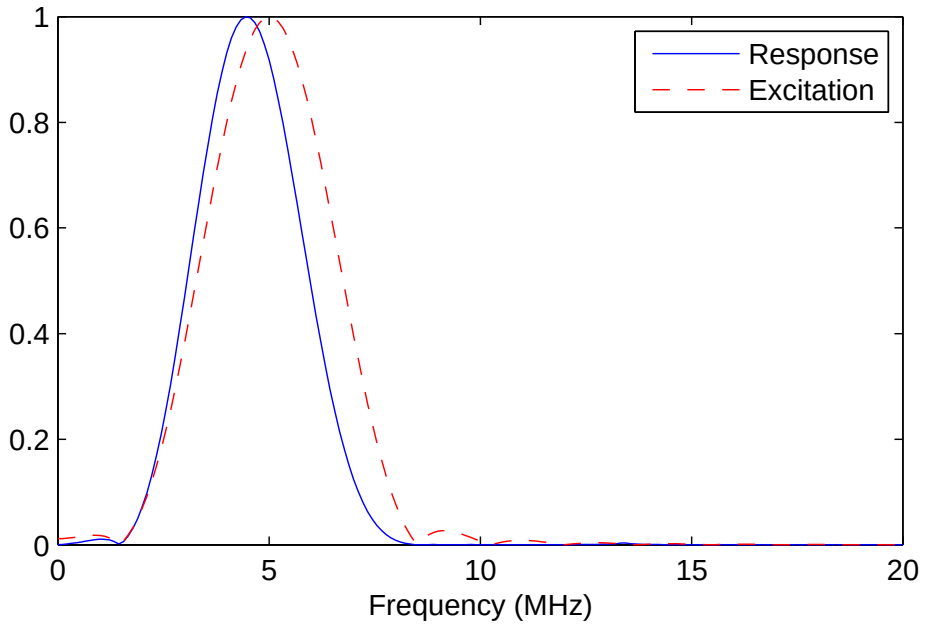

Figure 6.15: Comparison of the excitation force spectrum and the transducer response spectrum for $r_t = 5$ and $r_x = 5$ with normalized y-axis

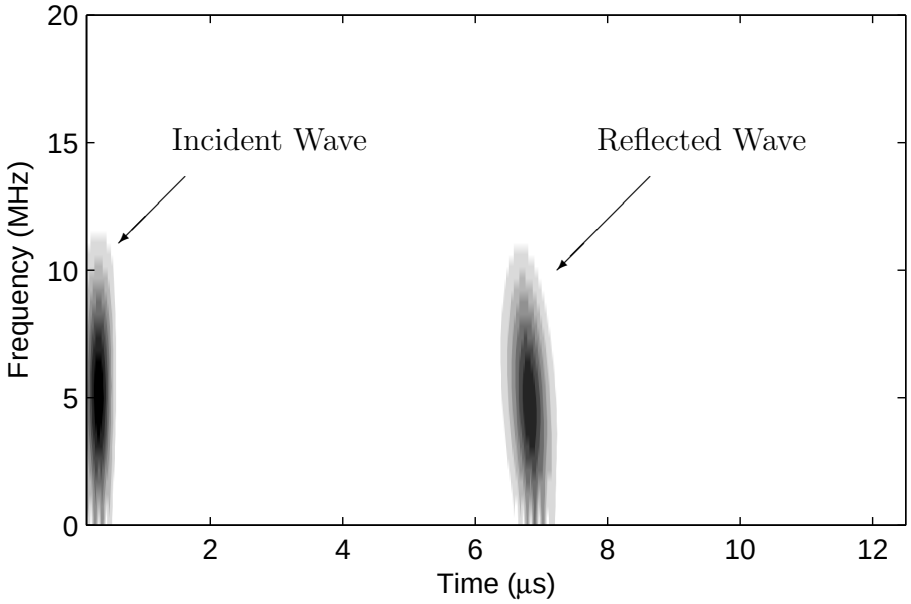

Figure 6.16: Transducer response spectrogram for $r_t = 15$ and $r_x = 5$

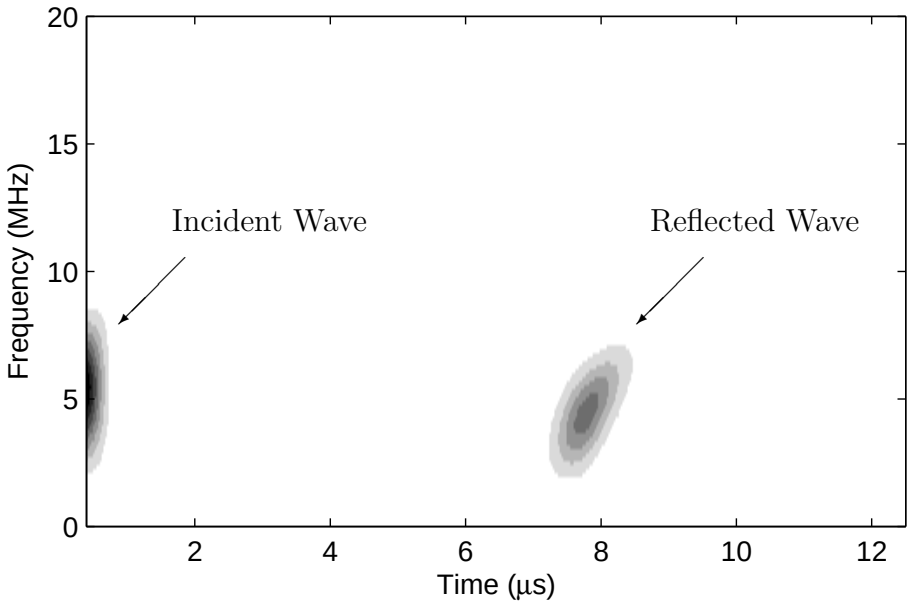

Figure 6.17: Transducer response spectrogram for $r_t = 5$ and $r_x = 5$

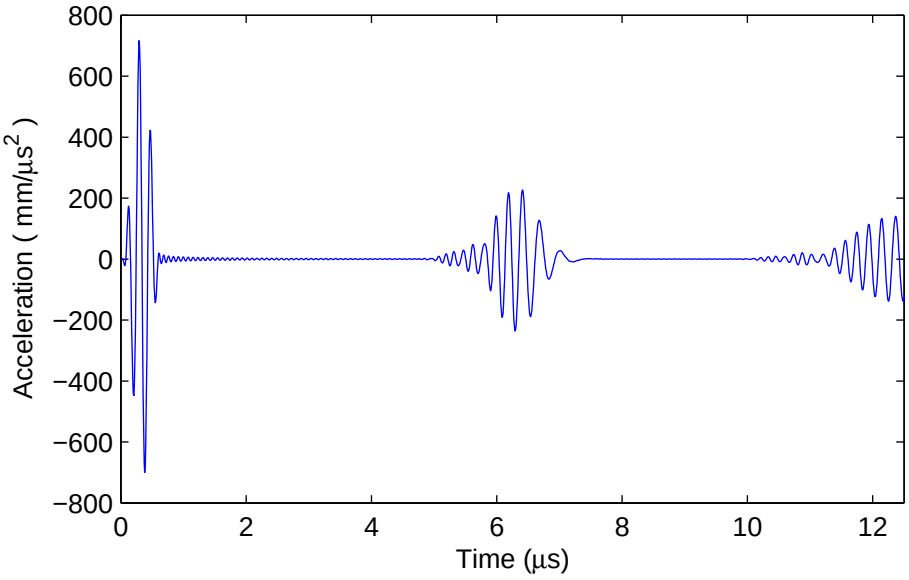

Figure 6.18: Transducer response for $r_t = 15$ and $r_x = 3$

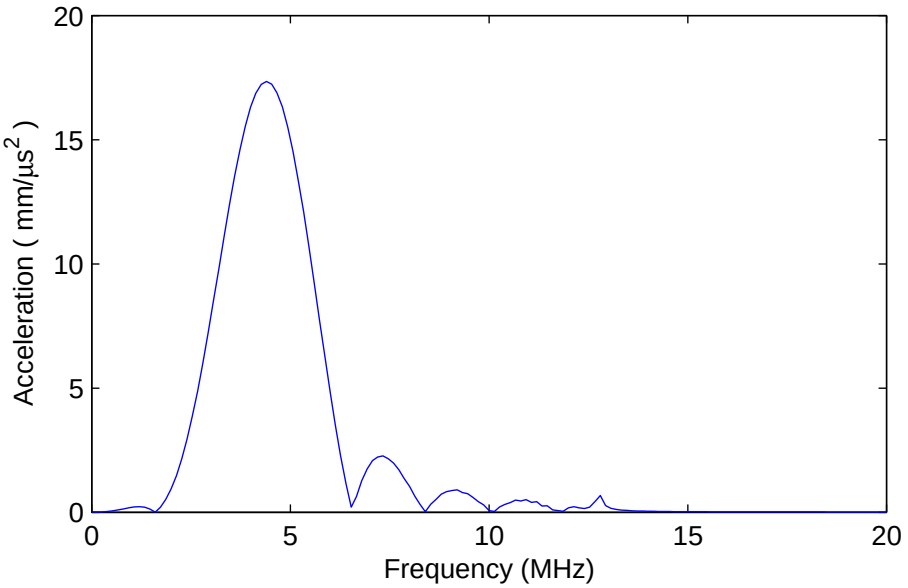

Figure 6.19: Transducer response spectrum for $r_t = 15$ and $r_x = 3$

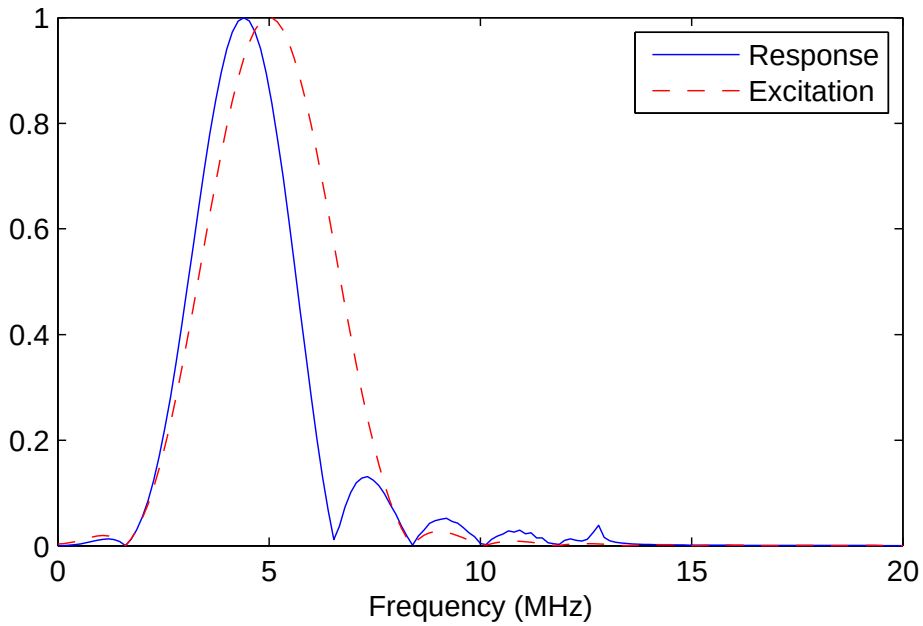

Figure 6.20: Comparison of the excitation force spectrum and the transducer response spectrum for $r_t = 15$ and $r_x = 3$ with normalized y-axis

6.1.2 Comparison of Plane182 and Plane183 elements

In general, a higher order element is more favorable when the solution is expected to be a smooth function; e.g. structural static analysis [157], while a lower order element type is preferred when dealing with wave propagation problems [169, 170]. To decide on the element order, we have compared a linear element, i.e. Plane182, with a quadratic element, i.e. Plane183.

Figures 6.21-6.23 show the transducer response when Plane183 is used, $r_t = 10$ and $r_x = 5$. Comparing to the corresponding results obtained using Plane182 in Figures 6.10-6.12, no improvement is observed when a higher order element is used. As presented in Table 6.1 there is no major change in the spectra of the excitation force and the transducer response, $d\{\mathbf{F}, \mathbf{A}\}$, or the frequency downshift values. Moreover, the computational time is closely related to the number of nodes. For the same number of elements, the number of nodes of the FE model meshed by Plane183 is approximately 2.5 times greater than the model meshed by Plane182. If we increase the number of elements of the model which uses Plane182 element by the same factor, i.e. to increase r_x to 12.5, we can achieve much more accurate results as shown in Figures 6.24-6.26 and Table 6.1.

Table 6.1: The difference between the normalized spectra of the excitation force and the received signal and the frequency downshift for different FE model parameters

Element Type	γ	r_t	r_x	$d\{\mathbf{F},\mathbf{A}\}$[1](%)	Frequency Downshift[2](%)
Plane182	0.01	15	5	0.6	2.2
Plane182	0.01	10	5	1.3	4.2
Plane182	0.01	5	5	9.0	11.2
Plane182	0.05	15	5	12.9	13.3
Plane182	0.01	10	12.5	0.4	0.0
Plane183	0.01	10	5	2.6	4.2

[1] F: Excitation force spectrum, A: Transducer response spectrum, and $d\{\mathbf{F},\mathbf{A}\}$ is defined by equation (6.8).
[2] Frequency downshift (%) $= \frac{f_{ce}-f_{cr}}{f_{ce}} \times 100$ where f_{cr} and f_{ce} denote the response center frequency and the excitation center frequency, respectively.

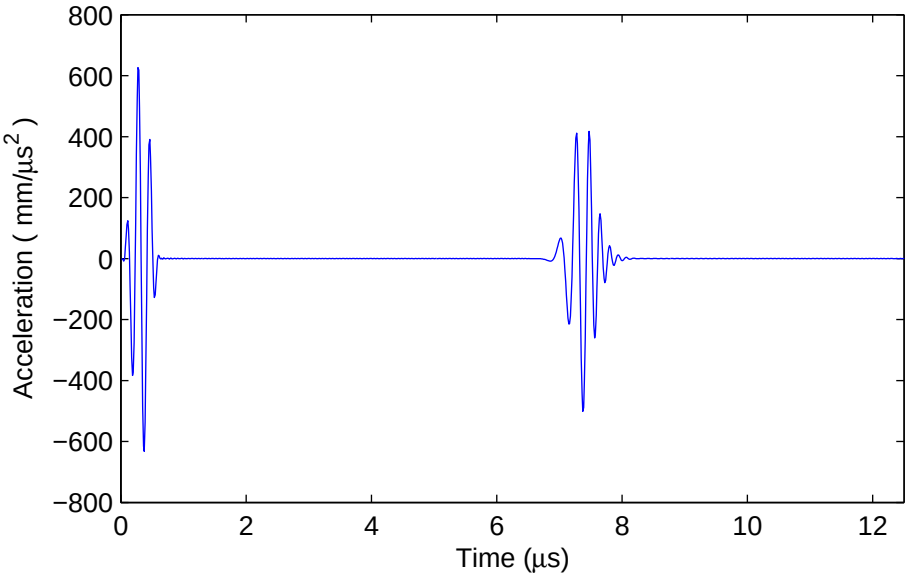

Figure 6.21: Transducer response for Plane183 element, $r_t = 10$ and $r_x = 5$

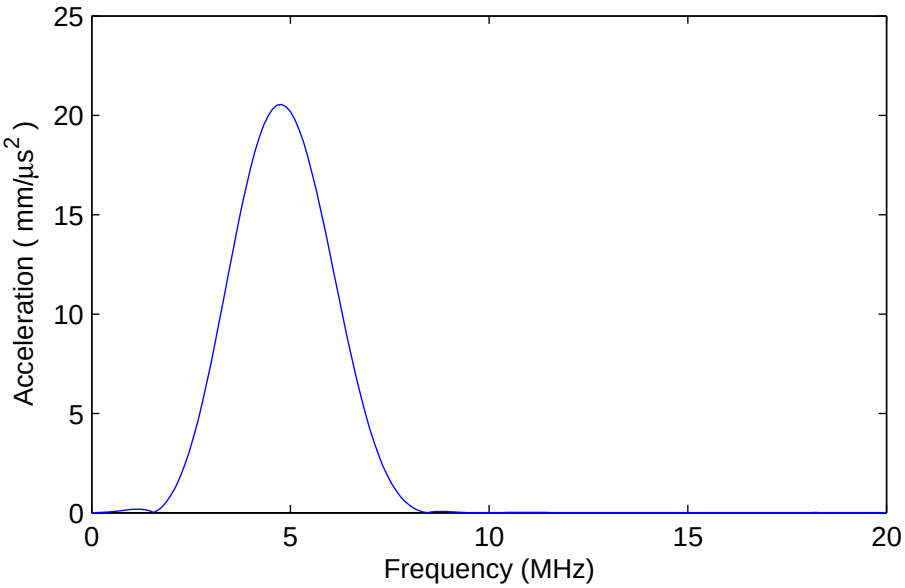

Figure 6.22: Transducer response spectrum for Plane183 element, $r_t = 10$ and $r_x = 5$

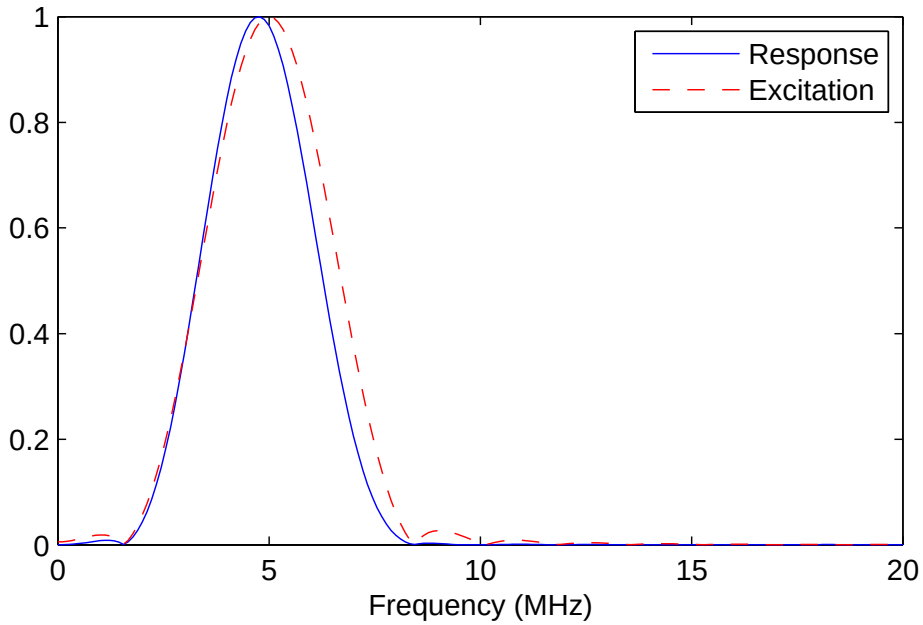

Figure 6.23: Comparison of the excitation force spectrum and the transducer response spectrum for Plane183 element, $r_t = 10$ and $r_x = 5$ with normalized y-axis

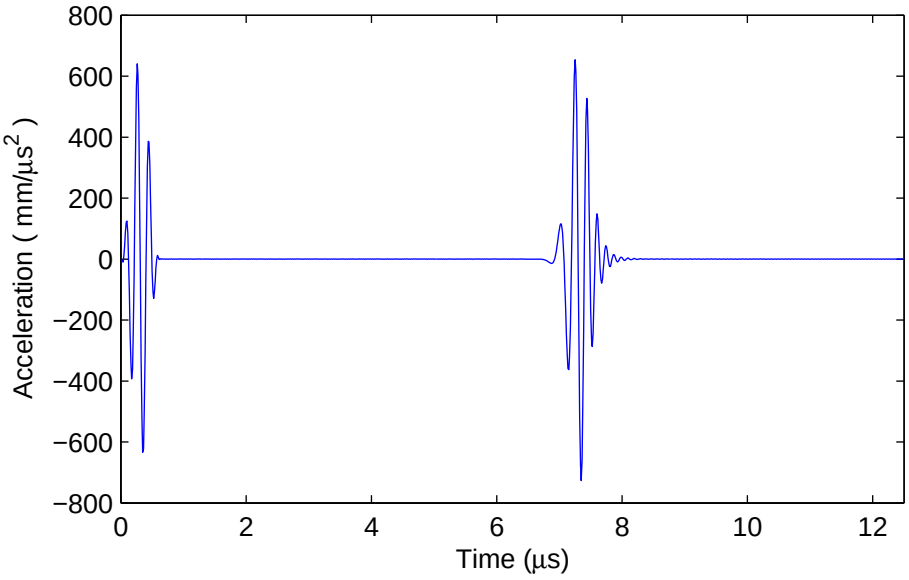

Figure 6.24: Transducer response for $r_t = 10$ and $r_x = 12.5$

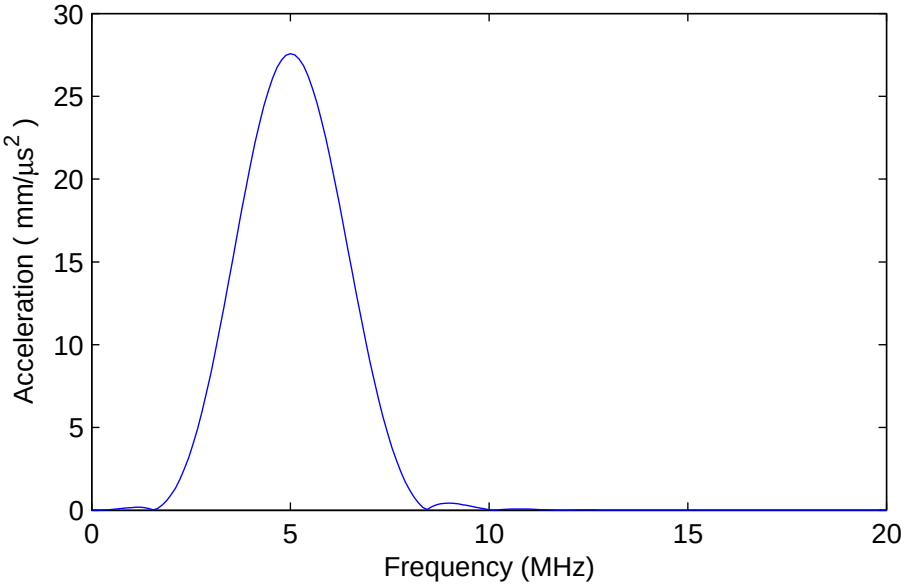

Figure 6.25: Transducer response spectrum for $r_t = 10$ and $r_x = 12.5$

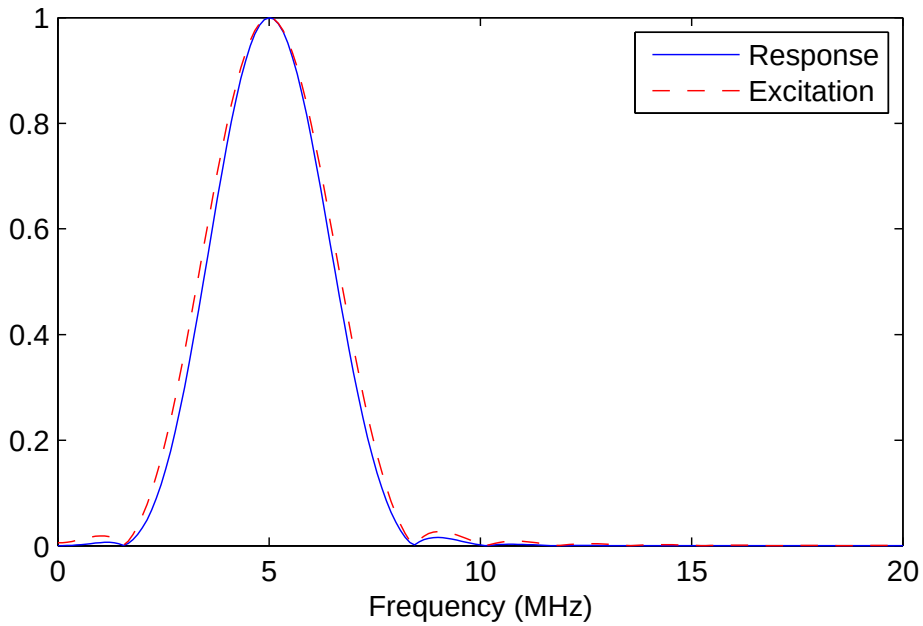

Figure 6.26: Comparison of the excitation force spectrum and the transducer response spectrum for $r_t = 10$ and $r_x = 12.5$ with normalized y-axis

6.2 FE modeling of ultrasonic angle beam testing

In this section, we model ultrasonic angle beam testing of a specimen with an inclined surface crack. These FEA results have been used in Chapter 5 for developing features that can be used to estimate the crack size and orientation. In this section, the FE model is validated first by comparing to experimental signals. Then, the FEA simulated signals for specimens with different crack orientations are presented.

6.2.1 Model Validation

We validate our model in two steps. In the first step, we simulate a specimen with no crack and compare the simulated signal with the experimental signal. This model allows us to check whether the guidelines we developed for 1D model is sufficient for a 2D model without dealing with the difficulties of modeling a crack.

In the second step, we model a specimen with crack and compare FE results with experimental data. This is the model whose results will be used for developing proper features for calculating crack size and orientation.

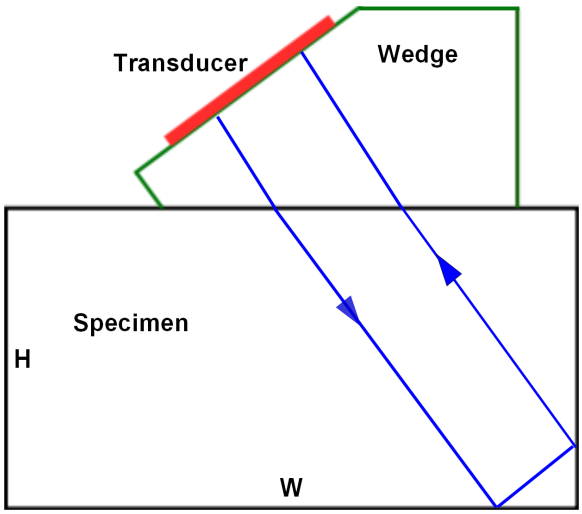

Figure 6.27: Geometry of the wedge and a specimen with no crack

Specimen with no crack

Figure 6.27 demonstrates the geometry of the specimen in which W=50 mm and H=23 mm. The experimental setup for this model is explained in Section 7.1.5. Figure 6.28 shows the simulated B-scan image. For easier comparison with the experimental data the origin of the time axis is set at the wedge delay. Comparing the simulated B-scan with the experimental B-scan shown in Figure 7.23 shows that the simulated B-scan and the experimental B-scan are generally similar to each other[1].

The time of arrival (TOA) of the echo is estimated from an arbitrary selected A-scan recorded at the distance of 10 mm (Figure 6.29). From Figure 6.29, the time of arrival is $20.08\mu s$. The theoretical time of arrival, $\tau_{theoretical}$, is equal to,

$$\tau_{theoretical} = \frac{2}{v}(H\cos\theta + x\sin\theta) = \frac{2}{3.229}(23\cos 45 + 22.8\sin 45) = 20.06\mu s \quad (6.10)$$

where $v = 3.229mm/\mu s$ is the shear wave velocity, $\theta = 45°$ is the refraction angle, H=23 mm is the height of the specimen and $x = 10 + 12.8 = 22.8mm$[2] is the distance from the probe index to the specimen's edge. A good agreement is observed between the theoretical TOA and the TOA obtained from FEM. Similar results have been obtained when different A-scans have been selected. Therefore, we can conclude that the FEM results can correctly predict the TOA.

To compare the experimental and FE signals, we have calculated the cross-correlation

[1]The FE simulation has been carried out for a smaller time duration and a smaller scanning span hence the second echo which has been seen in the experimental B-scan cannot be observed in the simulated B-scan.

[2]The distance from the beam index to the edge of the wedge is 12.8 mm.

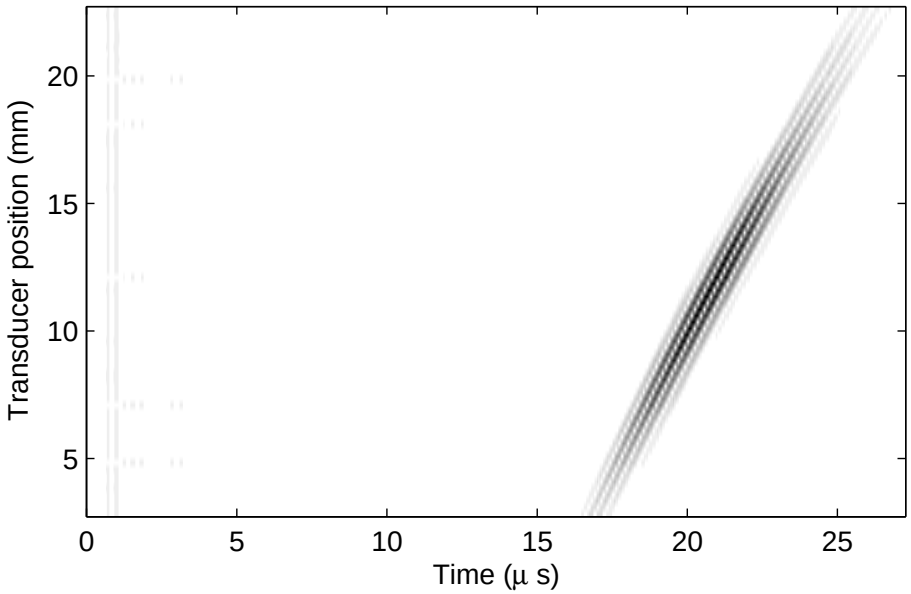

Figure 6.28: FE simulated B-scan of a specimen with no crack

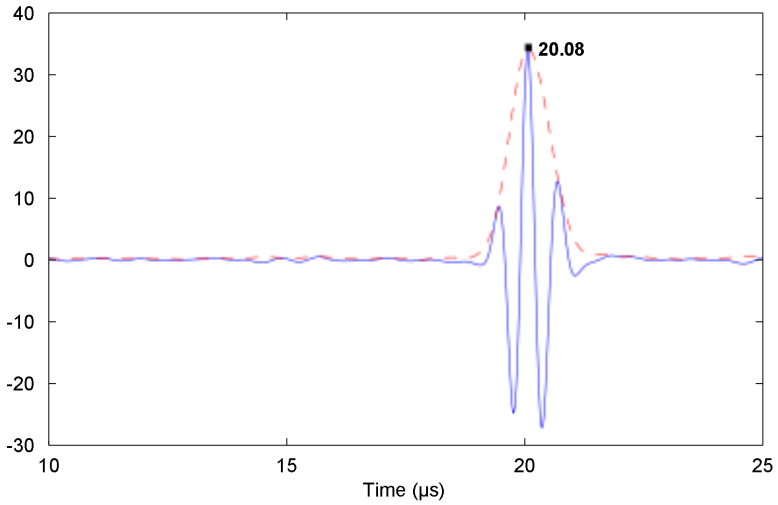

Figure 6.29: A-scan of a specimen with no crack, the distance from the near edge of the wedge to the edge of specimen = 10.1 mm

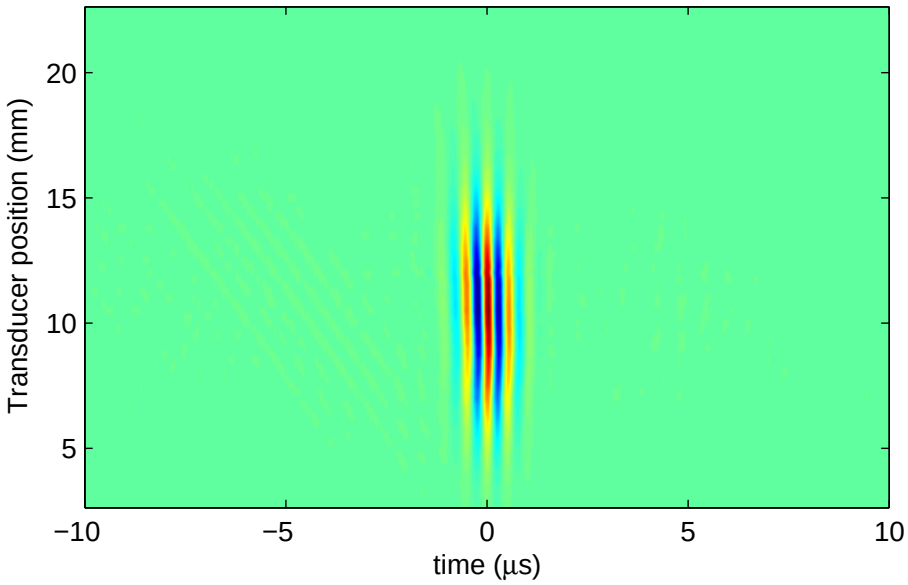

Figure 6.30: Cross-correlation between the experimental B-scan and FE simulated B-scan

between these two signals. The cross-correlation of two signals $f(t)$ and $g(t)$ is defined as

$$(f \star g)(t) = \int_{-\infty}^{\infty} f(\tau)g(t+\tau)d\tau \tag{6.11}$$

A cross-correlation with a strong peak indicates a strong correlation between two signals. If the peak occurs at point other than zero it shows that there is a time delay between two signals, otherwise they are synchronous. To calculate the cross-correlation between the experimental signal and the FE simulated signal, the cross-correlation of every two corresponding A-scans is calculated[1]. Figure 6.30 shows the cross-correlation and Figure 6.31 shows the normalized cross-correlation between experimental B-scan and FE simulated B-scan. As can be seen in these figures, there are strong peaks around zero. These peaks around zero can be consistently observed for all A-scans recorded at different transducer positions. This indicates a very good correlation between the experimental B-scan and the FE simulated B-scan. Therefore, in this case, our FE model can generate signals which are very close to experimental ones.

In order to examine the frequency downshift for this case, we have calculated the average frequency spectrum by averaging over frequency spectra of all A-scans. Figure 6.32 shows the normalized frequency spectra of the received signal and the

[1]Note that this is not a 2D cross-correlation because the cross-correlation integral is only taken over time.

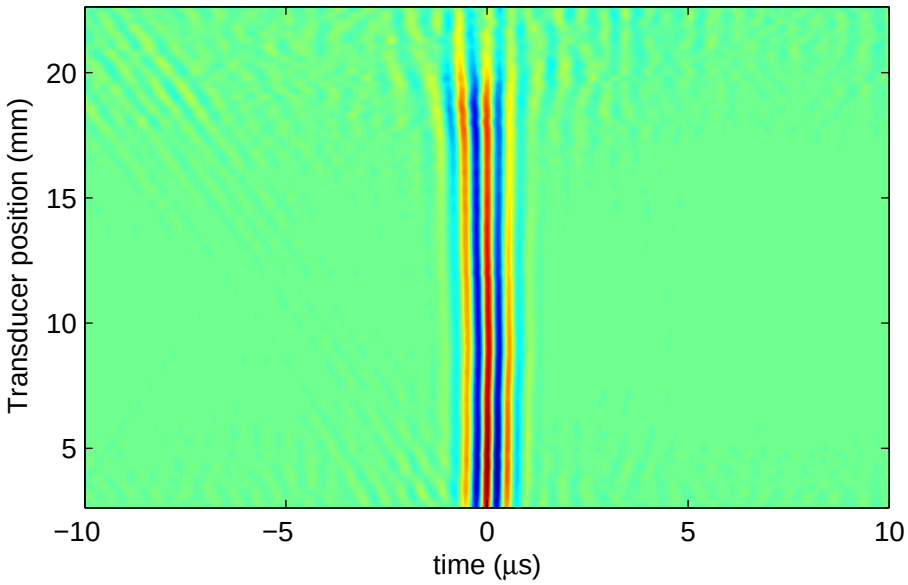

Figure 6.31: Normalized cross-correlation between the experimental B-scan and FE simulated B-scan

excitation force applied to the transducer. Each frequency spectrum is normalized by its peak. The center frequency of the transducer response is at 1.45 MHz while the center frequency of the force is at 2.25 MHz. Comparing to the one dimensional case the frequency downshift has increased because of the longer distance that wave travels. Therefore, due to this frequency downshift, the frequency of the received signal and associated parameters, such as pulse-width, should be treated with care when analyzing the FEM results.

In summary, we can conclude that in general, our FE model generates results which are very close to the experimental ones. In particular, the TOA values are very close to the experimental and theoretical values. This shows that using the parameters selected in this section, our FE model is able to accurately predict TOA. Nonetheless, there is considerable frequency downshift due to the numerical damping which should be taken into account when analyzing FE results. In the next section, we will add a crack to our model to validate our model in the presence of a crack.

Specimen with a crack

The geometry and mechanical properties of the FE model for the specimen with an inclined crack are shown in Figure 6.33. The transducer in the model is excited with a 3-cycle Hanning signal and the response of the transducer is calculated and stored. These simulated signals are then compared to the experimental signals presented

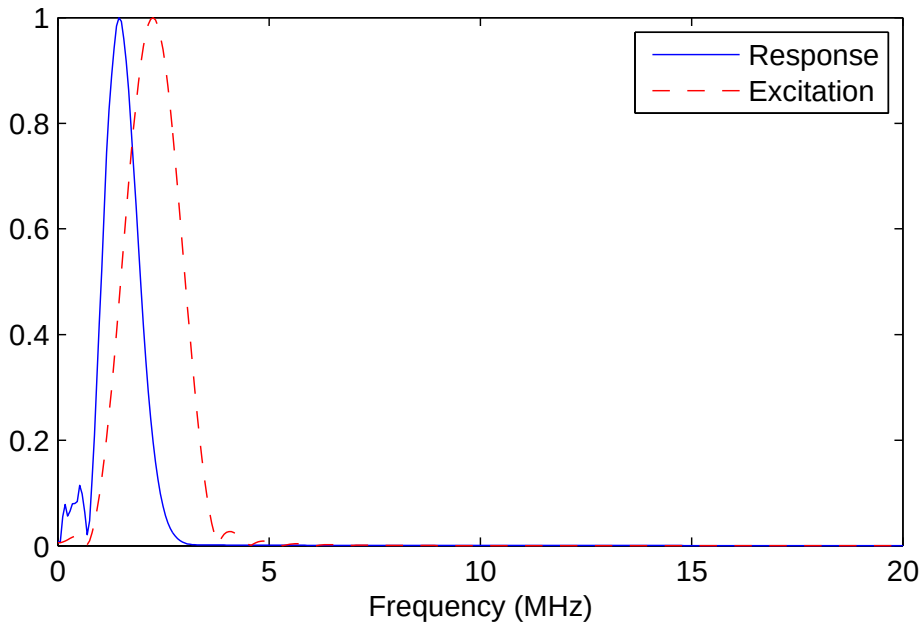

Figure 6.32: Comparison of the excitation force spectrum and the transducer response spectrum with normalized y-axis

in Section 7.1.4 for specimens with crack angles of 30°, 60°, 90°, 120° and 150° degrees to validate the FE model. For comparison, the cross-correlation between the experimental signal and FE simulated signal is computed as explained in the previous section. Prior to computation of the cross-correlation, the experimental signals were denoised using the method proposed in Chapter 3.

Figures 6.34-6.38 show the cross-correlation between the experimental and FE signals for different crack orientations. As can be seen, the peak of the cross-correlation occurs close to $t = 0\mu s$. This observation shows that the difference between the TOF values of the experimental and numerical signals is negligible.

6.2.2 FE simulated signals for specimens with different crack orientations

After validating the FE model, the ultrasonic wave propagation for specimens with different crack orientations is simulated using FEM. The crack angle is varied from 15° to 165° with a step size of 15°. Figures 6.39-6.49 show the simulated B-scans for different crack angles. These signals have been used in Chapter 5 for evaluation of the proposed method for estimating crack depth and orientation.

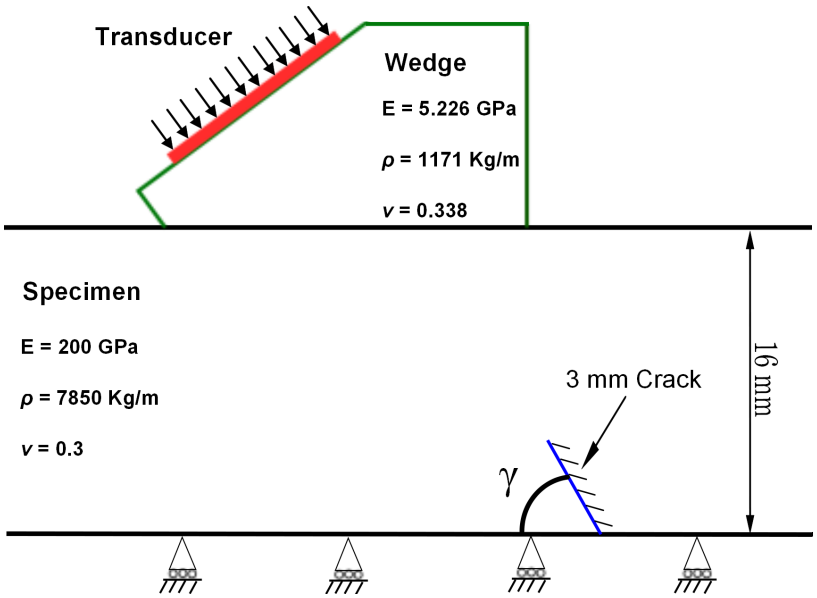

Figure 6.33: FE model of the specimen with an inclined crack

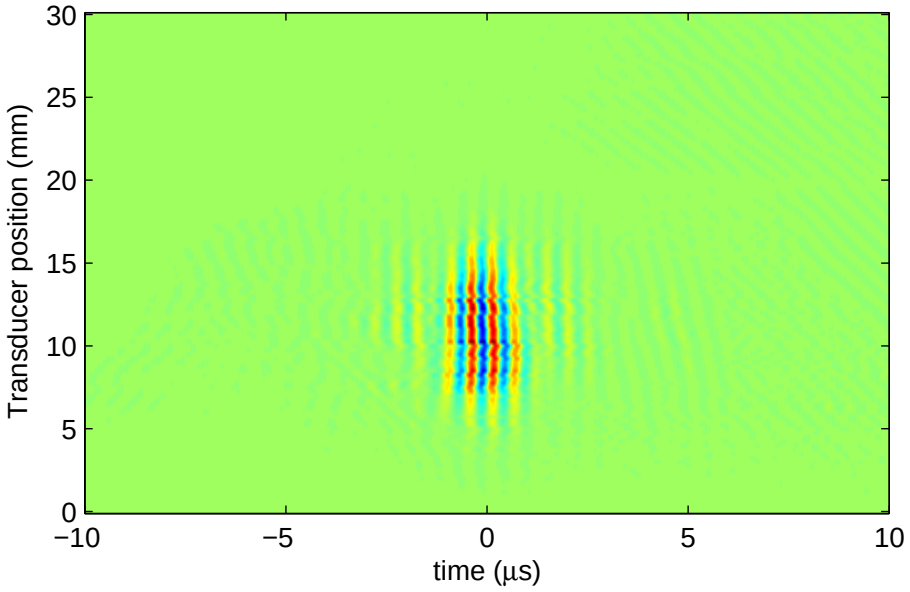

Figure 6.34: Cross-correlation between the experimental B-scan and FE simulated B-scan for the specimen with a 30° crack

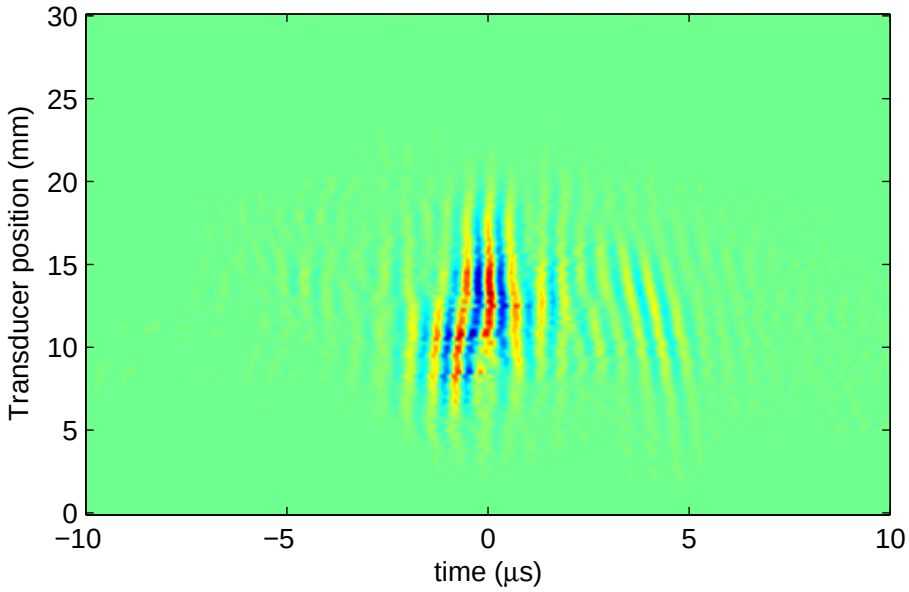

Figure 6.35: Cross-correlation between the experimental B-scan and FE simulated B-scan for the specimen with a 60° crack

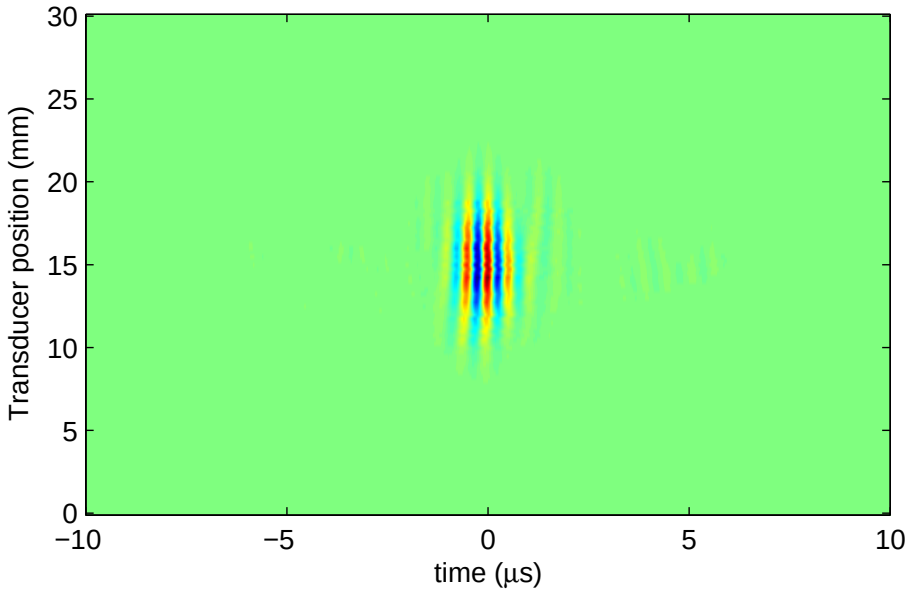

Figure 6.36: Cross-correlation between the experimental B-scan and FE simulated B-scan for the specimen with a 90° crack

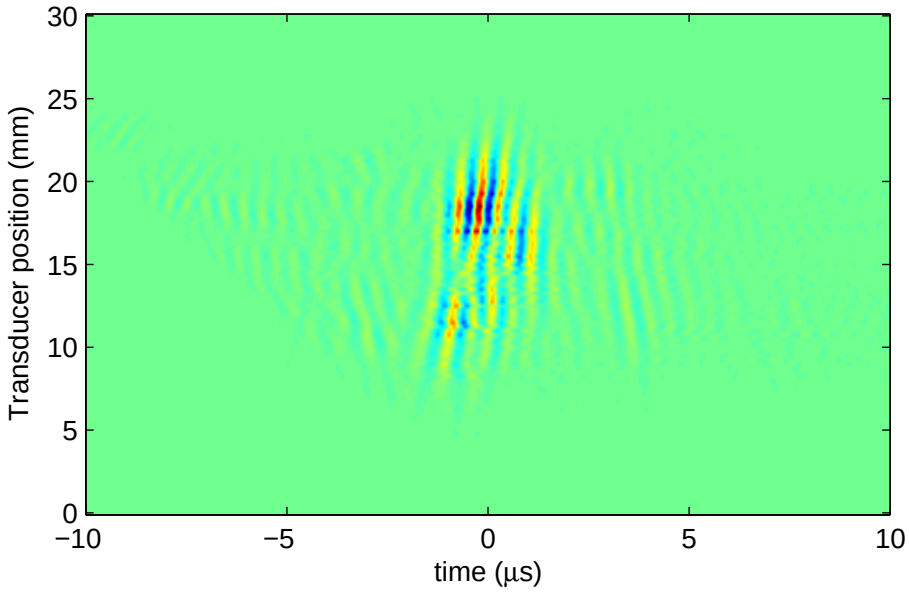

Figure 6.37: Cross-correlation between the experimental B-scan and FE simulated B-scan for the specimen with a 120° crack

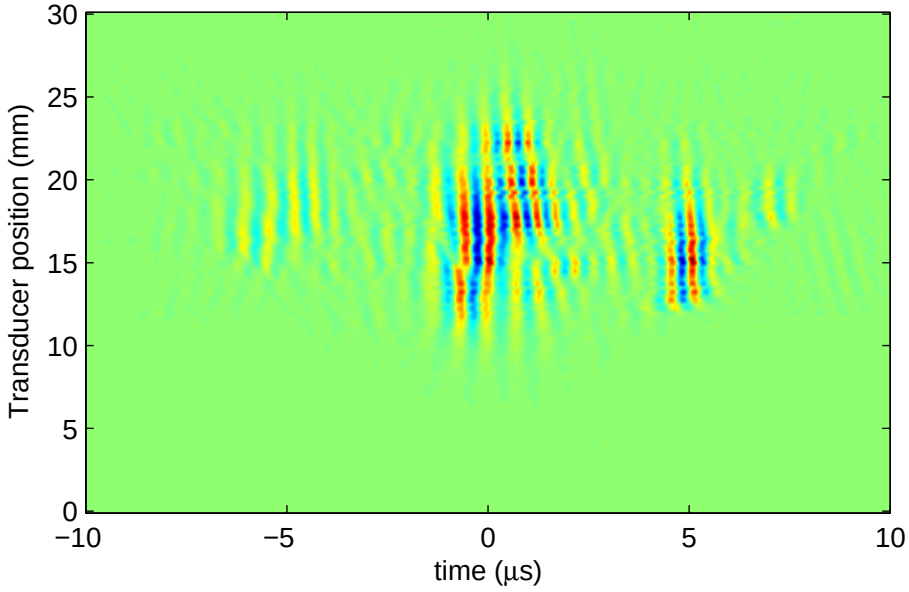

Figure 6.38: Cross-correlation between the experimental B-scan and FE simulated B-scan for the specimen with a 150° crack

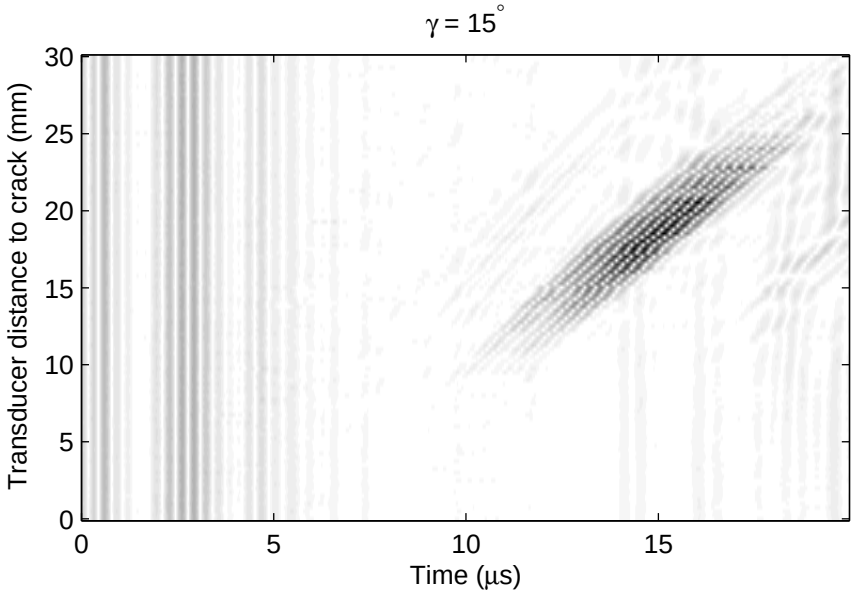

Figure 6.39: FE simulated B-scan of the specimen with a crack angle of 15°

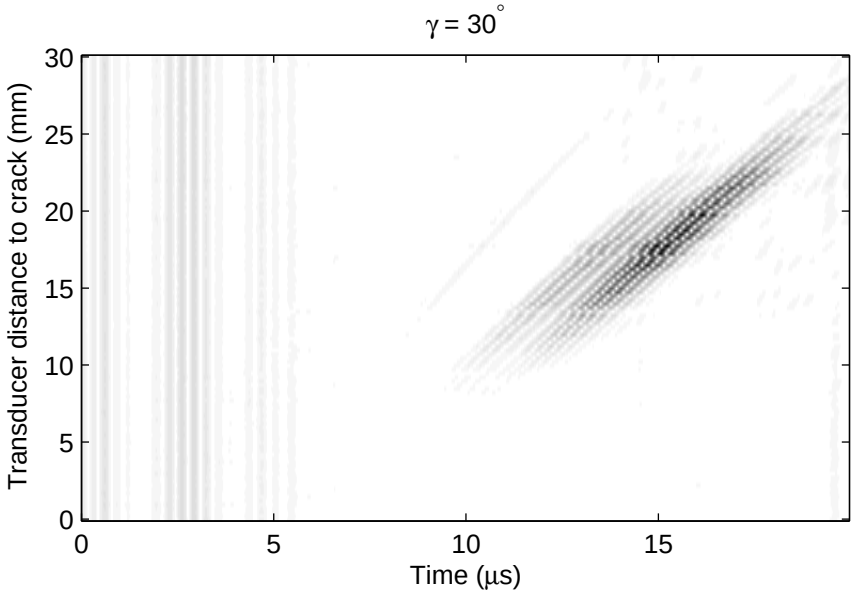

Figure 6.40: FE simulated B-scan of the specimen with a crack angle of 30°

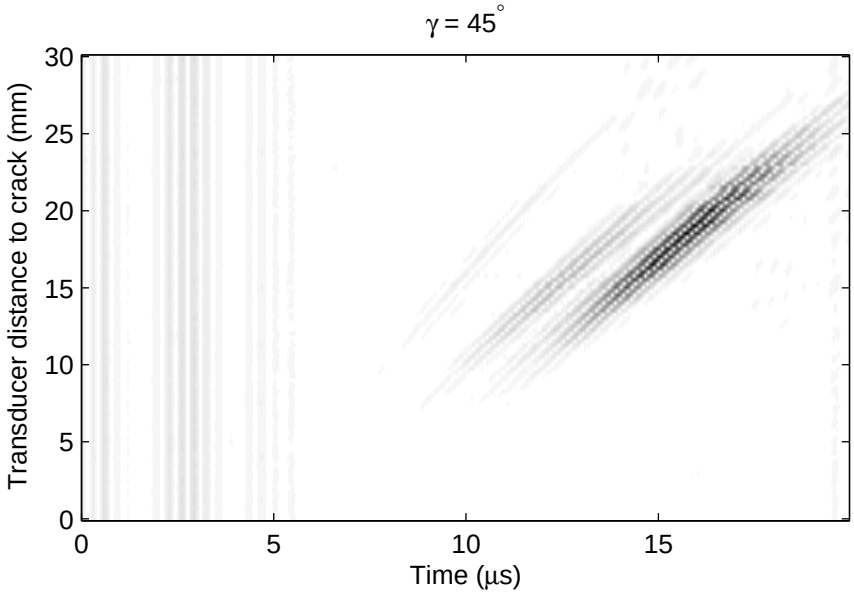

Figure 6.41: FE simulated B-scan of the specimen with a crack angle of 45°

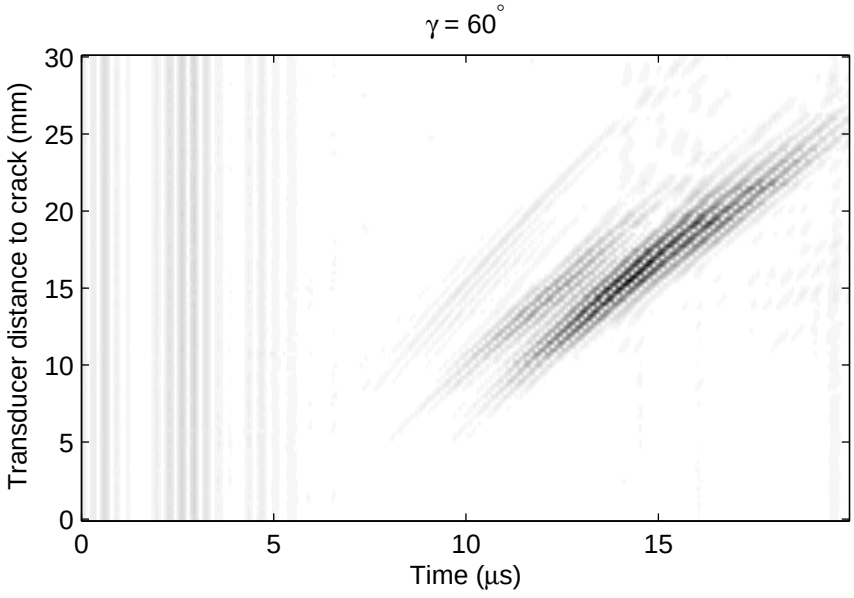

Figure 6.42: FE simulated B-scan of the specimen with a crack angle of 60°

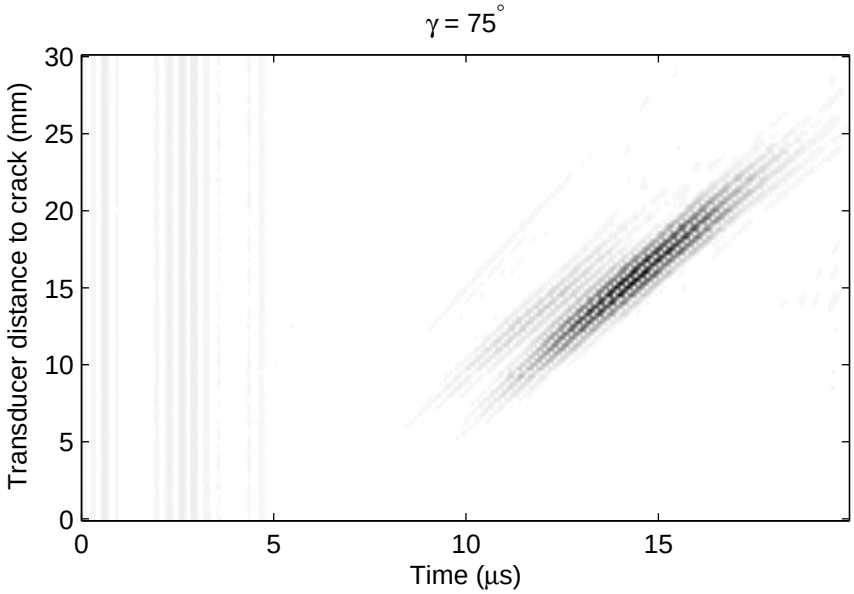

Figure 6.43: FE simulated B-scan of the specimen with a crack angle of 75°

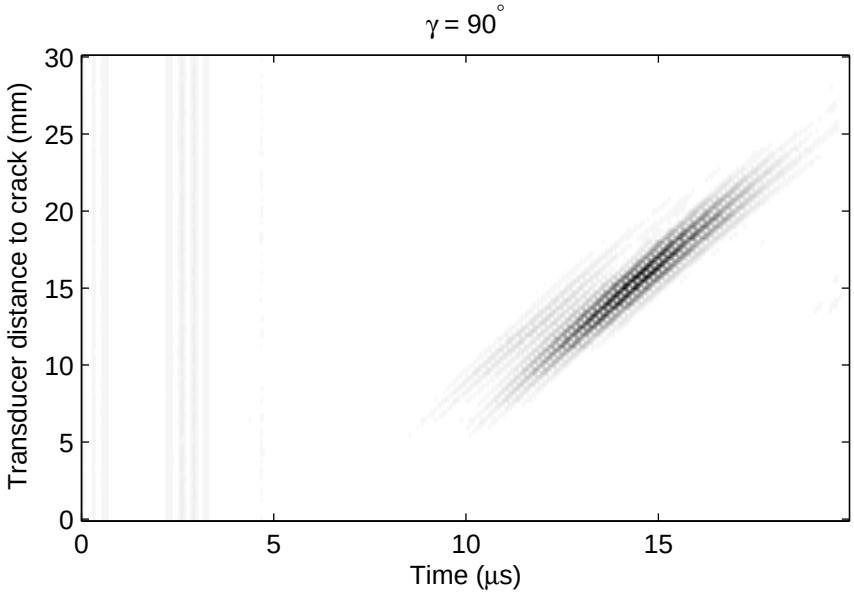

Figure 6.44: FE simulated B-scan of the specimen with a crack angle of 90°

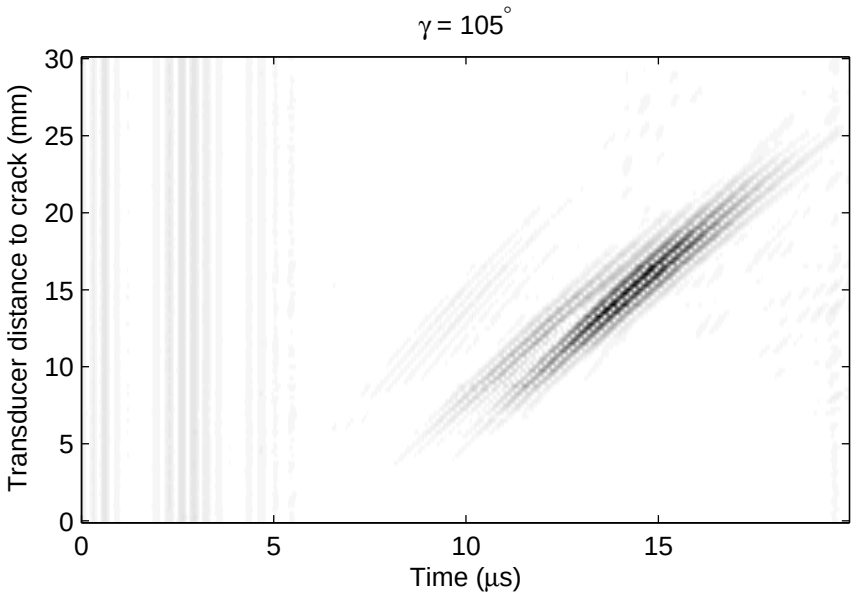

Figure 6.45: FE simulated B-scan of the specimen with a crack angle of 105°

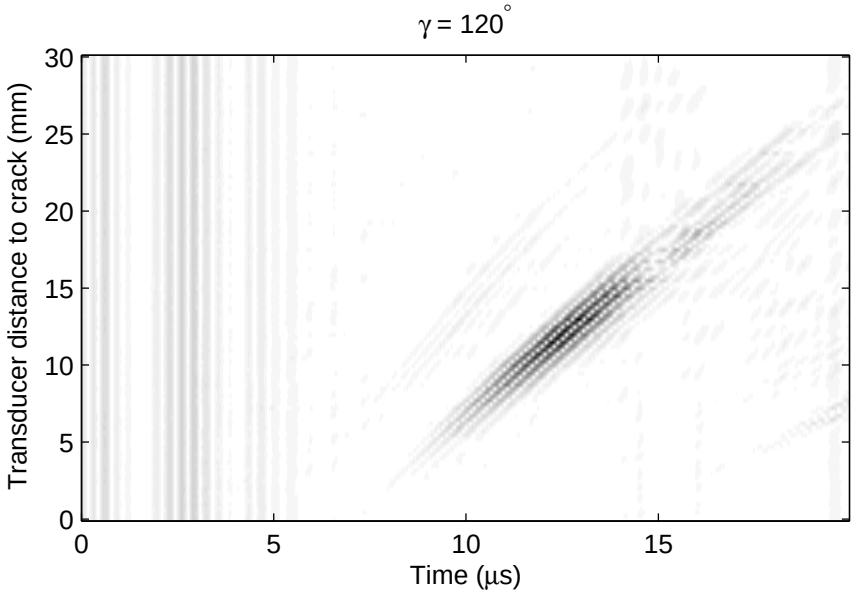

Figure 6.46: FE simulated B-scan of the specimen with a crack angle of 120°

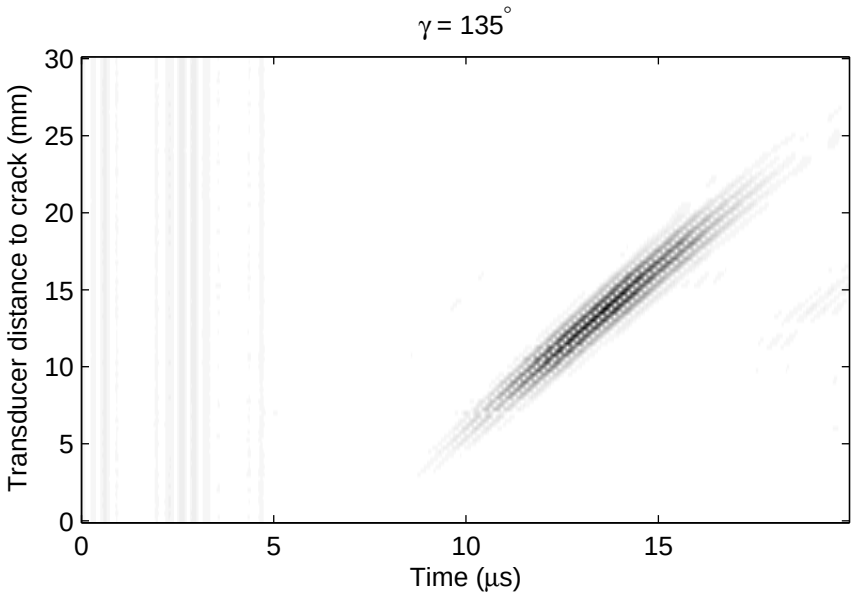

Figure 6.47: FE simulated B-scan of the specimen with a crack angle of 135°

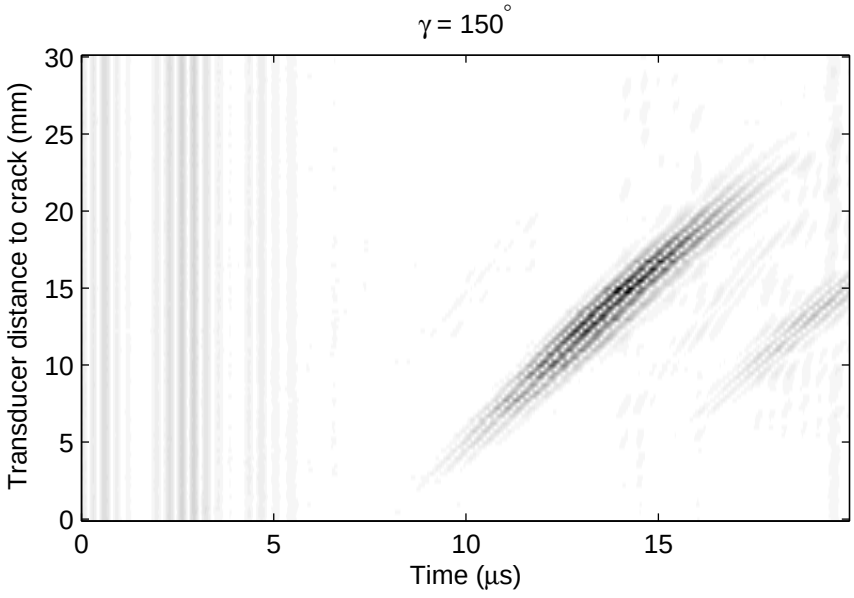

Figure 6.48: FE simulated B-scan of the specimen with a crack angle of 150°

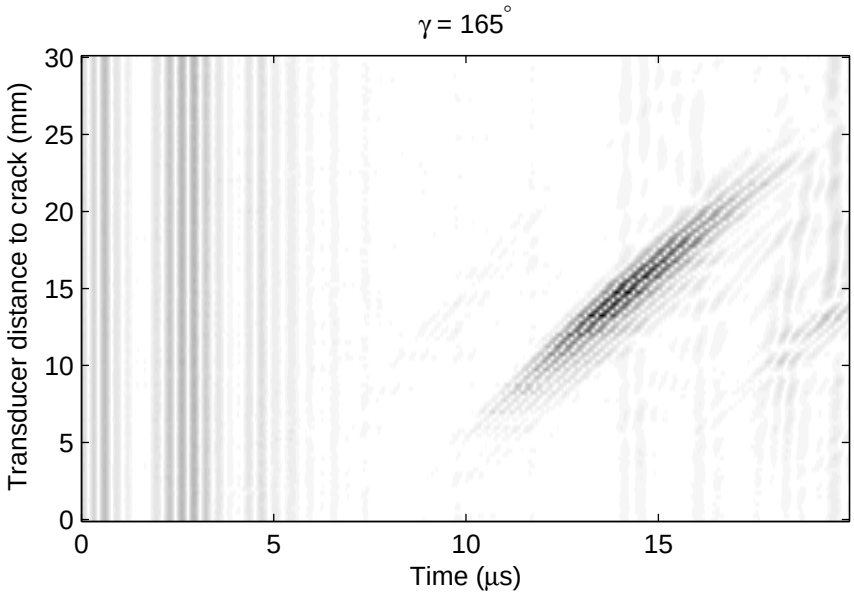

Figure 6.49: FE simulated B-scan of the specimen with a crack angle of 165°

6.3 Summary

The ultrasonic angle beam testing has been simulated using the finite element method. The selection of the proper parameters for the FE model has been investigated. By comparing to the experimental signals, it has been shown that the FE model with these selected parameters can accurately predict the TOF. This will serve our purpose in estimating crack depth and orientation from B-scan signal in Chapter 5. Yet, there are some deviation from the experimental signals which should be taken into account when analyzing the FE signals. The main deviations observed in the FE simulated signals, are the frequency downshift and increase in the pulse-width due to the numerical damping.

After validating the FE model, B-scan images have been simulated for cracks with different orientations. These simulated B-scans have been used in Chapter 5 for evaluation of the proposed method for estimating crack size and orientation.

Chapter 7

Experiments

In order to evaluate the performance of the denoising method proposed in Chapter 3, the parameter estimation method proposed in Chapter 4, and the crack size and orientation estimation method in Chapter 5, we have used the ultrasonic testing data available in the Reliability Research Lab at University of Alberta. Although the author of this thesis participated in conducting some of these experiments, the experiments were not designed or conducted as part of this thesis. The details of these experiments were documented in technical reports [1, 171, 172]. In addition, we have conducted two more experiments in this research program which are described in Section 7.1.4 and Section 7.1.5.

Pulse-echo and pitch-catch setups were used to collect experimental data. These two setups are widely used in ultrasonic fault detection and assessment. In both experimental setups, angle-beam shear waves were used for inspecting specimens on which surface cracks were approximated by creating a slot using electro-discharge machining (EDM). The angle of wedge is selected such that only the shear wave transmit into the test piece and the longitudinal wave reflects at the interface of the wedge and the specimen. This simplifies the interpretation of the received signal [173].

In the first set of experiments, pulse-echo setup was used to acquire B-scan images of specimens. On each specimen, a surface crack with the length ranging from 0.1mm to 3mm was introduced. The B-scan images acquired from this experimental setup allow us to evaluate the proposed two dimensional denoising method. In addition, the data from specimens with different crack lengths will be used to examine the effect of the crack length on the denoising and estimation results. A shorter crack length essentially results in a signal with a lower signal-to-noise ratio (SNR) and hence it influences the denoising and estimation results.

In addition to the data which was ready to use, we have designed two more

experiments. The first one is to examine the effect of the crack orientation on crack sizing. In the other experiment, we have scanned a specimen without a crack. In this case, a strong echo from the edge of the specimen is present in the received signal. Because the interpretation of the received signal is easier for this signal, we will use this signal for finite element model validation.

In the pulse-echo setup, when scanning the specimens, the crack was located on the far side (bottom surface). At least two echoes are expected to appear in the received signal when using this configuration: corner trap echo and tip diffraction echo [174]. Therefore, relative arrival time technique (RATT), which is used for crack sizing in this thesis, can be used in this configuration.

In the second set of experiments, pitch-catch setup was used to acquire A-scan signals. Due to lack of instruments to move two transducers together in a controlled manner, to send a pulse using one transducer and record the signal using the other one, no B-scan image was collected for this setup. The distance between two transducers was manually varied during the experiments. The energy level of the received signal depends on the distance between the two transducers. Therefore, signals with different SNR values are available from this setup. These data will be used to evaluate the performance of the parameter estimation method proposed in Chapter 4.

In the pitch-catch experiment, the objective is to receive the tip diffraction echo. Estimating the time of flight of this echo allows us to estimate the crack length. In this experiment, the crack was located on the top surface. Therefore, the time of flights of tip diffracted echo and backwall echo would be far enough to avoid overlap of these two echoes. Detecting a crack on the bottom surface using this setup is a challenging problem, because of the overlapping of the backwall echo with often a much weaker tip diffracted echo [175].

7.1 Pulse-echo setup

Ultrasonic pulse-echo is commonly used for fault detection as well as fault assessment. We have used experimental data collected using pulse-echo setup to test the proposed denoising method (Chapter 3) and parameter estimation method (Chapter 4) in this thesis.

7.1.1 Minimum temporal and spatial resolution

First, we will determine the necessary temporal and spatial resolution for the experiments. To avoid aliasing, the Nyquist frequency, which is half of the sampling frequency, should be higher than the maximum frequency of the sampled signal [176]. This gives the minimum temporal and spatial resolution which should be used in the experiment. Let $g(x,t)$ be the two-dimensional B-scan signal and $G(f_x, f_t)$ be its Fourier transform (FT). According to Nyquist-Shannon sampling theorem, the temporal sampling frequency, $f_{s,t}$, and the spatial sampling frequency, $f_{s,x}$, shall be selected to be at least twice the corresponding bandwidth of $G(f_x, f_t)$, i.e.

$$G(f_x, f_t) = 0, \;\; if \; |f_x| > \frac{f_{s,x}}{2} \; or \; |f_t| > \frac{f_{s,t}}{2}. \tag{7.1}$$

Let's recall from Section 2.4 that the 2D echo is modeled as

$$g(x,t) = e(x,t)cos(2\pi f_c(t - \tau(x)) + \phi) \tag{7.2}$$

where $e(x,t)$ is the envelope of echo and $\tau(x)$ is a linear function of x; that is $\tau(x) = ax + b$ where a and b are constants. Taking the FT of equation (7.2) gives

$$\begin{aligned} G(f_x, f_t) = &\frac{1}{2}E(f_x + af_c, f_t - f_c)exp(i(\phi - 2\pi f_c b)) \\ &+\frac{1}{2}E(f_x - af_c, f_t + f_c)exp(-i(\phi - 2\pi f_c b)), \end{aligned} \tag{7.3}$$

where $E(f_x, f_t)$ is the FT of $e(x,t)$.

In Section 2.4, the envelope of the echo, in turn, has been modeled as

$$e(x,t) = X(x)T(t - \tau(x)). \tag{7.4}$$

Taking the FT of equation (7.4), we obtain

$$E(f_x, f_t) = \overline{T}(f_t)\overline{X}(f_x + af_t)exp(-2\pi i f_t b) \tag{7.5}$$

where functions $\overline{T}$ and $\overline{X}$ are the Fourier transforms of T and X, respectively.

Inserting $G(f_x, f_t)$ from equation (7.3) into equation (7.1) gives,

$$E(f_x, f_t) = 0, \;\; if \; |f_x| > f_{s,x}/2 - af_c \; or \; |f_t| > f_{s,t}/2 - f_c. \tag{7.6}$$

Practically, it is reasonable to assume that $E(f_x, f_t) \approx 0$ in equation (7.6) if the power

of the component at (f_x, f_t) is smaller than the maximum power by at least M dB where $M \gg 0$. Thus, for a Gaussian echo we have,

$$\left|\frac{E(f_x, f_t)}{E(0,0)}\right| = \left|\frac{\overline{T}(f_t)}{\overline{T}(0)}\right| = exp(\frac{-(\pi f_t)^2}{\alpha_t}) < 10^{-M/20}. \tag{7.7}$$

After some algebraic manipulation we obtain,

$$min(f_{s,t}) = 2f_c + \frac{2}{\pi}\sqrt{\frac{M\alpha_t \ln 10}{20}}. \tag{7.8}$$

The frequency bandwidth of the transducer used in the pulse-echo experiment was 1.5 MHz, hence $\alpha_t = 16$ $(\text{MHz})^2$. For $M = 20$ the minimum sampling frequency is 8.4 MHz which is well below the sampling frequency of 100 MHz used in the experiment.

Let X(x) be a Gaussian function as well, then for the minimum spatial step size, we have,

$$\left|\frac{E(f_x, f_t)}{E(0,0)}\right| = \left|\frac{\overline{T}(f_t)\overline{X}(f_x + af_t)}{\overline{T}(0)\overline{X}(0)}\right| = exp(-\pi^2(\frac{f_t^2}{\alpha_t} + \frac{(f_x + af_t)^2}{\alpha_x})) < 10^{-M/20}. \tag{7.9}$$

For a given $f_{s,x}$, the condition expressed in equation (7.9) should hold for all values of f_t. This can be achieved by maximizing $E(f_x, f_t)/E(0,0)$ with respect to f_t. Letting partial derivative of $E(f_x, f_t)/E(0,0)$ with respect to f_t equal to zero results in,

$$\frac{E(f_x, f_t)}{E(0,0)} = exp(\frac{-(\pi f_x)^2}{a^2\alpha_t + \alpha_x}) < 10^{-M/20}. \tag{7.10}$$

Finally, after some algebraic manipulation we obtain

$$min(f_{s,x}) = 2af_c + \frac{2}{\pi}\sqrt{\frac{M \ln 10}{20}(a^2\alpha_t + \alpha_x)}. \tag{7.11}$$

The value of α_x is approximated by curve fitting for different slot sizes from 0.1 mm to 3 mm. Figure 2.17 depicts the curve fitting results for a specimen with a 3mm slot. By performing curve fitting using the experimental data from specimens with slot lengths from 0.1 mm to 3 mm we have found the maximum value of α_x to be $0.04\, mm^{-2}$. From equation (2.31) a is determined to be $0.438\mu\ s/mm$ and M is assumed to be 20. Substituting these parameter values in equation (7.11) gives a minimum spatial sampling frequency of $3.7mm^{-1}$ or a maximum step size of 0.27 mm; this is slightly larger than the 0.25 mm step size used in the pulse-echo experiment.

7.1.2 Instrumentation

Figure 7.1 illustrates the schematic of the experimental setup and Figure 7.2 shows pictures of the experimental setup. The test setup consists of Omniscan data acquisition system, Bi-slide positioning system, VXM stepping motor controller and a PC on which COSMOS software is installed. The COSMOS is used to program the bi-slide movement through the stepping motor controller. The Bi-slide system allows automated and accurate positioning of the ultrasonic transducer on the specimen. When the Bi-slide moves the transducer to a new position, the stepping motor controller also sends a pulse to Omniscan to trigger acquiring ultrasonic signal at the new transducer position. The transducer is Krautkramer, Benchmark Series, miniature angle beam transducer, 2.25MHz center frequency, 1.5 MHz bandwidth, and 0.5" element diameter. The wedge used in this experiment has a standard refracted shear wave angle of 45° in steel.

The transducer was moved linearly along the specimen to obtain a B-scan. At every step, 2048 data points were collected at a sampling frequency of 100 MHz. Each of these recorded data constitutes an A-scan. By each movement of the stepper motor, a pulse was also sent to the Omniscan to indicate the transducer position. Finally, a B-scan was produced consisting of A-scans collected at points along the scan line.

7.1.3 Specimens with different crack lengths

In this experiment, nine 4140-steel specimens (185mm x 40 mm x 16 mm) were tested. Figure 7.3 illustrates the test specimen dimensions. The nine specimens had nominal slot lengths of 0 mm, 0.1 mm, 0.3 mm, 0.5 mm, 1 mm, 1.5 mm, 2 mm, 2.5 mm and 3 mm, respectively. The length of each EDM cut was 40 mm (each cut was a full length cut along the width of specimens). Table 7.1 presents the actual length and width of specimens measured using a microscope [172].

Figure 7.4 illustrates the scanning span for this experiment. The positioning system was programmed to linearly move the transducer for a distance of 30 mm with a step size of 0.25 mm. The starting position of the transducer was at 30 mm distance, measured from the probe beam index to the EDM slot. All experiments were repeated three times to ensure the repeatability of data.

The gain level of input voltage to the transducers were varied from 5 dB to 60 dB with an increment size of 2.5 dB. This gain value was applied to the input signal. A smaller gain level leads to a weaker pulse and hence a weaker signal which in

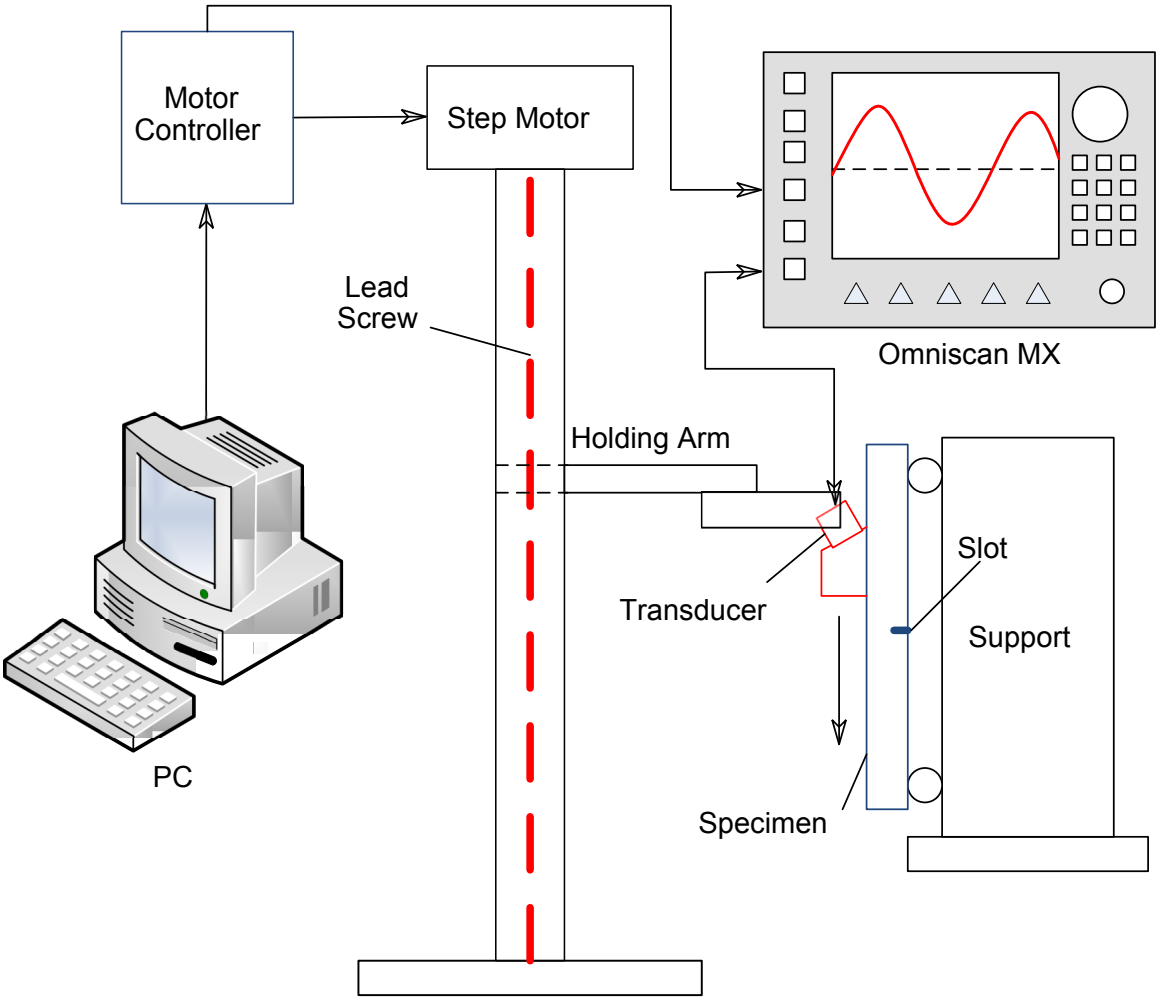

Figure 7.1: Schematic of the ultrasonic pulse-echo testing using Bi-slide [1]

Figure 7.2: Ultrasonic pulse-echo testing using Bi-slide [1]

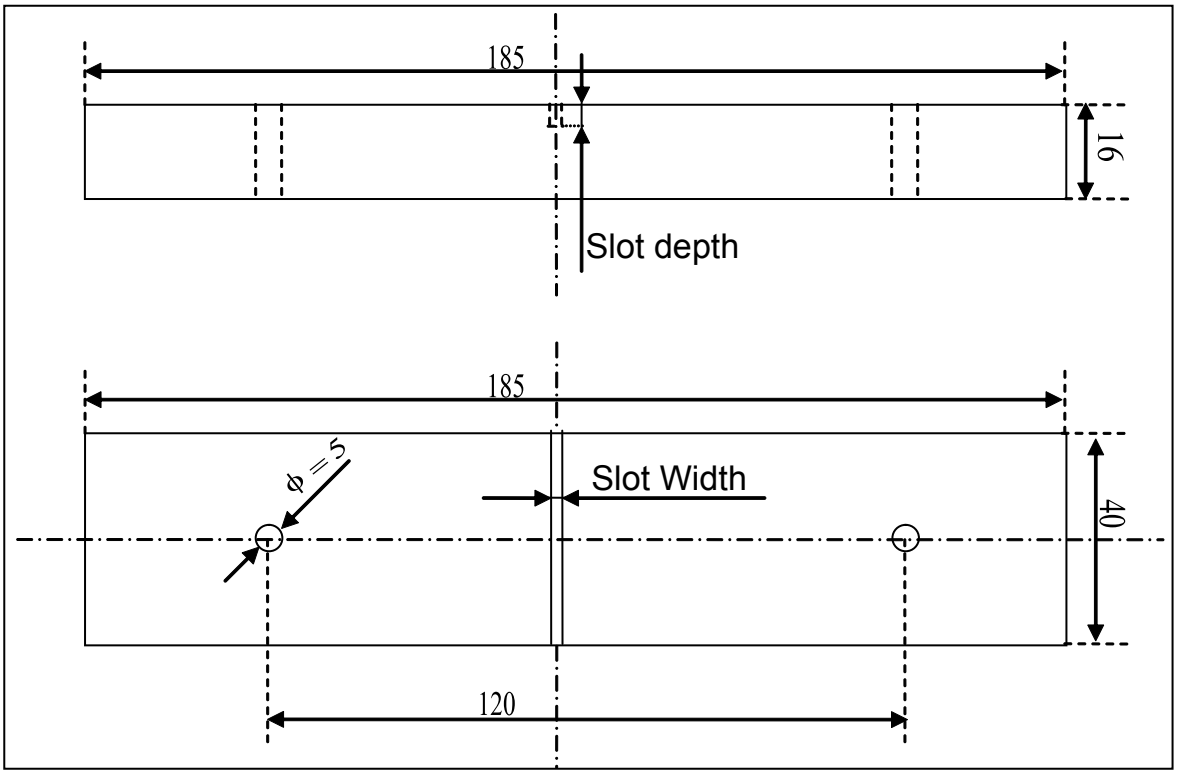

Figure 7.3: Specimen dimensions

Table 7.1: The length and width of the slots cut on the specimens (mm)

Nominal length	Measured length	Measured Width
0.1	0.112	0.171
0.3	0.281	0.168
0.5	0.502	0.193
1	1.021	0.189
1.5	1.519	0.192
2	2.032	0.217
2.5	2.548	0.203
3	3.056	0.208

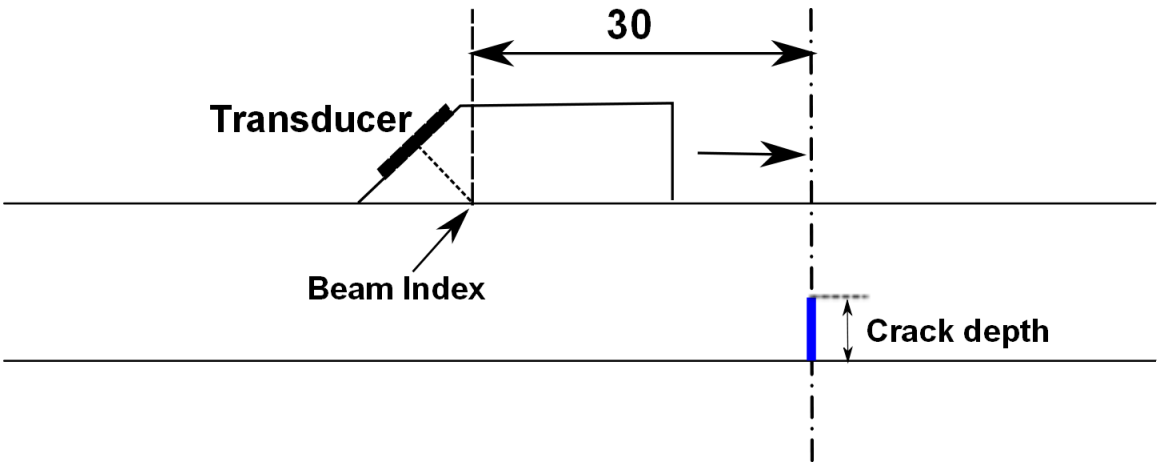

Figure 7.4: The scanning span

turn results in lower signal-to-noise ratio. However, greater gain levels may lead to acoustic saturation of the transducer [177] and/or over-range values. Acoustic saturation occurs when the ultrasonic transducer is excited with a signal beyond the transducer's dynamic range in which transducer has a linear behavior. Over-range values occur when the signal received by the transducer is not recorded properly when the signal is digitized. This is called data clipping. Therefore, it is not uncommon to see either low SNR for a small crack or a distorted signal for a large crack.

Figures 7.5-7.13 depict the B-scan images obtained at a gain level of 40 dB from the specimens with different crack lengths. In each plot, the horizontal axis represents time and the vertical axis represents the transducer position. The origin of the time axis is set at the moment when a predetermined waiting time, the wedge delay, is elapsed after triggering the input signal. The wedge delay is determined through a calibration process which establishes a zero position for the entry surface of the test piece. The calibration is performed using an OmniScan® unit as specified in Ref. [178]. The transducer position is measured from the beam index to the crack location as shown in Figure 7.4.

As can be seen in Figure 7.5, when there was no slot in the specimen, the only echoes in the received signal were those reflected at the interface of the wedge and the specimen due to mismatch of the acoustic impedances. These echoes are called wedge echo. The amplitude and the time of flight of these echoes were almost constant in all A-scans within the B-scan image and did not change as transducer moves along the specimen. Therefore, they appeared as vertical lines in the B-scan image.

In Figure 7.6, for a specimen with 0.1 mm slot, there was also another echo which was reflected from the corner of the slot. This echo becomes much stronger compared

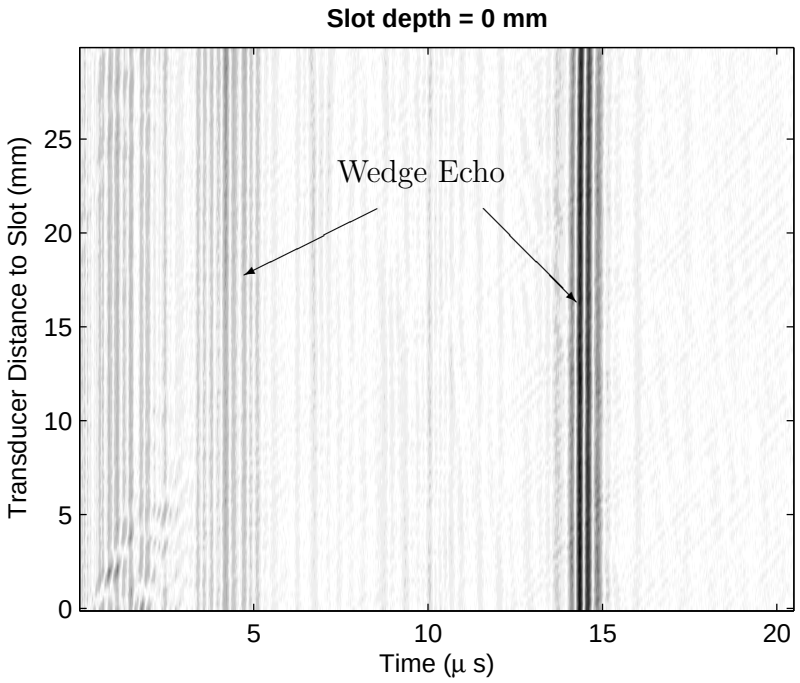

Figure 7.5: B-scan image of a specimen with no slot, Gain level: 40 dB

with the wedge echo for longer slots as shown in Figures 7.9-7.13. For example, as can be seen in Figure 7.13, for a 3 mm crack the amplitude of the corner trap echo was much greater than that of wedge echo. There was also another echo marked in Figure 7.13 as tip diffraction echo. This echo arrived earlier than the corner trap echo and was diffracted from the tip of crack. This echo is hardly evident in the B-scan images of smaller cracks such as 0.1 mm and 0.3 mm crack cases. Comparing the B-scans for different crack sizes shows that the echoes are stronger for longer cracks as more waves are reflected from a longer crack.

Figures 7.14 and 7.15 depict the 3D plots of the B-scan of specimen with slot lengths of 0.5 mm and 3 mm. It can be observed that some data for the 3 mm slot were clipped but for 0.5 mm slot no data was clipped (the maximum value for this data acquisition system is 128).

7.1.4 Specimens with different crack orientations

In addition to the aforementioned experimental data which were available in the Reliability Research Lab, we have designed and conducted an experiment to study the effect of the crack orientation on the parameter estimation results. This experiment is described in this section.

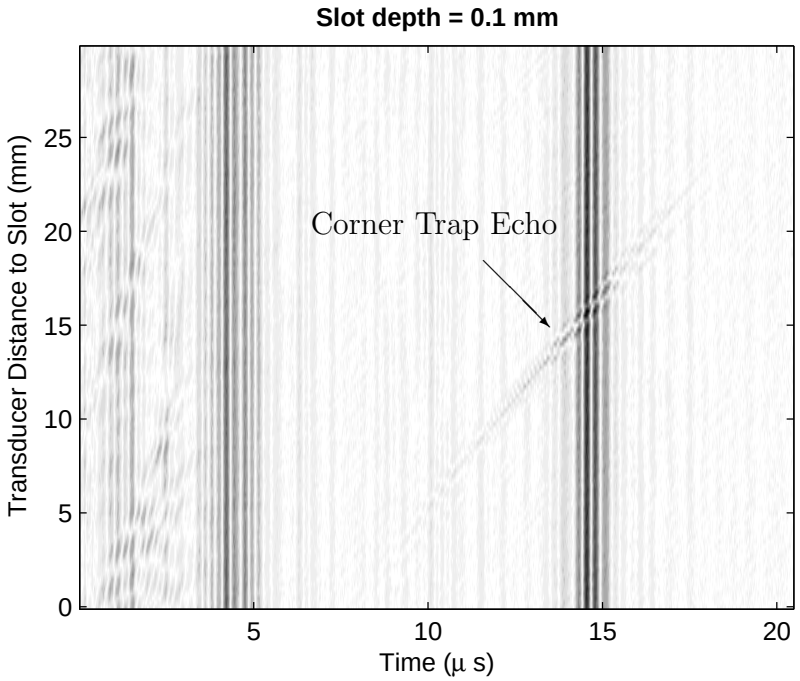

Figure 7.6: B-scan of a specimen with a slot length of 0.1 mm, Gain level: 40 dB

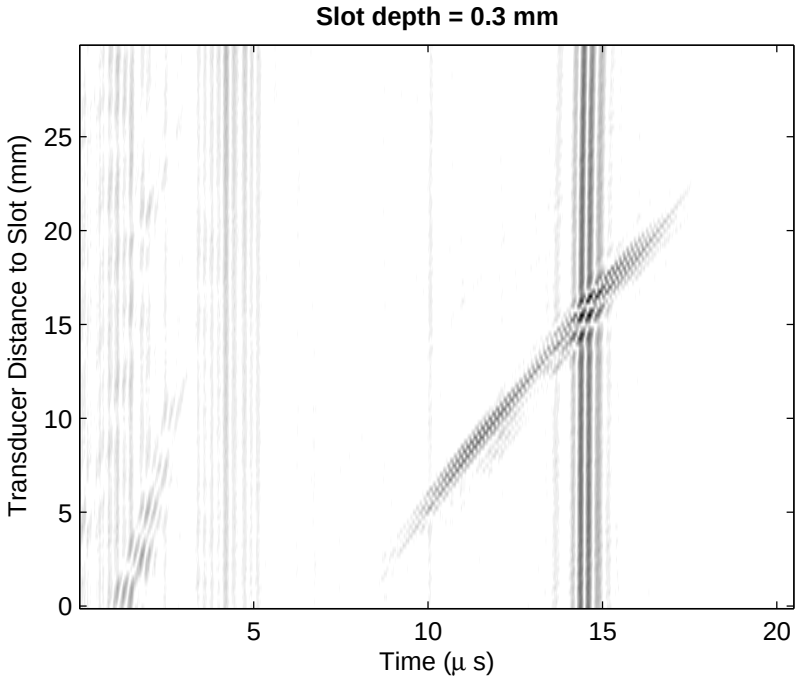

Figure 7.7: B-scan of a specimen with a slot length of 0.3 mm, Gain level 40 dB

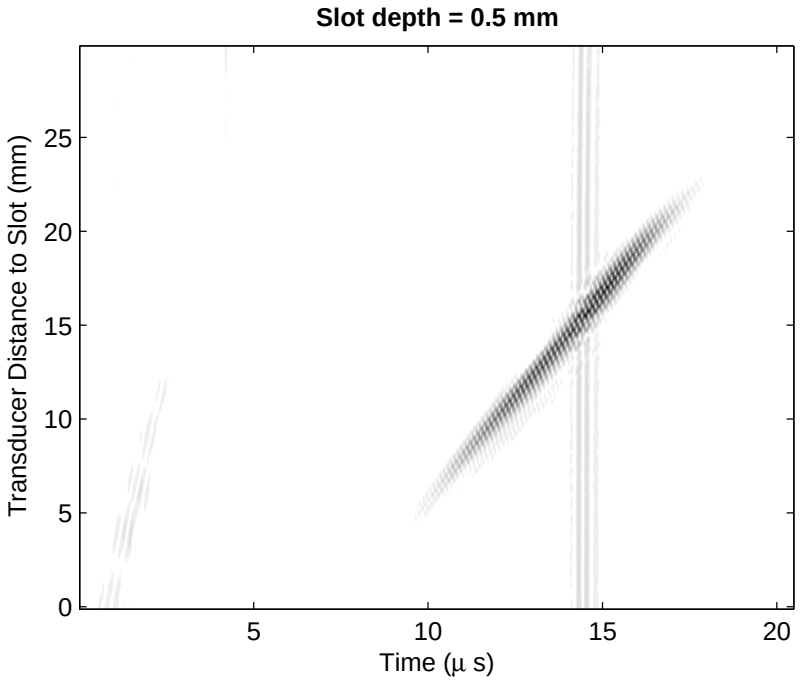

Figure 7.8: B-scan of a specimen with a slot length of 0.5 mm, Gain level: 40 dB

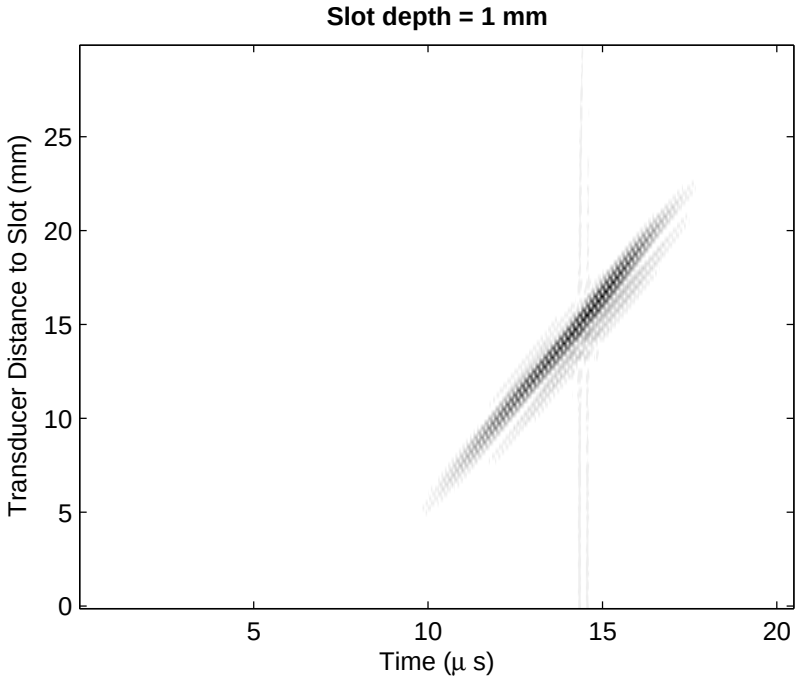

Figure 7.9: B-scan of a specimen with a slot length of 1 mm, Gain level: 40 dB

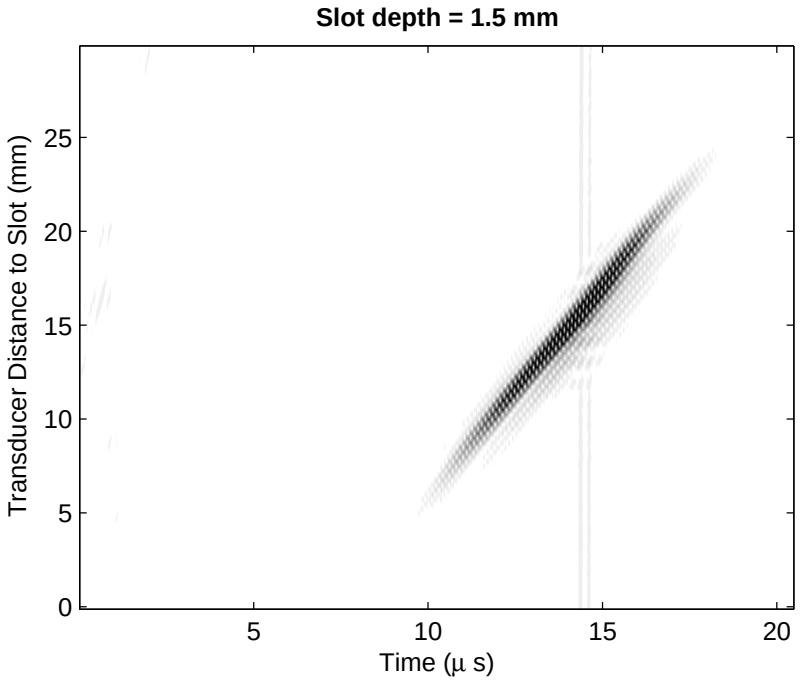

Figure 7.10: B-scan of a specimen with a slot length of 1.5 mm, Gain level: 40 dB

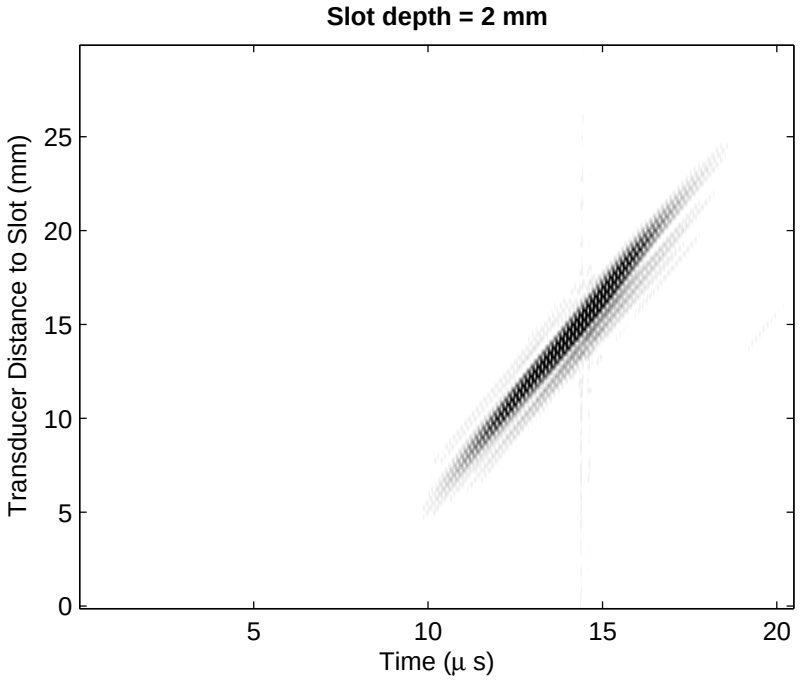

Figure 7.11: B-scan of a specimen with a slot length of 2 mm, Gain level: 40 dB

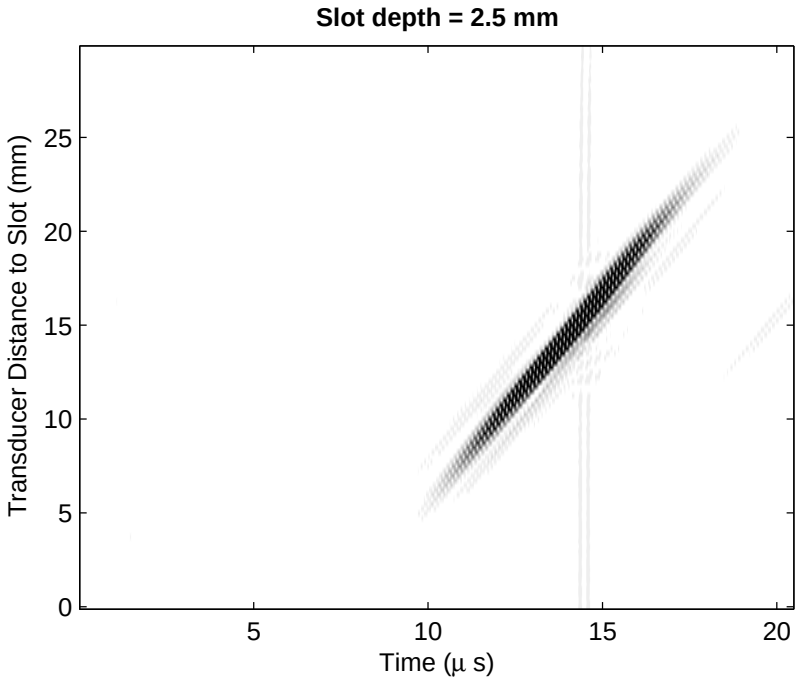

Figure 7.12: B-scan of a specimen with a slot length of 2.5 mm, Gain level: 40 dB

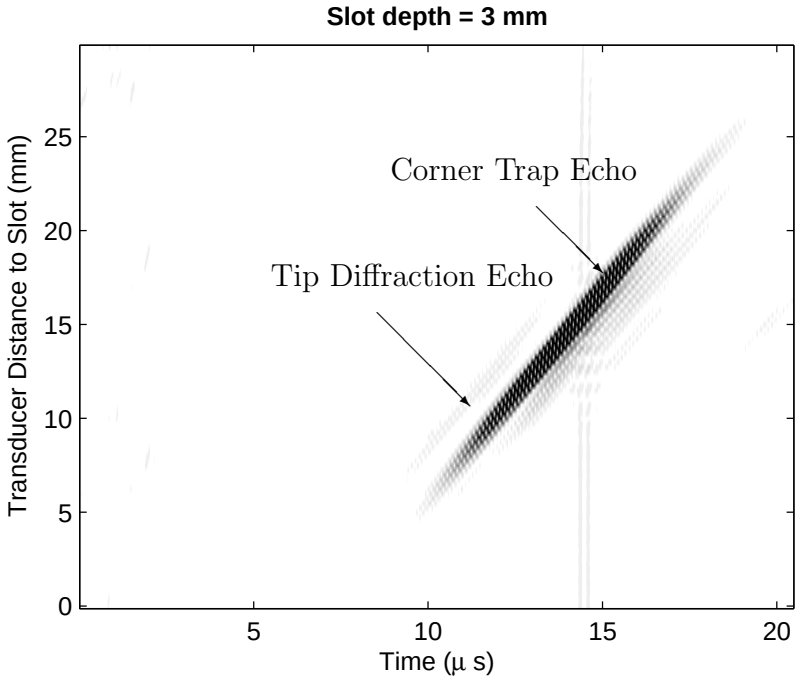

Figure 7.13: B-scan of a specimen with a slot length of 3 mm, Gain level: 40 dB

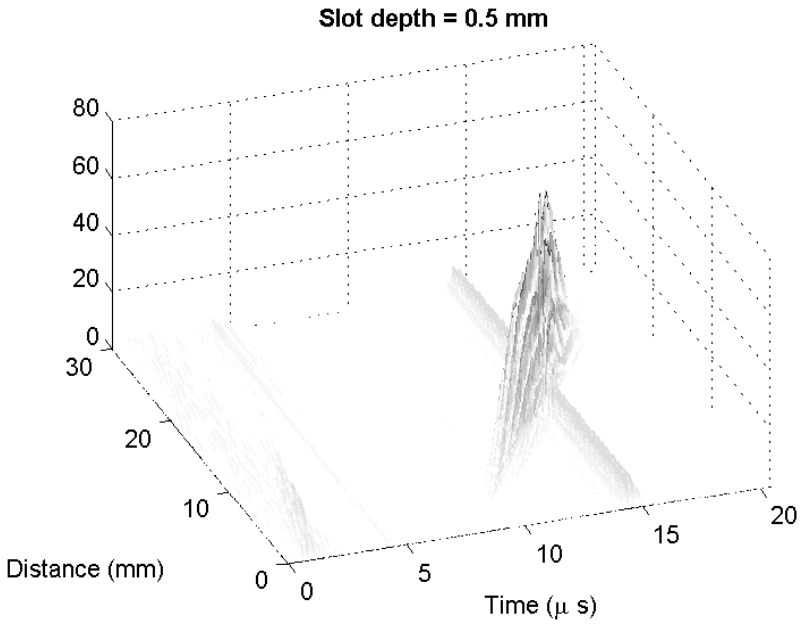

Figure 7.14: 3D B-scan plot of a specimen with a slot length of 0.5 mm, Gain level: 40 dB

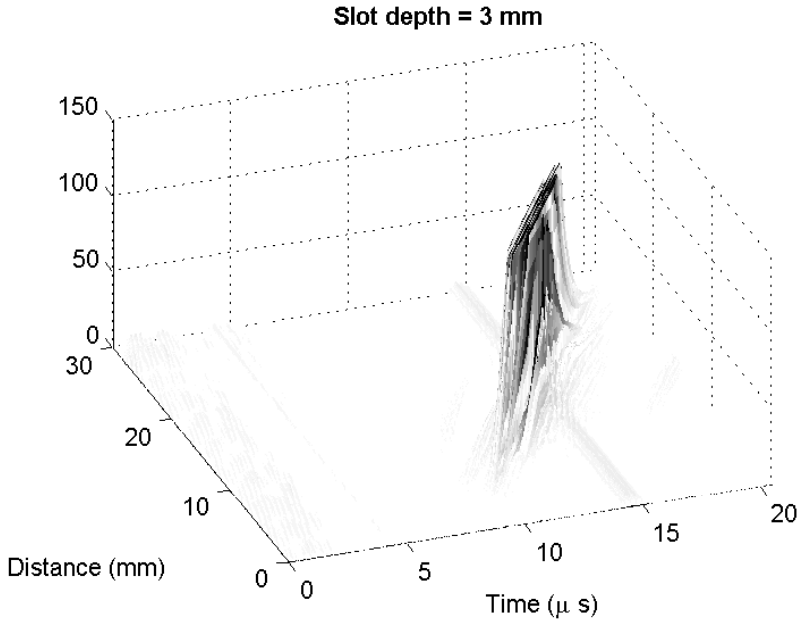

Figure 7.15: 3D B-scan plot of a specimen with a slot length of 3 mm, Gain level: 40 dB

In the middle of one 4140-steel specimen (185 mm x 40 mm x 16 mm) two slots with angles of 30 degrees and 60 degrees and length of 3 mm were created at two sides of the specimen using EDM. Figure 7.16 shows the specimen drawing and Figure 7.17 illustrates the ultrasonic scanning span. The experiment was conducted at the following crack angles: $30°, 60°, 120°$ and $150°$ (total of four sets of data). This was achieved by scanning the top surface and bottom surface of the specimen in two opposite directions. For example, scanning the $30°$ in one direction results in $30°$ dataset and scanning in the opposite direction results in $150°$ dataset. It would be insightful if the experiment is carried out for $45°$ and $135°$ in future studies as these two angles represent special cases at which the waves are either parallel or perpendicular to the crack. The experiment was conducted for gain levels of 30 dB, 40 dB, 50 dB and 60 dB. Combined with the data for 3mm slot at $90°$, which was explained in Sec. 7.1.3, there are data available for every $30°$ from $30°$ to $150°$ slot angle.

Figures 7.18-7.21 show the B-scan images for slot angles of $30°, 60°, 120°$ and $150°$. Generally, these figures resemble those of the $90°$ crack, yet there are some major differences. A major difference is that there are some extra echoes mostly within the first 5 μs of the B-scans. These echoes were generated by the crack on the top surface.

In this study, we consider only echoes reflected from the crack on the bottom surface. Since the echoes from the two cracks on the top and bottom surfaces did not overlap, they can be easily separated. The echoes from the crack on the top surface were located within the first 5 μs, while the echoes from the bottom surface did not appear till about 8 μs. For this reason, we can ignore the interactions between the two cracks.

7.1.5 Specimen without any crack

In order to validate the finite element model in Chapter 6, we have designed an experiment with a specimen without a crack. Since our objective is to evaluate the accuracy of the finite element analysis for proper selection of time step and element size, the experiment has been designed such that the received signal can be easily interpreted. This can be achieved by testing a specimen with no crack. The received signal for this experiment contains a clear strong echo from the edge of specimen.

Figure 7.22 shows the geometry of the specimen. The sampling frequency of 50 MHz was chosen for this experiment. The reason of selection of a smaller sampling frequency for this experiment is to collect data for a longer time - the total number of sampled data is fixed in the OmniScan software - as the height of specimen is larger

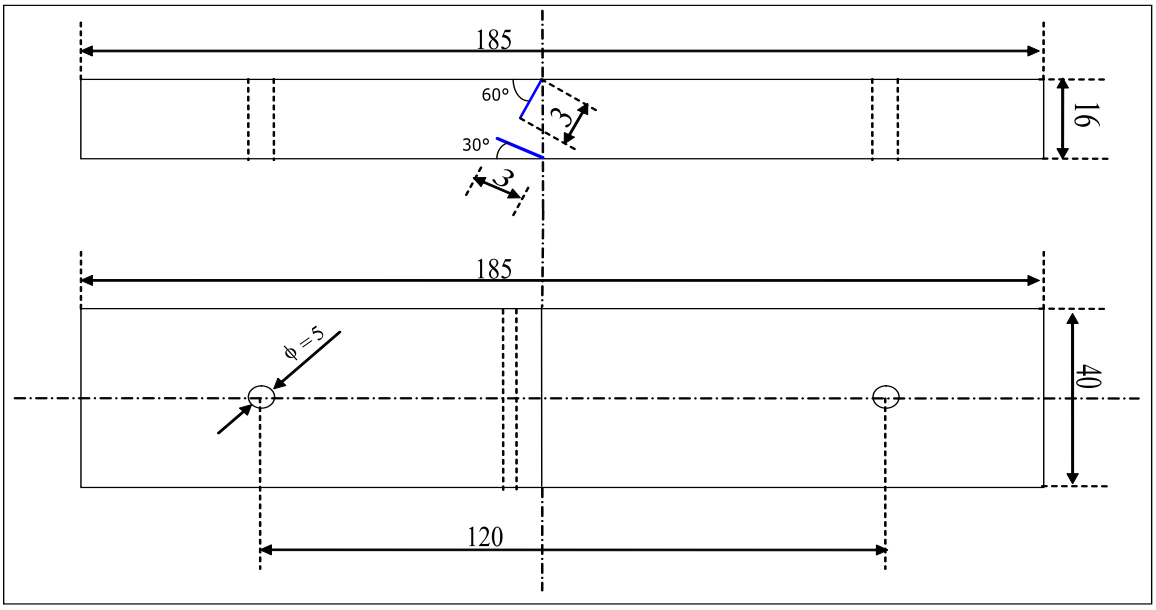

Figure 7.16: Specimen dimensions, all dimensions are in mm

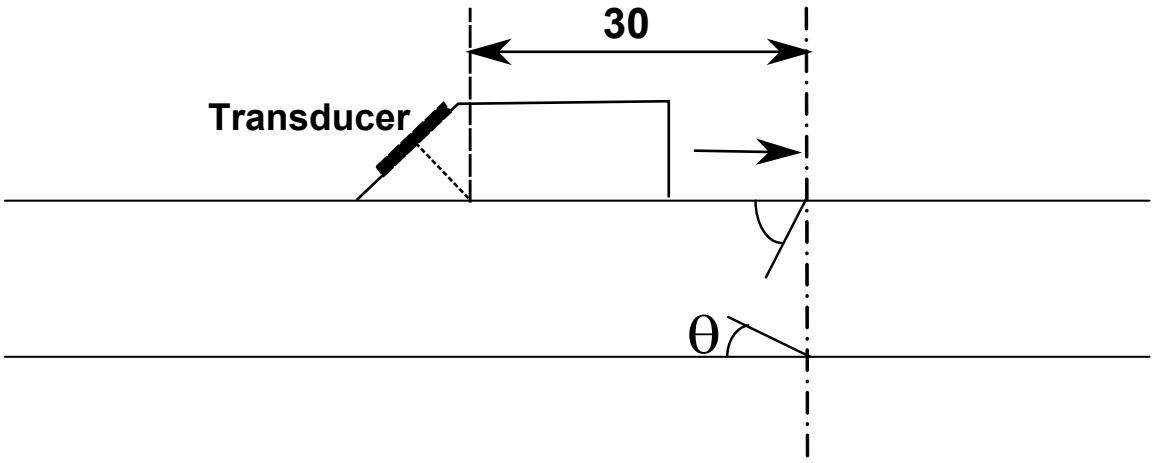

Figure 7.17: The scanning span

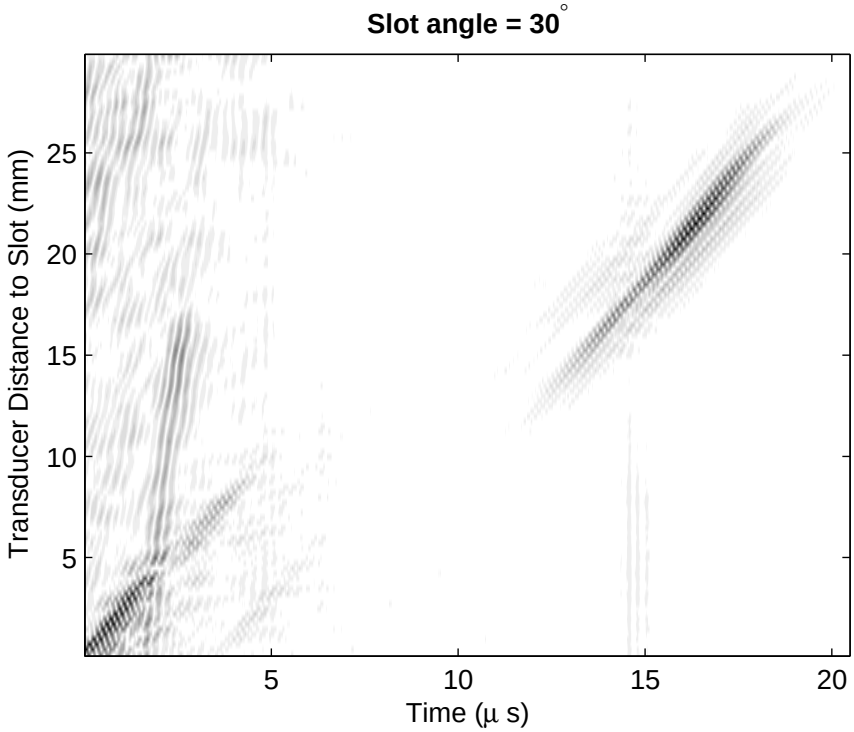

Figure 7.18: B-scan image of the specimen with a slot angle of 30°

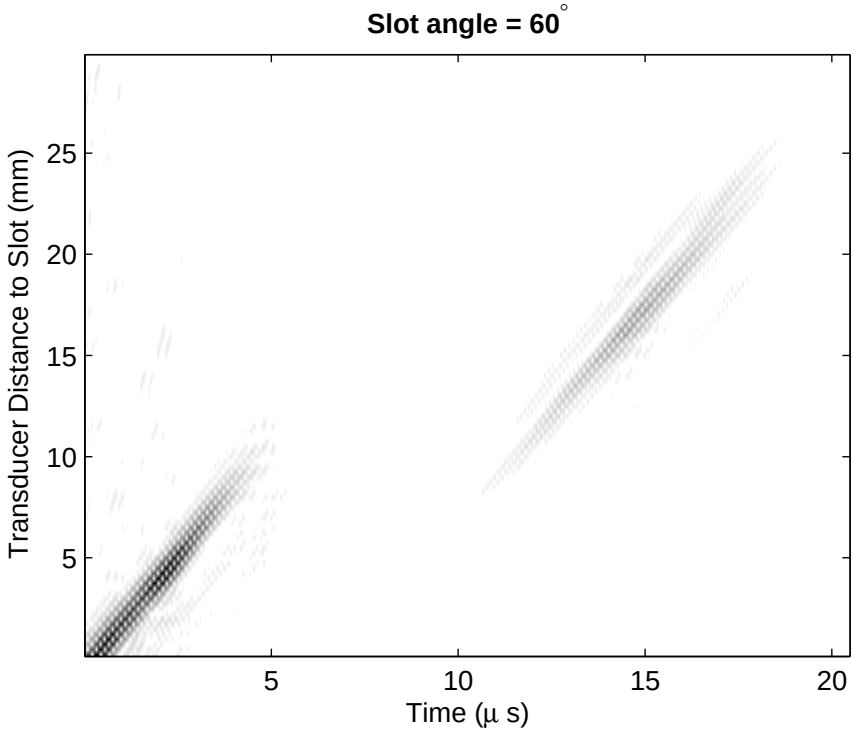

Figure 7.19: B-scan image of the specimen with a slot angle of 60°

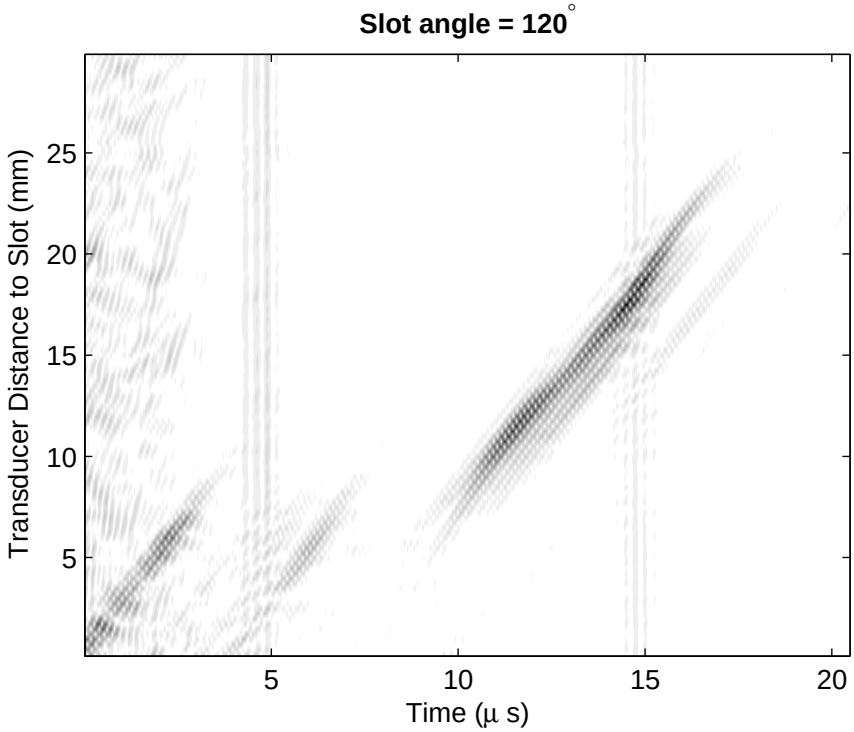

Figure 7.20: B-scan image of the specimen with a slot angle of 120°

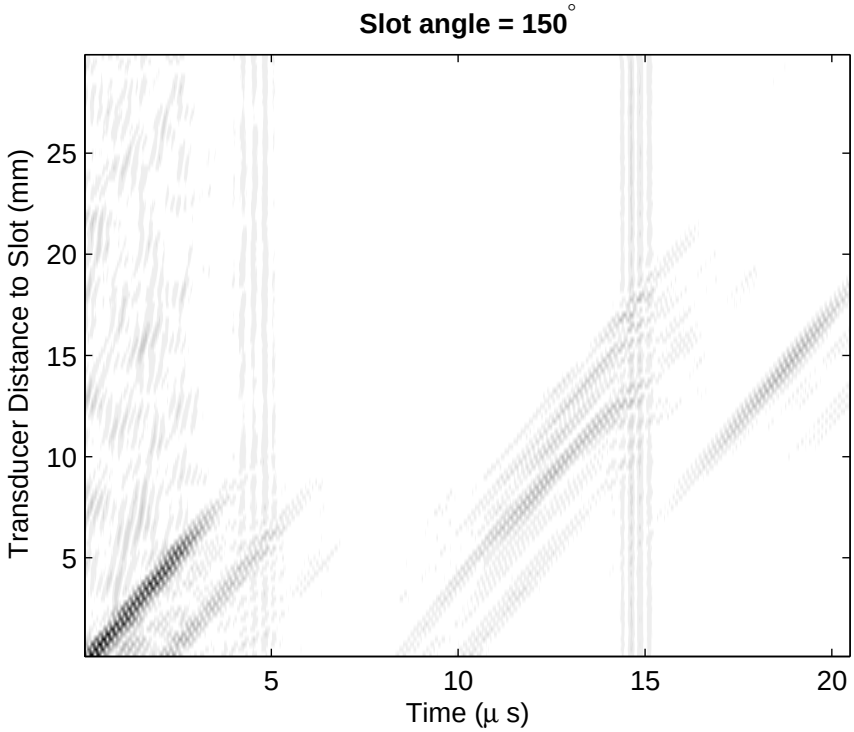

Figure 7.21: B-scan image of the specimen with a slot angle of 150°

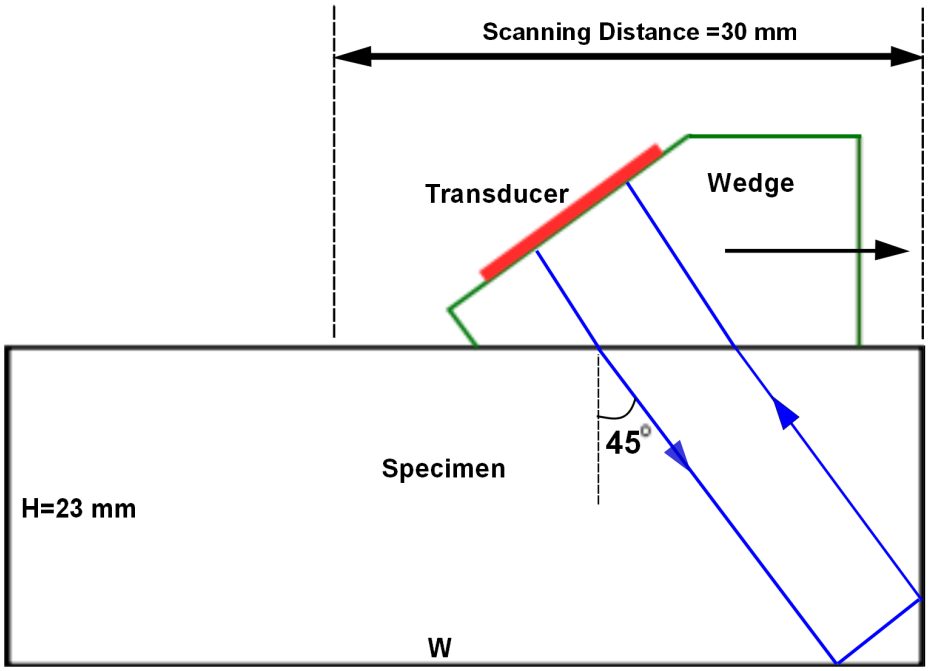

Figure 7.22: Specimen Geometry

than the specimens used in two previous set of experiments. The transducer was moved for a distance of 30 mm with a step size of 0.25 mm. The starting position of the transducer was at 30 mm distance, measured from the near edge of the wedge to the edge of the specimen. The distance between the near edge of the wedge and probe index is 12.8 mm so the scanning span was 42.8 mm - 12.8 mm from the probe index to the edge of the specimen. All other settings are similar to the experiment explained in Section 7.1.3.

Figure 7.23 shows an example of B-scan image collected in this experiment. Two echoes can be observed in this image. The first echo is the one reflected from the corner of the specimen. The second echo is due to double reflection as shown in Figure 7.24. The time of arrival of these two echoes can be used to confirm their sources.

Figure 7.25 shows an A-scan recorded at the distance of 10 mm. The time of arrival is obtained from the envelope's peak. Therefore, the length of the source of the first echo can be calculated as,

$$h = \frac{v\tau}{2\cos\theta} - x\tan\theta = \frac{3.229 \times 20.06}{2\cos 45} - 22.8\tan 45 = 23.00mm \tag{7.12}$$

where $v = 3.229mm/\mu s$ is the shear wave velocity, $\tau = 20.06\mu s$ is the time of arrival, $\theta = 45°$ is the refraction angle and $x = 10 + 12.8 = 22.8mm$ is the distance from the probe index to the specimen's edge. The estimated length of the source of the

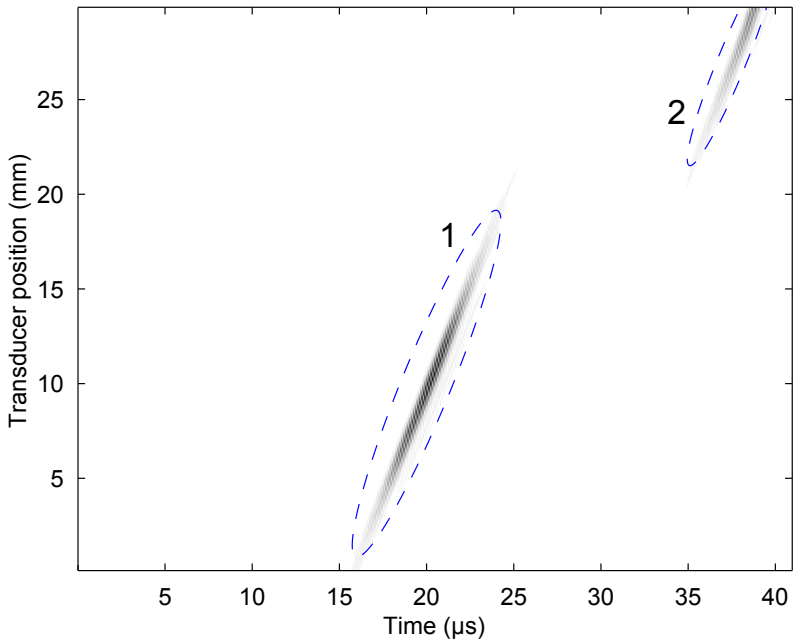

Figure 7.23: B-scan image of a specimen with no crack, Gain level = 25dB

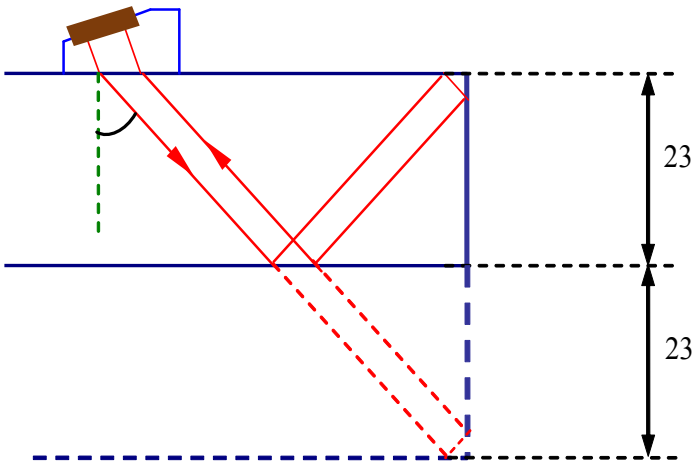

Figure 7.24: Schematic of the double reflected echo

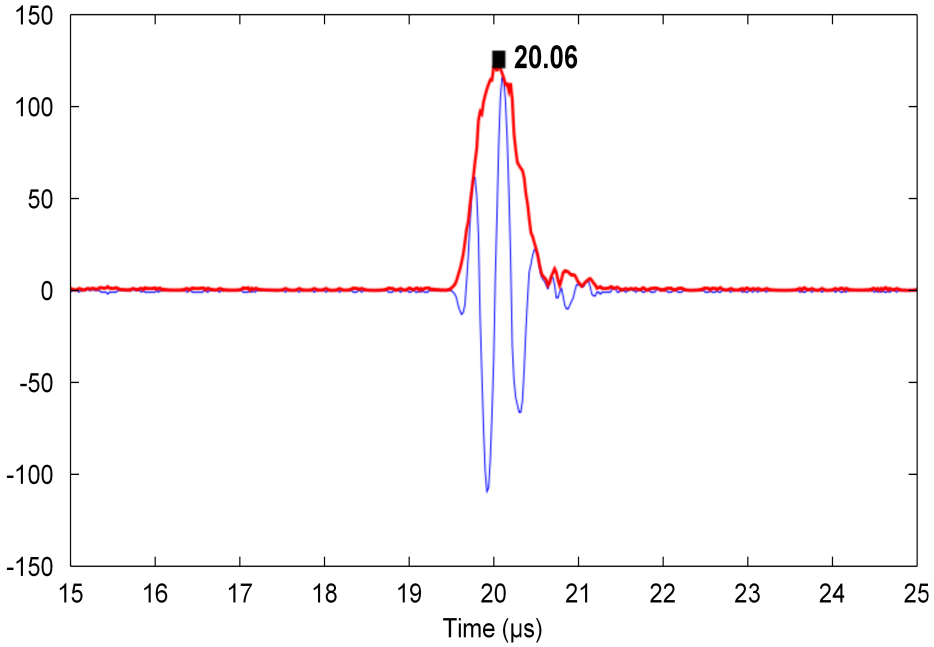

Figure 7.25: A-scan of a specimen with no crack, Gain level = 25dB, the distance from the near edge of the wedge to the edge of specimen = 10 mm

first echo is equal to the height of the specimen. This confirms that the first echo is reflected from the corner of the specimen. The length of the second echo can be estimated in the same way. The time of arrival is estimated to be $38.74\mu s$ when the transducer was positioned $30mm$ apart from the specimen edge. Therefore, the length of the second echo's source is

$$h = \frac{3.229 \times 38.74}{2\cos 45} - 42.8\tan 45 = 45.65mm. \tag{7.13}$$

The value of h obtained here is almost equal to $46mm(= 2 \times 23mm)$. As shown in Figure 7.24, this time of arrival corresponds to the double reflection.

7.2 Pitch-catch setup

Time of flight diffraction is widely used in practice for crack sizing [14]. TOFD utilizes ultrasonic pitch-catch setup. This method estimates the crack size using the time of flights of the echoes diffracted from the crack tips. Therefore, we have used the data from a pitch-catch experiment to assess the reliability of our proposed parameter estimation method in Chapter 4.

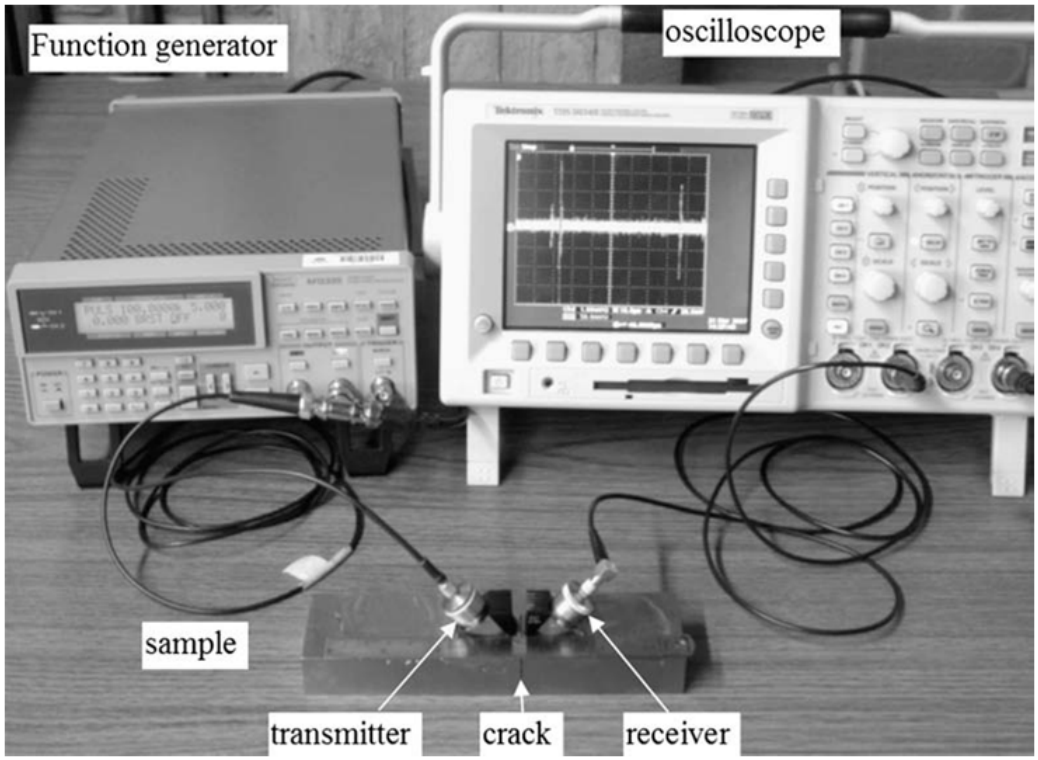

Figure 7.26: Pitch-Catch test setup

7.2.1 Instrumentation

Figure 7.26 shows the pitch-catch arrangement used in this experiment. Figure 2.10 depicts the schematic of the experimental setup. As indicated in Figure 2.10, $2s'$ denotes the distance between the front faces of the two wedges, $2s$ the distance between the beam index locations of the two transducers, H the thickness of the specimen, and d the length of the simulated crack. The location of the transducer beam index is marked on the wedge by the manufacturer. The front face of wedge used in our experiment is 12.8 mm from the transducer beam index; thus,

$$2s = 2s' + 25.6 \text{ (mm)}. \tag{7.14}$$

The transducer is a Krautkramer, Benchmark Series, miniature angle beam transducer, with a center frequency of 2.25MHz, a bandwidth of 1.5 MHz, and a diameter of 0.5". A GE Inspection Technologies W-211 model Lucite wedge was used in this experiment which has a standard refracted shear wave angle of 45° in steel. The specimen was made of mild steel. An AFG320 function generator and a TDS3000 series oscilloscope were used in the experiment. The function generator was set to generate

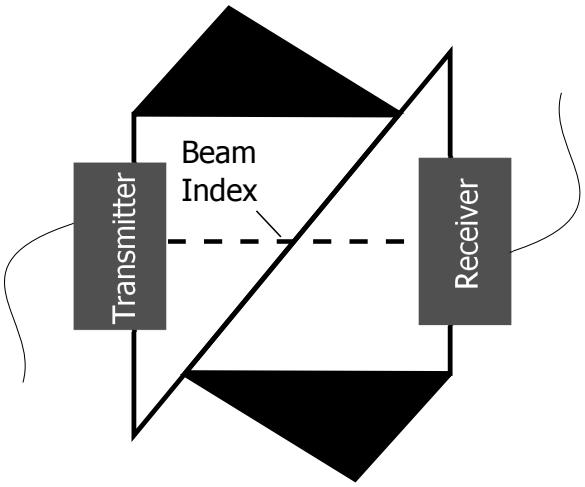

Figure 7.27: Sensor to sensor test setup used to measure wedge delay and collect reference signal

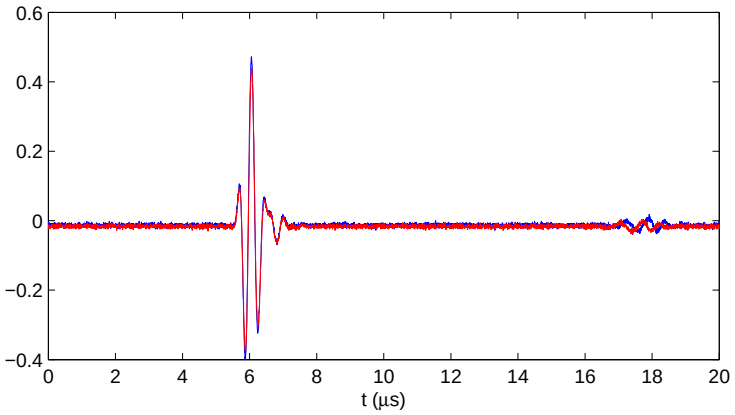

Figure 7.28: Reference signal for the cross-correlation method

a step function for triggering the 2.25MHz transmitter. The oscilloscope recorded the ultrasonic signal measured by the receiver at a sampling frequency of 100MHz. The sampling frequency was selected well above the transducer center frequency to avoid aliasing. Two repeated data samples were collected for each setting.

To calculate the TOFD, the wedge delay (the time that the wave travels in the wedge) needs to be calculated. To calculate the wedge delay, an experiment was conducted by placing the two transducers facing each other as shown in Figure 7.27. Figure 7.28 shows signals recorded on two trials. This signal will be also used as reference signal for the cross-correlation method in Chapter 4.

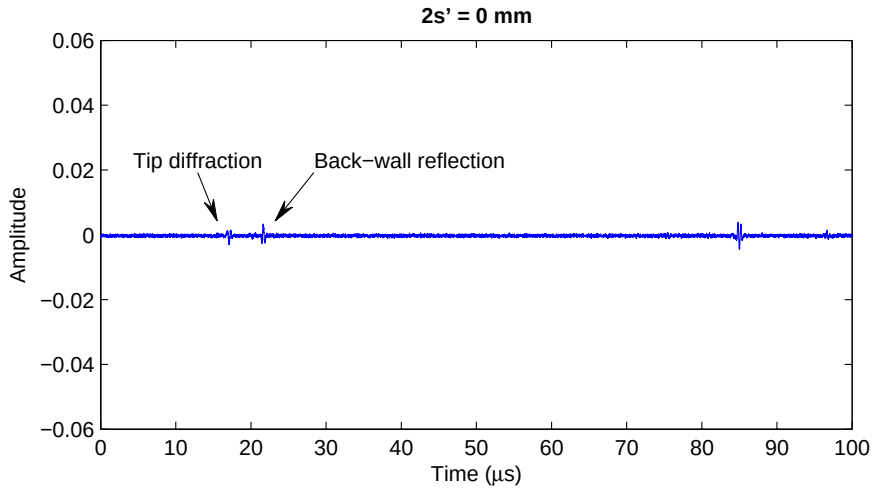

Figure 7.29: Experimental ultrasonic A-scan, $2s' = 0$

Time of Flight Diffraction Experiments

Two sets of experiments were conducted. In the first set, the two transducers were placed so the crack was located midway between the transmitter and the receiver. The thickness of the specimen was 22.5 mm, and the length of the edge crack was 12.5 mm. Ultrasonic signals were collected when the distance between the two wedges ($2s'$) were: 0 mm, 2 mm, 4 mm, 6 mm, 8 mm, and 10 mm.

Figures 7.29-7.34 show the ultrasonic A-scans for different wedge distances. In each A-scan, two echoes are marked: tip diffraction and backwall echoes. As can be seen, the amplitude of the backwall echo is greater than that of the tip diffraction. Generally, the larger the distance between the two transducers, the weaker the tip diffraction echo. This can be clearly observed by comparing Figure 7.34 with other figures.

The second experiment was conducted using similar settings. It was designed to examine the effect of the two transducers being placed asymmetrically around the crack. We kept the same distances between two wedges as the first experiment, but changed their distance to the crack position. For every 2s' distance, we conducted experiment when the distance, s'_1, between the transmitter's wedge and the crack took each of the following values: 0, 1, 2, ... , $2s'$.

Figures 7.35-7.39 show the ultrasonic A-scans for different locations of the transducers when the distance between two wedges was 4 mm. The amplitude and the time of flight values of both tip diffraction echo and backwall echo were almost the same for different A-scans.

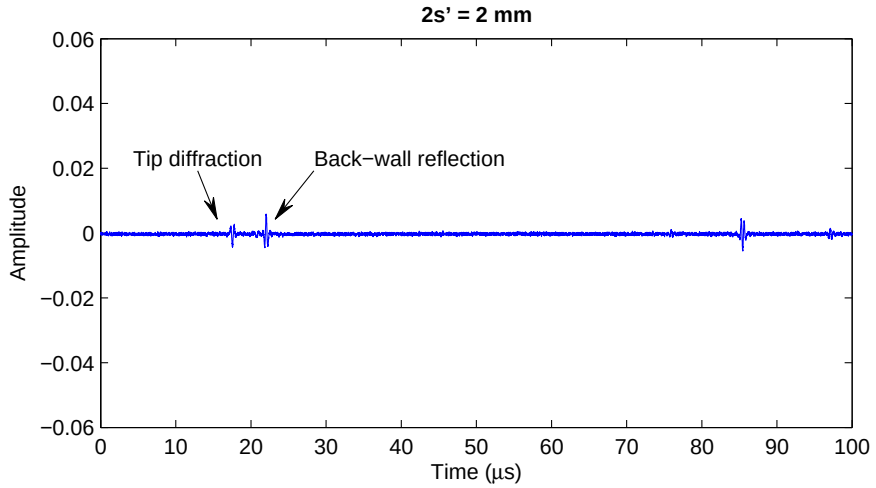

Figure 7.30: Experimental ultrasonic A-scan, $2s' = 2$

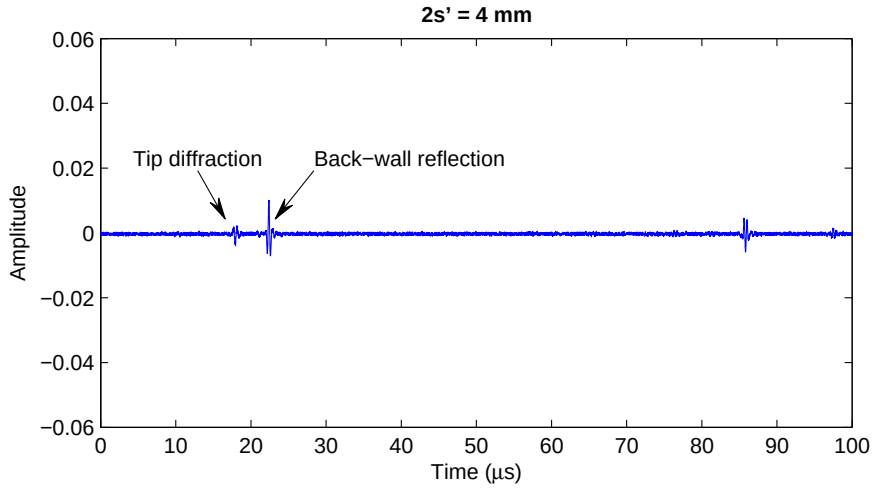

Figure 7.31: Experimental ultrasonic A-scan, $2s' = 4$

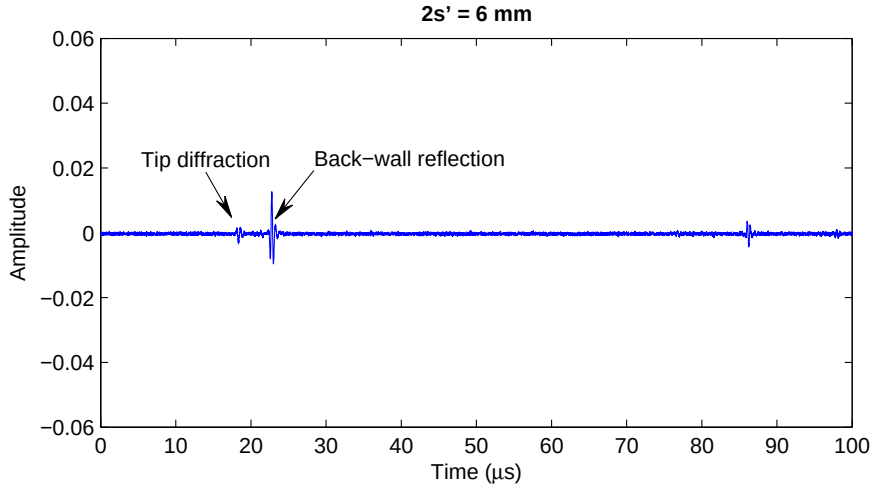

Figure 7.32: Experimental ultrasonic A-scan, $2s' = 6$

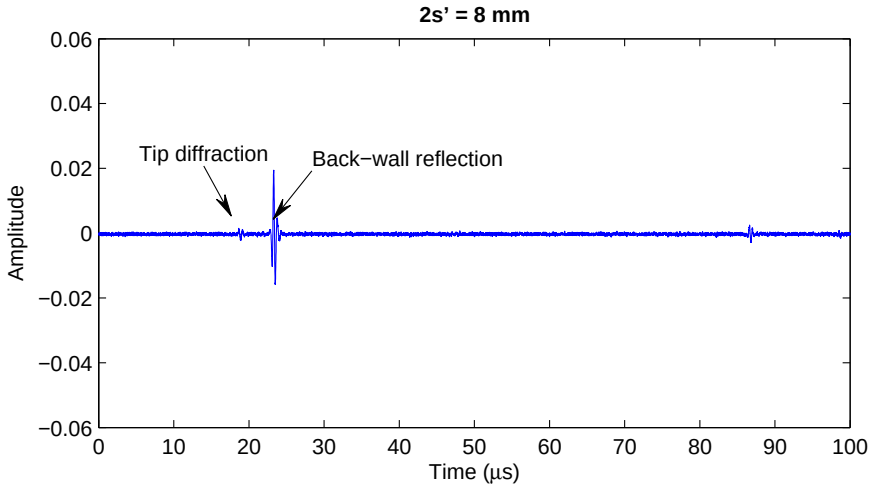

Figure 7.33: Experimental ultrasonic A-scan, $2s' = 8$

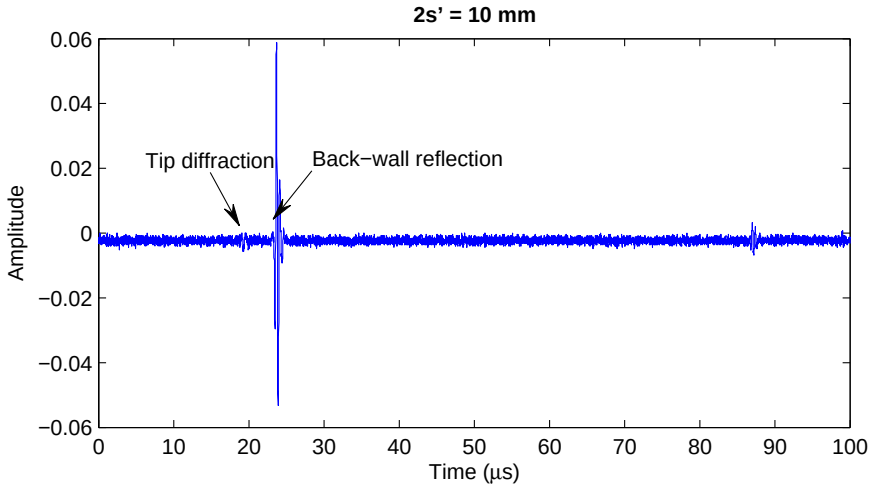

Figure 7.34: Experimental ultrasonic A-scan, $2s' = 10$

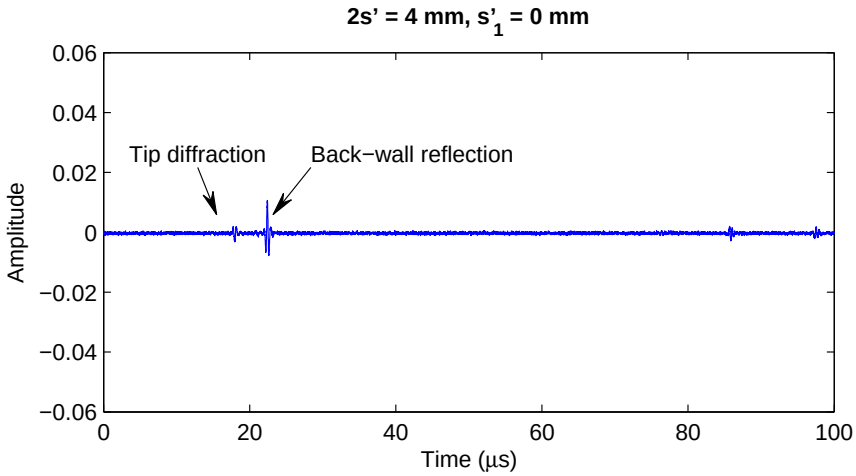

Figure 7.35: Experimental ultrasonic A-scan, $2s' = 4$, $s'_1 = 0$

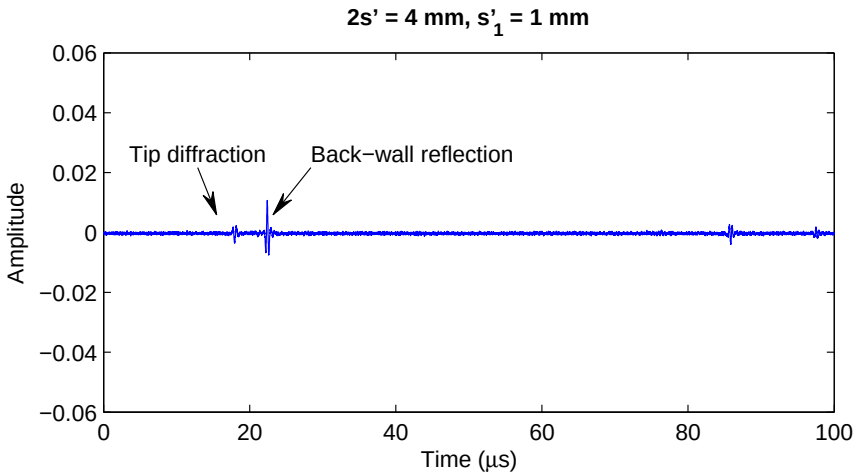

Figure 7.36: Experimental ultrasonic A-scan, $2s' = 4$, $s'_1 = 1$

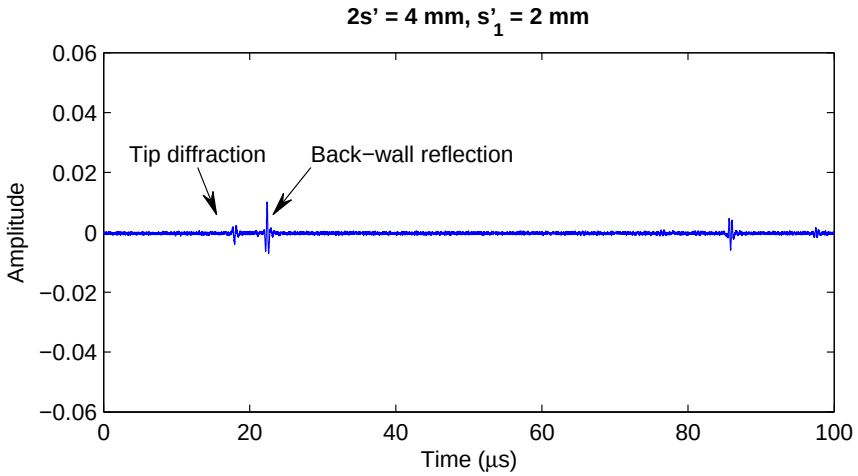

Figure 7.37: Experimental ultrasonic A-scan, $2s' = 4$, $s'_1 = 2$

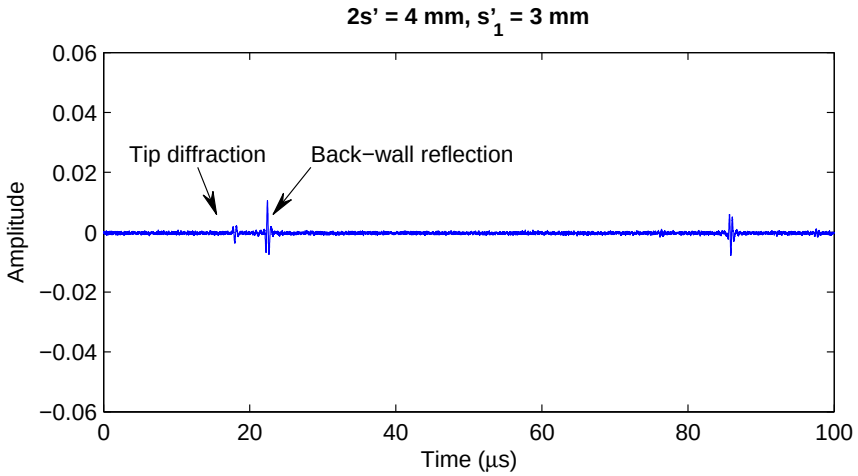

Figure 7.38: Experimental ultrasonic A-scan, $2s' = 4$, $s'_1 = 3$

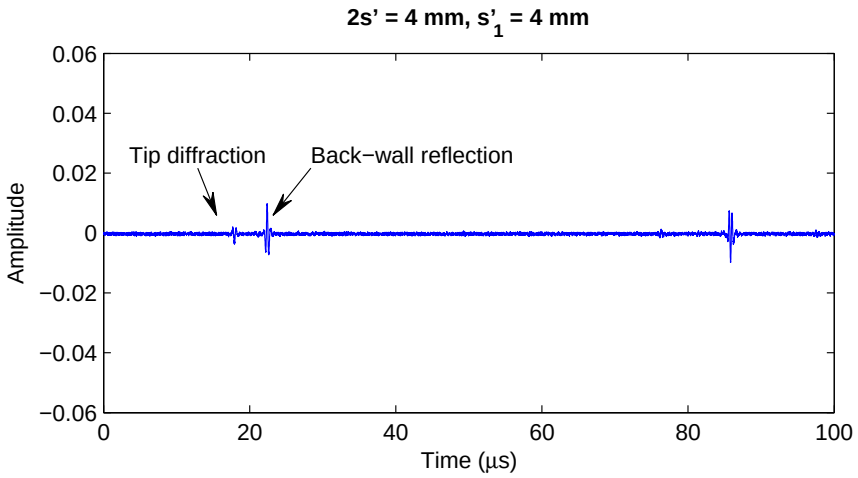

Figure 7.39: Experimental ultrasonic A-scan, $2s' = 4$, $s'_1 = 4$

7.3 Summary

In this chapter, the experimental data which are used throughout this thesis have been described. We have mostly used the experimental data which were available in the Reliability Research Lab at University of Alberta. In addition to these experimental data, we have conducted two more experiments which are explained in Sections 7.1.4 and 7.1.5.

For the pulse-echo setup, we have derived the equations for the minimum temporal and spatial resolution in order to avoid aliasing. Comparing these values and the step size and the sampling frequency used in the pulse-echo experiment shows that the aliasing is negligible.

Chapter 8

Summary and Conclusions

In this thesis, we have investigated different aspects of ultrasonic B-scan signal processing for damage detection and assessment. As shown in Chapter 4, B-scan signals can provide much more reliable estimation of the time of flight of ultrasonic echoes than A-scan signals. The TOF is the primary parameter which is used in crack size estimation. In addition, the B-scan images provide more information about the damage. For example, in Chapter 5, we have used B-scan images to estimate the crack orientation.

Because of these advantages and advances in hardware technology, the B-scan images are becoming increasingly more popular in NDT. However, little research has been reported on the ultrasonic B-scan signal processing. Therefore, we investigate B-scan signal denoising, parameter estimation and fault identification in this thesis.

8.1 Contributions of this Thesis

In Chapter 3, a method is proposed for removing noise from the ultrasonic pulse-echo B-scan image. The proposed method is based on the analytic wavelet thresholding which was originally proposed for denoising one-dimensional signals by Olhede and Walden [52]. In this method, the stationary wavelet coefficients were denoised based on the amplitude of the envelope of the signal. To extend this method to two dimensions, we have first addressed the problem of extracting the envelope of a two-dimensional signal. It has been shown that by introducing a reference vector the envelope of an ultrasonic pulse-echo B-scan image can be extracted. In addition, we have implemented a step to remove the interface noise. Using simulated and experimental signals, it has been shown that the proposed method can effectively remove both random noise and interface noise from the B-scan signal. Using the proposed

method, we could detect cracks as small as 0.1 mm based on the lab experimental data.

In Chapter 4, we have investigated the ultrasonic echo parameter estimation. A model-based method has been proposed for estimating parameters of the ultrasonic echo. In this method, the signal envelope is first extracted. Then, the parameters of the envelope is estimated using quasi maximum likelihood method. The envelope of the echo has fewer parameters than the echo itself. Using experimental A-scan signals, it has been shown that the proposed method performs better than the cross-correlation method and the maximum likelihood method which both utilize the original signals.

In addition, using the mathematical model proposed in Chapter 2 for the ultrasonic pulse-echo B-scan signal, we have shown analytically that the time of flight estimation based on the B-scan signal is more accurate than estimation based on the corresponding A-scan signal. We have also applied the proposed method to the B-scan signal. Again using experimental and simulated signals, we have shown that the TOF estimator based on the envelope of the echo is more accurate than the TOF estimator based on the echo. For comparison, two indicators have been used: a) estimated number of echoes error, and b) TOF error. The estimated number of echoes is related to the probability of detection and the false alarm rate. Therefore, this is a main indicator in NDT. The TOF error is related to crack size estimation error. The comparison shows the proposed method outperforms other methods especially in estimating the number of echoes.

In Chapter 5, a method has been proposed to estimate the crack depth and orientation for inclined cracks using B-scan signals. First, the relation between the crack orientation and depth and the parameters of the corner trap echo and tip diffraction echo has been derived theoretically. The resulting formula has been applied to experimental B-scans and the FE simulated B-scan signals. The results show that the proposed formula is able to estimate the crack depth and orientation.

The contributions of this thesis are summarized as follows:

- A mathematical model has been developed for the ultrasonic pulse-echo B-scan.
- A denoising method for removing random noise and interface noise from ultrasonic B-scans has been proposed.
- A model-based method has been proposed to estimate parameters of the Gaussian echo.

- The accuracy of the time of flight estimation from the B-scan signal is theoretically derived and compared to the accuracy of the time of flight estimation from the A-scan signal.
- The proposed parameter estimation method has been extended to two dimensions to estimate echo parameters from the B-scan.
- Theoretical equations have been derived to estimate the crack depth and orientation for the inclined cracks.

8.2 Future Works

In this thesis, ultrasonic signal denoising, parameter estimation and fault detection has been investigated. Yet, some aspects of the ultrasonic B-scan signal processing have not addressed and need more investigation. In parameter estimation, we have only considered the Gaussian echo model. Although the Gaussian echo model is used widely for modeling ultrasonic signals, it is not always applicable. In addition, the white Gaussian noise is assumed throughout this study. However, noise may follow a different distribution or be correlated. The performance of the proposed parameter estimation method needs to be investigated under these unidealized conditions.

We have applied the methods proposed in this thesis only to the signals obtained from contact transducers. Furthermore, except for the parameter estimation of the 1D signal, we have used signals only from the pulse-echo setup. The applicability of the proposed methods for ultrasonic signals obtained from the pitch-catch setup and the immersion setup should be investigated. In addition, only the surface cracks have been studied. Other types of faults such as voids and inclusions and also the cracks inside the material need to be investigated as well.

Bibliography

[1] Y. Zhang, C. C. Ng, A. Sahoo, H. Chen, and M. J. Zuo, "Inspection of EDM slots on steel blocks using omniscan," Department of Mechanical Engineering, University of Alberta, Edmonton, Alberta, Technical Report, June 2007.

[2] P. Cawley, "Non-destructive testingcurrent capabilities and future directions," *Proceedings of the I MECH E Part L Journal of Materials: Design and Applications*, vol. 215, no. 4, pp. 213–223, 2001. [Online]. Available: http://www.catchword.com/rpsv/cgi-bin/cgi?ini=xref&body=linker&reqdoi=10.1243/1464420011545058

[3] T. Kundu, *Ultrasonic Nondestructive Evaluation: Engineering and Biological Material Characterization*. CRC Press, 2004. [Online]. Available: http://books.google.ca/books?id=-aL4Li-j2mkC

[4] C. D. Wells, "The commercial role of ndt in the context of a changing world." *Insight*, vol. 36, pp. 334–341, 1994.

[5] V. Shanmugam, "NDT Tech Wars: Ultrasound vs. Radiography," Retrieved June 27, 2012, from http://www.frost.com/prod/servlet/market-insight-top.pag?docid=238750264, July 2011.

[6] R. Raj, T. Jayakumar, and M. Thavasimuthu, *Practical non-destructive testing*, 2nd ed. Woodhead Publishing, January 2001.

[7] B. Roberts, "Applying eddy current inspection," Prftechnik NDT GmbH, Germany, Tech. Rep., 1999.

[8] "NDT resource center, 2011." [Online]. Available: http://www.ndt-ed.org

[9] Radhakrishnan, *Welding Technology And Design*, 2nd ed. New Age International (P) Limited, Publishers, 2005.

[10] J. Krautkramer and H. Krautkramer, *Ultrasonic testing of materials*, 4th ed. Springer-Verlag, 1990.

[11] J. Venczel, "Oblique flaw detection using ultrasonic transducers," U.S. Patent 20 080 289 424, November 27, 2008.

[12] G. A. Matzkanin and H. T. Yolken, "Selecting a nondestructive testing method : Ultrasonic testing," *American Welding Society*, vol. 87, pp. 26–30, 2008.

[13] M. Moles, "Defect sizing in pipeline welds: What can we really achieve?" *ASME Conference Proceedings*, vol. 2004, no. 46792, pp. 31–39, 2004. [Online]. Available: http://link.aip.org/link/abstract/ASMECP/v2004/i46792/p31/s1

[14] J. Charlesworth and J. Temple, *Engineering Applications of Ultrasonic Time-of-Flight Diffraction*, 2nd ed. Research Studies Press LTD, 2001.

[15] W. H. Cubberly, R. Bakerjian, and S. of Manufacturing Engineers., *Tool and manufacturing engineers handbook*. Dearborn, Mich. :: Society of Manufacturing Engineers,, c1989.

[16] C. Scruby and L. Drain, *Laser Ultrasonics: Techniques and Applications*. A. Hilger, 1990. [Online]. Available: http://books.google.ca/books?id=KgXPqx9ST-wC

[17] R. Hou, D. Hutson, and K. J. Kirk, "Investigation of thin-film ultrasonic transducers for high-temperature applications," *INSIGHT*, vol. 54, no. 2, pp. 68–71, FEB 2012.

[18] D. Dhital and J. R. Lee, "A fully non-contact ultrasonic propagation imaging system for closed surface crack evaluation," *EXPERIMENTAL MECHANICS*, vol. 52, no. 8, pp. 1111–1122, OCT 2012.

[19] S. Colombo, A. Giannopoulos, M. Forde, R. Hasson, and J. Mulholland, "Frequency response of different couplant materials for mounting transducers," *NDT & E International*, vol. 38, no. 3, pp. 187 – 193, 2005, ¡ce:title¿Structural Faults and Repair¡/ce:title¿. [Online]. Available: http://www.sciencedirect.com/science/article/pii/S0963869504001008

[20] G. Dobie, R. Summan, S. Pierce, W. Galbraith, and G. Hayward, "A noncontact ultrasonic platform for structural inspection," *Sensors Journal, IEEE*, vol. 11, no. 10, pp. 2458 –2468, oct. 2011.

[21] F. Caleyo, J. Gonzalez, and J. Hallen, "A study on the reliability assessment methodology for pipelines with active corrosion defects," *INTERNATIONAL JOURNAL OF PRESSURE VESSELS AND PIPING*, vol. 79, no. 1, pp. 77–86, JAN 2002.

[22] M. Ahammed, "Probabilistic estimation of remaining life of a pipeline in the presence of active corrosion defects," *INTERNATIONAL JOURNAL OF PRESSURE VESSELS AND PIPING*, vol. 75, no. 4, pp. 321–329, APR 1998.

[23] M. Ahammed and R. Melchers, "Reliability estimation of pressurised pipelines subject to localised corrosion defects," *INTERNATIONAL JOURNAL OF PRESSURE VESSELS AND PIPING*, vol. 69, no. 3, pp. 267–272, DEC 1996.

[24] G. Chen and S. Dai, "Study on the reliability assessment methodology for pressure vessels containing defects," *INTERNATIONAL JOURNAL OF PRESSURE VESSELS AND PIPING*, vol. 69, no. 3, pp. 273–277, DEC 1996.

[25] K. Kolowrocki, "On applications of asymptotic reliability functions to the reliability and risk evaluation of pipelines," *INTERNATIONAL JOURNAL OF PRESSURE VESSELS AND PIPING*, vol. 75, no. 7, pp. 545–558, JUN 1998.

[26] J. Zhou and S. Shen, "A study on the reliability assessment methodology for pressure piping containing circumferential defects i: Computation method of failure probability of welded joint containing circumferential defects," *INTERNATIONAL JOURNAL OF PRESSURE VESSELS AND PIPING*, vol. 75, no. 9, pp. 679–684, AUG 1998.

[27] C. J. Hellier, *Handbook of nondestructive evaluation.* McGraw-Hill, 2001.

[28] J. Blitz and G. Simpson, *Ultrasonic methods of non-destructive testing*, 1st ed. Springer, 1996.

[29] D. O. Thompson, "Evolution of qnde's core interdisciplinary science and engineering base," *AIP Conference Proceedings*, vol. 1211, no. 1, pp. 3–25, 2010. [Online]. Available: http://link.aip.org/link/?APC/1211/3/1

[30] E. Ginzel, *Ultrasonic Testing in Canada*, 1st ed. Materials Research Institute, Waterloo, Canada: NDT.net, August 1996. [Online]. Available: http://www.ndt.net/article/map/ca_map/ca.htm

[31] E. Ginzel and M. Hoff, "Further developments in ultrasonic inspection of pipeline girth welds," *NDT.net*, vol. 1, no. 6, June 1996. [Online]. Available: http://www.ndt.net/article/ginz_pl/ginz_pl.htm

[32] J. L. Rose, *Ultrasonic waves in solid media.* Cambridge University Press, 1999.

[33] K. M. Mahmud, N. Baba, and R. Ohba, "Using of a diverse field algorithm in ultrasonic signal processing for nondestructive testing," *The European Physical Journal Applied Physics*, vol. 15, pp. 3–6, 2001.

[34] H.-C. Wu, N. Gupta, and P. Mylavarapu, "Blind multiridge detection for automatic nondestructive testing using ultrasonic signals," *Ultrasonics, Ferroelectrics and Frequency Control, IEEE Transactions on*, vol. 53, no. 10, pp. 1902 –1911, october 2006.

[35] L. Satyanarayan, K. B. Kumaran, C. Krishnamurthy, and K. Balasubramaniam, "Inverse method for detection and sizing of cracks in thin sections using a hybrid genetic algorithm based signal parametrisation," *Theoretical and Applied Fracture Mechanics*, vol. 49, no. 2, pp. 185 – 198, 2008. [Online]. Available: http://www.sciencedirect.com/science/article/B6V55-4R9GGMG-2/2/083f42f3072b8ede86c3279b996b8ae6

[36] G. H. Wilkie, T. J. Elm, and D. L. Engen, "Comparison of crack detection in-line inspection tools," in *Proceedings of the 4th International Pipeline Conference*, Calgary, Alberta, 2002, 'CD-ROM'.

[37] A. M. Sabatini, "A digital-signal-processing techniques for ultrasonic signal modeling and classification," *IEEE transactions on instrumentation and measurement*, vol. 50, no. 1, pp. 15–21, 2001.

[38] A. Raghavan and C. E. S. Cesnik, "Review of guided-wave structural health monitoring," *The Shock and Vibration Digest*, vol. 39, no. 2, pp. 91–114, 2007.

[39] X. Li, N. Bilgutay, and R. Murthy, "Spectral histogram using the minimization algorithm-theory and applications to flaw detection," *Ultrasonics, Ferroelectrics and Frequency Control, IEEE Transactions on*, vol. 39, no. 2, pp. 279 –284, Mar. 1992.

[40] K. Donohue and H. Cheah, "Spectral correlation filters for flaw detection," in *Ultrasonics Symposium, 1995. Proceedings., 1995 IEEE*, vol. 1, Nov. 1995, pp. 725 –728 vol.1.

[41] J. R. Houghton and P. Shen, "Ultrasonic reflector classification with autoregressive models," *Research in Nondestructive Evaluation*, vol. 1, pp. 235–246, 1990, 10.1007/BF01608221. [Online]. Available: http://dx.doi.org/10.1007/BF01608221

[42] A. K. Nandi, *Blind Estimation Using Higher-Order Statistics*. Springer, 1999.

[43] R. Miralles, L. Vergara, and J. Gosalbez, "Material grain noise analysis by using higher-order statistics," *Signal Process.*, vol. 84, pp. 197–205, January 2004. [Online]. Available: http://dx.doi.org/10.1016/j.sigpro.2003.10.007

[44] U. Abeyratne, A. Petropulu, J. Reid, T. Golas, E. Conant, and F. Forsberg, "Higher order versus second order statistics in ultrasound image deconvolution," *Ultrasonics, Ferroelectrics and Frequency Control, IEEE Transactions on*, vol. 44, no. 6, pp. 1409 –1416, Nov. 1997.

[45] H. Cygan, L. Girardi, P. Aknin, and P. Simard, "B-scan ultrasonic image analysis for internal rail defect detection," in *Proceedings of WCRR 2003*, Edinburgh, Scotland, 2003.

[46] D. Donoho, "De-noising by soft-thresholding," *Information Theory, IEEE Transactions on*, vol. 41, no. 3, pp. 613 –627, May 1995.

[47] L. White and B. Boashash, "Cross spectral analysis of nonstationary processes," *Information Theory, IEEE Transactions on*, vol. 36, no. 4, pp. 830 –835, jul 1990.

[48] M. Kreidl and P. Houfek, "Reducing ultrasonic signal noise by algorithms based on wavelet thresholding," *Acta Polytechnica*, vol. 42, no. 2, pp. 60–65, 2002.

[49] V. Matz, M. Kreidl, R. Smid, and S. Starman, "Comparison of de-noising methods used for emat signals," *NDT Welding Bulletin*, vol. 2006, no. Special, pp. 43–47, 2006.

[50] V. Kananen, J. Eskelinen, and E. Haeggstrom, "P1e-3 ultrasonic qnde instrument for quantitative inclusion and pore characterization of steel billets," in *Ultrasonics Symposium, 2007. IEEE*, October 2007, pp. 1373 –1376.

[51] H. Chen, M. J. Zuo, X. Wang, and M. R. Hoseini, "An adaptive morlet wavelet filter for time-of-flight estimation in ultrasonic damage assessment," *Measurement*, vol. 43, no. 4, pp. 570 – 585, 2010. [Online]. Available: http://www.sciencedirect.com/science/article/B6V42-4Y5GXW4-1/2/42dad3f21705a402e743f64d480f1db7

[52] S. C. Olhede and A. T. Walden, "Analytic wavelet thresholding," *Biometrika*, vol. 91, no. 4, pp. 955–973, 2004. [Online]. Available: http://biomet.oxfordjournals.org/content/91/4/955.abstract

[53] L. Satyanarayan, C. Sridhar, C. Krishnamurthy, and K. Balasubramaniam, "Simulation of ultrasonic phased array technique for imaging and sizing of defects using longitudinal waves," *International Journal of Pressure Vessels and Piping*, vol. 84, no. 12, pp. 716 – 729, 2007. [Online]. Available: http://www.sciencedirect.com/science/article/B6V3N-4PFW6H5-1/2/a3daabb8095c2277fcd5cdc33a54b7f6

[54] P. Ciorau, "Contribution to detection and sizing linear defects by conventional and phased array ultrasonic techniques," in *16th WCNDT 2004 - World Conference on NDT*, Montreal, Canada, 2004.

[55] M. Silk, "Changes in ultrasonic defect location and sizing," *NDT International*, vol. 20, no. 1, pp. 9 – 14, 1987. [Online]. Available: http://www.sciencedirect.com/science/article/pii/0308912687903671

[56] C. N. Shitole, O. Zahran, and W. Al-Nuaimy, "Combining fuzzy logic and neural networks in classification of weld defects using ultrasonic time-of-flight diffraction," *Insight*, vol. 49, no. 2, pp. 79–82, 2007.

[57] R. Demirli and J. Saniie, "Model-based estimation of ultrasonic echoes. part i: Analysis and algorithms," *IEEE Trans Ultrason Ferroelectr Freq Control*, vol. 48, no. 3, pp. 787–802, 2001.

[58] K. Ferrera, R. Algazi, and J. Liu, "The effect of frequency dependent scattering and attenuation on the estimation of blood velocity using ultrasound," *IEEE Trans. Ultrason., Ferroelect., Freq. Contr*, vol. 39, no. 6, p. 754767, November 1992.

[59] L. W. Schmerr Jr., *Fundamentals of Ultrasonic Nondestructive Evaluation: A Modeling Approach*. Plenum Press, 1998.

[60] V. N. Bindal, *Transducers for Ultrasonic Flaw Detection.* Narosa Pub House, 1999.

[61] S. Golan, L. Adler, K. V. Cook, R. K. Nanstad, and T. K. Bolland, "Ultrasonic diffraction technique for characterization of fatigue cracks," *Journal of Nondestructive Evaluation*, vol. 1, pp. 11–19, 1980, 10.1007/BF00566228. [Online]. Available: http://dx.doi.org/10.1007/BF00566228

[62] J. Davis, "Advanced ultrasonic flaw sizing handbook," *The e-Journal of Nondestructive Testing & Ultrasonics*, vol. 3, no. 11, 1998. [Online]. Available: http://www.ndt.net/article/1198/davis/davis2.htm

[63] M. Silk, *Sizing crack-like defects by ultrasonic means. Chapter 2 of Research Techniques in non-destructive testing*, R. S. Sharpe, Ed. San Diego: Academic, 1977, vol. III.

[64] "MIL-HDBK-728/6, Military Handbook: Ultrasonic Testing (16 DEC 1985), Department of Defence, United States of America." [Online]. Available: http://www.everyspec.com

[65] A. Kumar, K. V. Rajkumar, P. Palanichamy, T. Jayakumar, V. Patankar, V. Joshi, B. Lande, R. Chellapandian, K. Kasiviswanathan, and B. Raj, "Development and applications of c-scan ultrasonic facility," *Journal of Non-Destructive Testing and Evaluation*, vol. 4, no. 1, pp. 11–16, 2005.

[66] C. Chen, *Ultrasonic and Advanced Methods for Nondestructive Testing and Material Characterization.* World Scientific Publishing, 2007.

[67] G.-M. Zhang, C.-G. Hou, Y.-W. Wang, and S.-Y. Zhang, "Optimal frequency-to-bandwidth ratio of wavelet in ultrasonic non-destructive evaluation," *Ultrasonics*, vol. 39, no. 1, pp. 13 – 17, 2001. [Online]. Available: http://www.sciencedirect.com/science/article/B6TW2-41XVB0D-3/2/430a23774447a740c543dc82a4b7c266

[68] T. W. Liao and J. Ni, "An automated radiographic ndt system for weld inspection: Part i – weld extraction," *NDT & E International*, vol. 29, no. 3, pp. 157 – 162, 1996. [Online]. Available: http://www.sciencedirect.com/science/article/B6V4C-3WC4NKW-3/2/cff8b0ec267f6456fe72c683dd8ed397

[69] R. Demirli and J. Saniie, "A generic parametric model for ultrasonic signal analysis," in *Ultrasonics Symposium (IUS), 2009 IEEE International*, sept. 2009, pp. 1522 –1525.

[70] G. Cavaccini, M. Agresti, G. Borzacchiello, E. Bozzi, M. Chimenti, and O. Salvetti, "An evaluation approach to ndt ultrasound processes by wavelet transform," in *15th WCNDT- World Conference on NDT*, Roma, 2000.

[71] P. Bolland, L. Lew Yan Voon, B. Gremillet, L. Pillet, A. Diou, and P. Gorria, "The application of hough transform on ultrasonic images for the detection and characterization of defects in non-destructive inspection," in *Signal Processing, 1996., 3rd International Conference on*, vol. 1, Oct. 1996, pp. 393 –396 vol.1.

[72] K. Maalmi, A. El-Ouaazizi, R. Benslimane, L. Lew Yan Voon, A. Diou, and P. Gorria, "Crack defect detection and localization using genetic-based inverse voting hough transform," in *Pattern Recognition, 2002. Proceedings. 16th International Conference on*, vol. 3, 2002, pp. 257 – 260 vol.3.

[73] Y. Jayet, J. Baboux, M. Lethiecq, and M. Perdrix, "Response of a longitudinal transducer to a longitudinal or shear wave under oblique incidence," *Ultrasonics*, vol. 27, no. 2, pp. 91 – 96, 1989. [Online]. Available: http://www.sciencedirect.com/science/article/pii/0041624X8990019X

[74] M. R. Hoseini, M. J. Zuo, and X. Wang, "Two dimensional analytic wavelet thresholding and its application to ultrasonic pulse-echo b-scan denoising," in *CCECE'10*, 2010, pp. 1–5.

[75] M. R. Hoseini, M. J. Zuo, and X. Wang, "Denoising ultrasonic pulse-echo signal using two-dimensional analytic wavelet thresholding," *Measurement*, vol. 45, no. 3, pp. 255 – 267, 2012. [Online]. Available: http://www.sciencedirect.com/science/article/pii/S0263224111004441

[76] Z. Qi, Q. Pei-Wen, L. Qing-kun, C. Tian-lu, and H. Tao, "Application of empirical mode decomposition to ultrasonic signal," in *Ultrasonics Symposium, 2005 IEEE*, vol. 3, sept. 2005, pp. 1789 – 1792.

[77] D. V. Perov, A. B. Rinkevich, and Y. G. Smorodinskii, "Wavelet filtering of signals from ultrasonic flaw detector," *Russian Journal of Nondestructive Testing*, vol. 38, pp. 869–882, 2002, 10.1023/A:1023852822195. [Online]. Available: http://dx.doi.org/10.1023/A:1023852822195

[78] J. Lazaro, "Noise reduction in ultrasonic ndt using discrete wavelet transform processing," in *Ultrasonics Symposium, 2002. Proceedings. 2002 IEEE*, vol. 1, oct. 2002, pp. 777 – 780 vol.1.

[79] J. Lazaro, J. S. Emeterio, A. Ramos, and J. Fernandez-Marron, "Influence of thresholding procedures in ultrasonic grain noise reduction using wavelets," *Ultrasonics*, vol. 40, no. 1-8, pp. 263 – 267, 2002. [Online]. Available: http://www.sciencedirect.com/science/article/pii/S0041624X0200149X

[80] T. lu Chen, P. wen Que, Q. Zhang, and Q. kun Liu, "Ultrasonic signal identification by empirical mode decomposition and hilbert transform," *Review of Scientific Instruments*, vol. 76, no. 8, p. 085109, 2005. [Online]. Available: http://link.aip.org/link/?RSI/76/085109/1

[81] Y.-m. Mao and P.-w. Que, "Application of hilbert-huang signal processing to ultrasonic non-destructive testing of oil pipelines," *Journal of Zhejiang University - Science A*, vol. 7, pp. 130–134, 2006, 10.1631/jzus.2006.A0130. [Online]. Available: http://dx.doi.org/10.1631/jzus.2006.A0130

[82] E. Pardo, J. S. Emeterio, M. Rodriguez, and A. Ramos, "Noise reduction in ultrasonic ndt using undecimated wavelet transforms," *Ultrasonics*, vol. 44, Supplement, pp. e1063 – e1067, 2006, proceedings of Ultrasonics International and World Congress on Ultrasonics (WCU). [Online]. Available: http://www.sciencedirect.com/science/article/pii/S0041624X06001338

[83] E. Pardo, J. L. San Emeterio, M. A. Rodrguez, and A. Ramos, "Shift invariant wavelet processing of ultrasonic traces," in *XIX Congreso Internacional de Acstica (ICA2007)*. Sociedad Espaola de Acstica (SEA), 2007. [Online]. Available: http://hdl.handle.net/10261/5325

[84] Q. Zhang, P.-w. Que, and W. Liang, "Applying sub-band energy extraction to noise cancellation of ultrasonic ndt signal," *Journal of Zhejiang University - Science A*, vol. 9, pp. 1134–1140, 2008, 10.1631/jzus.A0720072. [Online]. Available: http://dx.doi.org/10.1631/jzus.A0720072

[85] M. Kubinyi and R. Smid, "Ultrasonic denoising with a modified wavelet filter," in *Intelligent Data Acquisition and Advanced Computing Systems (IDAACS), 2011 IEEE 6th International Conference on*, vol. 1, sept. 2011, pp. 479 –482.

[86] C. Burckhardt, "Speckle in ultrasound b-mode scans," *Sonics and Ultrasonics, IEEE Transactions on*, vol. 25, no. 1, pp. 1 –6, jan. 1978.

[87] J. Bamber and C. Daft, "Adaptive filtering for reduction of speckle in ultrasonic pulse-echo images," *Ultrasonics*, vol. 24, no. 1, pp. 41 – 44, 1986. [Online]. Available: http://www.sciencedirect.com/science/article/pii/0041624X86900727

[88] X. Hao, S. Gao, and X. Gao, "A novel multiscale nonlinear thresholding method for ultrasonic speckle suppressing," *Medical Imaging, IEEE Transactions on*, vol. 18, no. 9, pp. 787 –794, sept. 1999.

[89] D. Lai, N. Rao, C. hui Kuo, S. Bhatt, and V. Dogra, "An ultrasound image despeckling method using independent component analysis," in *Biomedical Imaging: From Nano to Macro, 2009. ISBI '09. IEEE International Symposium on*, 28 2009-july 1 2009, pp. 658 –661.

[90] R. Sivakumar and D. Nedumaran, "Article:comparative study of speckle noise reduction of ultrasound b-scan images in matrix laboratory environment," *International Journal of Computer Applications*, vol. 10, no. 9, pp. 46–50, November 2010, published By Foundation of Computer Science.

[91] J. Bordier, M. Fink, A. Le Brun, and F. Cohen-Tenoudji, "The random phase transducer in ultrasonic nondestructive testing of coarse grain stainless steel: An original tool to characterize multiple scattering effect," in *Ultrasonics Symposium, 1992. Proceedings., IEEE 1992*, oct 1992, pp. 877 –882 vol.2.

[92] Y. Cao, H. Zhu, and P. Yang, "Ultrasonic time of flight diffraction defect recognition based on edge detection," in *Biomedical Engineering and Computer Science (ICBECS), 2010 International Conference on*, april 2010, pp. 1 –4.

[93] I. Wells, P. C. Charlton, S. Mosey, and K. E. Donne, "Background noise removal in ultrasonic b-scan images using iterative statistical techniques," *Quality and Reliability Engineering International*, vol. 24, no. 8, pp. 873–879, 2008. [Online]. Available: http://dx.doi.org/10.1002/qre.902

[94] O. Rioul and M. Vetterli, "Wavelets and signal processing," *Signal Processing Magazine, IEEE*, vol. 8, no. 4, pp. 14 –38, oct. 1991.

[95] N. Ruiz-Reyes, P. Vera-Candeas, J. Curpin-Alonso, R. Mata-Campos, and J. Cuevas-Martnez, "New matching pursuit-based algorithm for snr improvement in ultrasonic ndt," *NDT & E International*, vol. 38, no. 6, pp. 453 – 458, 2005. [Online]. Available: http://www.sciencedirect.com/science/article/pii/S0963869504001549

[96] A. N. Akansu, W. A. Serdijn, and I. W. Selesnick, "Emerging applications of wavelets: A review," *Physical Communication*, vol. 3, no. 1, pp. 1 – 18, 2010. [Online]. Available: http://www.sciencedirect.com/science/article/pii/S1874490709000482

[97] S. Mallat, "A theory for multiresolution signal decomposition: the wavelet representation," *Pattern Analysis and Machine Intelligence, IEEE Transactions on*, vol. 11, no. 7, pp. 674 –693, jul 1989.

[98] C. E. Shannon, "A mathematical theory of communication," *SIGMOBILE Mob. Comput. Commun. Rev.*, vol. 5, no. 1, pp. 3–55, Jan. 2001. [Online]. Available: http://doi.acm.org/10.1145/584091.584093

[99] A. Gyaourova, R. Kamath, and I. Fodor, "Undecimated wavelet transforms for image denoising," Lawrence Livermore National Laboratory, Technical report UCRL-ID-150931, 2002.

[100] M. Lang, H. Guo, J. Odegard, C. Burrus, and J. Wells, R.O., "Noise reduction using an undecimated discrete wavelet transform," *Signal Processing Letters, IEEE*, vol. 3, no. 1, pp. 10 –12, jan. 1996.

[101] D. L. Donoho and I. M. Johnstone, "Ideal spatial adaptation by wavelet shrinkage 1 introduction," *Compare A Journal Of Comparative Education*, vol. 81, no. June 1992, pp. 425–455, 1993. [Online]. Available: http://biomet.oxfordjournals.org/cgi/content/abstract/81/3/425

[102] S. Mallat, *A Wavelet Tour of Signal Processing, Third Edition: The Sparse Way*, 3rd ed. Academic Press, 2008.

[103] R. R. Coifman and D. L. Donoho, "Translation-Invariant De-Noising," Department of Statistics, Tech. Rep., 1995.

[104] S. Sardy, "Minimax threshold for denoising complex signals with waveshrink," *Signal Processing, IEEE Transactions on*, vol. 48, no. 4, pp. 1023 –1028, apr 2000.

[105] G. Granlund and H. Knutsson, *Signal processing for computer vision*. Kluwer Academic Publishers, 1995. [Online]. Available: http://books.google.ca/books?id=uuSox2n3D1wC

[106] E. Bedrosian, "A product theorem for hilbert transforms," *Proceedings of the IEEE*, vol. 51, no. 5, pp. 868 – 869, may 1963.

[107] T. Blow and G. Sommer, "A novel approach to the 2d analytic signal," in *in CAIP*, 1999, pp. 25–32.

[108] R. Coifman and M. Wickerhauser, "Entropy-based algorithms for best basis selection," *Information Theory, IEEE Transactions on*, vol. 38, no. 2, pp. 713 –718, mar 1992.

[109] S. Mosey, P. C. Charlton, and I. Wells, "Iterative method for background noise removal in ultrasonic b-scan images," *Insight - Non-Destructive Testing and Condition Monitoring*, vol. 48, no. 11, pp. 677–681, 2006. [Online]. Available: http://www.ingentaconnect.com/content/bindt/insight/2006/00000048/00000011/art00007

[110] P. Petcher and S. Dixon, "A modified hough transform for removal of direct and reflected surface waves from b-scans," *NDT & E International*, vol. 44, no. 2, pp. 139 – 144, 2011. [Online]. Available: http://www.sciencedirect.com/science/article/pii/S0963869510001532

[111] Y. Lu, R. Demirli, G. Cardoso, and J. Saniie, "A successive parameter estimation algorithm for chirplet signal decomposition," *Ultrasonics, Ferroelectrics and Frequency Control, IEEE Transactions on*, vol. 53, no. 11, pp. 2121 –2131, november 2006.

[112] G. Baskaran, K. Balasubramaniam, and C. Lakshmana Rao, "Shear-wave time of flight diffraction (s-tofd) technique," *NDT and E International*, vol. 39, no. 6, pp. 458–467, 2006, cited By (since 1996) 14. [Online]. Available: http://www.scopus.com/inward/record.url?eid=2-s2.0-33745684593&partnerID=40&md5=39ca0c5210ddfdd58b1d3d722091f847

[113] A. White, J.-W. Hong, S. Hong, and J. Choi, "Parameter estimation for wavelet transformed ultrasonic signals," *NDT & E International*, vol. 44,

no. 1, pp. 32 – 40, 2011. [Online]. Available: http://www.sciencedirect.com/science/article/pii/S0963869510001118

[114] J. Verkooijen and A. Boulavinov, "Sampling phased array - a new technique for ultrasonic signal processing and imaging," *INSIGHT*, vol. 50, no. 3, pp. 153–157, MAR 2008, 4th Middle East Nondestructive Testing Conference 2007, BAHRAIN, DEC, 2007.

[115] Z. Lu, G. Wei, and F. Chen, "TOF estimation of ultrasonic echo signal for object location," *Information Technology Journal*, vol. 10, pp. 2182–2188, 2011. [Online]. Available: http://scialert.net/abstract/?doi=itj.2011.2182.2188

[116] N. Trimborn, "The time-of-flight-diffraction technique," *UTonline Journal*, vol. 2, no. 9, 1997. [Online]. Available: http://www.ndt.net/article/tofd/trimborn/trimborn.htm

[117] B. Xu, L. Yu, and V. Giurgiutiu, "Advanced methods for time-of-flight estimation with application to lamb wave structural health monitoring," in *7th International Workshop on Structural Health Monitoring*, Stanford, CA, USA, 2009.

[118] R. Jansohn and M. Schickert, "Objective interpretation of ultrasonic concrete images," in *Proc. of 7th European Conf. on Non-Destructive Testing (ECNDT)*, Denmark, 1998, p. 808815.

[119] D. R. Hull, H. E. Kautz, and A. Vary, "Measurement of ultrasonic velocity using phase-slope and cross-correlation methods," *ASNT Spring Conference*, 1985.

[120] Z. X. Ding and P. A. Payne, "A new golay code system for ultrasonic pulse echo measurements," *Measurement Science and Technology*, vol. 1, no. 2, p. 158, 1990. [Online]. Available: http://stacks.iop.org/0957-0233/1/i=2/a=010

[121] L. Angrisani and R. Schiano Lo Moriello, "Estimating ultrasonic time-of-flight through quadrature demodulation," *Instrumentation and Measurement, IEEE Transactions on*, vol. 55, no. 1, pp. 54 – 62, feb. 2006.

[122] I. Fodor. (2002) A survey of dimension reduction techniques. [Online]. Available: http://citeseerx.ist.psu.edu/viewdoc/summary?doi=10.1.1.8.5098

[123] R. Bellman, *Dynamic Programming*. Dover Publications, Mar. 2003. [Online]. Available: http://www.amazon.com/exec/obidos/redirect?tag=citeulike07-20&path=ASIN/0486428095

[124] W. H. Lawton and E. A. Sylvestre, "Elimination of linear parameters in nonlinear regression," *Technometrics*, vol. 13, no. 3, pp. pp. 461–467, 1971. [Online]. Available: http://www.jstor.org/stable/1267160

[125] P. Gammell, "Improved ultrasonic detection using the analytic signal magnitude," *Ultrasonics*, vol. 19, no. 2, pp. 73 – 76, 1981. [Online]. Available: http://www.sciencedirect.com/science/article/pii/0041624X81901116

[126] M. R. Hoseini, X. Wang, and M. J. Zuo, "Estimating ultrasonic time of flight using envelope and quasi maximum likelihood method for damage detection and assessment," *Measurement*, vol. 45, no. 8, pp. 2072–2080, October 2012.

[127] M. R. Hoseini, X. Wang, and M. J. Zuo, "Using ultrasonic pulse-echo b-scan signals for time of flight estimation," 2012, submitted to Measurement.

[128] S. Kay, *Fundamentals of Statistical Signal Processing: Estimation Theory*, ser. Prentice Hall Signal Processing Series. Prentice-Hall PTR, 1993, no. v. 1. [Online]. Available: http://books.google.ca/books?id=aFwESQAACAAJ

[129] A. Pertsch, J.-Y. Kim, Y. Wang, and L. J. Jacobs, "An intelligent stand-alone ultrasonic device for monitoring local structural damage: implementation and preliminary experiments," *Smart Materials and Structures*, vol. 20, no. 1, p. 015022, 2011. [Online]. Available: http://stacks.iop.org/0964-1726/20/i=1/a=015022

[130] C. Kuan, "The quasi-maximum likelihood method: Theory," in *Introduction to econometric theory*. Academia Sinica, 2001.

[131] D. R. Cox and N. Reid, "A note on pseudolikelihood constructed from marginal densities," *Biometrika*, vol. 91, no. 3, pp. 729–737, 2004. [Online]. Available: http://biomet.oxfordjournals.org/content/91/3/729.abstract

[132] A. Conn, N. Gould, and P. Toint, *Trust-Region Methods*, ser. Mps-Siam Series on Optimization. Society for Industrial and Applied Mathematics, 2000. [Online]. Available: http://books.google.ca/books?id=5kNC4fqssYQC

[133] *Optimization Toolbox 5 Users Guide*, Mathworks Inc., 2010.

[134] *Federal Standard 1037C: Telecommunications: Glossary of Telecommunication Terms*, Federal Standard Std., August 1996.

[135] Y. Zhang, Y. Wang, M. Zuo, and X. Wang, "Ultrasonic time-of-flight diffraction crack size identification based on cross-correlation," in *Electrical and Computer Engineering, 2008. CCECE 2008. Canadian Conference on*, may 2008, pp. 001 797 –001 800.

[136] M. Feldman, *Hilbert Transform Applications in Mechanical Vibration*. John Wiley & Sons, 2011.

[137] H. Akaike, "A new look at the statistical model identification," *IEEE Transactions on Automatic Control*, vol. 19, no. 6, pp. 716–723, Dec. 1974. [Online]. Available: http://dx.doi.org/10.1109/TAC.1974.1100705

[138] K. P. Burnham, "Multimodel inference: Understanding aic and bic in model selection," *Sociological Methods Research*, vol. 33, no. 2, pp. 261–304, 2004. [Online]. Available: http://smr.sagepub.com/cgi/doi/10.1177/0049124104268644

[139] H. Shono, "Is model selection using akaike's information criterion appropriate for catch per unit effort standardization in large samples?" *Fisheries Science*, vol. 71, no. 5, pp. 978–986, 2005. [Online]. Available: http://www.blackwell-synergy.com/doi/abs/10.1111/j.1444-2906.2005.01054.x

[140] H. Bozdogan, "Model selection and akaike's information criterion (aic): The general theory and its analytical extensions," *Psychometrika*, vol. 52, no. 3, pp. 345–370, 1987. [Online]. Available: http://dx.doi.org/10.1007/BF02294361

[141] D. Pagodinas, "Ultrasonic signal processing methods for detection of defects in composite materials," *ULTRAGARSAS*, vol. 45, no. 4, pp. 47–54, 2002.

[142] R. CEPEL, "The spatial cross-correlation coefficient as an ultrasonic detection statistic," Master's thesis, University of Missouri, 2007.

[143] C. Brillon, T. Armitt, and O. Dupuis, "TOFD inspection with phased arrays," in *17th World Conference on Nondestructive Testing*, October 2008.

[144] P. Ciorau, "Critical comments on detection and sizing linear defects by conventional tip-echo diffraction and mode-converted ultrasonic techniques for piping and pressure vessel welds," in *NDT.net*, vol. 11, no. 5, 2006.

[145] S. J. Klimu, D. J. Lesco, and J. C. Freche, "Ultrasonic technique for detection and measurement of fatigue cracks," Lewis Reseurch Center, Tech. Rep., 1965.

[146] M. G. Silk, "An evaluation of the performance of the tofd technique as a means of sizing flaws, with particular reference to flaws with curved profiles," *Insight*, vol. 38, pp. 280–287, 1996.

[147] M. R. Hoseini, X. Wang, and M. J. Zuo, "Modified relative arrival time technique for sizing inclined cracks," in preparation.

[148] M. Song, R. Haralick, and F. Sheehan, "Ultrasound imaging simulation and echocardiographic image synthesis," in *Image Processing, 2000. Proceedings. 2000 International Conference on*, vol. 3, 2000, pp. 420 –423 vol.3.

[149] B. Burger, C. Abkai, and J. Hesser, "Simulation of dynamic ultrasound based on ct models for medical education." *Stud Health Technol Inform*, vol. 132, pp. 56–61–, 2008. [Online]. Available: http://ukpmc.ac.uk/abstract/MED/18391257

[150] J. A. Johnson, N. M. Carlson, and D. M. Tow, "Ray trace calculations of ultrasonic fields," *Research in Nondestructive Evaluation*, vol. 3, no. 1, pp. 27–39, 1991. [Online]. Available: http://www.tandfonline.com/doi/abs/10.1080/09349849109409500

[151] N. Tole and H. Ostensen, *Basic Physics of Ultrasonographic Imaging*, ser. WHO/Diagnostic Imaging and Laboratory Technology Series. World Health Organization, 2005, ch. 5: Ultrasound Beam Shape, pp. 39–47.

[152] J. D. Buttram, "Crack orientation determination and detection using horizontally polarized shear waves," U.S. Patent 5 383 365, January 24, 1995.

[153] P. Reynolds and J. Mould, "Short course: Finite element modeling for ultrasonic applications: Part 1: FEA basics," in *IEEE Ultrasonics Symposium*, Netherland, 2005.

[154] J. Jin, *The Finite Element Method in Electromagnetics*, 2nd ed. Wiley-IEEE Press, 2002.

[155] I. M. Smith and D. V. Griffiths, *Programming the finite element method*, 4th ed. John Wiley and Sons, 2004.

[156] P. Wriggers, *Nonlinear Finite Element Methods*. Springer, 2010. [Online]. Available: http://books.google.ca/books?id=_LgGkgAACAAJ

[157] K. Bathe, *Finite element procedures*, ser. MIT video course. Prentice Hall, 1996. [Online]. Available: http://books.google.ca/books?id=AJBRAAAAMAAJ

[158] J. Schijve, *Fatigue of Structures and Materials*. Springer, 2009. [Online]. Available: http://books.google.ca/books?id=PFsJhYgvOG8C

[159] *Ansys® LS-Dyna user's guide, Release 13.0*, Ansys Inc., Southpointe, 227 Technology Drive, Canonsburge, November 2010.

[160] D. Baek, J. A. Jensen, and M. Willatzen, "Modeling transducer impulse responses for predicting calibrated pressure pulses with the ultrasound simulation program field ii," *The Journal of the Acoustical Society of America*, vol. 127, no. 5, pp. 2825–2835, 2010. [Online]. Available: http://link.aip.org/link/?JAS/127/2825/1

[161] *Ansys® Academic Research, Release 13.0, Mechanical APDL Element Reference*, Ansys Inc., 2010.

[162] R. Livesley, *Finite elements: an introduction for engineers*. Cambridge University Press, 1983. [Online]. Available: http://books.google.ca/books?id=0Hk6AAAAIAAJ

[163] F. Moser, L. J. Jacobs, and J. Qu, "Modeling elastic wave propagation in waveguides with the finite element method," *NDT & E International*, vol. 32, no. 4, pp. 225 – 234, 1999. [Online]. Available: http://www.sciencedirect.com/science/article/pii/S0963869598000450

[164] K.-J. Bathe and G. Noh, "Insight into an implicit time integration scheme for structural dynamics," *Computers & Structures*, vol. 9899, no. 0, pp. 1–6, 2012. [Online]. Available: http://www.sciencedirect.com/science/article/pii/S0045794912000107

[165] X. Sun, E. A. Witzel, H. Bian, and S. Kang, "3-d finite element simulation for ultrasonic propagation in tooth," *Journal of Dentistry*, vol. 36, no. 7, pp. 546 – 553, 2008. [Online]. Available: http://www.sciencedirect.com/science/article/pii/S0300571208001103

[166] J. Hoffman, *Numerical Methods for Engineers and Scientists, Second Edition,*. Taylor & Francis, 2001. [Online]. Available: http://books.google.ca/books?id=VKs7Afjkng4C

[167] J. Park and E. Kausel, "Numerical dispersion in the thin-layer method," *Computers & Structures*, vol. 82, no. 78, pp. 607 – 625, 2004. [Online]. Available: http://www.sciencedirect.com/science/article/pii/S0045794904000021

[168] R. Mullen and T. Belytschko, "Dispersion analysis of finite element semidiscretizations of the two-dimensional wave equation," *International Journal for Numerical Methods in Engineering*, vol. 18, no. 1, pp. 11–29, 1982. [Online]. Available: http://dx.doi.org/10.1002/nme.1620180103

[169] R. Cook, *Concepts and applications of finite element analysis*. Wiley, 2001. [Online]. Available: http://books.google.ca/books?id=b8seAQAAIAAJ

[170] P. Gupta, G. Giridhara, and S. Gopalakrishnan, "Damage detection based on damage force indicator using reduced-order fe models," *International Journal for Computational Methods in Engineering Science and Mechanics*, vol. 9, no. 3, pp. 154–170, 2008. [Online]. Available: http://www.tandfonline.com/doi/abs/10.1080/15502280801909127

[171] H. Chen, C. C. Ng, M. J. Zuo, and X. Wang, "Design of experiments for the pipeline project," Department of Mechanical Engineering, University of Alberta, Tech. Rep., 2007.

[172] M. R. Hoseini, C. C. Ng, and M. J. Zuo, "Measured dimensions of specimens & the EDM slots (plates)," Department of Mechanical Engineering, University of Alberta, Edmonton, Alberta, Technical Report, May 2007.

[173] *Standard Practice for Ultrasonic Angle-Beam Contact Testing*, American Society for Testing Materials Std. ASTM E587, 2010.

[174] L. Satyanarayan, A. Kumar, T. Jayakumar, C. Krishnamurthy, K. Balasubramaniam, and B. Raj, "Sizing cracks in power plant components using array based ultrasonic techniques," *Journal of Nondestructive Evaluation*, vol. 28, pp. 111–124, 2009, 10.1007/s10921-009-0053-9. [Online]. Available: http://dx.doi.org/10.1007/s10921-009-0053-9

[175] A. Jitsumori and T. Inari, "Detection of near-surface flaws using linear fm ultrasonic wave," *Japanese Journal of Applied Physics*, vol. 24S1, no. Supplement 24-1, pp. 100–102, 1985. [Online]. Available: http://jjap.ipap.jp/link?JJAPS/24S1/100/

[176] A. Oppenheim and R. Schafer, *Discrete-time signal processing*, 3rd ed., ser. Prentice-Hall signal processing series. Prentice Hall, 2010. [Online]. Available: http://books.google.ca/books?id=mYsoAQAAMAAJ

[177] N. Aurelle, D. Guyomar, C. Richard, P. Gonnard, and L. Eyraud, "Nonlinear behavior of an ultrasonic transducer," *Ultrasonics*, vol. 34, no. 2-5, pp. 187 – 191, 1996, proceedings of Ultrasonics International 1995. [Online]. Available: http://www.sciencedirect.com/science/article/B6TW2-3VRVTCH-11/2/95508878f1861cc1258edff69604275b

[178] *OmniScan Conventional Ultrasound Module*, R/D Tech, March 2006.